Shaping the interplay of free electrons and light with optical metasurfaces

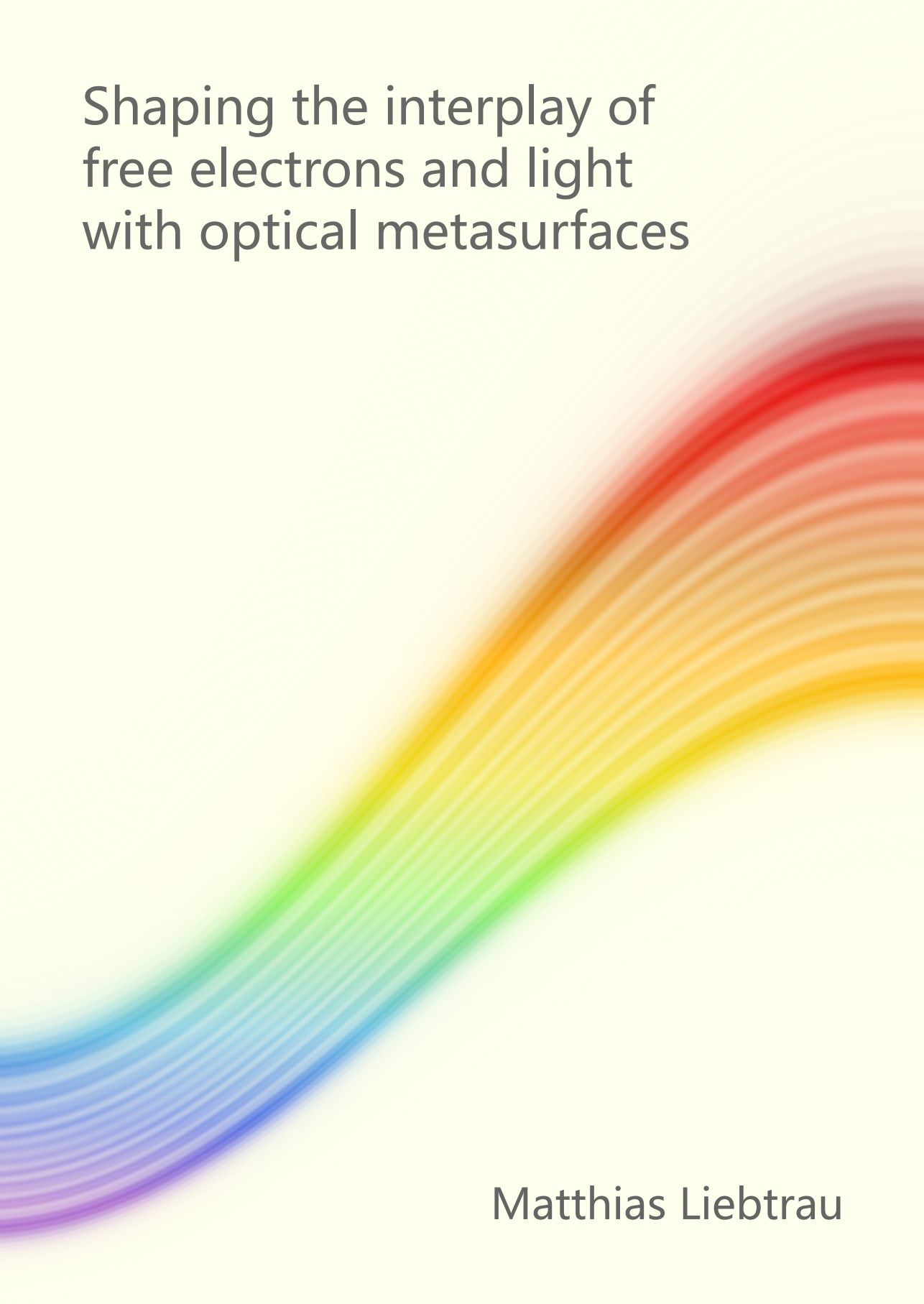

Matthias Liebtrau

SHAPING THE INTERPLAY OF FREE ELECTRONS AND LIGHT WITH OPTICAL METASURFACES

Revision September 2024: All changes to the original printed booklet of this thesis are listed in an Errata at the end of this document.

Shaping the interplay of free electrons and light with optical metasurfaces
Ph.D. Thesis, University of Amsterdam, September 2023
Matthias Liebtrau

ISBN: 978-94-6473-272-6

Cover design: *Analytically modelled far-field intensity distribution of Smith-Purcell radiation with a cylindrical wavefront that is emitted by a free-electron-driven metalens, as studied in Chapter 3.*

The work described in this thesis was performed between October 2018 and August 2023 at NWO-Institute AMOLF, Science Park 104, 1098 XG Amsterdam, The Netherlands.

This work is part of the Dutch Research Council (NWO). It has received funding by the European Research Council (ERC) under the European Union's Horizon research and innovation programme (Grant agreements No. 695343 (SCEON), No. 101017720 (eBEAM) and No. 101019932 (QEWS)).

A digital version of this thesis is available at:
https://ir.amolf.nl and https://www.lmpv.nl/theses/.

Printed by https://www.proefschriften.nl

SHAPING THE INTERPLAY OF FREE ELECTRONS AND LIGHT WITH OPTICAL METASURFACES

ACADEMISCH PROEFSCHRIFT

ter verkrijging van de graad van doctor
aan de Universiteit van Amsterdam
op gezag van de Rector Magnificus
prof. dr. ir. P.P.C.C. Verbeek
ten overstaan van een door het College voor Promoties ingestelde commissie,
in het openbaar te verdedigen in de Agnietenkapel
op donderdag 9 november 2023, te 10.00 uur

door Matthias Liebtrau
geboren te Keulen

Promotiecommissie

Promotor:	prof. dr. A. Polman	Universiteit van Amsterdam
Copromotor:	prof. dr. A.F. Koenderink	Universiteit van Amsterdam
Overige leden:	prof. dr. P.C.M. Planken	Universiteit van Amsterdam
	prof. dr. F.E. Schreck	Universiteit van Amsterdam
	dr. J. van de Groep	Universiteit van Amsterdam
	prof. dr. N. Talebi	University of Kiel
	prof. dr. C. Ropers	University of Göttingen

Faculteit der Natuurwetenschappen, Wiskunde en Informatica

Contents

1 Introduction **1**
1.1 The interplay of free electrons and light 3
1.2 Outline of this thesis 6

2 Spontaneous and stimulated electron-photon interactions in nanoscale plasmonic near fields **9**
2.1 Introduction 10
2.2 EELS, CL, and PINEM theory 11
2.3 Sample preparation 13
2.4 EELS and CL measurements 14
2.5 PINEM measurements 16
2.6 Numerical simulations 18
2.7 Spatial dependence 20
2.8 Dependence on electron energy 22
2.9 Discussion & conclusion 23
2.10 Methods 25

3 Cylindrical metalens for generation and focusing of free-electron radiation **29**
3.1 Introduction 30
3.2 Metalens theory 31
3.3 Sample fabrication and experimental setup 34
3.4 Metalens radiation patterns 35
3.5 Combined wavefront and polarization control 39
3.6 Discussion & conclusion 41
3.7 Supplementary Information 42
3.8 Appendix: Green's function formalism of the metalens 55

4 Free-electron-light coupling in an optical fibre-integrated metagrating **57**
4.1 Introduction 58
4.2 Sample preparation and experimental setup 60
4.3 Coherent and incoherent signal contributions 62
4.4 Analytical signal modelling 64
4.5 Free-electron light coupling via the metagrating 66
4.6 Discussion & conclusion 72
4.7 Appendix: Analytical derivation of the SPR signal 74

5 Low-energy electron spectroscopy in the scanning electron microscope **75**
5.1 Introduction 76
5.2 Original and modified RFA configurations 77
5.3 Experimental setup 78

5.4 Numerical simulations 79
5.5 Continous beam measurements with the original RFA 81
5.6 Pulsed beam measurements with the modified RFA 83
5.7 Discussion & conclusion 87

Bibliography **89**

List of publications and author contributions **109**

Summary **111**

Samenvatting **115**

Zusammenfassung **121**

Acknowledgements **127**

About the author **131**

1

Introduction

"There are two ways of spreading light:
to be the candle or the mirror that reflects it."
— Edith Wharton, 1902

Light is a diverse phenomenon that surrounds us in many different forms. Harnessing and controlling this phenomenon is becoming more and more relevant to satisfy the ever-growing demand for technological progress in our society. Over most of human history, light has only been accessible to us in the form of sunlight or as a fire. It took until the 19th century that the advent of the first incandescent light bulbs laid the foundation for our modern use of light. By exploiting the flow of current through a thin conductive wire, electrical power is converted into black-body radiation, most of which is released as heat and a small fraction of which is perceived as visible light. Over the decades, this approach has been complemented by numerous methods to generate light with much greater power conversion efficiencies and in a much more controlled fashion. Important examples include fluorescent light tubes that harness optical transitions in gas atoms, or light-emitting diodes that rely on the radiative recombination of electrical charges in a semiconductor [1]. In the early 1960s, another technological revolution was unleashed by the advent of the laser – an amplifier for light [2–6]. The laser relies on a reflective cavity that contains a gain medium, such as fluorescent gas or a semiconductor to compress and intensify light in a small volume [7]. Today, this invention is indispensable to virtually any application that requires a powerful light source in research and technology.

Fundamentally, light can be described both as an electromagnetic wave [10] and as a stream of particles that carry a discrete amount of energy and momentum, called photons [11]. In its role as a wave, the light comprises electric and magnetic field components which carry a frequency, wavelength, amplitude, polarization, and phase. As shown in Fig. 1.1, light is not just limited to what is perceived by the human eye.

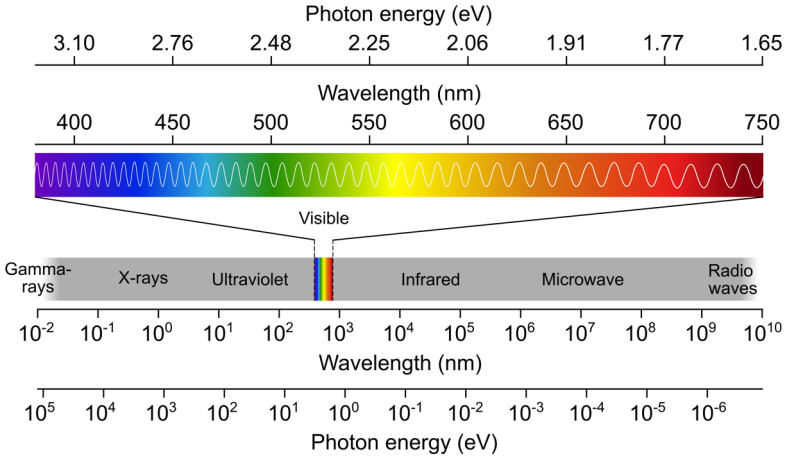

Figure 1.1: The electromagnetic spectrum. There are no hard boundaries between the different categories of radiation, but rather continuous transitions. Figure created on basis of refs. [8, 9].

Instead, light can assume many different forms, including radio waves that are used to broadcast information over large distances, microwave radiation that is used for telecommunication, infra-red (IR) radiation that transmits heat, ultraviolet (UV) radiation that enables the fabrication of computer chips, X-radiation that is applied for medical imaging, and highly-energetic gamma radiation that results from the decay of atomic nuclei. The wavelength and photon energy of light stand in inverse relation to one another. For example, the visible (VIS) spectrum extends in wavelength from approximately 380 nm (violet) to 750 nm (red), while the corresponding photon energies range from 3.26 eV to 1.65 eV electron-volts (eV). In this thesis, we focus on radiation in the IR-VIS-UV spectral range, hereinafter referred to as the optical regime.

The response of a material to a certain kind of radiation is determined by its dielectric properties. As light propagates through matter, its wavelength is compressed by the refractive index of the medium. This gives rise to refraction of light as it encounters the interface between two media [12]. In addition, impurities and defects in a material can generate optical transitions that lead to the absorption or emission of light. And furthermore, structured materials can scatter or guide light, thereby controlling its propagation, re-directing or even shaping the light [12]. Experimentally, such phenomena can be studied using spectroscopic and interferometric tools that probe the effect of a material on the spectral composition, the intensity, the phase and the polarization of light [13]. The spatial resolution at which such experiments can be performed is typically constrained by the optical diffraction limit, given by approximately half the wavelength of the light in the embedding medium. This is also known as the Abbe limit which defines the maximum spatial resolution of an optical microscope [14]. However, many interesting phenomena take place at much smaller length scales [15]. Specifically, in the proximity of tiny nanoparticles, the intensity of light can be enhanced on very small length scales, giving rise to the formation of localized optical near-fields [12, 16].

Among other uses, these near-fields permit metallic nanoparticles to stimulate and amplify photo-catalytic reactions [17–20]. In photovoltaics, the scattering of light by nanoscale structures can be harnessed to enhance light trapping in a solar cell [21–23]. And in integrated photonics, nanostructured materials can be used to manipulate and control the flow of light [24–27]. There is a long list of applications which rely on the spatial confinement of light at deep-subwavelength length scales [15], raising the question: how can such localized optical phenomena be studied experimentally?

1.1 The interplay of free electrons and light

With the advent of electron microscopy in 1931 it has become possible to resolve structural material features fully independent of the optical diffraction limit [29]. This is achieved by exploiting high-energy electrons (typically 5 - 300 keV) that undergo elastic and inelastic collisions with the constituent atoms of a material [30]. Interestingly, over the past two decades, it has been shown that electron microscopy also provides a powerful platform to probe optical phenomena at the nanometer length scale by exploiting the coupling of the transient electric field of the electrons to polarisable charges in a specimen [31–33]. This coupling is fundamentally different from the

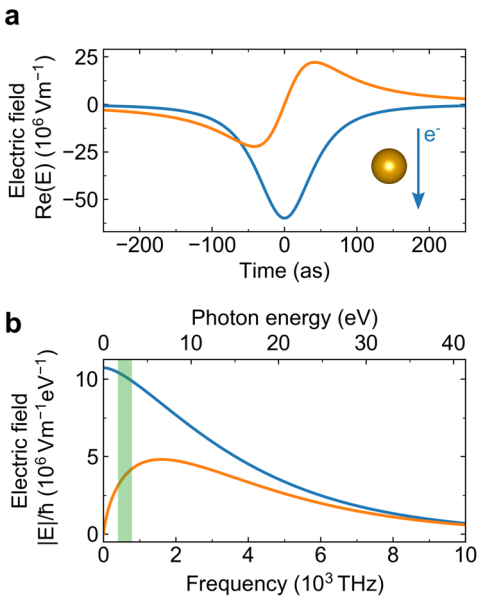

Figure 1.2: a Electric field of a swift free electron that acts on a gold nanosphere at a distance of 5 nm to the electron trajectory. The electron has a kinetic energy of 20 keV, corresponding to a velocity of approximately 27 % of the speed of light in vacuum. The blue and the orange curves represent the real parts of the radial and the longitudinal electric field components, respectively. **b** Spectral representation of the radial (blue curve) and longitudinal (orange curve) electron electric field components in **a**. The data are expressed in terms of the electromagnetic wave frequencies (bottom axis) and corresponding photon energies (top axis). Figure created on basis of ref. [28].

excitation of a material with light as it is highly localized in both space and time. As a consequence, the electron can drive optical phenomena on very small length and time scales, and over a very broad spectral range [28]. To illustrate this correlation, Fig. 1.2a shows the time evolution of the electric field that a swift free electron exerts on a gold nanosphere as it passes by in close proximity. The blue and the orange curves represent the radial and the longitudinal electric field components, respectively. As can be seen, the field undergoes a single cycle with a duration of less than a femtosecond. As further shown in Fig. 1.2b, this ultra-short electromagnetic pulse can be decomposed into a broad spectrum of electromagnetic waves with photon energies from zero to several tens of electron-volts, thus extending over the entire IR-VIS-UV spectral range.

As an electron polarises a material and couples to an optical excitation, it undergoes a spontaneous energy loss which can be probed experimentally using electron energy-loss spectroscopy (EELS) [34–37]. EELS is a common technique that was originally implemented in transmission electron microscopes (TEMs) to study bulk excitations by electrons upon inelastic scattering in a thin specimen [38, 39]. The advent of electron spectrometers, based on magnetic prisms that disperse electrons with an energy resolution much better than 1 eV, opened up an entirely new world of using EELS to study optical material properties [37, 40]. Nowadays, state-of-the-art EELS systems that are integrated in TEMs with a mono-chromated electron source provide an energy resolution down to a few tens of meV [41, 42], even enabling the observation of low-energy phononic excitations in the crystal lattice of a specimen [43–50].

Aside from the characteristic energy loss that an optical excitation leaves as a fingerprint on the electron, the decay of the induced polarization can give rise to the emission of far-field radiation, called cathodoluminescence (CL) [31, 51, 52]. The emitted light carries detailed information which can be retrieved using angle-, polarization- and time-resolved optical spectroscopy [53–62]. Historically, CL analysis has been mainly performed in scanning electron microscopes (SEM), where light is collected using a parabolic mirror. Lately, similar optics have been also introduced in TEM instruments, providing the benefit of a spatial resolutions down to the atomic scale [60, 62]. However, as compared to SEMs, TEMs typically feature very small specimen chambers with dimensions of a few mm which introduces substantial practical constraints.

Another exciting development in the field of electron microscopy is the recent advent of ultra-fast TEM (UTEM) [63–65]. In this approach, laser pulses are used to generate electron pulses as short as several hundred femtoseconds by photo-excitation of the electron cathode, enabling time-resolved spectroscopic measurements. This concept has laid the foundation for photon-induced near-field electron microscopy (PINEM) in which part of the pump laser light is used to optically excite a specimen [66]. Thereby, the laser induces an intense optical near field which is traversed by the electron pulse. As a consequence, the electrons can undergo energy-gain and -loss transitions by stimulated emission and absorption photons [66–70], which can be probed using a magnetic spectrometer as in EELS. The modulation of the electron energy spectrum provides a direct measure of the electron-light interaction strength [67–71]. In recent years, this correlation has been exploited to probe laser-induced optical near-field distributions in various photonic systems, such as carbon nanotubes [66], metallic nanostructures [70, 72–78], photonic crystal cavities [79], and much more [80–84].

The PINEM technique not only yields insights into the distribution of optical fields at the nanoscale. Just like light, electrons exhibit both a particle and a wave-like character [85–87]. According to the laws of quantum mechanics, one can only define a probability for an electron to be at a certain point in space for a given instance in time, as described by the electron wave function [88]. The emission and absorption of photons affects the energy and momentum distribution of the electron, which in turn results in a modulation of its wave function [68–70]. This phenomenon enables the realization of numerous fascinating phenomena as demonstrated in several recent experimental and theoretical publications [70, 71, 79, 81, 89–101]. For example, after its interaction with an optical field, the electron can split up into ultra-short electron wave packets, facilitating ultra-fast optical spectroscopic measurements at attosecond time scales [78, 80, 90, 91]. Furthermore, the electron wave function can be tailored in the plane transverse to its direction of propagation [92, 93], which may enable aberration corrections in an electron microscope [95]. And finally, the electron can be exploited as an information carrier for quantum applications in which light is used to imprint information onto the electron wave function [96, 98, 99].

The fundamental mechanisms that govern the exchange of energy between free electrons and light in EELS, CL, and PINEM are intimately linked [71, 76, 102]. While a photon in free space cannot exchange energy with an electron due to a violation of momentum conservation, the localization of photons in an optical near field introduces a momentum uncertainty that facilitates the interaction [69, 103]. From a wave-like perspective, this means that the optical field is composed of a distribution of evanescent field components which cannot propagate through space, but decay exponentially away from the material boundary [12]. These field components, called Fourier waves, feature wavelengths which are effectively shorter than that of light in free space. Figuratively speaking, this permits the electron to “surf” on a light wave which maintains a constant phase throughout the interaction, a condition known as electron-light phase matching [69, 104]. In the presence of an optical pump field as in PINEM, such a phase-matched interaction renders a net acceleration or deceleration which in turn causes the electron to undergo energy-gain or loss transitions in integer units of the photon energy. In EELS and CL, only an energy loss is possible, however, the electron-light coupling mechanism is fundamentally the same as in PINEM.

Photonic systems allow optical fields to be shaped such that phase-matching between free electrons and light can be optimized. This has been exploited in several recent experiments to enhance the PINEM effect, using a glass prism [82], microcavities [81, 83], and other dielectric structures [84, 99, 105, 106]. Vice versa, phase-matched interactions can also lead to strongly enhanced CL emission. One such example is the Smith-Purcell (SP) effect [107], in which a single electron polarizes a periodic system along a grazing trajectory, thereby inducing multiple radiative excitations that interfere in the far field. Due to the phase-lag between these excitations, the emitted light features a unique angular dispersion which depends on the pitch of the system and the electron velocity.

These fascinating new developments inspire further thoughts on how optical fields can be structured to manipulate their interaction with free electrons. A very powerful approach to tailor the fundamental properties of light relies on texturing the surface

of a material with a pattern of nanoscale structures, known as metasurfaces [108–113]. So far, a wide range of metasurface geometries have been demonstrated that can shape light fields in many different ways, enabling ultra-thin optical elements for imaging and focusing [114–118], polarization control [119, 120], analog image processing[121, 122] and optical computing [123, 124], non-linear frequency conversion [125–129], holography [130, 131], and many applications more [108–113]. In addition, recent advances have been made to design electrically, thermally and optically tunable metasurfaces that provide dynamic control over light [132]. These various capabilities render optical metasurfaces an ideal platform to prepare complex optical fields that efficiently couple to free electrons. In particular, the combination of phase-matched interactions with the resonant enhancement of light in nanostructures opens up a new dimension of control. The use of optical metasurfaces to harness, manipulate and control free-electron-light-matter interactions is an ambitious goal that requires many steps of exploration, several of which are addressed in this thesis.

1.2 Outline of this thesis

As a starting point, in **Chapter 2**, we experimentally study the fundamental correlation between the electron-light-matter interactions that govern EELS, CL and PINEM at the nanometer length scale. While their correlations have been theoretically explored in the past, there has been no experimental observation of all three electron-light interaction mechanisms on the same physical system so far. Here, we study the EELS, CL and PINEM responses of a chemically-synthesized gold nanostar with sharp conical protrusions that sustain highly localized optical near-field distributions in the VIS-NIR spectral range. The CL experiments were done in the SEM-CL instrument at AMOLF while the EELS and PINEM experiments were performed in a UTEM in the group of prof. Claus Ropers at the University of Göttingen. We show how all three techniques rely on the same fundamental phase-matching condition for the coupling between free electrons and light, and demonstrate how this affects the measured spatial near-field distributions of the nanotips.

In **Chapter 3**, we exploit the phase-matching condition for the coupling of electrons and light to design a metasurface that shapes the wavefront of Smith Purcell radiation (SPR), in collaboration with the groups of prof. Ido Kaminer at Technion and prof. Ady Arie at Tel Aviv University in Isreal. Specifically, we implement metalenses based on chirped nano gratings that generate converging or diverging SPR in the VIS-NIR spectral range. To characterize our samples, we apply hyperspectral angle-resolved CL detection in the SEM, revealing the far-field radiation patterns of our metalenses across a broad spectral range. Our measurements are complemented by numerical simulations and analytical theory that display the correlation between the experimental data and the effects of focusing and defocusing, as well as the underlying electron-near-field coupling mechanism.

The insights from Chapter 2 demonstrate the close correlation of photon emission and absorption by free electrons. This inspires the idea that the metasurface concept as explored in Chapter 3 could be also translated to PINEM experiments, in which an external optical pump field is being shaped to manipulate the electron itself. Vice-versa,

PINEM experiments correlated with CL analysis can provide a deeper fundamental understanding of the electron-light-matter interaction. However, so far, PINEM is primarily performed in TEMs which are equipped with suitable electron spectrometers, while CL is mostly implemented in SEMs which offer large specimen chambers with ample room for the integration of light collection optics. An implementation of both techniques, also in combination with EELS on a single platform is of great interest, however, has not been realized so far. In the next two chapters, we demonstrate how these three techniques can be brought closer together in the SEM.

In **Chapter 4**, we adapt the SP effect to demonstrate the coherent coupling of free-electrons and guided optical modes in a circular metallo-dielectric metagrating that is fabricated onto the input facet of a multi-mode optical fibre. Again, resorting to hyperspectral angle-resolved CL detection as in Chapter 3, we are able to resolve and distinguish the dispersion of SP radiation that is emitted into both free space and the fiber core, for a wide range of electron energies. Light detected by an external spectrometer reveals the coherent excitation of guided modes which are found to be spectrally filtered according to the finite numerical aperture of the fibre, and the characteristic dispersion of the SP effect in the fiber core. The concept of an optical-fibre integrated metasurface offers great potential to manipulate an optical pump field that is injected through the fiber, rendering a versatile platform to synthesize complex electron wave packets in the SEM.

Finally, in **Chapter 5** we explore the technical implementation of electron spectroscopy in the SEM, a prerequisite for PINEM, on the basis of an electrostatic retarding field energy analyzer (RFA) that was originally developed in the group of prof. P. Kruit at the Technical University of Delft. We introduce and characterize a modified version of the RFA that enables the acquisition of electron spectra over an energy range from 4 keV to 11 keV, at a resolution better than 1 eV and under pulsed electron beam conditions as typically employed in PINEM.

Overall, this thesis presents fundamental insights into the coupling of free electrons, light, and matter at the nanometer length scale. It shows how the use of optical metasurfaces opens up a powerful new direction to master this interaction at will, and how combined CL and PINEM experiments could be implemented on a single platform. These insights form the basis to generate novel forms of light, to resolve the dynamics of optical phenomena on ultra-small length and time scales, and to further harness and explore the electron wave nature through its interaction with light and matter.

2

Spontaneous and stimulated electron-photon interactions in nanoscale plasmonic near fields

Optical excitations in nanostructures can mediate the interaction of free electrons and photons on ultra-small length and time scales. This phenomenon involves both spontaneous and stimulated interaction mechanisms which have found spectacular applications in recent years. Nevertheless, detailed experimental insights into their fundamental correlations remain scarce so far. Here, we apply electron energy-loss spectroscopy (EELS), cathodoluminescence (CL) spectroscopy, and photon-induced near-field electron microscopy (PINEM) to probe the spectral and spatial characteristics of spontaneous and stimulated electron-photon interactions in the plasmonic near-field of a gold nanostar. Complemented by numerical simulations, we find a common spatial dependence of our measurements on the dipolar electric near-field distribution of a sharp conical nanotip that is resonantly excited by both the electrons themselves in EELS and CL, and by the optical pump in PINEM. Moreover, we show that the electron-photon coupling strength varies with the electron velocity, as determined by the spatial Fourier transformation of the field along the electron trajectory. As a result, our simulations suggest an optimum electron coupling velocity near the tip apex at kinetic energies of a few kilo-electron-volts. By demonstrating the fundamental correlation of EELS, CL and PINEM measurements at the nanometre length scale, our results provide a valuable contribution to the current understanding of free-electron-light-matter interactions.

2.1 Introduction

Photonic nanostructures enable the manipulation of light at deep-subwavelength length scales, opening up a wealth of opportunities for quantum technology, optical signal processing, photovoltaics, molecular sensing, chemical catalysis, and more [15]. Due to the diffraction limit of light, however, the experimental characterisation of these structures poses a fundamental challenge. Interestingly, recent years have shown that free electrons can be used to probe optical excitations in nanomaterials with extreme spatial, spectral and temporal resolutions [31–33].

When a swift free electron passes through or close to a specimen, its time-varying evanescent electric field polarizes the material within a fraction of a femtosecond. As a result, the electron can couple to optical material excitations across the entire ultraviolet-visible-near-infrared (UV-VIS-NIR) spectral range [28]. The energy transfer during this interaction can be measured experimentally using electron energy-loss spectroscopy (EELS) [32, 33, 37]. In addition, cathodoluminescence (CL) spectroscopy can be used to probe the subsequent emission of far-field radiation [32, 33]. Notably, the measured electron energy-loss and photon-emission probabilities are closely linked to the full and the radiative electromagnetic local density of states, respectively [133–135]. Thus, the two techniques are ideally suited for the correlated structural and optical characterization of plasmonic and dielectric nanoparticles [34, 40, 55, 136–138], optical waveguides [139–141], photonic crystal cavities [142, 143], and more [32, 33, 37].

Recently, EELS and CL have been complemented with photon-induced near-field electron microscopy (PINEM) [66]. In this technique, free electrons are used to probe the optical near-field of a nanostructure that is excited by an intense laser. While passing through this near field, the electrons undergo one or multiple energy-gain and energy-loss transitions by stimulated absorption and emission of photons [67–69]. As a consequence, the electron energy spectrum is expanded with sidebands that are evenly spaced by the pump photon energy $\hbar\omega_{\mathrm{L}}$. The population of these sidebands varies with the near-field integral along the electron trajectory and the statistics of the incident light [71], enabling spatially-resolved near-field measurements [70, 72, 73, 75, 79, 81, 144] with fs- and as-temporal [79–81] and meV-spectral resolutions [74]. The key to the PINEM mechanism lies in evanescent spatial Fourier components that bridge the momentum mismatch between free electrons and photons in free space, thus mediating the exchange of energy with the incident pump field. For sufficiently large laser intensities, this interaction can be a highly efficient process in which nearly every electron undergoes stimulated energy-gain or energy-loss transitions [70], even leading to hundreds of net photon exchanges [81, 82]. In contrast, the probability for an electron to spontaneously drive an optical excitation in EELS and CL is typically on the order of 10^{-5} to 10^{-3} per eV energy bandwidth [31].

The full exploitation of the rich new physics that the PINEM effect offers is just starting [32, 33, 70–75, 79–82, 90–92, 144]. Among others, recent work has focused on probing the phase-modulation of free electron wave packets by a coherent optical pump field, enabling phenomena such as the generation of attosecond electron pulse trains [80, 90, 91] or electron vortex beams [92]. The fundamental link between PINEM, EELS, and CL has been studied theoretically for small particles with dipolar resonances [102,

145]. However, a rigorous one-to-one experimental correlation of all three techniques on a single physical structure has not been reported to date.

In this work, we demonstrate spatially-resolved EELS, CL, and PINEM measurements of spontaneous and stimulated electron-photon interactions in the plasmonic near-field of a chemically-synthesized gold nanostar. The structure is composed of an ~50-nm spherical core and sharp conical protrusions that feature tip radii of curvature smaller than 3 nm [146]. As shown in previous works [146–156], these tips sustain dipolar surface plasmon resonances in the VIS-NIR spectral range that give rise to highly-localized optical near fields at the tip apexes, yielding an ideal geometry to compare EELS, CL, and PINEM measurements at the nanometre length scale. Supported by theory and numerical electromagnetic boundary-element method (BEM) calculations, we study the spectral and spatial correlations of the spontaneous and stimulated phenomena probed by the three different techniques. We discuss the dependence of our measurements on the electron velocity and link it to the spatial Fourier distribution of the optical near-field of the nanostar tips along the electron trajectory. Our work provides detailed insights into the correlations of spatially resolved EELS, CL, and PINEM measurements and the underlying spontaneous and stimulated electron-photon interactions.

2.2 EELS, CL, and PINEM theory

First, we consider the interaction of a point-like free electron with a simplified model geometry that is composed of a conical Au tip and a spherical Au core as illustrated in Fig. 1a. We assume that the electron propagates along the z direction, while the tip is oriented in x direction. In this configuration, the time-varying evanescent electric field of the electron couples to a dipolar resonance with a highly concentrated near-field distribution at the tip apex. Due to the back action of this field, the electron undergoes a spontaneous energy loss ΔE that is distributed around the tip resonance energy $\hbar\omega_0$. Subsequently, the energy absorbed by the particle is either dissipated as heat or radiated off as a photon, giving rise to the emission of CL.

In Fig. 2.1a, we plot the electric field $\mathbf{E}_\mathrm{e}$ induced by an electron with a kinetic energy of 20 keV as retrieved from a numerical electromagnetic boundary-element method (BEM) [157–159] calculation (see Methods). We show the real part of the field component that is oriented parallel to the electron trajectory at the tip resonance frequency ω_0 (corresponding to an energy of $\hbar\omega_0 = 1.73$ eV) for the moment that the electron reaches the minimum distance to the tip apex, i.e., $t = 0$. Due to the dipolar nature of the tip mode, the induced field is strongly localized near the tip apex, vanishing along the symmetry axis of the tip while showing opposite polarity above and below (upward field orientation in red; downward field in blue). For a qualitative discussion, we assume that the field is dominated by the dipolar mode field distribution $\mathbf{u}$ of the tip resonance, neglecting a contribution of the spherical core. Moreover, we suppose that the energy loss ΔE of the electron is much smaller than its initial energy E_kin. Within these limitations, the corresponding EELS and CL emission probabilities per unit frequency ω can be approximated as [31, 71, 102]

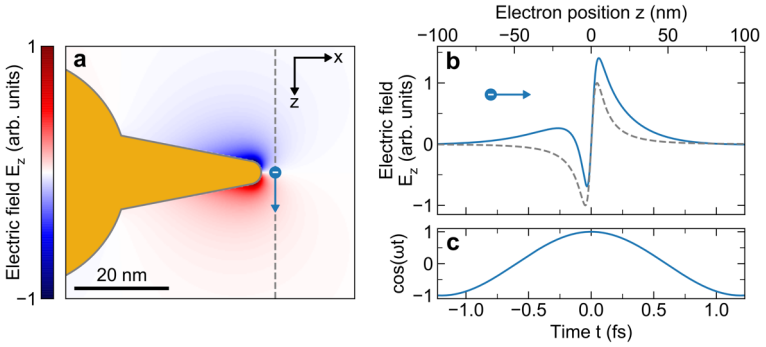

Figure 2.1: Electron-near-field interaction. BEM calculation for 20-keV-free-electron excitation of a three-dimensional model system that is composed of a conical Au nanotip and a spherical Au core (tip length 30 nm, cone aperture angle 22°, tip apex radius-of-curvature 2.5 nm, core diameter 50 nm). The electron passes 3 nm away from the tip apex along the dashed line perpendicular to the symmetry axis of the tip (z direction). **a** Frozen-time snapshot at minimum electron-apex distance ($t = 0$) of the z component of the induced electric field distribution at the tip resonance energy $\hbar\omega_0 = 1.73$ eV. **b** Dashed-grey curve: field profile along the electron trajectory in **a**, with $z = 0$ corresponding to the electron crossing the symmetry axis of the tip. Solid-blue curve: time evolution of the field as effectively experienced by the electron along its trajectory. **c** Time evolution of the optical phase of the field at the plasmon resonance frequency ω_0.

$$\Gamma_{\mathrm{EELS}}(\mathbf{R},\omega) \approx \frac{e^2}{\pi\hbar}\mathrm{Im}\{f(\omega)\}\left|\int_{-\infty}^{\infty} \mathrm{d}z\, u_z(\mathbf{R},z,\omega)\, e^{-i\frac{\omega}{v}z}\right|^2, \tag{2.1}$$

$$\Gamma_{\mathrm{CL}}(\mathbf{R},\omega) \approx \frac{2e^2\omega^3}{3\pi\hbar c^3} A\left|f(\omega)\right|^2\left|\int_{-\infty}^{\infty} \mathrm{d}z\, u_z(\mathbf{R},z,\omega)\, e^{-i\frac{\omega}{v}z}\right|^2, \tag{2.2}$$

where $\mathbf{R} = (x, y)$ and z denote the lateral and along-the-beam electron positions, respectively, e is the electron charge, v is the electron velocity, c is the speed of light in vacuum, $f(\omega)$ is a shape- and material-dependent polarization function, and A describes the radiation efficiency of the mode (e.g., $A = 1$ for a dipolar mode). The exponential term in the integral governing both Eqs. (2.1) and (2.2) describes the temporal phase oscillation of the field as the electron passes by the tip apex at a constant velocity v (time-position relation $t = z/v$). The solid-blue curve in Fig. 2.1b shows the corresponding excursion of the real part of the field as experienced by the electron over time. For reference, the dashed-grey curve shows a cross section through the field distribution displayed in Fig. 2.1a at $t = 0$, and the time evolution of its optical phase is plotted in Fig. 2.1c. Classically, we can say that the electron experiences subsequent acceleration and deceleration along its trajectory, leading to alternating positive and negative contributions to the coupling integral in Eqs. (2.1) and (2.2). As a result, Γ_{EELS} and Γ_{CL} depend only on the Fourier transformation of u_z at an electron-velocity-dependent spatial frequency $q = \omega/v$. This effectively corresponds to a wave that propagates in phase with the electron throughout the interaction [103]. Incidentally, in the limit of large electron velocities v, the integrand in Eqs. (2.1) and (2.2) becomes closer to anti-symmetric with

respect to $z = 0$ ($t = 0$), i.e., the solid-blue curve approaches the shape of the dashed-grey curve in Fig. 2.1b. Thus, its net integral is reduced and the electron couples less efficiently to the tightly confined tip mode.

Next, we consider the effect of a monochromatic optical pump field that is polarized along the symmetry axis and tuned to the resonance frequency of the tip. For typical illumination intensities on the order of a few hundreds of MW/cm^2, the light induces a much larger dipole moment than that generated by an individual electron. As a result, the coupling efficiency between the electron and the near-field of the tip is strongly enhanced at the pump frequency ω_L, facilitating both electron energy-gain and energy-loss transitions by stimulated absorption and emission of photons at an energy exchange $\hbar\omega_\mathrm{L}$. As demonstrated in ref. [70], the energy spectrum of the electron then evolves into a ladder of quantum coherent energy-gain and -loss states, with the population of the ladder states governed by Rabi oscillations in the electron-light energy exchange process.

The probability that an electron undergoes a net amount of n stimulated energy-gain or -loss transitions can be described by Bessel functions of the first kind, n^th order [69, 70]

$$P_n(\mathbf{R},\omega) = J_n^2\left(2\left|\beta(\mathbf{R},\omega)\right|\right)\delta(\omega-\omega_\mathrm{L}), \tag{2.3}$$

where β is the coupling coefficient between the electron and the time-varying laser-induced electric field $2\mathrm{Re}\left\{\mathbf{E}_\mathrm{L}e^{-i\omega_\mathrm{L}t}\right\}$. Within the same limitations as assumed above, this coupling coefficient can be written as [71, 91]

$$\left|\beta(\mathbf{R},\omega)\right| \approx \frac{e}{\hbar\omega}\sqrt{\eta I}\left|f(\omega)\right|\left|\int_{-\infty}^{\infty}\mathrm{d}z\,u_z(\mathbf{R},z,\omega)\,e^{-i\frac{\omega}{v}z}\right|, \tag{2.4}$$

where η denotes the excitation efficiency of the tip resonance by the incident pump field for a given angle of incidence and polarization, and I is the incident field intensity. Incidentally, it has been rigorously shown in ref. [71] that the coupling coefficient associated with a mode depends on its population n as $\left|\beta\right| \propto \sqrt{n}$, which again corroborates the dependence shown in Eq. (2.4) on efficiency and intensity because $n \propto \eta I$. For the sake of clarity, we note that the coupling coefficient β is denoted as g elsewhere [70, 81], accompanied by a leading factor of 1/2 due to a different normalization of the induced electric field as $\mathrm{Re}\left\{\mathbf{E}_\mathrm{L}e^{-i\omega_\mathrm{L}t}\right\}$ (without the leading factor of 2). Interestingly, Eqs. (2.1), (2.2), and (2.4) show that in the limit of an isolated dipolar tip mode, the square of the coupling strength $\left|\beta\right|$ has the same spatial dependence as the spontaneous electron energy-loss and photon-emission probability densities Γ_EELS and Γ_CL. Furthermore, $\left|\beta\right|^2$, equally scales with $\left|f(\omega)\right|^2$, as Γ_CL, demonstrating that both PINEM and CL depend on the radiative nature of the tip modes.

2.3 Sample preparation

The Au nanostar studied in this work was prepared by a modification of a seeded growth approach as reported in refs. [146, 160] with the details of the synthesis procedure outlined in the Methods section. A 30-nm-thin silicon nitride membrane was used to support the particle, ensuring minimum inelastic scattering of the electrons during

EELS and PINEM acquisition as well as minor mixing of defect luminescence with the desired CL signal. After EELS and PINEM measurements, the sample was cleaned by gentle O_2-plasma treatment for a duration of 30 s in order to minimize contamination effects during prolonged CL acquisition.

2.4 EELS and CL measurements

EELS and CL measurements were performed in a scanning transmission electron microscope (STEM) and a scanning electron microscope (SEM) at electron energies of 200 keV and 20 keV, respectively. The corresponding STEM and SEM images of the nanostar taken during data acquisition are shown in the insets in Fig. 2.2a,b. For the measurements, the electron beam was raster-scanned over the sample along a two-dimensional grid of pixels with dimensions of (2×2) nm^2. Figure 2.2a shows EELS spectra as resolved at the positions of four different tip apexes, and the nanostar core. We note that the spectra are numerically deconvolved by the contribution of the zero-loss peak (ZLP), substantially reducing spectral broadening due to the intrinsic energy spread of the electron beam (see Methods section) [161]. At the tips, we observe plasmonic resonances that give rise to pronounced maxima at 1.48 eV, 1.80 eV, 1.84 eV, and 1.94 eV, with a full-width-at-half-maximum (FWHM) on the order of 400 meV. The core shows a broad, comparably flat spectrum, with another faint peak near 1.0 eV. Figure 2.2b shows the CL spectra acquired at approximately the same five positions. Again, the tip spectra indicate distinct plasmonic resonances, with maxima peaking at energies of 1.76 eV, 1.80 eV, 1.97 eV, and 2.04 eV and an FWHM of approximately 200 meV. In the core spectrum, we observe resonant features of similar width, yet smaller amplitude, at 1.8 eV, 2.0 eV, and 2.4 eV.

As is evident from Fig. 2.2a,b, there is significant spectral overlap between the features associated with the different tips and the nanostar core. The high spectral resolution in CL permits the observation of shoulders on the low- or high-energy side of the peaks, indicating that an electron locally couples to more than one tip resonance. In good correspondence with the results of earlier experiments on Au nanostars [152, 154, 155], we attribute the high-energy peak near 2.4 eV to the plasmon resonance of the nanostar core. The side peaks in the core spectrum at 1.8 eV and 2.0 eV further indicate coupling between the core and tip modes, as suggested in ref. [149]. In EELS, the observation of the core resonance is obscured by multiple inelastic scattering events, with the low-energy feature near 1.0 eV presumably corresponding to a noise artefact of the applied ZLP deconvolution algorithm.

To disentangle the spectral and spatial contributions of the individual plasmon resonances, we fit an analytical model to our data assuming a dominant contribution of the resonances of the four tips labelled with Roman numerals I-IV in the insets in Fig. 2.2a,b. In CL, we also take into account the core resonance. In this approach, we neglect retardation effect, assuming that there is no simultaneous spectral and spatial overlap between the modes [134]. In the past, a similar procedure has been applied to disentangle plasmonic excitations of various systems, including nanostars [152], nano triangles [135], and branched nanostructures [162]. The details of the analysis procedure implemented here are given in the Methods section.

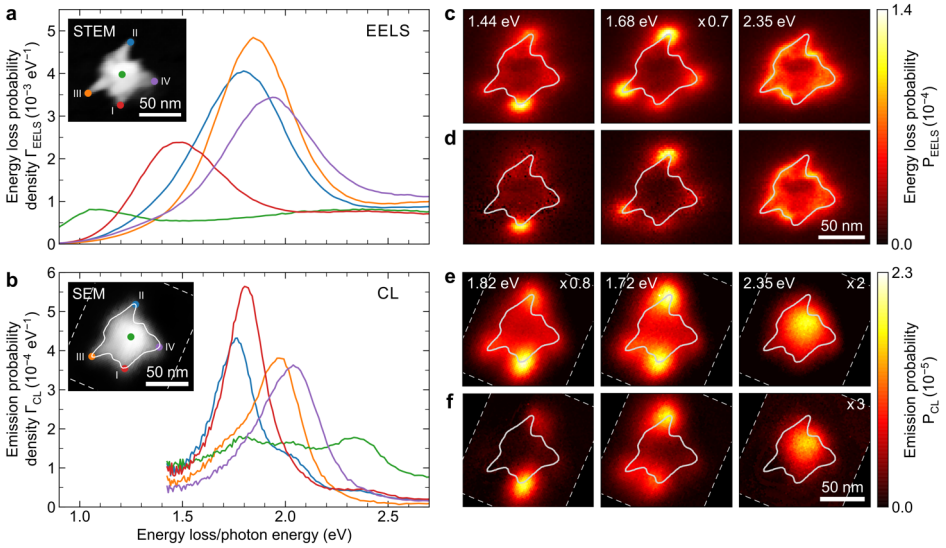

Figure 2.2: EELS and CL measurements. **a** 200 keV STEM-EELS and **b** 20 keV SEM-CL spectra taken at four different tips and at the core of the same chemically synthesized Au nanostar. Electron beam positions are indicated by the colour- matched dots in the insets, showing a STEM bright-field image and an SEM image of the nanostar. All spectra represent an average taken over 5×5 neighbouring pixels. Energy-filtered **c** EELS and **e** CL probability distributions as obtained for a bandwidth of ± 25 meV around the plasmon resonance energies indicated on the top. Fitted **d** EELS and **f** CL probability distributions, revealing the extracted contribution of the tip plasmon resonances to the raw energy-filtered maps in **c** and **e**. The boundaries of the original acquired data sets are indicated by the thin dashed lines in **b**, **e**, and **f**. The solid lines superimposed on the EELS and CL maps, and the SEM image illustrate the approximate contour of the nanostar as inferred from the STEM bright-field image in **a**.

An overview of resonance energies and linewidths derived from our fitting approach are given in Tab. I. The linewidths obtained from the CL data range between 0.16 eV and 0.27 eV, while the EELS analysis yields values between 0.33 eV and 0.44 eV. These substantial deviations indicate residual spectral broadening in EELS due to the intrinsic energy width of the electron beam. Comparing the resonant energies of tips II-IV, we find minor blue shifts of 2-5% in CL with respect to EELS, while tip I shows a considerable blue shift of 26%. Notably, earlier work on silver nano triangles has demonstrated spectral blue shifts between CL and EELS measurements that arise from energy dissipation in the particle itself and in the support substrate [135, 163]. However, we note that our EELS and PINEM measurements were taken first, followed by gentle O_2-plasma treatment of the sample. This procedure turned out to be vital in order to counter-act signal degradation and accompanying spectral blue shifts during prolonged CL acquisition (20-30 min). Therefore, we assume that a contamination with residual chemicals from the synthesis procedure and their reaction to the electron beam contributes to discrepancies between the EELS and CL responses of tips II-IV.

Additionally, the tips might have slightly deformed as a result of oxygen bombardment or laser-induced heating during PINEM acquisition, most likely explaining the substantial spectral shift of tip I. Indeed, as shown in ref. [146], the tip resonances are highly sensitive to the exact tip morphology, with decreasing sharpness and aspect ratio resulting in blue shifts of several tens to hundreds of meV.

In Fig. 2.2c,e, we show energy-filtered EELS and CL maps integrated over a bandwidth of ±25 meV around the resonance energies of tips I and II, as determined from the EELS and CL spectra, respectively, as well as the core resonance (see labels on the top left of each panel). In the latter case, the core region lights up in CL, while it remains mostly dark in EELS. The tip resonances are clearly observed by both techniques, giving rise to strong interaction maxima near the tip apexes. However, as a consequence of spectral overlap between the modes, we can observe multiple tips to light up for a given resonance energy. In Fig. 2.2d,f, we therefore show the amplitude distributions retrieved from the spectral analysis of our data, resolving the ambiguities in the raw energy-filtered maps. For reference, we also plot the contribution of a simple background model assuming a combination of plasmonic and inelastic scattering losses in EELS around 2.35 eV.

Table 2.1: Fitted plasmon resonance energies E_0 and FWHM linewidths γ as derived from the EELS and CL measurements (see Fig. 2.2a,b).

Resonance	EELS (200 keV)		CL (20 keV)	
	E_0 (eV)	γ (eV)	E_0 (eV)	γ (eV)
Tip I (red)	1.44	0.40	1.82	0.16
Tip II (blue)	1.68	0.36	1.72	0.27
Tip III (orange)	1.85	0.33	1.95	0.22
Tip IV (purple)	1.98	0.44	2.06	0.24
Core (green)	–	–	2.35	0.25

2.5 PINEM measurements

PINEM measurements were performed in the same STEM instrument as used for EELS acquisition at an electron energy of 200 keV. The instrument was operated in laser-triggered ultra-fast photoemission configuration, providing sub-picosecond electron pulses that were temporally synchronized with linearly-polarized 3.4-ps optical pump pulses of 1.55-eV central photon energy. The latter were injected nearly normal to the sample plane and had a peak intensity on the order of 1 GW/cm^2. As in EELS and CL, the electron beam was raster-scanned over a two-dimensional grid of pixels with dimensions of (2×2) nm^2. The inset in Fig. 2.3a shows a STEM high-angle-annular-dark-field (HAADF) image of the nanostar prior to PINEM acquisition, with the white arrow indicating the approximate orientation of the laser polarization. The main panel in Fig. 2.3a shows PINEM spectra taken near the apex of tip II with a resonance at 1.7 eV (as determined by EELS and CL) at distances of approximately 5 nm (blue curve) and 20 nm (orange curve) from the tip. At a distance of 20 nm, we observe a pronounced

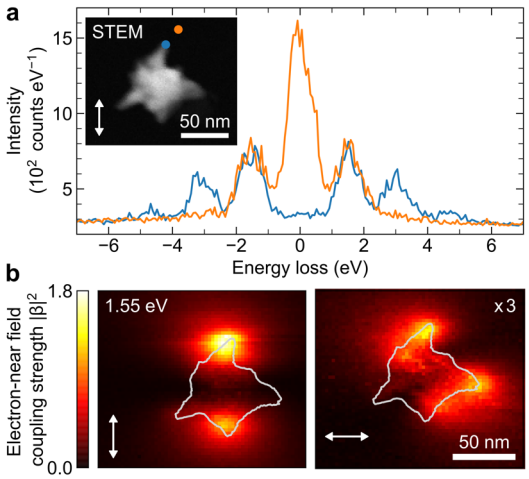

Figure 2.3: PINEM measurements. **a** 200 keV STEM-PINEM spectra of an Au nanostar corresponding to regions of strong (blue curve) and weak (orange curve) electron-near field coupling. The electron beam positions are indicated by the colour-matched dots in the inset, showing an HAADF image of the nanostar. The white double arrow represents the approximate in-plane polarization of the driving field. **b** Maps of the electron-near-field coupling strength derived from the energy spectra of the transmitted electrons for two orthogonal laser polarizations, as indicated by the white double arrows. The solid lines illustrate the approximate contour of the nanostar, as inferred from the HAADF image in **a**. Intensities in the right-hand panel have been scaled by a factor of 3.

ZLP accompanied by first-order photon emission and absorption peaks ($\pm\hbar\omega_L$) on the energy-gain and energy-loss sides of the spectrum. In contrast, at a distance of 5 nm, the ZLP is fully depleted, and the first-, second-, and third-order sidebands ($\pm n\hbar\omega_L$ for n =1,2, and 3) are populated. This trend indicates a substantial enhancement of the electron-near-field coupling strength with decreasing distance from the tip apex. Each sideband and the ZLP have an FWHM of ~0.9 eV, as primarily determined by the energy spread of the electron pulses. The latter mainly follows from excess energy as well as space charge-related effects in the photoemission process triggered by the second harmonic of the pump laser (photon energy 3.1 eV) [65, 164]. However, we note that a fundamental limit to the spectral resolution in PINEM is only imposed by the bandwidth of the optical pump field, as demonstrated in ref. [74].

To map out the laser-induced optical field, we derive the electron-near-field coupling constant $|\beta|$ from the PINEM spectrum recorded at every electron beam position. To this end, we approximate the electron energy distribution by a comb of $2N+1$ pseudo-Voigt profiles that are spaced by the photon energy $\hbar\omega_L$, each resembling the approximate line shape of the ZLP. The integral of the n^{th} profile is then determined by the occupation probability P of the n^{th} energy-gain and -loss sideband, which again follows from the local coupling constant $|\beta|$ according to Eq. (2.3) (see Methods section). On the left in Fig. 2.3b, we plot the spatial distribution of the squared electron-near-

field coupling strength $|\beta|^2$, for the same laser polarization as indicated in Fig. 2.3a. Similar spatial distributions to those obtained by EELS and CL are observed near the apexes of tips I and II, which are both approximately aligned with the laser polarization. Taking the EELS measurements as a reference, this agrees well with the fact that the corresponding resonance energies are closest to the central pump photon energy of 1.55 eV. Indeed, tip III, with its resonance further to the blue, shows almost no response although its symmetry axis is nearly aligned with that of tip II. To verify the correlation with the tip orientation, the right panel in Fig. 2.3b shows a $|\beta|^2$-map for the orthogonal laser polarization. Clearly, the coupling strength around tips I and II is now strongly reduced (note that the data are scaled by a factor of three), and tip IV, which is better aligned with the polarization, lights up. However, we see that the effect is comparably small since the tip resonance energy is furthest from the central pump photon energy. In addition, we note that the direction of incidence of the pump field strongly affects the excitation efficiency of a given tip mode. This behaviour might contribute to differences in the maximum electron-near-field coupling strength observed between tips I and II.

2.6 Numerical simulations

To complement our experimental data, numerical BEM calculations were performed to study the EELS, CL, and PINEM response of our model geometry introduced in Fig. 2.1. The optical pump field in PINEM is modelled by a monochromatic plane wave that is incident from the top and polarized along the symmetry axis of the tip. We assume resonant tip excitation at a pump photon energy of 1.73 eV. For the sake of simplicity, substrate effects are neglected.

Figure 2.4 shows 200 keV EELS (a) and 20 keV CL (b) spectra calculated for an electron passing through the centre of the spherical core (green curves) and 3 nm away from the tip apex (blue curves). For the electron passing near the tip, the tip resonance is clearly observed as a sharp maximum at 1.73 eV with a spectral linewidth of approximately 100 meV (FWHM). In the core spectra, the core resonance appears as a broader maximum near 2.4 eV, with the small peak at 1.73 eV indicating weak coupling to the tip resonance, in good agreement with the experiments. The insets show the x-y EELS and CL distributions as retrieved at 1.73 eV (bandwidth ±25 meV), revealing a strong interaction maximum near the tip apex. In Fig. 2.4c, we show 200 keV PINEM spectra calculated for the electron passing by the tip apex at distances of 3 nm (blue curve) and 20 nm (orange curve). For the larger distance, a pronounced ZLP and only the first-order energy-gain and -loss sidebands ($\pm\hbar\omega_\mathrm{L}$) are observed, while closer to the tip, the ZLP is fully depleted, and the first-, second-, and third-order sidebands ($\pm n\hbar\omega_\mathrm{L}$ for n =1,2, and 3) can be seen. In the calculations, a light intensity of 0.02 GW/cm^2 is chosen to best match the electron energy combs resolved experimentally. The inset on the left shows the calculated z component of the optically-induced near field E_L^z in the x-z symmetry plane of the tip. We find a similar spatial distribution as for the electron-induced field E_e^z plotted in Fig. 2.1a, showing that both distributions are dominated by the electric field profile u_z of the tip mode. In the inset on the right, we plot the x-y distribution of the squared electron-photon coupling strength $|\beta|$. Upon first inspection, there is good qualitative agreement between the EELS, CL, and PINEM

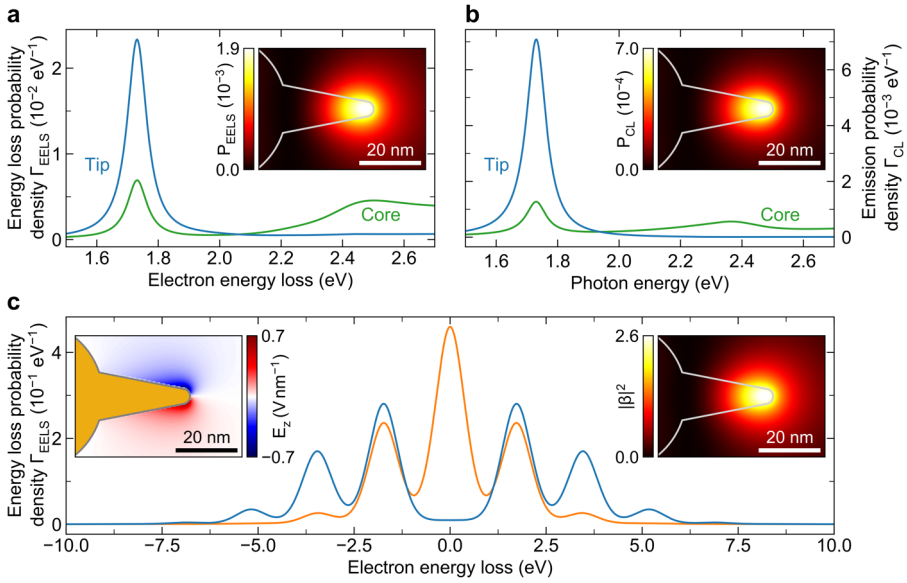

Figure 2.4: Numerical BEM calculations. BEM calculations of **a** 200 keV EELS and **b** 20 keV CL spectra for electrons passing through the centre of the spherical core (green) and 3 nm away from the tip apex (blue). The insets show the EELS and CL probability distributions obtained for a spectral bandwidth of ±25 meV around the tip resonance at 1.73 eV. **c** Calculated 200 keV PINEM spectra for electrons with an energy spread of 0.9 eV passing 3 nm (blue) and 20 nm (orange) away from the tip apex (plane wave pump field incident along z and polarized along x, $\hbar\omega_L$ =1.73 eV photon energy, and 20 MW/cm^2 intensity). The left inset shows a time snapshot of the z component of the optically induced near field in the x-z-symmetry plane of the tip; the right inset shows a x-y map of the calculated squared electron-photon coupling strength $|\beta|^2$.

maps, despite fundamentally different near-field excitation mechanisms.

Comparing the measured and calculated EELS and CL spectra, the maximum electron energy-loss probabilities are consistently found to surpass the corresponding photon-emission probabilities by one order of magnitude (cf. Fig. 2.2a,b and Fig. 2.4a,b). This observation can be attributed to strong non-radiative losses in the nanostar tips at optical frequencies [135]. However, in absolute terms, the measured EELS and CL amplitudes are again one order of magnitude smaller than those obtained from the model calculations, while the resonant linewidths are between two and four times larger, respectively. Such spectral broadening indicates a larger damping rate in the metal than predicted by the calculations. Furthermore, substrate effects [154, 165], electron-beam-induced carbon contamination, and non-local effects could contribute to the discrepancies at the extreme length-scale of the nanostar tips [166]. In addition, we note that artificial spectral broadening is introduced in EELS by the finite energy spread of the electron beam, while in CL, light is only collected in the upward hemisphere. Depending on the precise tip orientation, however, a significant fraction of radiation might be emitted into the substrate [154].

Comparing the measured and calculated PINEM spectra, the latter show a similar electron energy modulation for a one to two orders of magnitude lower pump field intensity. In the experiments this might be due to slight off-resonant tip excitation, reduced coupling efficiency in the presence of a substrate, imperfect laser alignment relative to the tip symmetry axis (polarization/direction of incidence), optical losses upon light injection into the STEM instrument, and large ohmic damping losses that are not fully covered by the calculations. Incidentally, for off-resonant tip excitation at 1.55 eV, a comparable electron energy modulation is obtained assuming an incident field intensity of 0.25 GW/cm^2. However, we note that an off-resonant excitation has a more drastic impact on the calculations because the tip resonance happens to be narrower than observed experimentally.

2.7 Spatial dependence

To study the spatial dependence of our EELS, CL and PINEM measurements, we plot intensity profiles along the symmetry axis of tip II and the model nanotip in Fig. 2.5. The experimental profiles are obtained by linearly interpolating and averaging the data within the dashed boxes shown in the insets. The EELS and CL data correspond to the fitted loss and emission probability distributions derived from the measurements presented in Fig. 2.2a,b at 1.68 eV and 1.72 eV, respectively. For PINEM, data were derived from an additional measurement that was performed at a higher resolution of (1×1) nm^2/pixel. In the calculations, we neglect a vanishing contribution of the core resonance due to its minor spectral overlap with the tip mode (see Fig. 2.4a,b).

To quantitatively compare the measured and calculated profiles, we fit a model to the data assuming an evanescent exponential decay of the electron-near-field coupling strength away from the tip apex with a characteristic $1/e$-decay length δ [65]. The signal along the tip is described by a half-Gaussian distribution that peaks at the tip apex, while the finite width of the electron probe is introduced by convolution with a Gaussian resolution function of standard deviation σ. The fitted curves (dashed lines) and deconvoluted model functions (dotted lines) are plotted in Fig. 2.5. We obtain beam widths of $\sigma_{\mathrm{CL}} = (5.3 \pm 0.2)$ nm for the CL, $\sigma_{\mathrm{EELS}} = (1.6 \pm 0.5)$ nm for the EELS, and $\sigma_{\mathrm{PINEM}} = (2.2 \pm 0.3)$ nm for the PINEM measurements. The characteristic decay lengths are found to be $\delta_{\mathrm{EELS}} = (8.7 \pm 0.3)$ nm, $\delta_{\mathrm{CL}} = (10.5 \pm 0.2)$ nm, and $\delta_{\mathrm{PINEM}} = (15.2 \pm 0.2)$ nm. The BEM calculations yield an identical decay length of 8.1 nm for EELS and PINEM at an electron energy of 200 keV, while a smaller value of 5.5 nm is obtained for CL at an electron energy of 20 keV (relative to the signal amplitude at the tip apex).

In comparison, the measured and calculated profiles show a very similar functional shape, with the maximum coupling strength occurring at or a few nanometres inwards from the tip apex. This result is in good agreement with the maxima observed in the electron- and laser-induced near-field distributions plotted in Fig. 2.1a and the left-hand inset in Fig. 2.4c. Excellent agreement between the measured and calculated decay lengths is found for EELS, while for CL and PINEM, the experimental values show an upwards deviation of almost 50%. Comparing the nanostar dimensions retrieved from our SEM and STEM images, we estimate a length scale uncertainty on the order of 10-20%. Additionally, we note that the model nanotip only approximates the actual

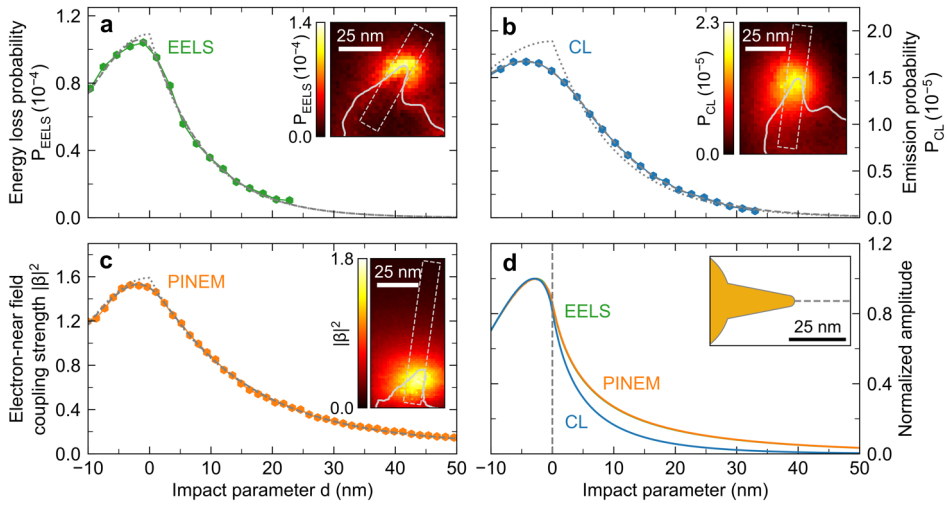

Figure 2.5: EELS, CL, and PINEM amplitude profiles. Line profiles through **a** 200 keV EELS (1.68 eV), **b** 20 keV CL (1.72 eV), and **c** 200 keV PINEM ($\hbar\omega_L$ = 1.55 eV photon energy) distributions along the symmetry axis of tip II. We also plot model fits assuming Gaussian broadening of the data due to the finite width of the electron beam (dashed curves) and deconvoluted model functions (dotted curves). An impact parameter of d = 0 nm corresponds to the inferred approximate position of the tip apex. **d**, BEM calculations of 200 keV EELS (green, hidden behind the PINEM curve), 20 keV CL (blue) and 200 keV PINEM (orange curve) profiles along the tip symmetry axis of the model geometry. The profiles are normalized to their respective amplitudes at the tip apex. As in the experiments, EELS and CL probabilities are calculated for a spectral bandwidth of ±25 meV around the tip resonance at 1.73 eV, while the PINEM interaction strength is calculated for laser polarization along the tip at an excitation energy of $\hbar\omega_L$ = 1.73 eV.

shape of tip II and thus might have a slightly different mode-field profile. For our SEM-CL instrument, a spatial accuracy limit of 3 nm was found in previous work [167], which is mostly determined by the comparably large electron beam probe width. In PINEM, an uncertainty of a few nanometres could be introduced by mechanical drift, which can result from nanoscale heat expansion under laser beam exposure. Such an effect is related to the relatively long acquisition times that are required to resolve PINEM spectra under pulsed electron beam conditions. Notably, a line profile through the measured PINEM distribution in Fig. 2.3b yields a decay length of ~10 nm at a shorter acquisition time per pixel, closer to the calculated value. Deviations between the measured distributions due to slightly different optical responses in EELS and CL, as well as off-resonant excitation at a photon energy of 1.55 eV in PINEM, are expected to be < 10% (corresponding to the relative differences in optical wavelength). However, we note that the laser polarization in PINEM does not perfectly align with the tip axis, which could cause a slight, mostly transverse broadening of the interaction maximum due to the contribution of other nearby sharp features to the local field enhancement.

It can be concluded that within experimental uncertainties of a few nanometres,

there is good agreement between the measured EELS, CL, and PINEM profiles. This is in line with Eqs. (2.1), (2.2), and (2.4) suggesting that in the limit of a single dipolar excitation, the observed spontaneous and stimulated electron-photon interactions share the same spatial dependence on the electric near-field distribution of the nanotip. Furthermore, our BEM calculations confirm that at an electron energy of 200 keV the EELS and PINEM profiles perfectly overlap, despite fundamentally different excitation mechanisms. Remarkably, however, for an electron energy of 20 keV the calculated CL profile decays somewhat faster, as could not be resolved experimentally. This subtle deviation demonstrates the dependence of the electron-near-field interaction strength on the integral over the field along the electron trajectory. As a result, electrons of different energies probe different spatial Fourier components as discussed below.

2.8 Dependence on electron energy

The energy dependence of the electron-near-field coupling strength is demonstrated in Fig. 6. The colour map represents the Fourier amplitude of the laser-induced electric field distribution plotted in Fig. 2.4c as a function of impact parameter d (i.e., distance away from the tip apex) and along-the-beam wave vector q (with the corresponding electron energies E_0 shown on top). The data are expressed in terms of the squared electron-photon interaction strength $|\beta|^2$.

Two striking trends can be observed in Fig. 2.6. For any spatial frequency q, or equivalently, electron energy E_0, the coupling strength rapidly falls off with the impact

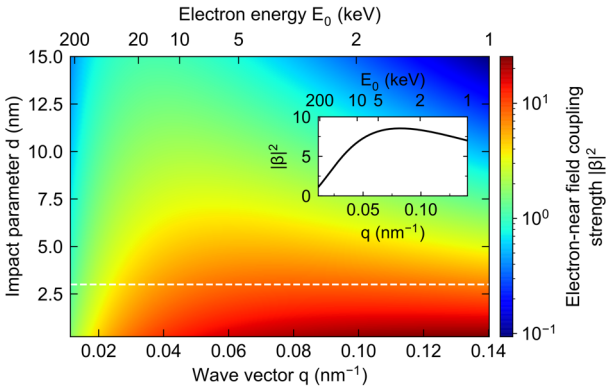

Figure 2.6: Electron energy dependence of the electron-near-field coupling strength. BEM calculation of the laser-induced electron-near-field coupling strength $|\beta|^2$ as a function of the along-the-beam wave vector $q = \omega/v$ and impact parameter d relative to the tip apex. Data are obtained for a fixed photon energy of $\hbar\omega_L = 1.73$ eV, matching the tip resonance energy and for varying electron energies E_0 (see top axis). Other excitation parameters are identical to those assumed in Fig. 2.4d and Fig. 2.5c. The inset shows a profile along the white dashed line for $d = 3$ nm, representing the local angular frequency spectrum of the field. For a given E_0, the electron can only couple to Fourier components with a spatial phase advance q along the electron trajectory, affecting both the amplitude and the spatial evolution of $|\beta|^2$ away from the tip apex.

parameter d, and the local maximum gradually shifts towards smaller values of q. We can understand this behaviour from the fact that the composition of the near field in terms of spatial Fourier components rapidly varies in the direction away from the tip apex. As a result, the maximum coupling strength occurs at an electron energy for which $2\pi/q$ coincides with the period of the Fourier component that locally dominates the angular frequency spectrum of the field. As an example, the inset shows $|\beta|^2$, as a function of q for an impact parameter of $d = 3$ nm. The maximum coupling strength is found at $q = 0.08$ nm^{-1}, corresponding to an electron with an incident energy $E_0 = 3.5$ keV. Increasing the distance from the tip, the higher spatial frequency components quickly die out, and the maximum coupling strength shifts towards larger electron energies. Importantly, Eqs. (2.1), (2.2), and (2.4) show that this trend is independent of the spontaneous or stimulated nature of the interaction. Incidentally, even the most intense near field cannot efficiently exchange energy with an electron if there is no suitable spatial Fourier component to enable a phase-matched interaction. This becomes apparent for the largest electron energies in Fig. 2.6, where the maximum interaction strength near the tip is substantially reduced compared to the lower electron energies. As discussed earlier, in the limit of very large electron velocities near the speed of light, the interaction with evanescent wave components is strongly reduced. Vice versa, when there are no field components with sufficiently large spatial frequencies, the interaction strength again decays with decreasing electron energy.

2.9 Discussion & conclusion

Our conclusions were derived in the limit of small plasmonic nanotips that support a single dipolar mode, yet they can be extended to more generic geometries if the electron-near-field interaction is considered as a sum of contributions of distinct optical eigenmodes that are determined by their spectral and spatial field properties [134, 135, 168]. For instance, EELS measurements on a mesoscopic plasmonic taper have shown that the electron selectively interacts with spatially overlapping circumferential modes, depending on the projection of their angular phase pattern along the electron trajectory [169]. Other than in EELS, however, we stress that the CL and PINEM responses of a sample generally depend on the coherent rather than incoherent superposition (i.e., the amplitude and relative phase) of the modes that are excited by the electron or the external pump field, respectively [134]. Incidentally, previous work has demonstrated a close relation between CL and optical scattering [135], underlining the mutual dependence of CL and PINEM on the far-field characteristics of a system. However, we recall that the CL signal can involve incoherent light emission that results from inelastic scattering losses in the bulk of a material or coherent radiation channels that are not accessible from the far field, such as transition radiation [28, 31, 170]. Additionally, we note that in this work, we have adopted a classical understanding of CL emission that is consistent with a point-like description of the electron [31]. Instead, recent work has explored the role of the electron wave nature on the emission of CL, including the transfer of coherence from an optical pump field to CL via a phase-modulation of the electron wave function [171–173].

Assuming that neither the electron velocity nor its trajectory is altered during the interaction (nonrecoil approximation), our BEM calculations show that rather low-energy electrons couple most strongly to the optical near field of the nanotip. This is a reasonable approximation for spontaneous single-photon exchanges as in EELS and CL, and the moderate energy-modulation of the electrons as observed in our PINEM experiments. Reassuringly, we find our results in good agreement with those of previous theoretical treatments of the electron-near-field interaction [104, 174–176]. In recent work [104, 174], the strong stimulated coupling between free-electron wave packets and the near field of small nanoparticles has been discussed beyond the adiabatic regime, i.e., taking into account the recoil upon momentum exchange with a photon. Despite a transverse diffraction of the electron wave packet, the interaction strength was found to peak at non-relativistic electron energies down to hundreds of eV, with the optimum coupling velocity following from phase-matching arguments [104, 174]. In other work [175], spontaneous electron energy-loss and photon-emission probabilities were studied by formulating the interaction of a generic dielectric object with the evanescent electric field of an electron as a scattering problem. It turns out that slow non-relativistic electrons reach overall larger near-field amplitudes than faster relativistic electrons, thus inducing a stronger scattering response close to the material boundary [175], also in agreement with previous work on small plasmonic structures [176]. Practically, however, we note that non-relativistic electron energies are not accessible in STEMs, while in SEMs the beam quality and thus the spatial resolution is typically a limiting factor.

In conclusion, we have demonstrated spatially resolved EELS, CL, and PINEM measurements of tightly confined optical near fields at the sharp tip apexes of an Au nanostar. Our data permit a one-to-one correlation of spontaneous and stimulated electron-photon interactions at the nanometre length scale. In EELS and CL, we observe the spontaneous coupling of free electrons to a number of plasmonic tip resonances in the VIS-NIR spectral range, while the stimulated interaction in PINEM strongly depends on the polarization of the pump field and its spectral overlap with these modes. We show that all three techniques resolve highly localized interaction maxima at the tip apexes with a lateral spatial extent on the order of 10 nm. In agreement with theory and supported by numerical simulations, we conclude that in the limit of a single nanotip with a dipolar resonance, spatial variations in the electron-photon interaction strength are independent of the excitation being driven by the electron itself (as in EELS and CL) or an external pump field (as in PINEM). Instead, the electron-photon coupling only varies with the dipolar mode profile of the tip. However, we also show that the coupling strength crucially depends on the electron velocity as determined by the spatial Fourier transformation of the field along the electron trajectory. Our results clarify the fundamental link between EELS, CL, and PINEM measurements, rendering a crucial contribution to the thorough understanding of electron-light-matter interactions at the nanometer length scale.

2.10 Methods

Nanostar synthesis

Au nanostars were prepared by modification of a previously reported procedure using a seeded growth approach [146, 160]. First, spherical Au seeds of approximately 12 nm diameter were produced by a modification of the well-known Turkevich method [177]. The seeds were synthesized by the subsequent addition of dehydrated trisodium citrate ($C_6H_5Na_3O_7 \cdot 2H_2O$, 11 mL, 0.1 M) and gold(III) chloride trihydrate ($HAuCl_4 \cdot 3H_2O$, 833 µL, 0.1 M) to boiling Milli-Q water (500 mL) at intervals of 10 min and under vigorous stirring. After 30 min of boiling, the solution was brought to room temperature, and the particles were added drop-by-drop under stirring to an aqueous polyvinylpyrrolidone (PVP) solution (500 mL, 0.27 mM). Finally, the Au nanoparticles were centrifuged (9000 rpm, 35 min) and dispersed in absolute ethanol (EtOH, 50 mL) to achieve a final Au concentration of 16.2×10^{-4} M. Next, Au nanostars were grown by the fast addition of PVP-coated Au seeds in EtOH (350 µL) to a PVP solution in N,N-dimethylformamide (DMF, 7 g, 35 mL), containing freshly prepared $HAuCl_4$ (75 µL, 0.12 M aqueous solution). Within 15 min, the colour of the solution turns blue, indicating the formation of Au nanostars. The solution was stirred overnight to ensure the reduction of all reactants. DMF and excess PVP were removed by several centrifugation steps: a first step at 7500 rpm for 40 min followed by four more iterations at 7000 rpm for 10 min each. For each step, the particles were resuspended in EtOH (35 mL). Eventually, Au nanostars (5 µL, 0.8 mM) were deposited on a TEM silicon nitride support membrane *via* spin coating (1st ramp: 500 rpm, 10 s; 2nd ramp: 3000 rpm, 30 s at an acceleration rate of 500 rpm/s), achieving a particle density of approximately 1.2 particles per μm^2. PVP (MW = 25 000) was purchased from Carl Roth GmbH & Co. KG, Germany. $HAuCl_4 \cdot 3H_2O$ (99.9 %), $C_6H_5Na_3O_7 \cdot 2H_2O$ (≥99.5 %), and EtOH (≥99.9%) were obtained from Sigma-Aldrich Inc., MO, USA. DMF (≥99%) was obtained from Fluka, Honeywell Inc., NC, USA. Silicon nitride support membranes (30 nm, TA3003X-SF-HR) were purchased from Norcada Inc., AB, Canada. All reactants were used without further purification. Milli-Q water (18 MΩ/cm) was used in all aqueous solutions, and all glassware was cleaned with aqua regia prior to usage.

EELS experiments

EELS and PINEM measurements were performed in STEM mode of a transmission electron microscope (JEM-2100F, JEOL Ltd., Japan) with modified Schottky field emission source. The width of the electron-probe beam was set to 1.5 nm. The spectral scans were recorded using an energy filtering and imaging device (CEFID, CEOS GmbH, Germany) equipped with a scintillator-coupled CMOS camera (TemCam-XF416ES, TVIPS GmbH, Germany) that was operated in sync with a universal scan generator (USG, TVIPS GmbH). EELS and PINEM spectra were acquired at binning resolutions of 15.6 meV and 16.6 meV, respectively. For EELS, a continuous electron beam was used with an initial energy spread of ~0.5 eV (ZLP FHWM). For PINEM, the instrument was operated in laser-triggered photoemission configuration in which sub-picosecond electron probe pulses are synchronized with picosecond optical pump pulses. To this

end, an amplified Ti:sapphire laser system (RegA, Coherent Inc., CA, USA) was operated, emitting femtosecond pulses with a central photon energy of 1.55 eV (λ = 800 nm) and a spectral bandwidth of 65 meV (35-nm bandwidth) at a repetition rate of 600 kHz. The optical pump pulses were dispersively stretched to a 3.4-ps pulse duration in a 19 cm bar of dense flint glass (SF6). The sample was excited under near-normal incidence (parallel to the electron beam) with the light transmitted through a linear polarizer and injected at an average power of 4 mW. At the sample, a focal spot diameter of ~15 µm was achieved, corresponding to a maximum peak intensity on the order of 1.1 GW/cm^2. Synchronous sub-picosecond electron-probe pulses were generated by photoemission from the Schottky field emitter using the second harmonic of the fundamental laser beam (for further details see Ref. [65]). The energy spread of the electron pulses was 0.9 eV. PINEM and EELS spectra were acquired at integration time constants of 500 ms and 120 ms, respectively. The EELS spectra were numerically deconvolved by the ZLP as measured upon electron beam transmission through the silicon nitride support membrane. This was achieved using 20 iterations of a Richardson-Lucy (RL) algorithm [161] as implemented in the Hyperspy Python library [178]. Absolute EELS probabilities were obtained by normalizing the spectra to the total count rate of electrons passing through the silicon nitride support membrane.

CL experiments

CL measurements were performed in an SEM instrument (FEI Quanta FEG 650, Thermo Fisher Scientific Inc., MA, USA) equipped with an integrated half-parabolic light collection mirror that was focused onto the sample from above (angular coverage of 1.46π sr). The CL spectra were acquired using a commercial optical setup for CL analysis (SPARC Spectral, DELMIC BV, The Netherlands) [179] (spectral resolution ~10 meV, acquisition time constant 350 ms). In order to compensate for the effect of mechanical instabilities or electrostatic charging, a software-controlled drift correction algorithm was applied at time intervals of 1 s. The background luminescence from the silicon nitride support membrane was measured separately and subtracted from the raw CL data. To correct the data for the spectral system response and derive absolute CL emission probabilities, transition radiation (TR) from the flat surface of a single-crystalline Al sample was exploited as a reference source. The measured spectrum was normalized to the expected TR spectrum as calculated from the analytical expression in ref. [31], yielding a spectral calibration curve as described in ref. [170]. For the calculations, the optical constants of the Al crystal were derived from spectroscopic ellipsometry measurements.

EELS and CL data analysis

In EELS, the tip resonances were represented by a sum of Gaussian distributions, reflecting the approximate shape of the ZLP. A background associated with (multiple) inelastic scattering events was modelled using a Gaussian error function that rises from zero to a constant amplitude at energies > 2.4 eV. Furthermore, a Gaussian centred between 2.3 eV and 2.9 eV was added to account for weak plasmonic contributions from the core and/or other tips. Another Gaussian that is bound to energies below 1.3 eV was used to account for the noise artefact of the RL algorithm in spectra with

a low signal-to-noise ratio. Plasmon resonances in CL were described by a sum of pseudo-Voigt distributions, capturing both their natural Lorentzian line shape as well as inhomogeneous broadening i.e., due to electron-beam-induced carbon contamination. A constant background was used to account for the emission of TR or weak incoherent luminescence that originates upon direct electron impact onto the nanostar. To globally determine the central energy E_0 and linewidth γ (FWHM) of the tip (and core) resonances, the EELS and CL spectra were first averaged over segments of 10×10 pixels. The above model was then fitted to the data using a least-square minimization algorithm. Subsequently, each spectrum was fitted separately using the given values of E_0 and γ to determine the local contribution of the tip (and the core) resonances.

PINEM data analysis

The derivation of the electron-near-field coupling constant from the PINEM spectra was performed following a similar procedure as described in the supplementary information to ref. [75]. Here, the initial electron energy distribution (i.e., prior to the near-field interaction) was represented by a pseudo-Voigt profile with a Lorentzian-like contribution of 25% and an FWHM of 0.9 eV. Furthermore, a Gaussian distribution of the coupling constant $|\beta|$ was assumed with a standard deviation of $\Delta|\beta| / |\beta| = 0.2$ to account for residual spatial and temporal averaging in the strongly inhomogeneous optical near field. These effects arise from both the finite probe size of the electron beam and the temporal profile of the optical pump pulses.

Numerical simulations

Numerical simulations were performed using the three-dimensional implementation of the BEM approach [157] as provided by the MNPBEM17 Matlab toolbox [158, 159] with optical constants for Au taken from tabulated optical data [180]. A triangular mesh was used to discretize the nanoparticle surface, with the meshing density gradually increasing from the tip shaft to the tip apex in order to account for highly localized charge accumulation. Electron-induced fields as well as EELS and CL probabilities were calculated using built-in functions for electron-beam excitation while assuming a finite beam width of 0.1 nm (see ref. [159] for details). For PINEM, a plane wave was assumed to be incident from above and polarized along the symmetry axis of the tip. The induced optical field was then calculated on a grid of points inside and outside the particle, extending up to half a wavelength above and below the tip apex. The stimulated coupling strength was obtained from the complex-valued plane-wave-induced optical field $\mathbf{E}_\mathrm{L}$ using the expression $e/(\hbar\omega)\int \mathrm{d}z E_\mathrm{L}^z(z) e^{-i(\omega/v)z}$. For electron trajectories intersecting with the nanoparticle, no integration points were spaced closer than 0.25 nm to the surface to avoid numerical artefacts due to divergence of the fields at the Au/vacuum interface.

3

Cylindrical metalens for generation and focusing of free-electron radiation

Metasurfaces provide a powerful approach to generate and control light by a pattern of nanoscale structures with tailored optical properties. Recently, this concept was applied to control free-electron radiation phenomena, promising the advent of versatile light sources that can be operated in otherwise hardly accessible spectral regimes. Here, we experimentally demonstrate spectral and angular control over the generation of radiation by free electrons that excite a metasurface under grazing incidence. Specifically, we study metalenses based on chirped nanogratings that simultaneously emit and shape Smith-Purcell radiation (SPR) in the visible to near-infrared spectral regime. In good agreement with theory, we observe the signatures of strongly convergent and divergent cylindrical radiation wavefronts using hyperspectral angle-resolved far-field imaging in a scanning electron microscope. Furthermore, we theoretically explore combined control over the polarization and wavefront of SPR by designing a split-ring-resonantor (SRR) metasurface. Our work highlights the potential of merging metasurfaces with free-electron excitation mechanisms for the implementation of ultra-fast and ultra-broadband radiation sources.

3.1 Introduction

Metasurfaces provide unprecedented control over light down to the sub-micrometer scale [109, 181–184], facilitating planar optical components for imaging [116, 117] and focusing [114–118], polarization control [119], wave front shaping [185, 186], analogue image processing [121, 122, 124], and holography [130, 131, 187]. In addition, metasurfaces can be used to manipulate the generation of light itself, enabling processes such as non-linear frequency conversion [125–129], spin-orbit-coupled lasing [188], and tailored quantum-light emission [189, 190]. The key to all these functionalities lies in a pattern of subwavelength-scale structures, the so-called meta-atoms, that provide a collective scattering response to an incident optical field. While these patterns are typically designed to match far-field illumination schemes [109, 114–119, 121, 122, 124–131, 181–188], the same approach can be applied to control near-field excitation mechanisms [189, 190] with a plethora of possibilities yet to be explored.

One such possibility is to embed metasurfaces with free-electron radiation phenomena. Free electrons can directly couple to electromagnetic excitations in nanophotonic structures on ultra-short time scales [31–33, 80, 90, 91, 101, 191–193], enabling the generation of coherent radiation [194–196] in otherwise hardly accessible spectral regimes, such as the terahertz (THz) [197], ultraviolet (UV) [198], and X-ray [199] ranges. Moreover, the electron wave function can be confined on length scales far beyond the diffraction limit of light, enabling the localized excitation of metasurfaces with a multitude of functionalities that are encoded into nano metric structural parameters.

Previous works have demonstrated the emission of structured light by metasurfaces that are excited by a beam of free electrons under normal incidence, including effects such as lensing, optical vortex beam generation, and polarization control [54, 195, 200–202]. The light yield in this configuration, however, is typically low due to the short electron-sample interaction range. Instead, electrons that excite a metasurface under grazing incidence can couple to a large number of meta-atoms along their trajectory. As a result, the electron imprints a well-defined phase profile onto the metasurface that is determined by the electron velocity. This gives rise to an effect known as electron-light phase-matching, i.e., a match between the electron velocity and the phase velocity of the induced optical field [31, 82, 103, 169]. The benefits of such phase-matched interactions are threefold: First, the electron velocity turns into an effective and easily accessible tuning knob to generate coherent radiation over an ultra-broad spectral range. Secondly, the intensity and spectral bandwidth of the emitted light can be controlled by the number of meta-atoms that are excited by the electron. And finally, different functionalities can be encoded into a single metasurface by varying structural parameters such as the periodicity, duty cycle (fill factor), and unit cell morphology.

In periodic systems such as a grating, a well-known example for the phase-matched interaction between free electrons and light is the Smith-Purcell (SP) effect [107]. The SP effect describes the emission of broadband radiation into discrete diffraction order by a free electron that excites the system under grazing incidence [107, 203, 204]. Interestingly, recent studies have shown that periodic nanostructures can be engineered to control the spectral [205] and polarization [206, 207] properties of the SP radiation (SPR). However, the greater challenge of sculpting the spatial and angular distribution of the

emission has only been explored theoretically thus far [205, 208–211] or demonstrated by an analogous experiment using evanescent optical waves that excite a metasurface [212]. In particular, the challenge of focusing SPR has been pursued theoretically by many researchers [205, 208, 209, 213], driven by the urgent technological demand for effective lenses and other optical components in spectral regimes such as the extreme UV or the soft X-ray domain.

In this work, we provide the first experimental demonstration of a metasurface lens (metalens) for phase-matched free-electron light emission. Specifically, our structures are designed to imprint a cylindrical wavefront onto the emission of SPR with a convex or concave curvature in the visible (VIS) to near infra-red (NIR) spectral regime. The radiation profiles of converging and diverging metalenses are characterized using hyperspectral angle-resolved far-field imaging [55, 56] inside a scanning electron microscope. Remarkably, we achieve a coherent electron-sample interaction range over more than 100 metagrating periods, resulting in the emission of light into effective numerical apertures (NA) of 0.48 ± 0.05 and 0.45 ± 0.05, respectively.

Building up on the metalens concept, we finally present numerical simulations of a split-ring resonator (SRR) metasurface that provides simultaneous focusing and polarization control over SPR by shifting the lateral position of the electron beam with respect to the SRR meta-atoms. Our work demonstrates the wide range of possibilities that open up by merging metasurfaces with phase-matched free-electron radiation mechanisms. By complementing traditional far-field excitation schemes, this new concept holds great potential for the tunable generation of coherent radiation with arbitrarily tailored spatial, angular, and polarization properties in otherwise hardly accessible spectral regimes.

3.2 Metalens theory

To elaborate the design of an SP metalens as proposed in previous works [205, 208, 209, 213], we first recall the theory of the conventional SP effect [107]. The far-field radiation that is emitted by an electron of normalized velocity $\beta = v/c$ passing near a grating with a constant period Λ fulfils the characteristic dispersion relation [107]

$$\lambda = \frac{\Lambda}{m}\left(\beta^{-1} - \cos\Theta\right), \tag{3.1}$$

where λ is the emission wavelength, m is the diffraction order, and Θ is the elevation angle with respect to the direction of electron propagation, hereinafter referred to as the z direction. Notably, Eq. (3.1) effectively resembles a phase-matching condition for the coupling between the electron and the near-field of the grating. The latter provides the necessary excess momentum for a photon to be scattered by the electron into free space [203], as discussed in detail in Section S2 of the Supporting Information.

For SPR to assume an arbitrary phase front $\phi(z)$ along the electron trajectory, we can consider a superposition of plane waves which are emitted into a distribution of angles $\cos\Theta(z) = \lambda/(2\pi)\mathrm{d}\phi(z)/\mathrm{d}z$ [205, 208]. Such a variation can be achieved by a metagrating that supports near-field components with a spatially-dependent excess momentum, as described by a generalized formulation of Snell's law in refs. [183, 184]. Resorting back to Eq. (3.1) and assuming a nominal design wavelength λ_0, we obtain a

metagrating with a variable pitch of the form

$$\Lambda(z) = \frac{m\lambda_0}{\beta^{-1} - \frac{\lambda_0}{2\pi}\frac{\mathrm{d}\phi(z)}{\mathrm{d}z}}. \tag{3.2}$$

Notably, from this expression, the conventional SP dispersion relation is again recovered assuming a linear phase front $\phi(z) = 2\pi z \cos\Theta/\lambda_0$, i.e., a plane wave that is emitted at an angle Θ.

The SP metalenses studied in this work are designed to emit light into a cylindrical wave front with a phase profile $\phi(z) = \mp 2\pi\sqrt{z^2+f^2}/\lambda_0$, where $\pm f$ is the nominal focal distance of the lens with respect to the grating plane. As a result, SPR is focused or defocused in the x-z plane perpendicular to the grating plane while retaining azimuthal divergence along the y direction. From Eq. (3.2) the correponding pitch of the metalenses follows as

$$\Lambda(z) = \frac{m\lambda_0}{\beta^{-1} \pm \frac{z}{\sqrt{z^2+f^2}}}, \tag{3.3}$$

which, in practice, we implement by sampling $\Lambda(z)$ over a range of discrete values z_n, with the pitch of the n^{th} grating element evaluated at $z_n = z_{n-1} + \Lambda(z_{n-1})$. Furthermore, we choose to maintain a constant 50% duty cycle (i.e., fill factor), such that the width of each grating element scales in proportion to $\Lambda(z)$, as depicted in Fig. 3.1.

Figure 3.1a schematically illustrates the operation of a metalens with a converging emission wavefront. For the nominal design wavelength λ_0, the lens emits light into a focal spot at $z = 0$ and $x = f$, while for any other wavelength λ, the focus moves to a different position within the x-z plane. Intuitively, this phenomenon can be understood by considering the local emission of SPR from each subsection of the grating. In this picture, the waves emitted from $z < 0$ towards the nominal focus at $(0, f)$ propagate at an acute angle with respect to the electron trajectory, those emitted near $z = 0$ propagate at a right angle, and those emitted from $z > 0$ propagate at an obtuse angle. However, waves that are scattered under a given angle can only exist if the local excess momentum provided by the metagrating permits phase matching with the electron. Hence, at the desired focal point, only waves of the nominal design wavelength λ_0 interfere constructively, while light emitted at smaller or larger wavelengths is focused to a different point below or above the optical axis, respectively.

The converging or diverging character of the SP metalens, and hence the curvature of the emitted wavefronts, is directly related to the orientation of the grating chirp as determined by the sign of $\phi(z)$. Thus, for the same values $|f|$ and λ_0 (as specified in the caption of Fig. 3.1), the diverging or converging metalenses only differ by an inverted chirp. The numerical aperture (NA) of the SP metalens is given as

$$NA = L\left(2|f|\sqrt{1 + L^2/\left(4|f|^2\right)}\right)^{-1}, \tag{3.4}$$

where L is the total physical length of the grating. In an experiment, however, we note that the effective interaction length L_{eff} of an electron with the structure can be reduced due to a non-ideal beam-sample alignment or a finite beam divergence, practically

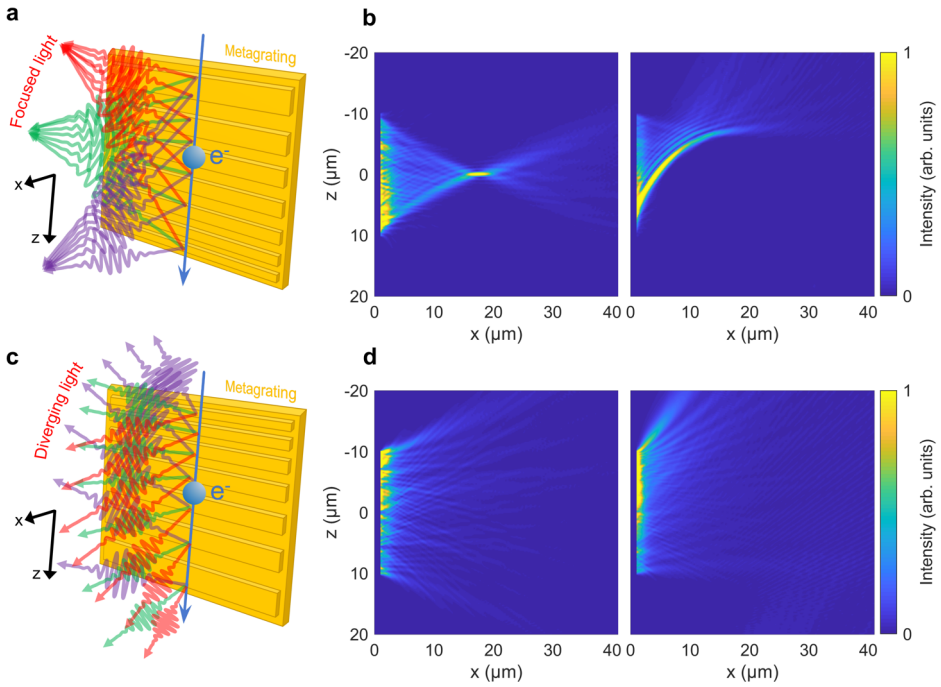

Figure 3.1: Focused emission of Smith-Purcell radiation (SPR) by a free electron-driven metalens: concept and simulation. **a** Schematic illustration of a free electron that excites a chirped metagrating with a decreasing period along the electron trajectory. As a result, light is emitted into a converging wavefront, with different wavelengths converging to different focal spots in the plane perpendicular to the grating surface. At the nominal design wavelength λ_0 (green rays; see Eq. (3.3)), light converges to a focus at a distance f from the metagrating and opposite its centre. At longer and shorter wavelengths (purple and red rays), both lateral and longitudinal aberrations cause opposing focal shifts along the electron trajectory and relative to the grating plane. **b** Normalized full-wave three-dimensional FDTD simulation of the near-field induced by a 30-keV electron that passes in close proximity to the structure in **a**, assuming a length of 20 μm and a pitch ranging from 228 nm to 163 nm as determined by Eq. (3.3). For the nominal design wavelength $\lambda_0 = 580$ nm (left), the simulation reveals a tight focus in the direction perpendicular to the grating surface with the light emitted into an effective NA of 0.5. For a red-shifted wavelength $\lambda = 660$ nm (right), the focusing effect occurs in an upwards direction with the focal spot distorted by a caustic shape. **c** The same as in **a**, yet with an inverted chirp, resulting in a divergence of the emitted SPR (as opposed to focusing). The direction of divergence for shorter and longer wavelengths is inverted as well. **d** Normalized full-wave FDTD simulation of the near-field distribution obtained by inversion of the structure simulated in **b**. The emitted light diffracts as if its focal plane was located at a distance f behind the grating plane.

limiting the achievable NA. Due to the grating chirp, a finite interaction length further affects the spectral emission pattern, yielding a distinct difference in the far-field profile of the converging and diverging metalenses as discussed below and elaborated further in Section S3 of the Supplementary Information.

To complement the above theoretical discussion, we also performed numerical simulations using a full-wave finite-difference in the time-domain (FDTD) solver (Lumerical, Ansys Cananda Inc.). Fig. 3.1b,d shows the simulated near-field patterns of a converging and a diverging metalens with focal lengths of $f = \pm 17$ µm for a nominal emission wavelength of $\lambda_0 = 580$ nm and 30-keV electron-beam excitation ($\beta \approx 0.328$), assuming an interaction length of $L = 20$ µm. The simulations show the induced near-field patterns at wavelengths of 580 nm and 660 nm. Clearly, the expected focusing and defocusing behaviour is observed for the nominal wavelength, while caustics appear at 660 nm when light is focused off-axis. Such chromatic aberrations can be efficiently predicted by a ray-optics model of the SP lens effect, as provided in ref. [205] and reviewed for completeness in the Supplementary Information, Section S1. Notably, we observe a variation in the intensity of the electron-induced near-field right above the grating plane which consistently shows a decay towards the larger periodicities at the top and bottom of the converging and diverging metalenses, respectively. We attribute this to a change in the electron-near-field excitation efficiency as the dimensions of the grating bars are gradually altered (for more information, see Supplementary Information, Section S5).

3.3 Sample fabrication and experimental setup

To experimentally demonstrate the metalens concept, chirped metagratings with dimensions of 20 µm × 20 µm were fabricated according to the design parameters provided in Fig. 3.1. In addition, a conventional SP grating was fabricated as a reference sample with a constant 189-nm pitch. The structures were patterned into a 40-nm thin gold film using focused ion beam (FIB) milling (FEI Helios, Thermo Fisher Scientific Inc.), with the gold sputter-coated onto a flat 400 µm thick silicon substrate and a 3-nm Cr adhesion layer (see Fig. 3.2). Minor milling imperfections are not expected to have a significant impact on the performance of the samples since it has been shown the SP effect is rather robust against structural defects [214].

The experimental far-field characterization of the samples was performed in a scanning electron microscope (FEI Quanta FEG 650, Thermo-Fisher Scientific Inc.) that is fitted with a commercial light collection setup for spectral- and angle-resolved cathodoluminescence analysis (SPARC Spectral, Delmic B.V.) [179]. As schematically depicted in Fig. 3.3, light was collected from inside the microscope via an off-axis half-parabolic mirror, with the sample vertically mounted from below and parallel to the optical axis of the light collection optics. By careful adjustment of the sample tilt, the effective electron-sample interaction length L_{eff} was optimized to exploit the full length of the grating structures ($L = 20$ µm) and thus achieve SP emission within the maximum possible NA.

The alignment of the samples with respect to the focal point of the parabolic mirror was performed by collecting incoherent cathodoluminescence from the uncoated top

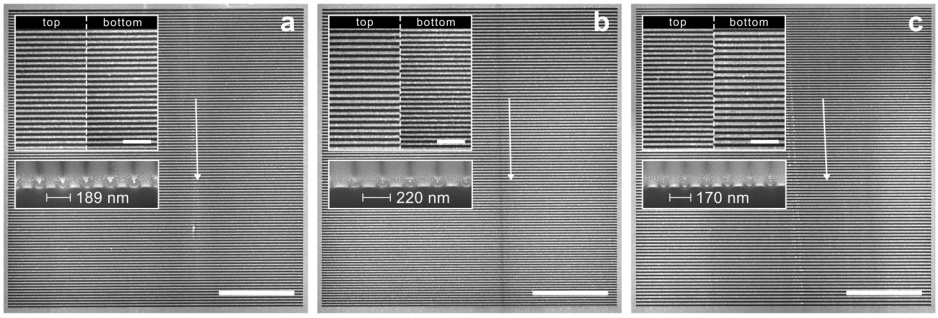

Figure 3.2: Fabricated Smith-Purcell metalens samples. **a** Reference grating with 189 nm pitch and a 50% fill factor. **b** Converging and **c** diverging metalenses of opposite chirps with a pitch ranging from 163 nm to 228 nm and a 50% fill factor, corresponding to a design focal length of $f = \pm 17$ µm at a nominal emission wavelength of $\lambda_0 = 580$ nm. The reference grating was chosen to yield dominant SP emission into a similar spectral range as its chirped counterparts. The top insets in each panel show the variation of the pitch within the last few microns above and below the top and bottom of the structures, respectively. The bottom insets show FIB cross sections through the grating rulings near the top, with a layer of platinum enhancing the imaging contrast. The scale bars in the main panels and the insets are 5 µm and 1 µm, respectively. White arrows indicate vertical traces of carbon contamination as seen as dark lines that are deposited by the grazing electrons perpendicular to the grating rulings. Chains of brighter spot-like depositions are also observed, presumably corresponding to larger carbon accumulations upon direct impact of electrons during the beam-sample alignment process.

edge of the silicon substrate. The electron beam was then translated to graze the grating surface at a few nanometres distance. As further explained in the caption of Fig. 3.3, the light collection setup was operated in hyperspectral angle-resolved detection mode [55, 56], simultaneously acquiring the far-field spectral response and the angular emission profile (with respect to the elevation angle ($\theta = \Theta - 90°$) of our metalenses in a single measurement. Subsequently, the raw experimental data were corrected for the collection solid angle and the spectral system response, as described in Section S8 of the Supplementary Information. In accordance with the near-field simulations shown in Fig. 3.1, all measurements were performed at an electron energy of 30 keV.

3.4 Metalens radiation patterns

The left-hand panel in Fig. 3.4a shows the angular dispersion of conventional SPR as emitted by the reference grating, in good agreement with the analytical expression given in Eq. (3.1) for $\Lambda = 189$ nm (red-dashed line). Remarkably, the narrow width of the dispersion curve on the order of a few nm (fixed-angle cross-section shown in the right-hand panel) indicates a coherent excitation of the entire sample ($L_{\text{eff}} \approx 20$ µm), leading to the interference of light waves that are emitted by a total of more than 100 grating periods. On the contrary, the radiation patterns of the converging and diverging metalenses shown in Fig. 3.4b,c are characterized by broadband emission for any angle θ, modulated by distinct oscillations. As opposed to the regular SP grating, the local

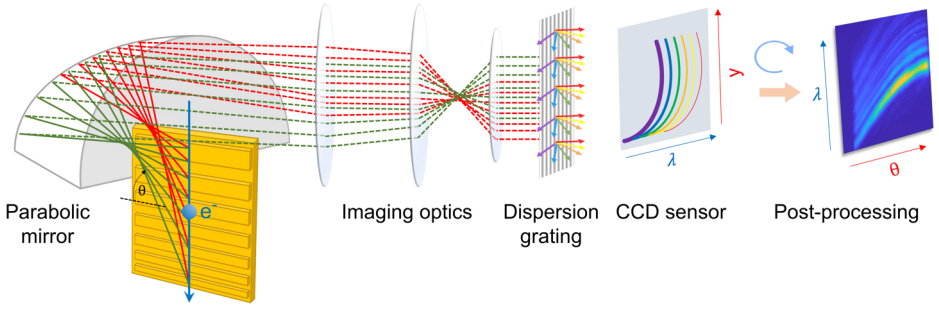

Figure 3.3: Hyperspectral angle-resolved light collection setup. The experimental setup is designed for a simultaneous characterization of the far-field spectrum and angular emission profile of a sample under electron beam exposure. A 3.3 nA, 30-keV electron beam passes through a 600 µm hole at the top of a parabolic mirror that is carved into a solid block of aluminium. The mirror is cut-off 500 µm above its focal plane, enabling light collection from a minimum zenith angle of $\theta_{\mathrm{min}} = 11°$ (with respect to the direction perpendicular to the electron beam).The grating structures are aligned parallel to the optical axis of the parabolic mirror, using piezo-electric actuators with sub-micron precision (controlling the position of the mirror) and a mechanical micrometer stage (controlling sample placement and tilt). The electron beam is aligned such that it grazes the sample at a few nm distance, with the upper edge of the metagratings positioned less than 10 µm below the mirror focus. Light emitted parallel to the sample plane (rays depicted as solid lines) is first collected and collimated by the parabolic mirror (rays depicted as dashed lines). Then, a three-lens optical telescope projects the collimated rays onto a 100 µm wide slit aperture (not shown) at the entrance of a spectrometer. Thus, only light that is collected within a narrow azimuthal angular range around the central axis of the mirror is transmitted. Eventually, the light is dispersed by a diffraction grating and scattered onto a CCD sensor, where the horizontal and vertical position onto the CCD sensor plane translate into a wavelength and emission angle (conversion between y and θ, as detailed in the Supplementary Information, Section S8). We note that, although the light collected in this configuration is emitted almost parallel to the grating surface, all relevant features of the metalens emission patterns are retained, as is predicted by theory and as also evident from the simulations shown in Fig. 3.4.

momentum modulation of the grating near-field along the electron trajectory gives rise to a multitude of closely spaced radiation bands with the typical SP dispersion curvature, each originating from a different subsection of the metalenses. The similar spectral bandwidths observed for both structures again attests to a sustained electron-near field interaction along the full length of the patterns.

To further interpret the experimental data, we resort to a hybrid simulation approach that combines the near-field distributions obtained by the full-wave numerical near-field simulations shown in Fig. 3.1, with a geometrical ray-tracing analysis (Zemax OpticStudio) of the experimental light collection setup. The results of this procedure are presented in the middle panels of Fig. 3.4. For the reference grating, a similarly narrow dispersion curve is observed as in the experiments, featuring excellent overlap with the theoretical dispersion relation for $\Lambda = 189$ nm (red-dashed line). Likewise, the simulation results for the converging and diverging metalenses match well with

the oscillatory emission patterns observed in the experiments, extending over similar spectral and angular ranges (see cross-sections at selected angles shown in the right-hand panels of Fig. 3.4b-c). In Section S2 of the Supplementary Information, we additionally provide an analytical model that accurately predicts the oscillatory features of the observed emission patterns and shows that this effect can be reduced to phase-matching between the electron and the grating near field. The excellent agreement of the experimental data with both the theory and the simulations provides strong indirect evidence for the desired curved emission wavefronts, and corresponding near-field effects of focusing and defocusing.

Furthermore, our simulations reveal two key features that clearly distinguish the far-field characteristics of the converging and diverging SP metalenses: First, the hyperspectral measurements show a slope in the λ-θ plane marked by the dashed white lines in Fig. 3.4b,c. This measured feature is in full agreement with the hybrid simulation approach – showing an opposite trend for each type of lens and thus

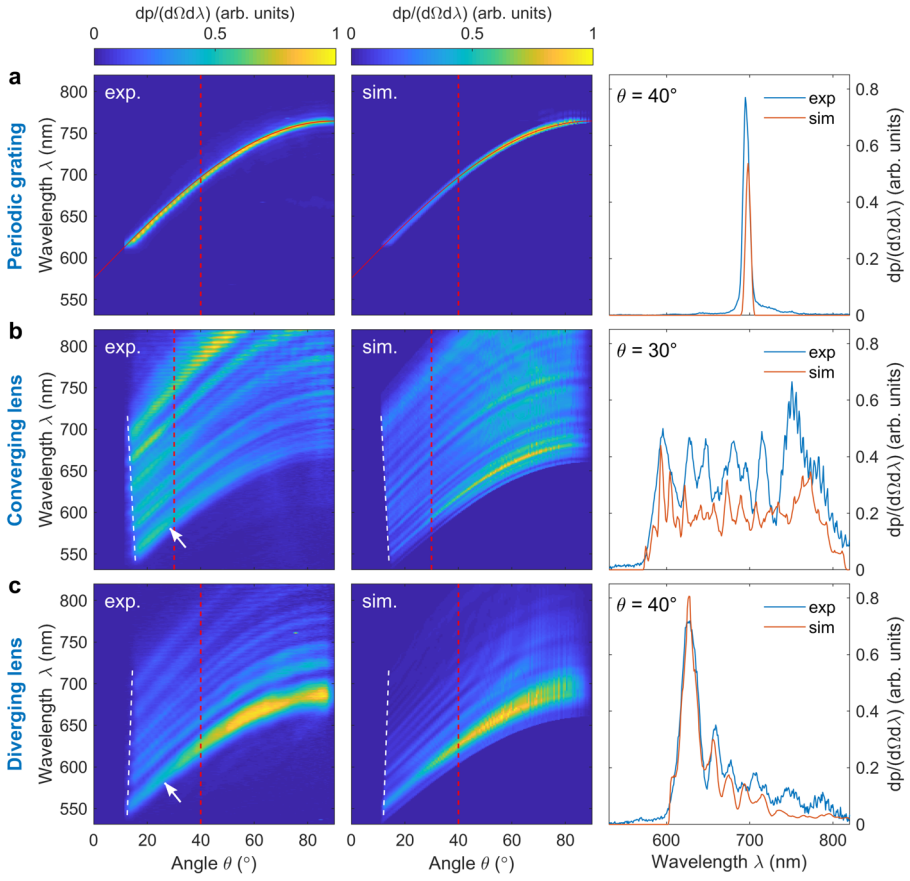

Figure 3.4: Far-field observation of SP focusing/defocusing at 30-keV electron excitation. **a** Experimental (left) and simulated (middle) hyperspectral angle-resolved emission pattern of the conventional (periodic) SP grating (red dashed line follows the SP dispersion given in Eq. (3.1) for $\lambda = 189$ nm). Right: fixed-angle cross section at $\theta = 40°$, revealing a narrow spectral line width on the order of a few nm for both the measurement (blue line) and simulation (red line). **b** Experimental (left) and simulated (middle) hyperspectral angle-resolved radiation patterns of the converging SP metalens. Imaging aberrations cause a negative slope at small emission angles (white dashed line) where the patterns are cut-off by the edge of the parabolic light collection mirror. The arrow indicates the angular emission cut-off at the nominal design wavelength $\lambda_0 =$ 580 nm. Right: fixed-angle cross section for $\theta = 30°$ showing characteristic spectral oscillations with similar relative amplitude, position, width and amplitude in both the simulations (red line) and measurement (blue line) (angle cross-section marked as a red dotted line, angle chosen to show best fit). **c** Experimental (left) and simulated (middle) hyperspectral angle-resolved emission patterns of the diverging SP metalens. In this case, imaging aberrations cause an opposing positive slope along the collection cut-off of the mirror (white dashed line). The arrow indicates the angular cut-off at 580 nm. Right: fixed-angle cross section for $\theta = 40°$ extracted from simulations (red line) and measurement (blue line). Again, the experimental and numerical data appear in good agreement with respect to the position, width, relative amplitude and envelope of prominent spectral features, with the best agreement occurring close to the nominal design wavelength $\lambda_0 = 580$ nm. However, towards the upper spectral cut-off, the measurements reveal slightly larger relative emission into longer wavelengths than predicted by the simulations for both the converging and diverging metalenses.

indicating sensitivity to the wavefront curvature. The opposite trends arise from a slight defocusing in the imaging system (such as an on-axis shift of the detector plane) that causes opposing aberrations for opposite incoming phase fronts. Secondly, the observed emission patterns – and in particular their spectral power distributions – are highly sensitive to the angle between the metalenses and the incident electron beam. We attribute this to the rapid evanescent decay of the grating near field upon interaction with the electrons as the grazing distance is gradually increased. For positive grazing angles, this results in enhanced emission into the longer and shorter wavelengths from the top sections of the converging and diverging metalenses, respectively. For negative grazing angles, an opposite trend may be expected, however, the interaction is abruptly truncated upon collision of the electron with the sample. In the experiments, we assume a range of grazing angles due to both beam divergence and possibly a minor tilt in the beam-sample alignment. By carefully comparing simulations and measurements, we find that the experimental features are best recovered assuming a divergent electron beam that comprises multiple trajectories with grazing angles varying between $-0.05°$ to $0.05°$ (for both lens types).

Notably, the observed spectral intensity variations between the emission patterns of the converging and the diverging metalenses are also consistent with a ray-optics picture [205] in which the generation of SPR at different wavelengths is correlated with different subsections of the structure. The orientation of the emitted rays is then uniquely defined by the local SP dispersion relation. Further details on this discussion are provided in Section S3 of the Supplementary Information, including reference measurements, analytical model predictions for electron incidence under variable grazing angles as well as complementary simulations for varying degrees of beam divergence.

For a quantitative analysis of the metalens emission patterns, we determine an effective NA by identifying the upper and lower cut-off emission angles at the nominal design wavelength of 580 nm (taken to be the midpoint between the angles corresponding to 10% and 90% of the maximal intensity, with the spacing between them taken as the uncertainty). Thus, we find an NA of 0.48 ± 0.05 and 0.45 ± 0.05 for the converging and the diverging metalenses, respectively, in good agreement with the desired NA of 0.5. In Section S5 of the Supplemental Information we further provide an estimate of the metalens radiation efficiency, reaching the order of 10^{-3} photons per electron.

3.5 Combined wavefront and polarization control

To complement the conceptual findings of our experimental study, we finally illustrate the potential of metasurfaces as a tool to manipulate free-electron light emission and sculpture its spatial distribution by exploring combined control over the wavefront and polarization of SP radiation. For this purpose, we theoretically study a split-ring resonator (SRR) metasurface with a chirped pitch as defined by Eq. 3.3, rendering a cylindrical metalens with arbitrary tunable polarization [206, 215]. SRR meta-atoms are chosen due to their low-order symmetry as well as their bi-anisotropic nature [216], permitting coupling between electric and magnetic modes. Thus, the SRR meta-atoms allow for efficient focusing of light with a polarization component along the direction orthogonal to the electron trajectory (horizontal polarization in Fig. 3.5a), in stark contrast to conventional SP radiation in which this polarization state is fully suppressed.

The SRR geometry, depicted in Fig. 3.5a, was optimized using numerical FDTD simulations to model the focusing effect for the horizontal polarization at a nominal emission wavelength of $\lambda_0 = 550$ nm and 30 keV incident electron energy. The bottom inset in Fig. 3.5a shows reflection spectra of the SRR meta-atom for excitation by a plane wave under normal incidence that is polarized along the horizontal and the vertical directions, respectively. For the horizontal polarization (red curve), the intended working point $\lambda_0 = 550$ nm is situated to the left of a reflectivity dip at 584 nm, which we avoid to ensure efficient far-field scattering. For the vertical polarization (blue curve), however, a desirable dip in reflection occurs at $\lambda_0 = 642$ nm, admitting another working point for a metalens based on the same SRR meta-atom but with an adjusted periodicity. The left-hand panels of Fig. 3.5b show the near-field intensity distributions obtained for the two different structures, clearly revealing the desired focusing effect at the respective operation wavelengths. For reference, the right-hand panels show 2D intensity cross-sections as extracted from the focal plane, and at negative and positive distances of approximately one Rayleigh length.

Fig. 3.5c,d shows a quantitative analysis of the polarization state of the emitted light within the focal plane (i.e., the intensity contributions by the vertical and horizontal polarizations, and the corresponding polarization ellipse), as a function of the electron beam position relative to the SRR meta-atoms, for both lens designs. Notably, the polarization possesses a growing horizontal component for an electron beam trajectory closer to the gap edge of the SRRs due to enhanced coupling to modes with a horizontal dipole moment (see the Section S7 of the Supplementary Information for a more thorough analysis of the coupling process and its effect on the emitted polarization).

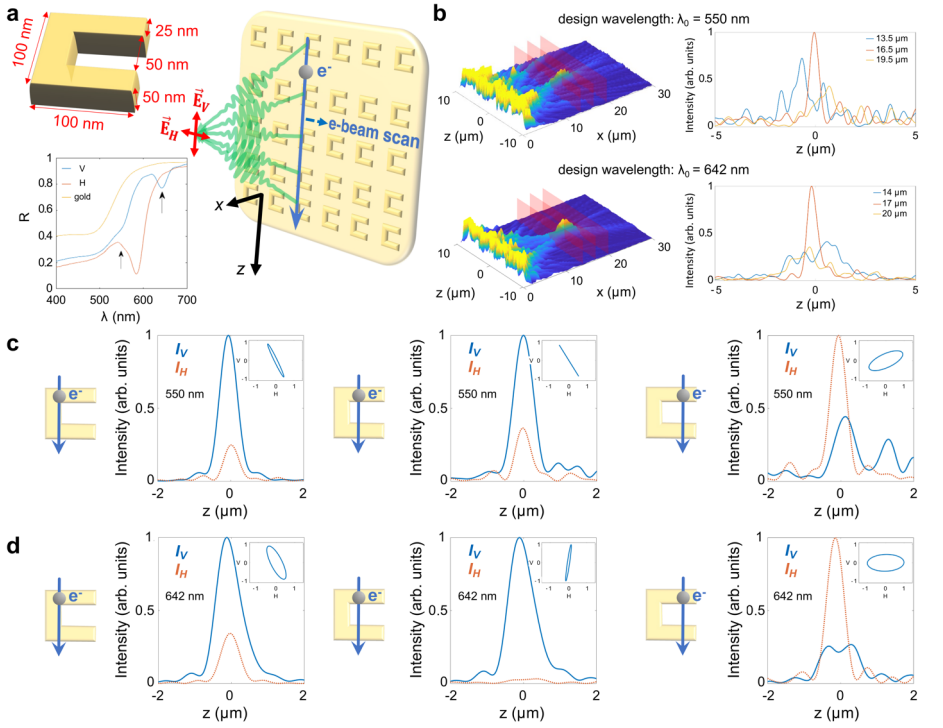

Figure 3.5: SRR metasurfaces for SP metalensing with tunable polarization. **a** Top right inset: schematic illustration of an SRR metalens, excited by a tightly collimated electron beam that is scanned along the horizontal direction relative to an array of SRR meta-atoms. Due to the bi-anisotropy of the SRRs, light is emitted into both vertical and horizontal polarizations. Top left inset: model geometry of an SRR meta-atom. Bottom left inset: periodic SRR metasurface reflection spectra upon excitation by a plane wave under normal incidence with a horizontal (red curve) or vertical polarization (blue curve). The reflection spectrum of a planar gold film is shown for reference (orange curve). Arrows mark two working points for metalenses with nominal design wavelengths of $\lambda_0 = 550$ nm and $\lambda_0 = 642$ nm. **b** Left: normalized intensity of the electron-induced optical field along the x-z plane for the two metalenses. Right: cross sections at approximately one Rayleigh length before and after, and within the focal plane of the metalenses (marked in red on the left). **c**, **d** Focal intensity profiles of the vertical and horizontal polarization components for different electron impact parameters relative to the centre of the SRR meta-atoms (-25 nm, 0 nm, and 25 nm). Data in **c** and **d** correspond to the metalenses with working points $\lambda_0 = 550$ nm and $\lambda_0 = 642$ nm, respectively. Insets: polarization ellipse of the emitted light.

3.6 Discussion & conclusion

In conclusion, we have fabricated and experimentally characterized converging and diverging free-electron-driven metalenses based on the emission of Smith-Purcell radiation (SPR) by a chirped metagrating. Our hyperspectral angle-resolved far-field measurements were found in good agreement with the results of numerical simulations as well as analytical model predictions, indirectly capturing the desired lens functionalities and revealing numerical apertures as high as 0.48±0.05 and 0.45±0.05, respectively. Our results provide the first experimental evidence that the wavefront of SP emission can be arbitrarily controlled by a tailored metagrating, with a focusing effect as a specific example.

The concept of spatially-modulated SP radiation demonstrated here could be utilized to produce efficient, focused light sources in the X-ray and extreme-ultraviolet (EUV) regimes, possibly enhanced by material [217] or structural resonances [218, 219]. Notably, in such extreme spectral regimes, the metalens design could be implemented by well-established fabrication approaches based on thin-layer deposition of nm or sub-nm thickness [213]. Furthermore, we emphasize that the concept of an SP metalens may be transferred to the inverse Smith-Purcell effect [220], in which the energy and shape of an electron beam could be altered by shaping the wavefront of an optical pump field.

To bring our work into a broader context, we emphasize the vast number of degrees of freedom that can be attained by merging metasurfaces with phase-matched free-electron radiation phenomena. As opposed to most conventional far-field excitation schemes, free-electron-driven metasurfaces have the potential to simultaneously incorporate various functionalities and to generate tunable radiation with virtually arbitrary spatial, spectral, temporal, and polarization properties. We emphasize that these prospects fundamentally arise from the highly localized nature of the electron–light–matter interaction with respect to both space and time (as opposed to a dipole or plane-wave excitation source). Structures such as the proposed two-dimensional SRR metasurface permit the transverse scanning of a tightly focused electron beam over its relative position with respect to the meta-atom and over different meta-atom arrays, with different shapes, resonances, and periodicities. The interaction with individual arrays of meta-atoms provides control over the angular, frequency, and even temporal response, thus significantly increasing the number of metasurface functionalities. Moreover, using wide-spread electron beams or multi-electron bunches could permit simultaneous excitation of different meta-atom arrays in the transverse dimension. In the first scenario, the excitations driven by consecutive electrons are incoherent [173, 221] enabling amplitude modulation of the emitted radiation, while in the second case, interference effects can be harnessed to achieve both a transverse and a longitudinal wavefront modulation.

3.7 Supplementary Information

S1 Ray-optics model of the metalens

The design of an Smith Purcell metalens can be derived from a ray-optics approach as proposed in ref. [205]. In this picture, the wave front of SPR is shaped by introducing a relation between the angle Θ that a ray encloses with the direction of electron propagation, and the position z from which it is emitted along the electron trajectory. Assuming a generic phase profile $\phi(z)$ and a nominal design wavelength λ_0, we can write this relation as [205]

$$\cos\Theta(z) = \frac{\lambda_0}{2\pi}\frac{\mathrm{d}\phi(z)}{\mathrm{d}z}, \tag{S1.1}$$

which upon insertion into Eq. (3.1) yields a spatially variable grating pitch. To model our metalenses, we introduce a cylindrical phase profile $\phi(z) = \mp 2\pi\sqrt{z^2+f^2}/\lambda_0$, with the negative and positive signs representing converging and diverging wave fronts, respectively. Thus, we obtain a chirped metagrating as described by Eq. (3.3). By inserting the latter back into Eq. (3.1), the emission angle is recovered as a function of the emission wavelength, with the first diffraction order ($m = 1$) given as

$$\cos\Theta(z) = \mp\frac{\lambda}{\lambda_0}\frac{z}{\sqrt{z^2+f^2}} + \left(1-\frac{\lambda}{\lambda_0}\right)\beta^{-1}. \tag{S1.2}$$

We can now study the focusing properties of the SP metalenses as a function of the emission wavelength. Limiting ourselves to SPR that is emitted at small angles relative to the surface normal, the substitution $\theta = \Theta - \pi/2$ permits a small-angle approximation of the form

$$\theta(z) \approx \pm\frac{\lambda}{\lambda_0}\frac{z}{f} - \left(1-\frac{\lambda}{\lambda_0}\right)\beta^{-1} = \pm\frac{z}{\tilde{f}(\lambda)} - \Delta\theta(\lambda), \tag{S1.3}$$

with $\tilde{f}(\lambda) = \frac{\lambda_0}{\lambda}f$ and $\Delta\theta(\lambda) = \left(1-\frac{\lambda}{\lambda_0}\right)\beta^{-1}$. For off-nominal wavelengths, it follows that the emission of the metalenses is subject to both longitudinal and lateral chromatic aberrations as represented by the parameters $\tilde{f}(\lambda)$ and $\Delta\theta(\lambda)$, respectively. These aberrations show opposing trends for red and blue shifts $\Delta\lambda$ relative to λ_0, as also illustrated in Fig. S1.1a for $\Delta\lambda = \pm 30$ nm and $\lambda_0 = 580$ nm. In addition, the model reveals a caustic distortion of the focus, in good agreement with the near-field distributions retrieved from rigorous full-wave numerical simulations as shown in Fig. 3.1. Notably, since $\Delta\theta(\lambda)$ scales inversely proportional to the electron velocity, chromatic aberrations can be compensated in the lateral direction by adjusting the electron energy. This effect is demonstrated in Fig. S1.1b by the example of an SP metalens with a nominal design wavelength of $\lambda_0 = 580$ nm that is excited by 5-keV electrons. At a wavelength of $\lambda = 590$ nm, the emission shows a distorted focus, accompanied by an off-axis shift. By increasing the electron energy to 30 keV, the desired focal spot is recovered, and aberrations are largely eliminated.

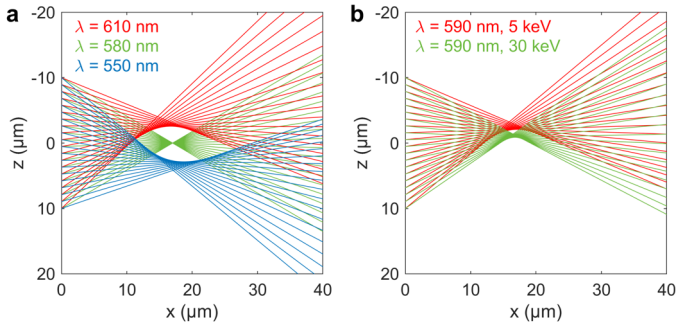

Figure S1.1: Ray-optics model of the Smith Purcell metalens. **a** Rays emitted by a converging SP metalens with a nominal design wavelength $\lambda_0 = 580$ nm, for different emission wavelengths $\lambda = 550$ nm, 580 nm, and 610 nm. For the off-nominal wavelengths, we observe both lateral and longitudinal aberrations, combined with a caustic distortion of the focus. **b** Chromatic aberration correction by tuning the electron energy. A converging SP metalens with nominal design wavelength $\lambda_0 = 580$ nm at 5 keV electron energy shows slight chromatic aberrations for emission at $\lambda = 590$ nm. The aberrations are corrected by increasing the electron energy to 30 keV.

S2 Wave-optics model of the metalens

In this section, we derive an analytical model that allows us to correlate the far-field characteristics of our Smith Purcell metalenses with the underlying electron-near-field coupling mechanism. To this end, we consider first a generic photonic system that supports a single electromagnetic excitation with normalized electric mode field distribution $\mathbf{u}(\mathbf{r})$. The probability for a point-like free electron of kinetic energy E_0 to excite this system at frequency ω and thus suffer a corresponding energy loss $\hbar\omega \ll E_0$ can be written as [71]

$$p_{\text{loss}} = \left| \frac{e}{\hbar\omega} \int_{-\infty}^{\infty} \mathrm{d}z\, \mathbf{u}\left(\mathbf{r}_{\perp,0}, z; \omega\right) \cdot \hat{\mathbf{z}}\, e^{-i\frac{\omega}{v}z} \right|^2, \tag{S2.1}$$

where e is the elementary charge, v is the electron velocity, $\hat{\mathbf{z}}$ is the unit vector in the direction of electron propagation, and $\mathbf{r}_{\perp,0} = \left(x_0, y_0\right)$ denotes the transverse electron coordinates. The coupling integral governing Eq. (S2.1) corresponds to the Fourier transformation of the field $\mathbf{u}(\mathbf{r})$ as projected onto the electron trajectory at an electron-velocity-dependent spatial frequency $q = \omega/v$. Physically, this imposes a phase-matching condition which can be only fulfilled if light is slowed down by either material dispersion or boundary conditions, i.e., in the evanescent near-field of a nanostructure [103].

In our Smith Purcell experiments, the measured radiation patterns are determined by the far-field envelope $\boldsymbol{\mathcal{E}}_\infty(\mathbf{r},\omega)$ of the electron-induced electric field $\boldsymbol{\mathcal{E}}(\mathbf{r},\omega)$. Thus, the observed radiation patterns are governed by the same electron-near-field coupling integral as the loss probability in Eq. (S2.1). To demonstrate this correlation, we consider grating structures that are patterned along the z direction, in line with the convention used in the main text. For an observer that is located at a large distance r away from the

source, we can write the measured differential photon emission probability as [12]

$$\frac{\mathrm{d}^2 p_{\mathrm{rad}}}{\mathrm{d}\Omega \mathrm{d}\omega} = \frac{r^2 \varepsilon_0 c}{\pi \hbar \omega} \left| \boldsymbol{\mathcal{E}}_\infty (r\hat{\mathbf{n}}, \omega) \right|^2 , \tag{S2.2}$$

where $\hat{\mathbf{n}}$ is the direction of observation, $\mathrm{d}\Omega$ denotes an infinitesimal small collection solid angle element, and ε_0 is the vacuum permittivity. Under the simplifying assumption of a lossless and non-dispersive medium, we may choose to expand the electric field in terms of normal modes $\mathbf{u}_\mathbf{k}$ which are uniquely defined by the boundary-value problem imposed by the grating geometry [12]. By treating the grating near-field as superposition of planar Fourier waves, we can chose an ansatz according to the following considerations: The near-field of a regular grating has to inherit the grating periodicity, giving rise to Fourier waves with excess momentum $m\hbar g\hat{\mathbf{z}}$, where m is the harmonic order of the reciprocal grating constant $g = 2\pi/\Lambda$. In contrast, the pitch of the chirped metalenses, slowly varies along z. Thus, the Fourier components acquire a phase that can be locally approximated by an integral of the form $m\int_0^z \mathrm{d}z' \frac{2\pi}{\Lambda(z')}$. For harmonic orders $|m| > 0$, the excess momentum provided by the different metagrating geometries ensures phase-matching between the electron and the near-field while causing an evanescent decay of the field amplitude in the direction perpendicular to the grating surface, here taken to be the x direction. Hence, the normal modes of the periodic reference grating and the chirped metalenses admit expressions of the form

$$\mathbf{u}_\mathbf{k}(\mathbf{r}) = \begin{cases} \sum_m \mathbf{A}_{\mathbf{k},m} e^{i\left(\sqrt{k^2 - k_y^2 - \left(k_z + \frac{2\pi}{\Lambda} m\right)^2} x + k_y y + \left(k_z + \frac{2\pi}{\Lambda} m\right) z\right)}, & \text{grating,} \\ \sum_m \mathbf{A}_{\mathbf{k},m} e^{i\left(\sqrt{k^2 - k_y^2 - \left(k_z + \frac{2\pi}{\Lambda(z)} m\right)^2} x + k_y y + k_z z + m\int_0^z \mathrm{d}z' \frac{2\pi}{\Lambda(z')}\right)}, & \text{metalenses,} \end{cases} \tag{S2.3}$$

with $\mathbf{A}_{\mathbf{k},m}$ the Fourier expansion coefficients. Notably, in this ansatz, the index $\mathbf{k} = (k_x, k_y, k_z)$ can be identified as the wave vector of the plane-wave-component ($m = 0$) of each mode, i.e., the component which is eventually scattered into the far-field. Thus, for emission into free-space, the magnitude of $\mathbf{k} = k_0\hat{\mathbf{n}}$ follows a continuous dispersion relation $k_0 = \omega/c$. In the Appendix, we apply a classical Green's function formalism to derive Eq. (S2.2) in terms of these normal modes as

$$\frac{\mathrm{d}^2 p_{\mathrm{rad}}}{\mathrm{d}\Omega \mathrm{d}\lambda} \propto \left|\mathbf{A}_{k_0\hat{\mathbf{n}},0}\right|^2 \left| \int_{-\infty}^{\infty} \mathrm{d}z\, \mathbf{u}_{k_0\hat{\mathbf{n}}}\left(\mathbf{r}_{\perp,0}, z; \omega\right) \cdot \hat{\mathbf{z}}\, e^{-i\frac{\omega}{v}z} \right|^2 , \tag{S2.4}$$

where $\left|\mathbf{A}_{k_0\hat{\mathbf{n}},0}\right|^2$ (the Fourier coefficient of the plane-wave component of the mode) captures the material- and geometry-dependent angular radiation pattern of mode $\mathbf{k}$. Note that in this model only a single mode $\mathbf{u}_{k_0\hat{\mathbf{n}}}$ is assumed to contribute to the far-field amplitude emitted into a given direction $\hat{\mathbf{n}}$ and at a particular wavelength λ. Remarkably, up to a different normalization, we thus find the dependence of Eq. (S2.4) on the modal near-field to closely resemble the form of the electron energy-loss probability in Eq. (S2.1). This is also corroborated by a rigorous quantum mechanical treatment of the problem for small dipolar emitters in refs. [102]. Substituting $k_z = k_0 \cos\Theta$ into our ansatz for the grating modes, and limiting ourselves to a contribution by the $m = 1$

Fourier component (corresponding to first-order Smith-Purcell emission), we eventually find

$$\frac{\mathrm{d}^2 p_{\mathrm{rad}}}{\mathrm{d}\Omega \mathrm{d}\lambda} \propto \left|\mathbf{A}_{k_0\hat{\mathbf{n}},0}\right|^2 \left|\mathbf{A}_{k_0\hat{\mathbf{n}},1}\cdot\hat{\mathbf{z}}\right|^2 \cdot \begin{cases} \left|\int_{-\infty}^{\infty} \mathrm{d}z\, e^{-\kappa x_0(z)} e^{ik_0\left(\cos\Theta-\beta^{-1}+\frac{\lambda}{\Lambda}\right)z}\right|^2, & \text{grating,} \\ \left|\int_{-\infty}^{\infty} \mathrm{d}z\, e^{-\kappa x_0(z)} e^{ik_0\left(\cos\Theta z-\beta^{-1}z+\int_0^z \mathrm{d}z' \frac{\lambda}{\Lambda(z')}\right)}\right|^2, & \text{metalenses,} \end{cases} \tag{S2.5}$$

where $\kappa \approx \frac{2\pi}{\lambda}\sqrt{\beta^{-2}-1}$ defines the evanescent decay of the near-field amplitude away from the grating plane. We note that in Eq. (S2.5) the electron is permitted an incident grazing angle $\alpha_t \neq 0$ such that $x_0(z) = x_0 + \tan\alpha_t\,(z-z_0)$.

In general, the Fourier coefficients of the grating near-field that determine the terms $\left|\mathbf{A}_{k_0\hat{\mathbf{n}},0}\right|^2$ and $\left|\mathbf{A}_{k_0\hat{\mathbf{n}},1}\cdot\hat{\mathbf{z}}\right|^2$ have a highly non-trivial dependence on both the direction of observation $\hat{\mathbf{n}}$ and the wavelength λ. Thus, for a quantitative comparison between theory and experiment, we resort to a numerical solution of Maxwell's equations in the main text, taking into account the details of the metasurface geometry as well as material dispersion. However, fortunately, the relevant features associated with the electron near-field coupling mechanism are fully recovered by the remaining integral terms in Eq. (S2.5). To demonstrate this correlation, we first consider a vanishing grazing angle $\alpha_t \approx 0$. From the upper entry of Eq. (S2.5), the conventional first-order SP dispersion relation is immediately recovered through a delta function $\frac{\mathrm{d}^2 p_{\mathrm{rad}}}{\mathrm{d}\Omega \mathrm{d}\lambda} \propto \delta\left(\lambda - \Lambda\left(\beta^{-1}-\cos\Theta\right)\right)$, strictly reflecting the electron-light-phase-matching condition addressed above. In the measurements, a finite interaction range L introduces spectral broadening, as also reproduced by a truncation of the integral in Eq. (S2.5). This is illustrated in Fig. S2.1a, using the structural parameters of our reference grating given

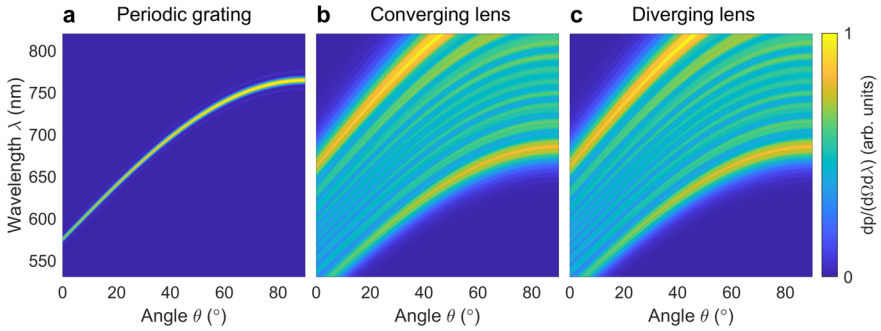

Figure S2.1: Analytical model of the SP metalens. Calculated radiation patterns of **a** the periodic reference grating, **b** the converging metalens, and **c** the diverging metalens considering only the contribution of electron-near-field phase-matching. Calculations are according to the design parameters used in the main text, assuming 30-keV electron excitation at a constant grazing distance of x_0 = 20 nm. For the metalenses, the theory accurately predicts multiple curved emission bands, in good agreement with the experimental observations.

in the main text. The lower entry of Eq. (S2.5) is further specified by substituting the expression for $\Lambda(z)$ from Eq. (3.3), yielding the local phase accumulation of the first order grating mode ($m = 1$) as

$$\int_0^z \mathrm{d}z' \frac{2\pi}{\Lambda(z')} = \frac{2\pi}{\lambda_0}\int_0^z \mathrm{d}z' \left(\beta^{-1} \pm \frac{z'}{\sqrt{z'^2+f^2}}\right) = \frac{2\pi}{\lambda_0}\left(\beta^{-1}z \pm \sqrt{z^2+f^2}\right). \tag{S2.6}$$

Thus, we are finally left with an expression of the form

$$\frac{\mathrm{d}^2 p_{\mathrm{rad}}}{\mathrm{d}\Omega \mathrm{d}\lambda} \propto \left|\int_{-L/2}^{L/2} \mathrm{d}z e^{i\left(\frac{2\pi}{\lambda}\cos\Theta + \frac{2\pi}{\lambda_0}\left(1-\frac{\lambda_0}{\lambda}\right)\beta^{-1}\right)z} e^{\pm i\frac{2\pi}{\lambda_0}\sqrt{z^2+f^2} - \kappa x_0(z)}\right|^2, \tag{S2.7}$$

where the integral was adapted to the finite physical extent of the metalenses. Calculated probability patterns for the converging and diverging metalenses per the design parameters used in the main text are shown in Fig. S2.1b and c, respectively. The theory accurately reproduces the occurrence of multiple curved emission bands over a wide spectral bandwidth, in good agreement with the experimental data. However, as opposed to the measurements, the calculated radiation patterns are identical for the two types of metalenses. This is because the opposing curvature of the emission wavefronts cannot be distinguished by their far field intensities, but requires additional phase information. Thus, under ideal conditions as assumed in theory, the metalens emission patterns only differ in the near-field (see simulations in Fig. 3.1 in the main text). Yet, as detailed in the main text, we stress that in practice the wavefront curvatures can be told apart owing to defocusing aberrations of the experimental imaging setup. Furthermore, in the following section we show that a non-zero grazing angle α_t leaves an opposite signature on the far-field emission of the two lens types.

S3 Effects of non-ideal beam-sample alignment

In our experiments, the radiation patterns of the converging and diverging metalenses are clearly distinguished by their spectral intensity distributions. As it turns out, the main cause of this difference is a non-vanishing grazing angle between the incident electron beam and the grating plane, as well as a finite beam divergence. In the following, we demonstrate this effect by distinguishing positive (i) and negative (ii) grazing angles for which electrons propagate away from and towards the sample, respectively.

First, in Fig. S3.1 we compare radiation patterns as obtained from Eq. (S2.7) for perfect grazing incidence with those predicted for small positive (i) grazing angles of $\alpha_t = 0.05°$ and $\alpha_t = 0.10°$. In this case, electrons are passing closer by the top of the metalenses than by the bottom, causing a rapid exponential decay of the electron-near-field coupling strength along the electron trajectory. As a result, the converging and diverging metalens radiation patterns are spectrally skewed towards the long and short emission wavelengths, respectively. Remarkably, this effect is in good agreement with the linear relation between the SP emission wavelength and the local grating period that is prevalent in the interaction, allowing for two essential conclusions: Each radiation band can be associated with a different subsection of the metalens and their intensities scale with the local near-field coupling strength. However, we note that our analytical

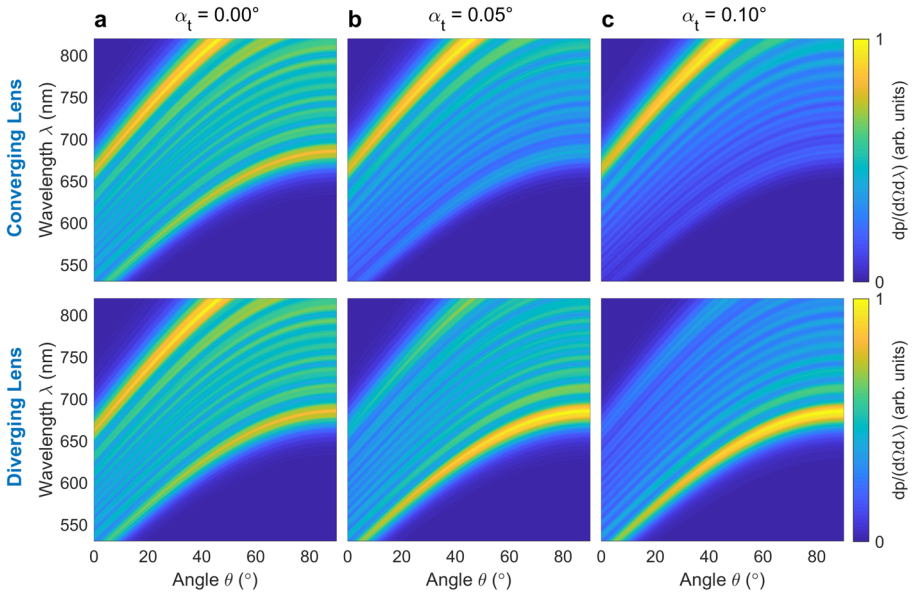

Figure S3.1: Metalens radiation patterns for electron incidence under small positive grazing angles. Analytical model calculations assuming 30 keV electron excitation at a minimum grazing distance of 20 nm. For increasing grazing angle, we consistently observe a skew of the converging and diverging metalens radiation patterns towards the long and short emission wavelengths, respectively. This can be related to an exponential dependence of the SP excitation efficiency with the grazing distance, as is evident from Eq. (S2.7).

model does not recover spectral features associated with material dispersion or the details of the metalens geometry, requiring rigorous numerical simulations as provided in the main text.

To illustrate the effect of negative (ii) grazing angles, Fig. S3.2 shows experimental data for $\alpha_t \approx -1°$ to $-2°$. In this case, the interaction is terminated upon collision of the electrons with the sample at just a few microns distance from the top of the metagratings. As a result, the converging and diverging metalens radiation patterns are strongly skewed towards the long and short emission wavelengths, respectively, in good agreement with the theory. In contrast, the emission of the periodic SP grating maintains overlap with the regular SP dispersion relation as to be expected. However, we note that a shorter electron-near- field interaction length results in both spectral broadening and a reduced radiation efficiency. Moreover, we observe that the emission probability is gradually damped towards decreasing emission wavelengths. For grazing distances on the order of a few tens of nanometers, this could be related to the exponential decay term in Eq. (S2.7), predicting stronger coupling to near-field components with a larger wavelength and thus a smaller evanescent decay constant κ.

Finally, we consider a combination of both positive and negative grazing angles, allowing us to emulate the effect of a divergent electron beam. To include effects of material dispersion and geometrical features, we perform numerical simulations

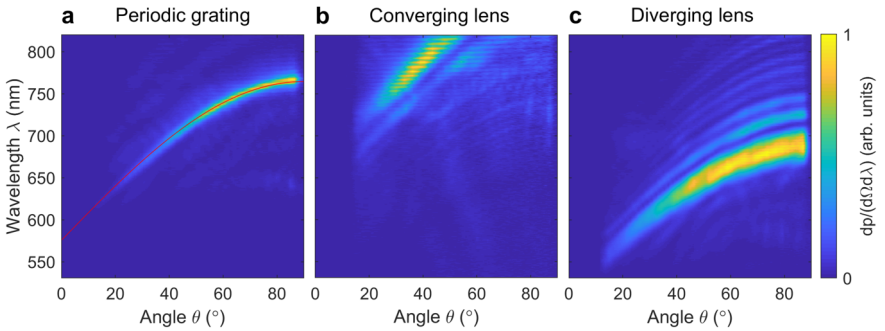

Figure S3.2: Experimental SPR patterns for truncated electron-beam-sample interaction at negative grazing angles. A 30-keV electron beam excites **a** the reference grating, **b** the converging metalens, and **c** the diverging metalens at a small negative grazing angle $\alpha_t \approx -1^\circ$ to -2°. In this configuration, the beam axis intersects with the sample surface after a few microns distance from the top of the metagratings, abruptly truncating the interaction. For reference, the red line in a represents the theoretical SP dispersion for a grating with a pitch of 189 nm.

for a range of electron trajectories that span grazing angles $-0.05^\circ \leq \alpha_t \leq 0.05^\circ$, and $-0.10^\circ \leq \alpha_t \leq 0.10^\circ$. The resulting radiation patterns are plotted in comparison to the experimental data in Fig. S3.3. For reference, the results obtained for perfect grazing incidence are also shown. Notably, we observe clear spectral trends that are consistent with the intuition gained from our analytical theory. The best agreement between experiment and simulations is found assuming a range of angles $-0.05^\circ \leq \alpha_t \leq 0.05^\circ$, as stated in the main text. This corresponds to a beam divergence angle smaller than 2 mrad which is a reasonable value for a scanning electron microscope [222]. However, we conclude that the exact form of the acquired metalens radiation patterns is very sensitive to a combination of parameters including the grazing distance, grazing angle, beam divergence as well as the exact sample geometry and the effect of material dispersion.

S4 Numerical FDTD simulations

To numerically simulate free-electron radiation over a broad spectral range, we resort to a commercial three-dimensional full-wave finite-difference in the time domain (FDTD) solver (Lumerical Inc., FDTD solutions). The electron beam excitation is emulated by an array of dipoles with a phase-lag that is determined by the electron velocity v. This simple model representation can be deduced as follows: Consider a point-like electron that is propagating in z direction along a trajectory with transverse coordinates $\mathbf{r}_{\perp,0} = (x_0, y_0)$. In this limit, we can represent the electron beam by a current density of the form

$$\mathbf{j}(\mathbf{r},\omega) = \hat{\mathbf{z}} e \delta\left(\mathbf{r}_\perp - \mathbf{r}_{\perp,0}\right) e^{i\frac{\omega}{v}z}. \tag{S4.1}$$

Furthermore, a point-like dipole can be expressed in terms of a dipole-moment as

$$\mathbf{d}(\mathbf{r},\omega) = \mathbf{d}(\omega)\delta\left(\mathbf{r}_\perp - \mathbf{r}_{\perp,0}\right)\delta\left(z - z_0\right) e^{i\frac{\omega}{v}z_0}. \tag{S4.2}$$

Choosing $\mathbf{d}(\omega) = d(\omega)\hat{\mathbf{z}}$ and combining the above two expressions we obtain a source

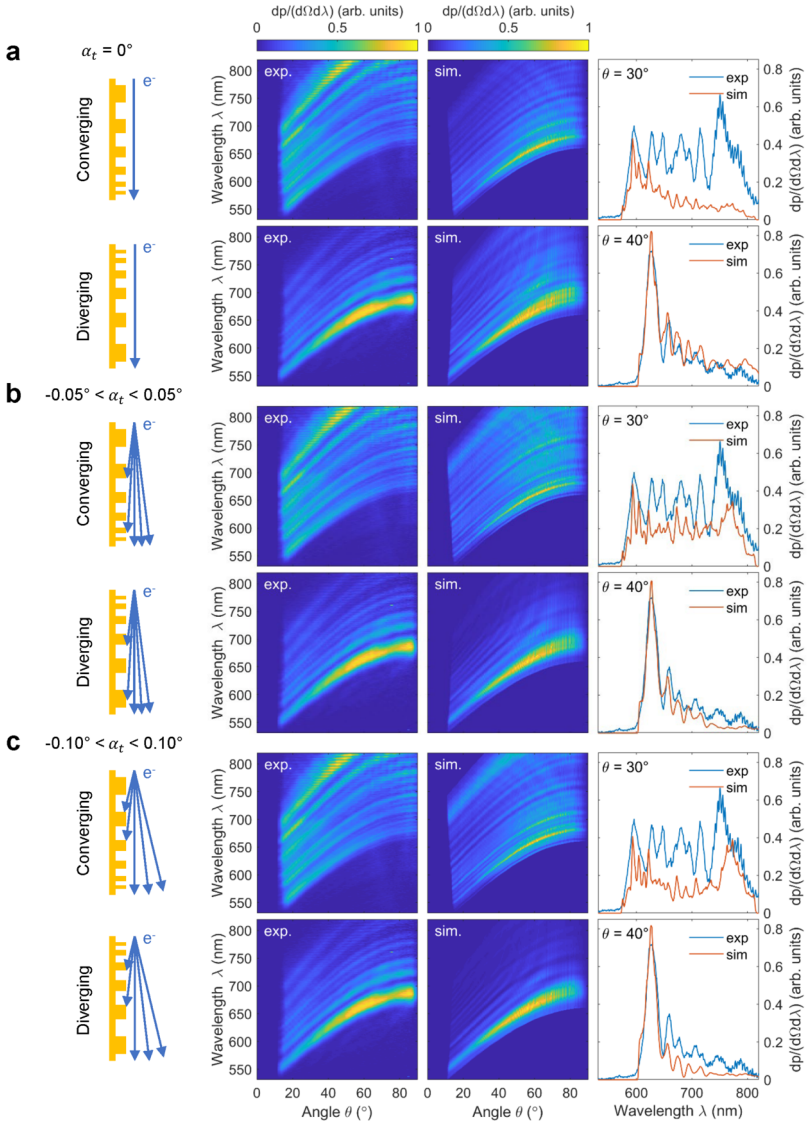

Figure S3.3: Numerical hybrid simulations of metalens radiation patterns for divergent electron beam excitation in comparison to the experimental data. Each simulation incorporates 5 electron trajectories within the angular ranges specified in **a**, **b**, and **c**. The best agreement between simulations and the experimental data is obtained for a beam divergence of $-0.05° \leq \alpha_t \leq 0.05°$ (as also seen by comparing the emission spectra for selected angles shown on the right). As in the experiments, numerical data are obtained for 30 keV incident electron energy, with the grazing distance assumed to be 5 nm.

current of the form

$$\mathbf{j}(\mathbf{r},\omega) = d(\omega)\hat{\mathbf{z}}\delta\left(\mathbf{r}_\perp - \mathbf{r}_{\perp,0}\right)\sum_n e^{i\frac{\omega}{v}z_n}\delta\left(z - z_n\right), \tag{S4.3}$$

with the z_n spaced by a distance much smaller than the wavelength (5 nm). The electron-induced nearfield is recorded using a frequency domain monitor placed 1 µm away from the electron beam source, either parallel or perpendicular to the grating plane (depending on the orientation of the desired collection). To reveal the focusing and defocusing effects shown in Fig. 3.1 of the main text, the recorded vectorial fields were numerically propagated in free space to a range of distances from 1 µm to 40 µm. The far-field data used for the Zemax ray-tracing analysis in Fig. 3.4 were obtained by a software integrated near-to-far-field transformation algorithm.

S5 SPR excitation efficiency

As described in ref. [175], the maximum excitation efficiency for visible and near-infrared SP radiation by 30-keV electrons in an SEM is of the order of 10^{-4} to 10^{-3} for a grating with a length of a few tens of microns. To estimate the radiation efficiency of our metagratings from our simulations, we recall that the electron beam is modeled by a chain of dipole sources as elaborated in Section S4. Thus, the total optical power that is radiated into the far-field must be proportional to the combined power of all dipole sources, with a total of 4 pW. Fig. S5.1 shows the emitted spectral power density, both for the periodic reference grating and for the converging metalenses. We assume perfect parallel incidence of the electrons at 30 keV kinetic energy with a total interaction range of 20 µm (close to the experimental conditions). By integrating over the corresponding spectra, we extract radiation efficiencies of $2.3\cdot10^{-3}$ and $2.4\cdot10^{-3}$ for the periodic grating and the converging metalens, respectively, in good agreement with the values predicted in ref. [175].

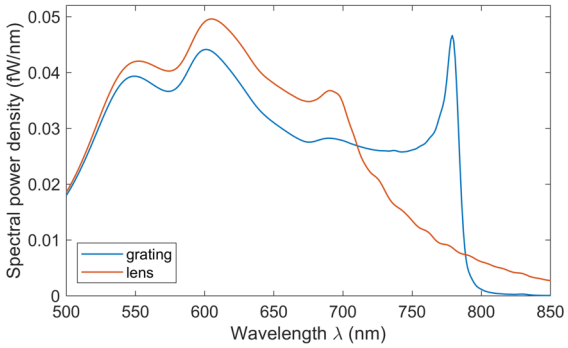

Figure S5.1: Numerically simulated spectral power density of SPR emitted by the reference grating and the converging metalens.

S6 Geometrical variations of the electron near-field coupling efficiency

Close inspection of the near-field simulations shown in Fig. 3.1 of the main text reveals a variance in intensity along the surface of the metalenses. For a fixed emission wavelength, we can relate this effect to variations in the electron-near-field coupling efficiency as a function of the grating period. To support this interpretation, Fig. S6.1 shows the electron-induced near-field intensity upon excitation of different gratings with periodicities in the range of $\Lambda = 150$ nm to $\Lambda = 250$ nm. The simulations are performed for a fixed emission wavelength of $\lambda = 580$ nm, assuming 30-keV electrons that graze the structures at a distance of 5 nm. The data qualitatively capture the intensity variations observed near the surface of the metalenses, showing a similar decay with increasing period. For completeness, we note that the coupling efficiency also scales with the emission wavelength as determined by the evanescent decay constant κ of the near-field away from the grating plane in Eq. (S2.7).

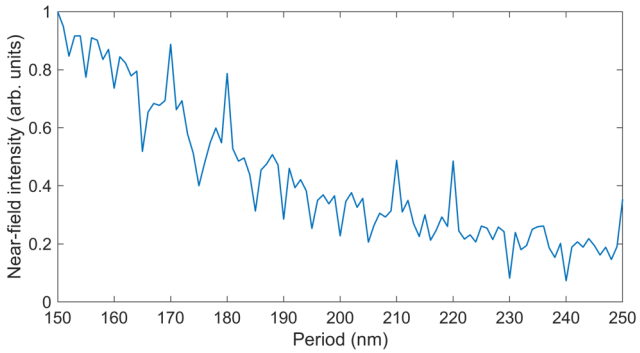

Figure S6.1: Electron-induced near-field intensity of a periodic grating as a function of the pitch. Simulations are performed assuming excitation by 30-keV electrons, at a grazing distance of 5 nm, and $\lambda = 580$ nm emission wavelength. Clearly, a global decrease in near-field intensity is observed with increasing pitch, in good agreement with the intensity variations observed near the surface of the metalenses in Fig. 3.1 of the main text.

S7 Near-field analysis of SRR meta-atoms

To discuss resonant near-field effects in the SRR metasurface proposed in Fig. 3.5, we consider a decomposition of the SRR meta-atoms into two arms that form a dimer and a connecting rod which acts as an individual antenna (a similar structure was rigorously explored in ref. [223]). For an electron passing near the closed edge of the meta-atom, the induced near field is expected to be dominated by optical modes of the connecting rod. Thus, the SRR would primarily emit vertically (V) polarized radiation, similar to the emission by a dipole that aligns with the direction of electron propagation. On the other hand, for an electron passing near the opposing open edge, we expect dominant coupling to the dimer modes, increasing the contribution of a horizontally (H) polarized component to the emitted radiation. For the SRR metasurface with a working point at 550 nm, this is corroborated by the polarization ellipse in Fig. 3.5c, as well as the total electron-induced near-field distributions shown in Fig. S7.1a. For an SRR metalens with

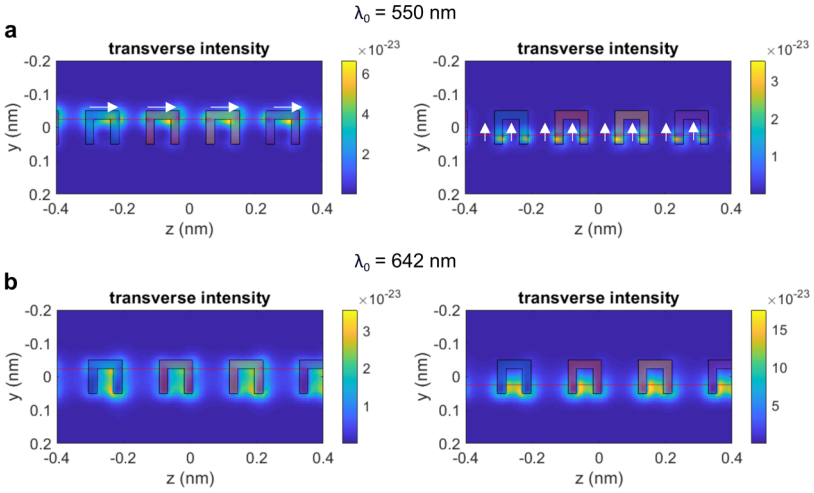

Figure S7.1: In-plane near-field intensity distributions of SRR meta-atom arrays excited by a 30-keV electron at the two design wavelengths of $\lambda_0 = 550$ nm and $\lambda_0 = 642$ nm. The red lines indicate the electron trajectory.

another working point at a 642 nm excitation wavelength, Fig. 3.5a shows a dip in the reflectivity for the V polarization. Thus, in general, more energy is transferred to the near-field of the V-polarized mode (which does not necessarily indicate subsequent coupling to radiation). As to be seen in Fig. S7.1b, this effect seems to extend the SRR mode beyond the rod excitation, when the electron impinges at -25 nm relative to the SRR center (left). The dimer excitation continues to dominate even when the electron passes the meta-atoms at +25 nm (right).

S8 Spectral and angular system response calibration

The hyperspectral angle-resolved emission patterns shown in this work were acquired using a Czerny-Turner spectrograph equipped with a 500 nm blazed dispersion grating (300 lines/mm) and a back-illuminated charge-coupled device (CCD) sensor array (Andor Newton DU940P-BU). The system is aligned such that the spectral and angular information are projected onto the horizontal and vertical sensor axes, respectively. A vertical slit aperture with a horizontal width of 100 µm was introduced to only transmit light that is collected within a narrow azimuthal angular range around the optical axis of the parabolic light-collection mirror. The measured radiations patterns were acquired at an electron beam current of approximately 3.3 nA for durations of 300 s and 250 s for the metalenses and the reference grating, respectively.

The spectral system response function of the light collection setup was determined according to a similar procedure as described in ref. [170]. In brief, transition radiation (TR) excited by a 30-keV electron beam was collected from the planar surface of a mono-crystalline aluminum sample using hyperspectral angle-resolved light detection. The resulting emission pattern was integrated over all angles and normalized to the

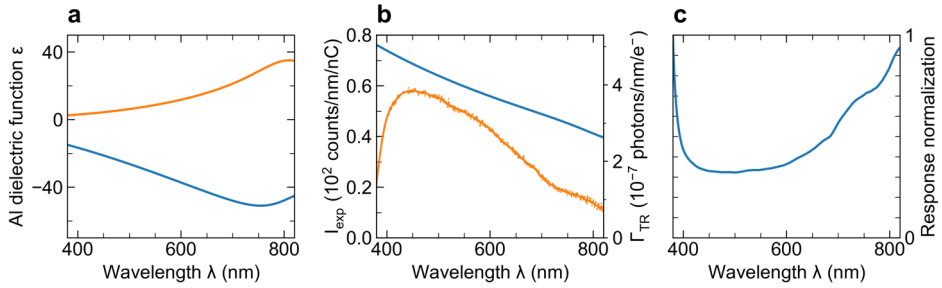

Figure S8.1: Spectral response calibration of the light collection setup. **a** Real (blue) and imaginary part (orange) of the dielectric function of a mono-crystalline Al sample emitting transition radiation (TR). **b** Integrated TR spectrum as obtained for 30-keV electron beam excitation in hyperspectral angle-resolved light detection mode. A smoothening function (solid orange curve) was applied to the experimental data I_{exp} (orange dotted curve) in order to avoid noise artefacts upon normalization by the calculated TR emission probability Γ_{TR} (solid blue curve). **c** Inverted spectral response function of the light collection setup applied to normalize the measured intensity distributions.

analytical TR expression given in ref. [31] (see Fig. S8.1b). For the calculations, optical constants of the aluminium crystal were derived from spectroscopic ellipsometry measurements (see Fig S8.1a). We stress that a full angle-resolved spectral response calibration was omitted since the emission of TR is strongly suppressed in the direction of the surface normal [31]. However, considering a dominant contribution by the spectrograph (dispersion grating, CCD sensor), angular features are assumed to have little effect on the overall spectral system response curve (see Fig. 8.1c).

Following refs. [55–57], the vertical pixel arrays of the CCD sensor were calibrated for the zenith emission angle θ by mapping the one-dimensional projection of the light collection mirror onto its parabolic contour in the plane spanned by the electron beam and the optical axis of the imaging system. For the n^{th} pixel in an array, the corresponding emission angle θ_n was derived from an expression of the form

$$\theta_n = \frac{\pi}{2} + \arctan\left(az_n - \frac{1}{4az_n}\right), \tag{S8.1}$$

where $a = 0.1\ \mathrm{mm}^{-1}$ is the parabola coefficient and z_n denotes the vertical coordinate of a mirror surface element above the focal plane. The latter was calculated as $z_n = z_0 + n\,(z_N - z_0)\,/\,(N+1)$, where $z_0 = 0.5$ mm and $z_N = 11.5$ mm correspond to the lower and upper mirror cut-offs, respectively, and $N+1$ is the total number of enclosed pixels. In addition, the hole for electron beam transmission provides a useful reference for upwards emission at an angle $\theta = 90°$. Eventually, the calibrated data were normalized to the collection solid angle using an expression of the form

$$\mathrm{d}\Omega_n = A\frac{2az_n^2 - x_n}{\left(x_n^2 + z_n^2\right)^{\frac{3}{2}}}, \tag{S8.2}$$

with A a system-dependent constant and $x_n = az_n^2 - (4a)^{-1}$.

We note that the above procedure is optimized for light emission by a point source that is precisely aligned with the mirror focal plane. In our Smith Purcell experiments, however, light is emitted by elongated sources that extend more than 20 µm below the focus. Reassuringly, a ray-tracing analysis has revealed little distortion of the angular system response by the precise vertical mirror-sample alignment. Nevertheless, we found significant chromatic aberrations that are correlated with the curvature of the emission wavefronts. For reference, this effect is also reproduced in Fig. S10, showing the emission patterns of our model structures as projected onto the CCD sensor plane, prior to the transformation of the vertical sensor coordinates into angles. At the bottom, the patterns are truncated by the lower cut-off of the light-collection mirror, with opposing slopes distinguishing the two metalenses.

Due to minor system imperfections, we note that the experimental data feature additional chromatic aberrations that manifest as a common slope in the projection of the hole for electron transmission. Thus, the measured patterns were calibrated by linear adaptation of the lower and upper boundaries on the CCD sensor that mark the reference coordinates z_0 and z_N for each spectral data slice λ_m, with a small uncertainty of 1 to 2 pixels. However, to maintain and unambiguously recover wave-front related aberrations, we stress that the exact same calibration parameters were used for both the converging and diverging metalenses. In addition, the calibration of the reference SP grating was verified against the theoretical SP dispersion relation. The error introduced by the calibration uncertainty can be estimated as

$$\Delta\theta_n = \frac{a + \frac{1}{4az_n^2}}{1 + \left(az_n - \frac{1}{4az_n}\right)^2}\Delta z = \frac{2az_n + \cot\theta_n}{1 + \cot^2\theta_n}\frac{\Delta z}{z_n} \tag{S8.3}$$

where Δz is given by the size of the CCD sensor pixels of 2×13.5 µm (data on vertical sensor axis were binned two-fold). Thus, for the lower cutoff angle $\theta_0 \approx 11°$, we obtain $\Delta\theta_0 \approx \tan\theta_0\,(\Delta z / z_0) \lesssim 1°$.

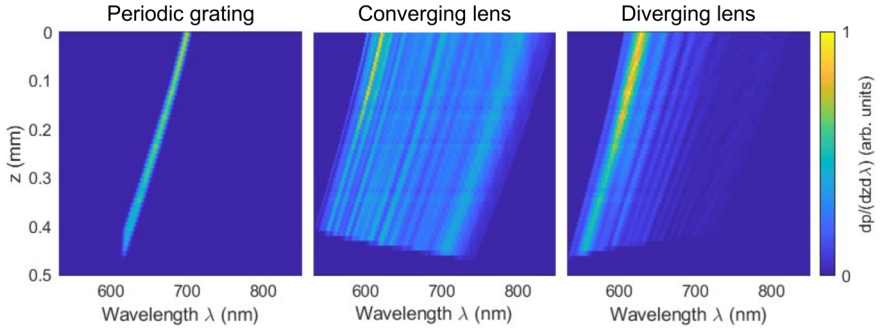

Figure S8.2: Ray-tracing projection of the simulated metalens and reference grating radiation patterns onto a planar screen. At the bottom, the metalens radiation patterns are truncated along a line with opposing slope, revealing wave-front-related chromatic aberrations in the projection of the lower cutoff of the parabolic light collection mirror as observed in the experiments.

3.8 Appendix: Green's function formalism of the metalens

In the following, we apply a classical Green's function formalism to derive approximate expressions for the far-field radiation patterns of our Smith-Purcell metalenses under the assumptions posed in section S2. First, we note that the far-field amplitude $\boldsymbol{\mathcal{E}}_\infty(r\hat{\mathbf{n}},\omega)$ of an electric field $\boldsymbol{\mathcal{E}}(\mathbf{s},\omega)$ that is given in a reference plane $\mathbf{s}$ with surface normal $\hat{\boldsymbol{\sigma}}$ can be obtained from an expression of the form (cf. chapter 3.4 of ref. [12]):

$$\boldsymbol{\mathcal{E}}_\infty(r\hat{\mathbf{n}},\omega) = -\frac{ik_0}{2\pi}\hat{\mathbf{n}}\cdot\hat{\boldsymbol{\sigma}}\frac{e^{ik_0 r}}{r}\int \mathrm{d}^2\mathbf{s}\, e^{-ik_0\hat{\mathbf{n}}\cdot\mathbf{s}}\boldsymbol{\mathcal{E}}(\mathbf{s},\omega), \tag{A1}$$

where $\hat{\mathbf{n}}$ is the direction of observation, and $k_0 = \omega/c$ is the wave number. By modelling the electron as a moving point charge, the field $\boldsymbol{\mathcal{E}}(\mathbf{r},\omega)$ itself can be linked to a source current $\mathbf{j}(\mathbf{r},\omega) = \hat{\mathbf{z}}e\delta\left(\mathbf{r}_\perp - \mathbf{r}_{\perp,0}\right)e^{i\frac{\omega}{v}z}$ via (cf. chapter 2.10 of ref. [12])

$$\boldsymbol{\mathcal{E}}(\mathbf{r},\omega) = i\omega\mu_0\int \mathrm{d}^3\mathbf{r}'\,\overleftrightarrow{\mathbf{G}}\left(\mathbf{r},\mathbf{r}',\omega\right)\cdot\mathbf{j}\left(\mathbf{r}',\omega\right) \tag{A2}$$

where $\hat{\mathbf{z}}$ is the unit vector in the direction of electron propagation, $\mathbf{r}_{\perp,0}$ denotes the transverse electron coordinates, and $\overleftrightarrow{\mathbf{G}}\left(\mathbf{r},\mathbf{r}',\omega\right)$ is the dyadic Green's tensor. The latter constitutes a self-contained electromagnetic representation of the system that is excited by the electron. To derive an approximate analytical expression for $\overleftrightarrow{\mathbf{G}}\left(\mathbf{r},\mathbf{r}',\omega\right)$, we introduce a set of normal modes $\mathbf{u}_\mathbf{k}(\mathbf{r})$ with mode index $\mathbf{k}$ and eigenfrequencies $\omega_\mathbf{k}$ that satisfy the wave equation $\nabla\times\nabla\times\mathbf{u}_\mathbf{k}(\mathbf{r}) - \frac{\omega_\mathbf{k}^2}{c^2}\mathbf{u}_\mathbf{k}(\mathbf{r}) = 0$ as well as the orthogonality relation $\int \mathrm{d}^3\mathbf{r}\,\mathbf{u}_\mathbf{k}(\mathbf{r})\cdot\mathbf{u}^*_{\mathbf{k}'}(\mathbf{r}) = \delta_{\mathbf{k}\mathbf{k}'}$ [12]. Thus, $\overleftrightarrow{\mathbf{G}}\left(\mathbf{r},\mathbf{r}',\omega\right)$ can be evaluated in terms of a mode expansion (cf. chapter 8.4 of ref. [12])

$$\overleftrightarrow{\mathbf{G}}\left(\mathbf{r},\mathbf{r}',\omega\right) = \sum_\mathbf{k} c^2\frac{\mathbf{u}_\mathbf{k}(\mathbf{r})\otimes\mathbf{u}^*_\mathbf{k}(\mathbf{r}')}{\omega_\mathbf{k}^2-\omega^2}, \tag{A3}$$

with the summation running over all supported eigenmodes, and $\mathbf{a}\otimes\mathbf{b}$ denoting the dyadic product of vectors $\mathbf{a}$ and $\mathbf{b}$. Choosing an ansatz for the metalenses as introduced in Section S2, the index $\mathbf{k}$ can be identified as the far-field wave vector component of the grating modes with orientation $\hat{\mathbf{k}}$, magnitude k, and continuous dispersion relation $\omega_\mathbf{k} = ck$. Hence, the sum in Eq. (A3) can be transformed into an integral, yielding the Green's tensor as

$$\begin{aligned}
\overleftrightarrow{\mathbf{G}}\left(\mathbf{r},\mathbf{r}',\omega\right) &= c^2\int\frac{\mathrm{d}^3\mathbf{k}}{(2\pi)^3}\frac{\mathbf{u}_{k\hat{\mathbf{k}}}(\mathbf{r})\otimes\mathbf{u}^*_{k\hat{\mathbf{k}}}(\mathbf{r}')}{\omega_{k\hat{\mathbf{k}}}^2-\omega^2}\\
&= \frac{c^2}{8\pi^3}\int\mathrm{d}\Omega\int\mathrm{d}k\frac{k^2}{2\omega_{k\hat{\mathbf{k}}}}\left(\frac{1}{\omega_{k\hat{\mathbf{k}}}-\left(\omega+i\gamma\right)}+\frac{1}{\omega_{k\hat{\mathbf{k}}}+\left(\omega+i\gamma\right)}\right)\mathbf{u}_{k\hat{\mathbf{k}}}(\mathbf{r})\otimes\mathbf{u}^*_{k\hat{\mathbf{k}}}(\mathbf{r}')\\
&= \frac{1}{16\pi^3}\int\mathrm{d}\Omega\int\mathrm{d}k\,k\left(\frac{1}{k-\frac{1}{c}\left(\omega+i\gamma\right)}+\frac{1}{k+\frac{1}{c}\left(\omega+i\gamma\right)}\right)\mathbf{u}_{k\hat{\mathbf{k}}}(\mathbf{r})\otimes\mathbf{u}^*_{k\hat{\mathbf{k}}}(\mathbf{r}')\\
&= \frac{i\omega}{8\pi^2 c}\int\mathrm{d}\Omega\,\mathbf{u}_{\frac{\omega}{c}\hat{\mathbf{k}}}(\mathbf{r})\otimes\mathbf{u}^*_{\frac{\omega}{c}\hat{\mathbf{k}}}(\mathbf{r}'),
\end{aligned} \tag{A4}$$

where in the last step we have exploited Cauchy's integral identity to write $k = \omega/c$, assuming a vanishing loss term $\gamma \to 0$ and disregarding unphysical solutions for negative frequencies [12]. We can now turn back to Eq. (A2) to express the electron-induced electric field as

$$\begin{aligned}\boldsymbol{\mathcal{E}}(\mathbf{r},\omega) &= -\frac{\omega^2\mu_0}{8\pi^2 c}\int \mathrm{d}\Omega\, \mathbf{u}_{\frac{\omega}{c}\hat{\mathbf{k}}}(\mathbf{r})\left(\int \mathrm{d}^3\mathbf{r}'\, \mathbf{u}^*_{\frac{\omega}{c}\hat{\mathbf{k}}}\left(\mathbf{r}'\right)\cdot\mathbf{j}\left(\mathbf{r}',\omega\right)\right)\\ &= -\frac{\omega^2\mu_0}{8\pi^2 c}e\int \mathrm{d}\Omega\, \mathbf{u}_{\frac{\omega}{c}\hat{\mathbf{k}}}(\mathbf{r})\left(\int \mathrm{d}z'\int \mathrm{d}^2\mathbf{r}'_\perp\, \mathbf{u}^*_{\frac{\omega}{c}\hat{\mathbf{k}}}\left(\mathbf{r}'_\perp,z'\right)\cdot\hat{\mathbf{z}}\,\delta\left(\mathbf{r}'_\perp-\mathbf{r}_{\perp,0}\right)e^{i\frac{\omega}{v}z'}\right). \end{aligned} \tag{A5}$$

As a last step, we need to derive the corresponding far-field amplitude from Eq. (A1). To this end, we may choose a reference plane $\mathbf{s}$ that is oriented orthogonal to the direction of observation $\hat{\mathbf{n}}$, yielding

$$\boldsymbol{\mathcal{E}}_\infty(r\hat{\mathbf{n}},\omega) = \frac{ie\mu_0\omega^3}{16\pi^3c^2}\frac{e^{i\frac{\omega}{c}r}}{r}\int \mathrm{d}\Omega\left(\int \mathrm{d}z\, \mathbf{u}_{\frac{\omega}{c}\hat{\mathbf{k}}}\left(\mathbf{r}_{\perp,0},z\right)\cdot\hat{\mathbf{z}}\,e^{-i\frac{\omega}{v}z}\right)^*\int \mathrm{d}^2\mathbf{s}\,\mathbf{u}_{\frac{\omega}{c}\hat{\mathbf{k}}}(\mathbf{s}). \tag{A6}$$

Next, we exploit that only the propagating Fourier components have a non-vanishing far-field contribution. Hence, the remaining surface integral over $\mathbf{s}$ can be evaluated as

$$\int \mathrm{d}^2\mathbf{s}\,\mathbf{u}_{\frac{\omega}{c}\hat{\mathbf{k}}}(\mathbf{s}) = \int \mathrm{d}^2\mathbf{s}\mathbf{A}_{\frac{\omega}{c}\hat{\mathbf{k}},0}e^{i\frac{\omega}{c}\hat{\mathbf{k}}\cdot\mathbf{s}} = 4\pi^2\frac{c^2}{\omega^2}\mathbf{A}_{\frac{\omega}{c}\hat{\mathbf{k}},0}\delta\left(\hat{\mathbf{k}}-\left(\hat{\mathbf{k}}\cdot\hat{\boldsymbol{\sigma}}\right)\hat{\boldsymbol{\sigma}}\right). \tag{A7}$$

Inserting the result back into Eq. (A6) and integrating over all possible orientations of $\hat{\mathbf{k}}$, it follows that $\hat{\mathbf{k}} \parallel \hat{\boldsymbol{\sigma}} = \hat{\mathbf{n}}$. Thus, we are left with the electron-induced far-field amplitude in the form

$$\boldsymbol{\mathcal{E}}_\infty(r\hat{\mathbf{n}},\omega) = ie\omega\mu_0\frac{e^{i\frac{\omega}{c}r}}{4\pi r}\mathbf{A}_{\frac{\omega}{c}\hat{\mathbf{n}},0}\left(\int \mathrm{d}z\, \mathbf{u}_{\frac{\omega}{c}\hat{\mathbf{n}}}\left(\mathbf{r}_{\perp,0},z\right)\cdot\hat{\mathbf{z}}\,e^{-i\frac{\omega}{v}z}\right)^*. \tag{A8}$$

With Eq. (S2.2) the corresponding emission probability per unit frequency and unit solid angle element can be written as [12]

$$\frac{\mathrm{d}^2p}{\mathrm{d}\Omega\mathrm{d}\omega} = \frac{\alpha\omega}{4\pi^2c^2}\left|\mathbf{A}_{\frac{\omega}{c}\hat{\mathbf{n}},0}\right|^2\left|\int \mathrm{d}z\, \mathbf{u}_{\frac{\omega}{c}\hat{\mathbf{n}}}\left(\mathbf{r}_{\perp,0},z\right)\cdot\hat{\mathbf{z}}\,e^{-i\frac{\omega}{v}z}\right|^2, \tag{A9}$$

where $\alpha = e^2/(4\pi\varepsilon_0\hbar c)$ is the fine structure constant. Finally, we obtain the desired emission probability with respect to the emission wavelength in the form

$$\frac{\mathrm{d}^2p}{\mathrm{d}\Omega\mathrm{d}\lambda} = \left|\frac{\mathrm{d}\omega}{\mathrm{d}\lambda}\right|\frac{\mathrm{d}^2p}{\mathrm{d}\Omega\mathrm{d}\omega} = \frac{\alpha}{\lambda^3}\left|\mathbf{A}_{k_0\hat{\mathbf{n}},0}\right|^2\left|\int \mathrm{d}z\, \mathbf{u}_{k_0\hat{\mathbf{n}}}\left(\mathbf{r}_{\perp,0},z\right)\cdot\hat{\mathbf{z}}\,e^{-i\frac{\omega}{v}z}\right|^2, \tag{A10}$$

with $k_0 = \omega/c = 2\pi/\lambda$.

4

Free-electron-light coupling in an optical fibre-integrated metagrating

Free electrons can couple to optical material excitations on ultra-small length and time scales, enabling the generation of coherent radiation and providing control over the wave function of the electrons themselves. Here, we exploit the Smith-Purcell (SP) effect to experimentally study the coherent coupling of free electrons and light in a circular metallo-dielectric metagrating that is fabricated onto the input facet of a multi-mode optical fibre. Using hyperspectral angle-resolved far-field imaging in a scanning electron microscope, we probe the angular dispersion of SP radiation (SPR) that is generated in both free space and in the fibre by an electron beam that grazes the metagrating at nanoscales distance. Furthermore, we analyse the spectral distribution of SPR that couples to guided optical modes and correlate it with the numerical aperture of the fibre. By varying the electron energy between 5 keV and 30 keV, we observe the emission of SPR from the ultraviolet to the near-infrared spectral range and up to the third emission order. In addition, we detect incoherent luminescence that is generated by electrons penetrating the input facet of the fibre and scattering inelastically. As result, we find a Fano resonance that is coupled to a Rayleigh anomaly of the metagrating, and that overlaps with the angular dispersion of second-order SPR at 20 keV. Our findings demonstrate the potential of optical fibre-integrated metasurfaces as a versatile platform to implement novel light sources and to synthesize free-electron quantum states with light.

4.1 Introduction

In free space, the exchange of energy between free electrons and photons is usually forbidden due to the violation of momentum conservation [69]. In the vicinity of nanostructures, however, the formation of localized optical fields can mediate their interaction [103]. In recent years, this phenomenon has been harnessed to probe optical material properties on ultra-small length and time scales, to generate coherent radiation over an ultra-broad spectral range, and to manipulate the wave function of free electrons in both space and time [31–33, 101]. To further advance these developments, new insights into the interaction of free electrons, light and matter, and how to control it, are of great interest.

The interaction of free electrons and light in nanomaterials can occur both as a spontaneous and as a stimulated process [31, 67, 68, 76, 102]. On the one hand, the evanescent electromagnetic field of the electron itself can drive optical material excitations across a broad spectral range from the extreme ultraviolet (XUV) to the far infrared (IR) [28, 31]. During this process, the electron undergoes a subtle energy loss that is correlated with the local density of optical states (LDOS) [31, 133, 134]. The radiative component of the LDOS gives rise to the emission of cathodoluminescence (CL) [134, 224], the properties of which can be probed experimentally using angle- and polarization-resolved CL spectroscopy [53, 55]. On the other hand, the near-field of a material that is excited by an external optical pump field can induce discrete electron energy-gain and energy-loss transitions by mediating the stimulated emission and absorption of photons at the pump photon energy [67–69]. In photon-induced near-field electron microscopy (PINEM) [66], the resulting modulation of the electron energy spectrum is exploited as a measure of the electron-photon coupling strength, enabling spectrally- [74], spatially- [72, 73, 76], temporally- [79–81], polarization- [66, 72, 75, 76], and phase-resolved near-field measurements [78, 225]. Furthermore, the same mechanisms can be harnessed to manipulate the phase and amplitude of the electron wave function itself [70, 94], facilitating the synthesis of ultra-short free-electron wave packets [80, 90, 91, 97], electron vortex beams [92], and complex free-electron quantum states [98, 99].

For free electrons and photons to couple, the optical field that mediates their interaction has to contain a spatial Fourier component that remains in phase with the electron throughout the interaction, a condition known as electron-light-phase matching [103]. As a result, the interaction is highly dependent on the electron velocity, with slow electrons favouring high spatial frequency components in tightly concentrated optical fields, while fast electrons preferentially couple to more extended field distributions [76, 104, 169, 175]. Nevertheless, a localized field is naturally composed of a broad distribution of spatial Fourier components. Hence, the fraction of electromagnetic energy that mediates the interaction is typically small. In contrast, systems that comprise a large number of nanostructures permit to shape the coupling of free electrons and light, much like optical metasurfaces that tailor optical fields in real space and the Fourier domain [108, 110–113].

A well-known example for the coupling of free electrons and light in periodic systems is the so-called Smith Purcell (SP) effect [107]. The SP effect arises if an electron

polarizes the system along a grazing trajectory, leading to the emission of broadband radiation into discrete diffraction orders m. Assuming a grating of pitch p that is excited orthogonal to the rulings, the angular dispersion of this radiation can be written as [107]

$$\omega(\theta) = 2\pi c \frac{m}{p} \left(\beta^{-1} + n\sin\theta\right)^{-1}, \tag{4.1}$$

with ω the frequency, $\beta = v/c$ the electron velocity in units of the speed of light in vacuum c, θ the emission angle, and n the refractive index of the surrounding medium. Here, the emission angle is defined relative to the surface normal of the grating, with $\theta = -90°$ corresponding to the direction of propagation of the electron. The light waves that couple to the electron in the near-field of the grating carry spatial frequencies that are determined by the wave vector of the outgoing photons and the harmonic orders of the reciprocal lattice constant [203, 226]. Thus, for each harmonic order m, only a single combination of emission angle and frequency enables electron-light-phase matching as addressed above.

Since its discovery several decades ago [107], the SP effect has been extensively explored in the literature, both theoretically and experimentally [204]. The recent advent of optical metasurfaces offers great potential to control this phenomenon by tailoring the spectrum [175, 205, 211, 214], the angular distribution [209, 226, 227], as well as the polarization of SPR [206, 207, 226, 227]. Similarly, the inverse SP effect [84, 105, 106, 220, 228] can be harnessed in metasurfaces to mediate the exchange of energy between free electrons and an optical pump field as in PINEM. However, interfacing such structures with suitable optics for the extraction or injection of radiation, respectively, poses another experimental challenge. A few years ago, the authors of refs. [229, 230] have demonstrated an approach based on metallic nano gratings that are fabricated onto the input facet of an optical fibre to simultaneously generate and couple SPR into guided waves. This has enabled the extraction of SPR through the fibre from the visible (VIS) to the ultraviolet (UV) spectral range. However, the angular features of the coupling between free electrons and light in such a geometry have not been studied yet.

In this work, we apply hyperspectral angle-resolved (HSAR) far-field imaging in a scanning electron microscope (SEM) [55, 56] to probe the angular dispersion of the SP effect in a circular metallic metagrating that is fabricated onto the cleaved input facet of a multi-mode optical fibre. Our measurements reveal the characteristic signature of SPR that is generated on both the free-space side and the fibre-core side of the metagrating by exploiting radiation that leaks out of the fibre. Furthermore, we measure the spectral distribution of SPR that couples into guided waves and correlate it with the numerical aperture (NA) of the fibre. By varying the electron energy from 5 keV to 30 keV, we observe SPR across the entire UV to NIR spectral range, and up to the third diffraction order. Additionally, we find that electrons penetrating the input facet of the fibre generate incoherent defect luminescence that interferes with a Rayleigh anomaly of the metagrating. As a result, a Fano resonance is observed that overlaps with the dispersion of second-order SPR at 20 keV. The analysis of our data is supported by an analytical model that allows us to efficiently describe and distinguish the spectral and angular features of SPR and the incoherent signal contributions.

The findings presented in this work are of great relevance to the design of novel

electron-light coupling geometries for harnessing the SP effect in both light-collection and optical-pump configurations. The simultaneous observation of SPR and a Fano resonance demonstrates the unique potential of metasurfaces to combine, enhance, and control the coupling of free electrons and light by exploiting collective optical excitations such as lattice resonances [211, 231, 232]. In addition, the fibre geometry facilitates time-dependent studies of the electron-light-matter interaction while offering great potential for the implementation of novel ultrafast spectroscopy techniques.

4.2 Sample preparation and experimental setup

Using focused ion beam milling (FEI Helios 600, Thermo-Fisher Scientific, Inc.), a circular metagrating was fabricated onto the input facet of a metal-coated multi-mode optical fiber (numerical aperture NA = 0.22, 105-µm diameter silica core, 10-µm cladding, CFML2L05, Thorlabs, Inc.). The coating consists of a 5-nm thick Cr adhesion layer and a 45-nm thick Au film that are applied by sputter deposition (EM ACE600, Leica, Inc.). An SEM micrograph of the resulting structure is shown in Fig. 4.1a. The metagrating comprises 237 concentric rings with a nominal radial pitch of 200 nm and a maximum diameter of 100 µm. The rings are separated by approximately 100-nm wide gaps that extend into the silica substrate of the fibre core. In the centre, a 5-µm diameter patch is retained as an alignment marker. A close-up view in Fig. 4.1b shows a few milling defects that result from the crystallographic disorder of the metal coating [233]. However, as demonstrated in previous work [214], minor fabrication imperfections do not cause a substantial distortion of SPR as long as the desired periodicity of the pattern remains.

Figure 4.1c shows a simplified overview of the experimental setup that is used for the observation of the SP effect in the far field and through the fibre. We operate a conventional SEM instrument (FEI Quanta FEG 650, Thermo-Fisher Scientific Inc.) that emits an electron beam with kinetic energies in the range of 5 keV – 30 keV (beam current 0.8 nA – 1.6 nA). The beam is focused to a spot size of a few tens of nanometres, and aligned with the metagrating along a grazing trajectory. SPR that is emitted into the far field is collected by an off-axis half-parabolic mirror that is focused onto the metagrating from above while the electron beam is transmitted through a narrow aperture. The collected light is free-space coupled into an optical setup for hyperspectral angle-resolved (HSAR) far-field imaging (SPARC Spectral, Delmic B.V.) [55, 56]. A vertical slit aperture at the entrance of the setup filters out the light that has been collected near the symmetry plane of the mirror. Subsequently, the light is dispersed by a diffraction grating and projected onto a two-dimensional silicon sensor array, with the horizontal and the vertical sensor axes resolving the spectral and the angular information, respectively. Radiation that is transmitted through the fibre is fibre-coupled into an optical spectrometer with a liquid-nitrogen cooled silicon sensor (Spectra Pro 2300i, Princeton Instruments, Inc.). For this purpose, the fibre is fitted with a stainless-steel ferrule connector that is coupled to the input fibre of a fibre-optic vacuum feed through as to be seen in Fig. 4.1d.

For the acquisition of HSAR data in the NIR spectral range, a long-pass filter with a cut-off energy of 2.48 eV is used to avoid spectral overlap between the first and second diffraction order of the diffraction grating. Thus, signal artefacts are eliminated up

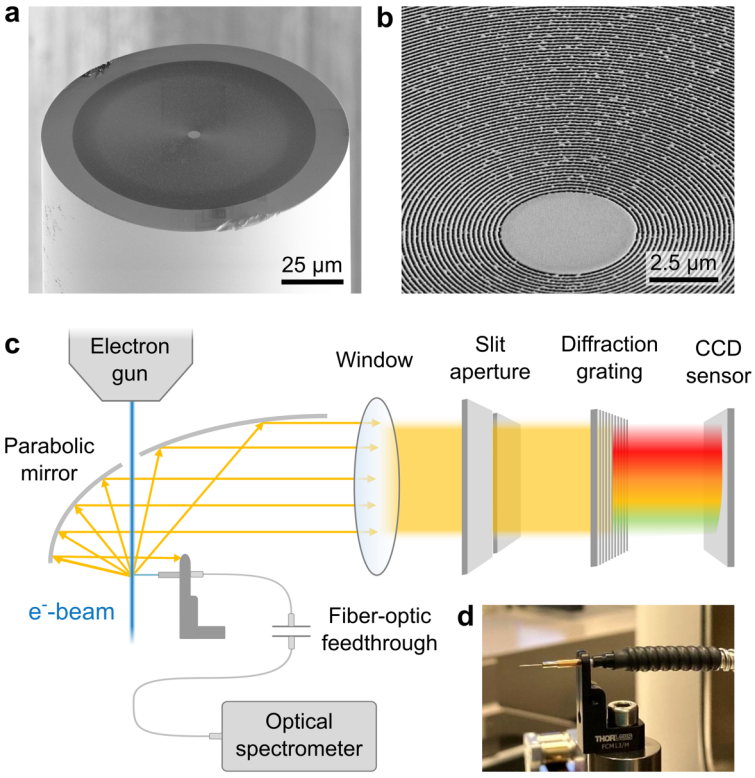

Figure 4.1: a SEM micrograph of a circular metallic metagrating that is fabricated onto the cleaved input facet of a multi-mode optical fibre. **b** Close-up view of concentric rings in the centre of the pattern with a 200-nm radial pitch. **c** Simplified schematic overview of the experimental setup that is used for the observation of the SP effect through the fibre and in the far-field. The electron beam of an SEM is aligned with the metagrating along a grazing trajectory, simultaneously generating SPR in free space and inside the fibre. **d** Photograph of the patterned fibre with a stainless-steel ferrule connector that is coupled to a standard multi-mode fibre-optic patch chord. The sample is mounted on a motorized stage that can be tilted to achieve an optimum beam-sample alignment.

to half the cut-off photon energy of 1.24 eV. Likewise, a long-pass filter with a cut-off energy of 1.97 eV is installed inside the fibre-coupled spectrometer. To retrieve absolute photon emission probabilities per incident electron, the HSAR data are calibrated using a reference measurement of transition radiation that is excited at the surface of a mono-crystalline Al sample as described in Section S8 of Chapter 3. The spectra acquired through the fibre are corrected for the spectral system response using the reference spectrum of a halogen white-light lamp. The angular light collection range that is spanned by the parabolic mirror ranges from $\theta_{\mathrm{min}} \approx 11^{\circ}$ at the mirror apex to $\theta_{\mathrm{max}} \approx 133^{\circ}$ at the opening, with $\theta = 0^{\circ}$ corresponding to light that is collected normal to the metagrating. However, due a shadow introduced by the sample holder, the lower limit is effectively shifted to $\theta_{\mathrm{min}} \approx 46^{\circ}$ - 47° (depending on the precise vertical

mirror-sample alignment). In addition, the aperture that transmits the electron beam blocks the collection of light between 86.4° and 93.4°. Further details regarding the angular calibration and the post-processing of the raw experimental data can be found in Section S8 of Chapter 3.

4.3 Coherent and incoherent signal contributions

Figure 4.2a shows an HSAR measurement that is acquired for a 30-keV electron beam grazing the centre of the metagrating. The data are compiled from two consecutive measurements in the UV-VIS and NIR spectral ranges that are merged at a photon energy of 1.56 eV. On both sides of the metagrating, several striking features are observed that can be divided into coherent and incoherent radiation phenomena as discussed in detail below.

First, we consider two narrow curved bands with spectral onsets near 1.55 eV and 3.10 eV at angles $\theta < 90°$. These bands can be readily identified as the emission of first- and second-order SPR in free space. As shown by the red-dashed curves, the data are in good agreement with the theoretical dispersion relation predicted by Eq. (4.1) for $n = 1.0$, $m = 1, 2$ and $p = 198.0$ nm. At angles $\theta > 90°$, we find another similar band with an opposite curvature and a spectral onset close to 1.4 eV. Intriguingly, this observation demonstrates the emission of first-order SPR into the fibre by electrons that excite the back side of the metagrating. The collected light leaks through the cladding layer and is subsequently refracted at the fibre/vacuum interface, leading to an effective dispersion relation of the form

$$\omega(\theta) = 2\pi c \frac{m}{p} \left(\beta^{-1} + \sqrt{n^2 - \cos^2\theta} \right)^{-1}, \tag{4.2}$$

where the emission angle is shifted according to Snell's law. The resulting dispersion curve is in excellent agreement with the data for $n = 1.46$, $m = 1, 2$ and $p = 198.0$ nm (red-dashed line). For reference, we also draw the second-order curve ($m = 2$), which, however, cannot be correlated to a measured signal. The red shift between SPR inside the fibre and in free space is determined by the refractive index of the silica core as described by Eq. (4.1). We note that the transmissivity of the metal coating is estimated to be of the order of a few percent with the skin depth of 13 nm in Au and 20 nm in Cr at a photon energy of 1.4 eV. However, on the sidewalls of the fibre the coating might be thinner and less uniform, therefore being more transparent.

Next, we turn our attention to two flat incoherent emission bands on the backside of the metagrating ($\theta > 90°$), each with a broad spectral distribution around photon energies of 1.9 eV and 2.7 eV. Due to alignment imperfections and the intrinsic divergence of the electron beam, these bands arise from electrons that penetrate the input facet of the fibre and scatter inelastically, thereby generating radiative defect excitations in the silica network. In good correspondence with previous reports in the literature, the low- and high-energy emission bands can be assigned to non-bridging oxygen hole centres (NBOHCs) and oxygen deficient centres (ODCs), respectively [234, 235]. Notably, the signal amplitude of the ODC band is similar in magnitude to that of the first-order SP bands. As a result, the second diffraction order of the ODC band in the spectrometer

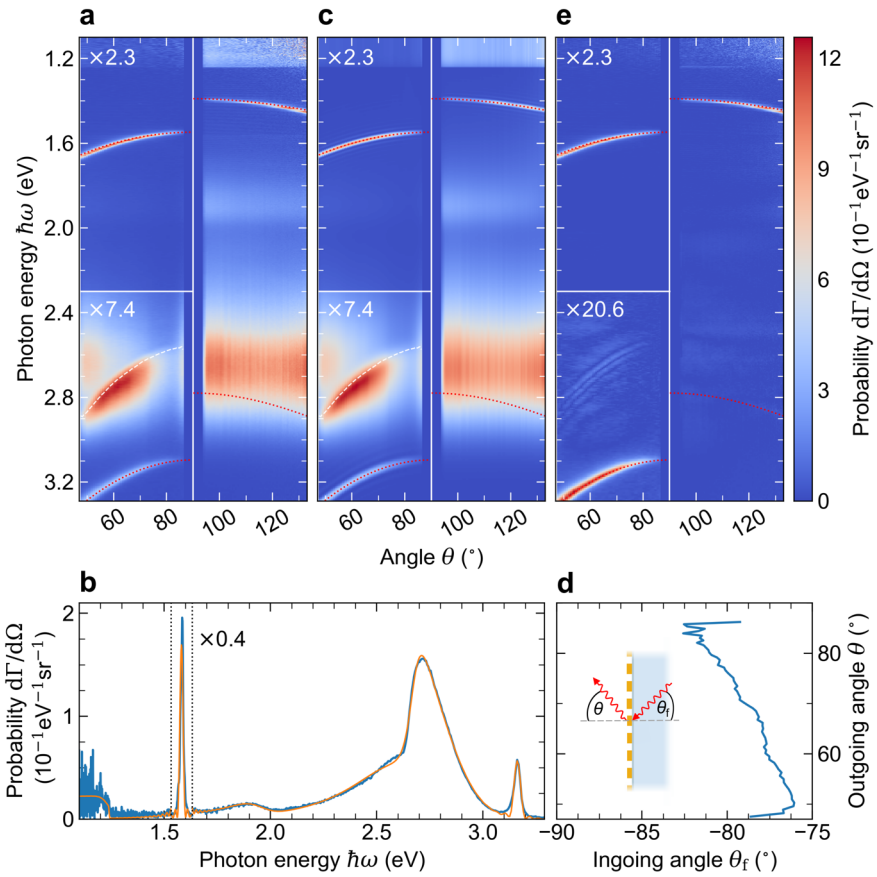

Figure 4.2: a HSAR measurement of far-field radiation induced by a 30-keV electron beam that is aligned with the centre of the metagrating along a grazing trajectory. The data reveal the coherent excitation of SPR as well as the generation of incoherent defect luminescence that occurs due to the penetration of electrons into the fibre. The dotted-red lines represent the expected theoretical dispersion curves of first- and second-order SPR that is observed from both the free space and the fibre-core sides of the metagrating at angles smaller and larger than 90°, respectively (cf. Eqs. (4.1) and (4.2). The white-dashed line represents a model fit to the angular dispersion of a Fano resonance that occurs due to a Rayleigh anomaly of the metagrating (cf. Eq. (4.3)). All curves are retrieved assuming a grating pitch of $p = 198.0$ nm, and a refractive index of the fiber core of $n = 1.46$. **b** Spectral cross cut through the data in **a** at an angle of $\theta \approx 66°$. The measurement (blue curve) is superimposed with a fitted model curve (orange) that is used to separate the coherent and incoherent signal contributions. The signal of first- and second-order SPR corresponds to the two narrow peaks at 1.6 eV and 3.2 eV, while the Fano resonance is observed by the large asymmetric peak with a maximum near 2.7 eV. **c** Collection of analytical model curves fitted to each spectral data slice of the measurement in **a**. **d** Fitted correlation between the in- and outgoing angles of photons that couple to the Rayleigh anomaly of the metagrating as illustrated in the inset. **e** Absolute value of the SPR signal as retrieved by subtracting the incoherent signal contributions of the model curves in **c** from the experimental data in **a**.

causes an artificial background signal below 1.24 eV, as explained above.

The NBOHC and the ODC bands are also observed on the free-space side of the metagrating ($\theta < 90°$), however, their intensities are much reduced. Instead, we find another striking feature with a strong dispersive curvature that overlaps with the ODC spectral range between 2.55 eV and 2.90 eV. For reference, Fig. 4.2b shows a spectral cross cut through the data at an angle of $\theta \approx 66°$. The spectrum features a large asymmetric peak with a maximum near 2.7 eV that is superimposed with the ODC band. Interestingly, we find that this observation can be explained by the interference of incoherent luminescence that is partly diffracted in the plane of the metagrating and partly transmitted directly into free space. As a result, a Fano resonance occurs that is coupled to a Rayleigh anomaly [236] of the metagrating [237, 238]. The latter follows an angular dispersion relation of the form

$$\omega_\mathrm{f}(\theta) = 2\pi c \frac{m}{p} \left(\sin\theta - n \sin\theta_\mathrm{f}\right)^{-1}, \tag{4.3}$$

with ω_f the photon frequency, m the diffraction order, and θ_f and θ the incident and outgoing angles of the diffracted photons, respectively. Since the free-space wavelength of the observed light is larger than the grating pitch, we note that only in- and outgoing angles of opposite sign are supported by the metagrating, corresponding to the $m = 1$ diffraction order. Moreover, no Rayleigh anomaly can exist for light that is diffracted back into the fiber, in good agreement with the absence of the phenomenon at angles $\theta > 90°$. To exclude the contribution of a coherent process, a reference measurement has verified that the Fano resonance is also observed when the electron beam impacts onto the top edge of the fibre. In addition, the dispersion of the Fano peak is found to be independent of the electron energy as further demonstrated below, in stark contrast to the dispersion of SPR (cf. Eq. (4.1)).

4.4 Analytical signal modelling

To facilitate an in-depth analysis and interpretation of our experimental data, we resort to an analytical modelling approach that allows us to efficiently separate the coherent and incoherent signal contributions. For simplicity, the SPR signal is modelled assuming that the electron beam propagates at a constant grazing distance d to the metagrating. Thus, as derived in the Appendix, the spectral line shape of the m^{th} SP emission order is given by

$$S_m(\omega) = A_m e^{-2\kappa d} \left| \frac{\sin\left(N_m \frac{\phi}{2}\right)}{\sin\left(\frac{\phi}{2}\right)} \right|^2 \left| \mathrm{sinc}\left(m - \frac{\phi}{2\pi}\right) \right|^2, \tag{4.4}$$

with A_m the signal amplitude, and N_m the number of unit cells that couple to the far field. The leading term in this expression describes an exponential decay of the signal strength with the grazing distance d, where $\kappa \approx \frac{\omega}{c}\sqrt{\beta^{-2} - n^2}$ is the frequency-dependent decay constant. This behaviour follows from the evanescent decay of the Fourier wave in the near-field of the metagrating that mediates the excitation of SPR as discussed above and described in more detail in Section S2 of Chapter 3. The remaining two terms can

be interpreted in close analogy to the diffraction of light by an array of N slits. Here, the middle term accounts for the interference between the slits and the last term captures the diffraction pattern of an individual slit, i.e., a single unit cell of the metagrating. The SP dispersion relation enters both terms through the parameter $\phi = \frac{\omega}{c}\left(n\sin\theta + \beta^{-1}\right)p$, which we alternatively write as $\phi = \frac{\omega}{c}\left(\sqrt{n^2 - \cos^2\theta} + \beta^{-1}\right)p$ to take into account the refraction of SPR at the fiber/vacuum interface (cf. Eq. (4.2) for $\theta > 90°$). Notably, Eq. (4.4) shows that the spectral line shape of the SP signal is primarily determined by the number of unit cells N that couple to the electron beam. Due to minor beam-sample alignment imperfections and the inherent beam divergence, however, this value is typically lower than the total number of unit cells in the metagrating. Therefore, we estimate an effective N_m to describe the signal of each SP order separately, while assuming a fixed constant distance of $d = 10$ nm.

To capture the Fano resonance on the free-space side of the metagrating ($\theta < 90°$) we use an expression of the form [239]

$$F(\omega) = \frac{\left(q+\varepsilon\right)^2 + b}{\left(1+\varepsilon^2\right)} G(\omega), \tag{4.5}$$

with $\varepsilon = \hbar\left(\omega - \omega_\mathrm{f}\right)/\gamma$ the reduced photon energy, γ the Fano linewidth, q the Fano parameter, and $G(\omega)$ the spectrum of the incoherent defect luminescence. The parameter b accounts for a flattening of the typical dip on the low energy side of the Fano resonance due to optical material losses [239]. The NBOHC and the ODC bands are modelled as a superposition of two exponentially-modified Gaussian distributions given by

$$G_i(\omega) = \frac{A_i}{2}\exp\left(\alpha_i\hbar\left(\omega - \omega_i\right)\right)\operatorname{erfc}\left(\frac{1}{\sqrt{2}\sigma_i}\left(\alpha_i\sigma_i^2 + \hbar\left(\omega - \omega_i\right)\right)\right), \tag{4.6}$$

where $\operatorname{erfc}(x)$ denotes the complementary error function, A_i is the amplitude, $\Gamma_i = 2\sqrt{2\ln 2}\sigma_i$ is the linewidth, α_i is the asymmetry parameter, and $\hbar\omega_i$ is the mean photon emission energy of defect i. Lastly, to cover the artificial background signal due to the ODC band in the NIR spectral range, we introduce a combination of two sigmoidal functions with a joint transition point at 1.24 eV. While this choice has no explicit physical motivation, it provides an efficient representation of the data, also in view of an elevated noise floor near the silicon band edge at 1.12 eV. To fix the parameters $\hbar\omega_i$ and Γ_i in Eq. (4.6), we perform a separate HSAR measurement in which the electron beam is aimed at the alignment marker in the centre of the metagrating (thereby minimizing the generation of SPR). By applying a least-squares minimization algorithm, we fit a background model to the measured spectra for all angular samples on the backside of the metagrating and in the spectral data range between 1.51 eV and 3.29 eV. Thus, we obtain mean photon emission energies of $\hbar\omega_\mathrm{NBOHC} \approx 1.95$ eV and $\hbar\omega_\mathrm{ODC} \approx 2.80$ eV, as well as spectral line widths of $\Gamma_\mathrm{NBOHC} \approx 0.13$ eV and $\Gamma_\mathrm{ODC} \approx 0.33$ eV, in good agreement with values previously reported in the literature [234, 235].

The orange curve in Fig. 4.2b shows a least-squares fit of the full model to the spectrum at $\theta \approx 66°$, assuming $n = 1.46$, $m = 1, 2$ and $p = 198.0$ nm. We find excellent agreement of the Fano model with the large asymmetric peak at 2.7 eV and the incoherent background due to the NBOHC and ODC bands. The signal of first- and

second-order SPR is observed as two narrow peaks with maxima at approximately 1.58 eV and 3.16 eV, respectively. Their corresponding line widths are captured assuming an excitation of $N_1 = 80$ and $N_2 = 40$ unit cells in the metagrating. The large difference between these values can be ascribed to the exponential decay of the SP excitation efficiency with the photon energy and thus the SP order as determined by the decay constant κ in Eq. (4.4).

Fig. 4.2c shows a complete set of model fits to all spectra within the angular data range of the measurement in Fig. 4.2a. The curves are based on the same assumptions for the parameters n, m, p, d, N_1, and N_2 as specified above, while all the remaining parameters are fitted separately. The model consistently captures the spectral and angular features of both the coherent and incoherent radiation phenomena. For reference, we superimpose the dispersion curves of first- and second-order SPR as defined by Eqs. (4.1) and (4.2) (red-dotted curves). Moreover, we plot the dispersion of the Fano resonance in both Fig. 4.2a and 4.2c (white-dashed curve) using the fit parameters ω_f and θ_f. Following the signal intensity along this curve, we find that the Fano peak gradually varies in amplitude, reaching a maximum visibility between $\theta \approx 55°$ and $\theta \approx 70°$. We anticipate that this intensity distribution is correlated with both the spectral distribution of the ODC band and the angular distribution of the photons that are generated inside the fiber. Also, the precise angle-dependent diffraction efficiency of the metagrating is expected to affect the signal. For reference, Fig. 4.2d shows the correlation between the fitted incident angle θ_f and the corresponding outgoing angle θ, with the inset illustrating their relative orientation. As a prevalent trend, we find an increase of the enclosed angle $\delta\theta = \theta - \theta_f$ with decreasing energy of the diffracted photons $\hbar\omega_f$; in good agreement with the typical dispersion of a Rayleigh anomaly. Fig. 4.2e shows the SPR signal as retrieved by subtracting the fitted incoherent signal from the data in Fig. 4.2a. We plot the absolute value of this difference to best represent the correspondence between the fit and the measurement. As clearly seen by the second-order SP band, our filtering procedure excellently isolates the SPR signal, facilitating a detailed analysis of free-electron-light coupling via the metagrating.

4.5 Free-electron light coupling via the metagrating

Figure 4.3 shows the effect of the electron energy on the angular dispersion of SPR. In six consecutive measurements, the electron energy is lowered from 30 keV to 5 keV, corresponding to a reduction of the electron velocity from $\beta \approx 0.33$ to $\beta \approx 0.14$. After the measurement at 15 keV, the sample was re-aligned relative to the parabolic light collection mirror. Therefore, the lower cut-off angle at 5 keV and 10 keV is slightly increased by approximately 1.5 degrees. The SPR signal is separated from the incoherent background contributions using the same filtering procedure as described above. To this end, a constant grating pitch p is chosen between 198.0 nm and 199.0 nm, assuming a small error margin of $\Delta p = 1$ nm. Moreover, to account for differences in beam quality between the different electron energies, the parameter N_m is estimated separately. At 5 keV, the signal-to-noise ratio is too low to reasonably fit the data, however, the incoherent signal contribution is negligible due to little penetration of electrons into the fibre. For reference, all measurements are overlaid with the dispersion curves of

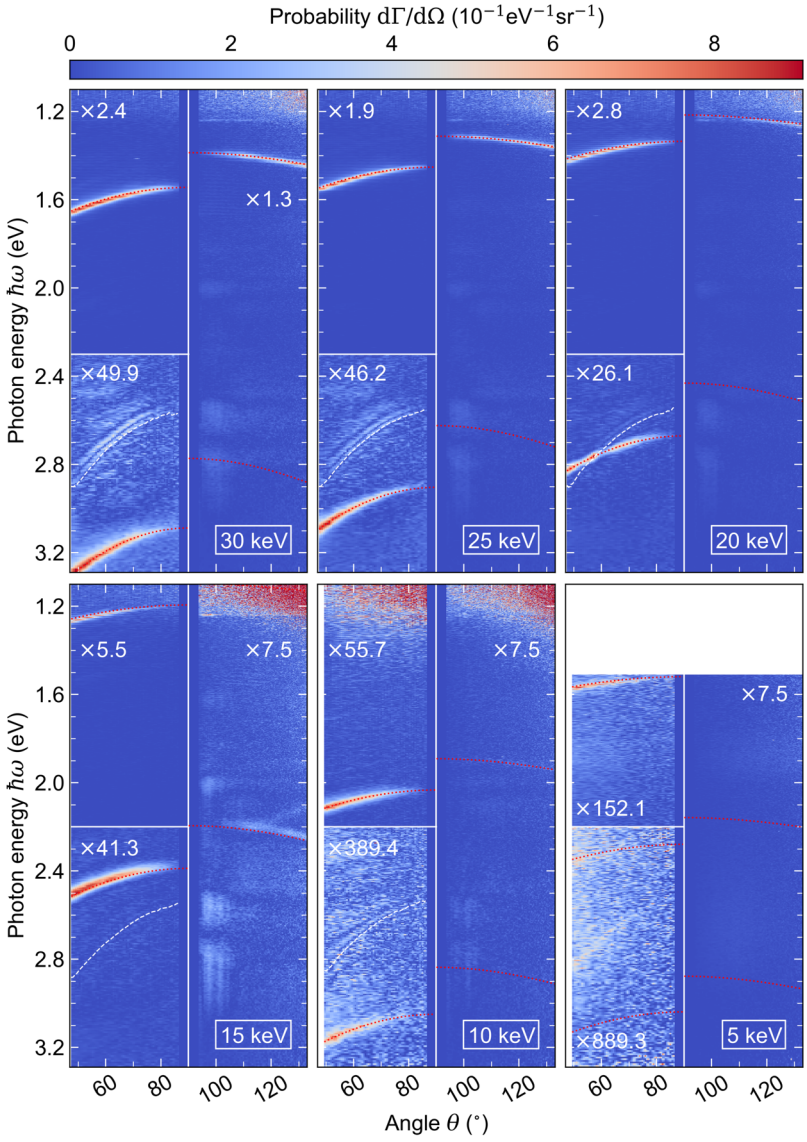

Figure 4.3: Measured dispersion of the SPR signal as a function of the electron energy. All signal distributions except for the data at 5 keV are processed using the same filtering procedure as described in Fig. 4.2. The red-dotted lines show the calculated dispersion curves of all SP orders within the spectral range of observation (Eq. (4.1) and (4.2)). The curves are derived assuming grating pitches p between 198.0 nm and 199.0 nm. In addition, the fitted dispersion of the Fano resonance (Eq. (4.3)) is superimposed with the panels from 30 keV to 10 keV. At 20 keV, this dispersion overlaps with the second-order SP band in free space.

the SP orders that fall within the spectral range of observation as calculated from Eqs. (4.1) and (4.2). In addition, the fitted dispersion of the Fano resonance is represented by the white-dashed line in each panel, confirming that the phenomenon is an incoherent process that does not shift with the electron energy.

On the free-space side of the metagrating, we observe first- and second-order SP bands at electron energies from 15 keV to 30 keV. The measurements at 5 keV and 10 keV reveal second- and even third-order SP bands. On the silica side, the first-order SP band is detected at 20 keV and above, while at 15 keV a faint signature of the second order is retrieved. Overall, the measurements demonstrate a consistent red-shift of the SPR signal with decreasing electron energy, in good quantitative agreement with the theory. Comparing the signal amplitudes, the excitation strength of first-order SPR in free space is approximately one and two orders of magnitude larger than those of the second and the third orders, respectively. These ratios follow from the intensity distribution of the Fourier waves that couple to the electron in the near-field of the metagrating. Modelling the field profile along the electron trajectory by a square wave with an effective duty cycle η, the relative intensity of the Fourier components can be approximated as $\mathrm{sinc}^2(\eta m)$, where m is the harmonic order of the reciprocal lattice constant $2\pi/p$. For $\eta = 0.5$ only odd orders m can exists in the grating, hence, there would be no generation of second-order SPR. For $\eta = 0.7$, the intensities of the second and the third emission orders reach $\sim 1/3$ and $\sim 1/60$ of the first-order intensity, respectively. The actual intensity ratios between the SPR bands, however, are not only dependent on the precise geometry of the metagrating but also on the frequency dependence of the exponential decay term in Eq. (4.4). This contributes to an additional drop in excitation efficiency with increasing SP order as explained above. Remarkably, we note that the signals of first-order SPR on the silica and the free-space sides of the metagrating are similar in amplitude, despite attenuation of the latter in the metal coating of the fibre. Possibly, this could be attributed to multiple scattering inside the fiber, resulting in the redirection of light that is otherwise emitted under too large azimuthal angles to pass through the slit aperture in the HSAR imaging setup.

Fig. 4.4a,b shows the spectra of first- and second-order SPR integrated over the angular data range on the free-space side of the metagrating. The measurement at 5 keV is not shown here due to its low signal-to-noise ratio. The first-order SP signals are modulated by artificial spectral oscillations due to an etaloning effect in the silicon detector at NIR frequencies. Interestingly, a downwards trend in the excitation efficiency of first-order SPR is observed with decreasing electron energy (Fig. 4.4a), whereas the excitation efficiency of second-order SPR remains rather constant (Fig. 4.4b). A detailed theoretical discussion of how these efficiencies scale with the electron velocity is provided in ref. [175]. It is shown that the optimum coupling velocity strongly depends on the product of the grazing distance d and the exponential decay constant κ of the Fourier wave that couples to the electron. Using the approximation $\kappa \approx \frac{\omega}{c}\sqrt{\left(\frac{2\pi c}{\omega}\frac{m}{p} - \sin\theta\right)^2 - 1}$ [226], we find that for $m = 1$, $\hbar\omega = 1.6$ eV, and $\theta = 0°$, a grazing distance of $d = 25$ nm translates to $\kappa d \approx 0.76$. For this situation, the theory in ref. [175] predicts a monotonic increase of the SPR emission probability with the electron velocity. However, up to a maximum velocity of $\beta \approx 0.33$ as reached in our

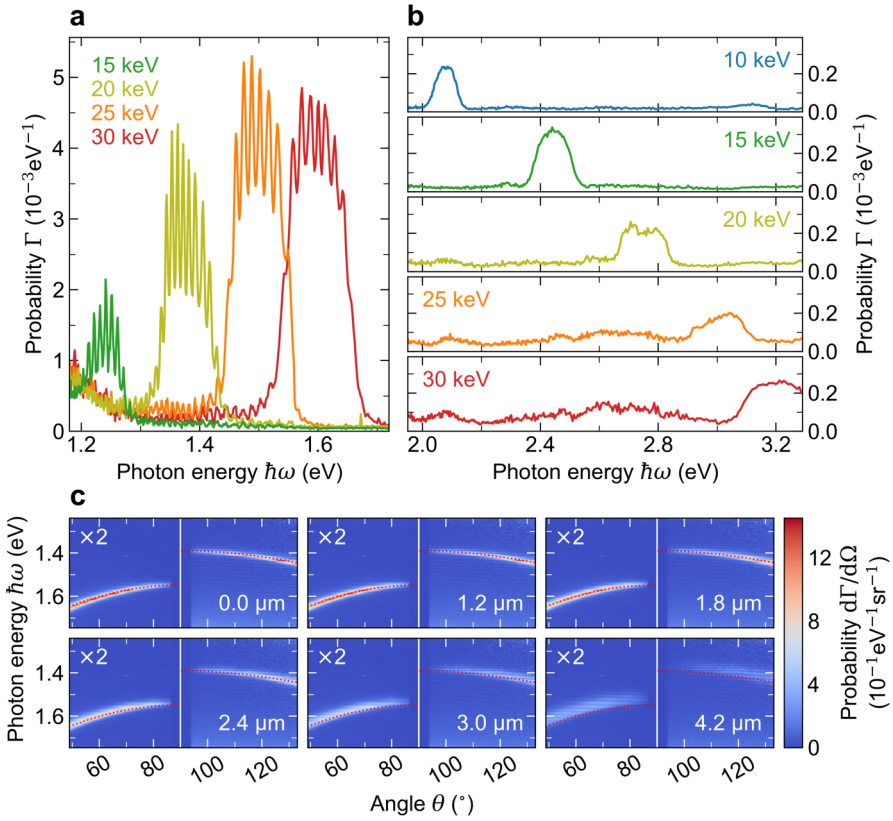

Figure 4.4: Quantitative spectral distributions of **a** first- and **b** second-order SPR that is generated on the free-space side of the metagrating as a function of the electron energy. The data are retrieved by integrating the detected HSAR far-field distributions in Fig. 4.3 over the full range of light collection angles $\theta < 90°$. The spectral signal oscillations in **a** occur due to an etaloning effect in the silicon sensor of the HSAR imaging setup. **c** Measured dependence of the angular dispersion of first-order SPR as collected from both sides of the metagrating on the horizontal alignment of the electron beam relative to the symmetry axis of the circular metagrating. With increasing distance from the centre (see respective labels), the excitation efficiency of SPR decreases, the dispersion shifts to the red, and broadens spectrally.

experiments, this probability and its variation with the electron energy is predicted to be comparatively small [175]. Moreover, we note that the effective excitation strength of SPR is determined by a distribution of grazing distances due to the finite width of the electron beam, the inherent beam divergence, as well as alignment imperfections. Since the performance of the electron optics degrades below 20 keV, this could further explain the comparatively low SPR signal amplitude at 5 keV.

To further quantify the interaction strength between the electrons and metagrating, we integrate over the first- and second-order SPR signals at 30 keV (spectral bandwidth ~ 0.2 eV), yielding absolute photon emission probabilities per electron of $\sim 4.7 \cdot 10^{-4}$ and $\sim 5.0 \cdot 10^{-5}$, respectively. In addition, in Fig. 4.4c, we demonstrate the effect of the horizontal electron-beam alignment relative to the symmetry axis of the circular metagrating at an electron energy of 30 keV. As the horizontal spacing is increased, we observe a consistent red-shift and spectral broadening of the first-order SP bands in free space and in the fibre. Moreover, the signals gradually fade out in intensity. These observations demonstrate that the electron beam couples to a decreasing number of unit cells with an effective distribution of grating pitches that increase in magnitude away from the centre, due to the circular geometry of the metagrating.

Finally, we turn our attention to the coupling of SPR into guided optical modes that are supported by the fibre. As illustrated in Fig. 4.5a, photons that are emitted under sufficiently small angles relative to the optical axis of the fibre undergo total internal reflection at the core/cladding interface. This condition is determined by the NA of the fibre which defines the maximum angle at which light can be injected into a cleaved input facet from free space. Hence, SPR that is generated on the backside of the metagrating couples to guided modes within an angular range of $\delta\theta = 2\arcsin(NA/n)$. For reference, Fig 4.5b shows an analytical calculation of the spectral and angular distribution of SPR inside the fibre induced by a 20-keV electron beam (Eq. (4.4)). The vertical dashed lines enclose the component of SPR that couples into guided modes assuming an NA of 0.22. In addition, the dotted vertical line indicates the maximum collection angle of the parabolic mirror in the HSAR imaging setup, and the dashed-dotted curve represents the dispersion of SPR that escapes from the fibre as described by Eq. (4.2). The left and right top panels in Fig. 4.5c show spectra that are detected through the fibre at variable electron energies between 10 keV and 20 keV. The large broadband peak at the high energy end of the spectra corresponds to the tail of the NBOHC band as discussed above. Superimposed with this band, a distinct signal contribution is observed that gradually shifts to the blue with increasing electron energy. This signal corresponds to the guided component of first-order SPR that is generated on the back side of the metagrating. To filter out the incoherent background, we again resort to a least-squares fit of an analytical model based on Eq. (4.6) and a pseudo-Voigt profile that describes the SPR signal. By subtracting the fitted incoherent contribution from the data, we find the spectra shown in the bottom panels in Fig. 4.5c for the different electron energies. The dashed vertical lines indicate the cut-off photon energies that correspond to the guided fraction of SPR within the NA of the fibre according to Eq. (4.1). As can be seen, the extracted SPR signal is in excellent agreement with the calculated spectral cut-off energies, corroborating that the dispersion of SPR inside the fibre behaves as predicted by the theory.

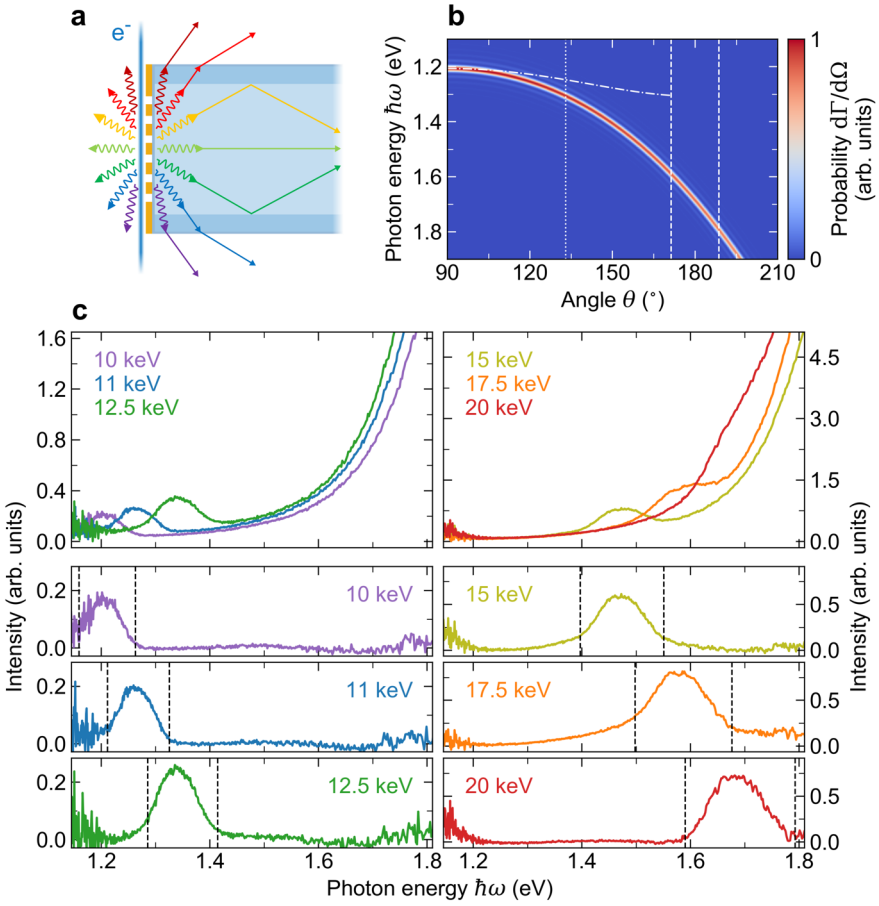

Figure 4.5: a Illustration of SPR that is generated in- and outside the fibre by an electron beam that excites the metagrating in free space. Light inside the fibre that is emitted under sufficiently large angles penetrates through the cladding layer and refracts at the fibre/vacuum interface. The remaining waves undergo total internal reflection at the core/cladding interface, thereby coupling to guided optical modes. **b** Analytical calculation of the spectral and angular distribution of first-order SPR that is generated on the fibre-core side of the metagrating at an electron energy of 20 keV (Eq. (4.4) with $N_1 = 60$, $p = 200$ nm, $n = 1.46$, and $d = 10$ nm). The dashed-dotted curve shows the corresponding dispersion of SPR that leaks out of the fibre, with the dotted vertical line indicating the maximum collection angle of the parabolic mirror in the HSAR imaging setup. The two dashed vertical lines enclose the fraction of SPR that is emitted within the NA of the fibre. **c** Large top panels: Spectral distribution of radiation collected through the fibre for excitation of the metagrating at variable electron energies between 10 keV and 20 keV. Small bottom panels: Extracted SPR signal as retrieved by fitting an analytical model curve to the data and subtracting the contribution of an incoherent signal background. For each electron energy, the dashed vertical lines indicate the lower and upper cut-off photon energies of SPR that is emitted within the NA of fibre as predicted by Eq. (4.1) for $m = 1$, $p = 200$ nm, $n = 1.46$.

4.6 Discussion & conclusion

In this work, we have studied the coupling between free electrons and light in a circular metallo-dielectric metagrating that is fabricated onto the input facet of an optical fibre. Using HSAR far-field imaging in an SEM, we have experimentally resolved the angular dispersion of SPR that is excited on both the free-space and the fibre-core sides of the metagrating for variable electron energies between 5 keV and 30 keV. We observe first-, second-, and third-order emission of SPR in the UV to NIR spectral range with an angular dispersion that consistently follows the theory. Furthermore, we find good correspondence between the numerical aperture of the fibre and the spectral distribution of first-order SPR that couples into guided optical modes. Aside from these coherent excitations, we also detect a broadband distribution of incoherent defect luminescence that is generated by electrons penetrating the input facet of the fibre, and scattering inelastically. Light that leaks out of the fibre is found to interfere with a Rayleigh anomaly of the metagrating, giving rise to a Fano resonance. At an electron energy of 20 keV the dispersion of this phenomenon overlaps with the emission of second-order SPR, demonstrating that the metagrating geometry can be further optimized to enhance and control the SP effect by exploiting resonant electromagnetic phenomena such as lattice resonances [211, 231, 232]. Comparing the measured signal amplitudes, we find that the excitation strength of first-order SPR in free space is approximately one and two orders of magnitude larger than those of the second and the third orders, respectively. These ratios can be ascribed to the different Fourier wave amplitudes of the SP modes in the near-field of the metagrating as well as an exponential decay of SP excitation efficiency with the energy of the emitted photons. The corresponding absolute photon emission probabilities of first- and second-order SPR are found to be $\sim 4.7 \cdot 10^{-4}$ and $\sim 5.0 \cdot 10^{-5}$, respectively.

For reference, we note that the authors of ref. [175] report a theoretical maximum emission probability of SPR in the visible spectral range of the order of 10^{-3} for a grating with a total length of 10 µm and a spectral bandwidth of 0.1 eV. A similar value is also obtained from simulations in Section S5 of Chapter 3. However, the calibration of the experimental signal intensities is optimized for CL emission processes that resemble the angular distribution of transition radiation (TR) [170, 226]. In contrast, the emission of SPR is highly directional which renders an uncertainty on the measured photon emission probabilities. Furthermore, the excitation strength of SPR is highly-dependent on the grazing distance of the electron beam relative to the metagrating. As mentioned above, this distance can vary substantially along the beam path due to the inherent beam divergence, as well as beam-sample alignment imperfections. Incidentally, in ref. [76], the same TR-based calibration procedure yields CL emission probabilities in the order of 10^{-5} for the excitation of plasmonic resonances in the tips of a mono-crystalline gold nanostar. Here, the electron beam is targeted directly at the nanostar tips, enabling a maximum coupling efficiency between the electrons and the induced optical field. In comparison, the excitation of the metagrating is less controlled, the grating rulings are expected to be more lossy, and the emission of SPR is a non-resonant phenomenon. Nevertheless, the metagrating provides a large number of unit cells that contribute to the radiation, likely explaining an overall larger probability for the emission of first-order

SPR compared to the emission of CL by the tip resonances.

The results presented in this work provide valuable insights into the design of future metasurface geometries that mediate the coupling between free electrons and light through an optical fibre. For example, lattice resonances based on plasmonic or dielectric structures enable efficient coupling of SPR to highly localized near-field distributions while simultaneously controlling its spectrum and polarization [211, 231, 232]. By further introducing ultra-short electron pulses, this provides a promising pathway towards ultra-fast fibre-based light sources. Alternatively, high-quality-factor cavities that are coupled to an optical fibre can be used to enhance the coupling efficiency between free electrons and light within a narrow spectral range [83]. However, due to the comparatively low spatial field confinement, such geometries are typically not suited for slow electrons in SEM. Instead, the nano-metric structure of metasurfaces provides maximal freedom to harness and engineer the SP effect. The precise arrangement of meta-atoms allows controlling the amplitude of suitable SP orders and can be also adapted by exploiting the refractive index contrast between the fibre substrate and free space. Vice versa, the concept of fibre-integrated metasurfaces offers great potential to mediate the coupling of light to slow free electrons, rendering an efficient platform for preparing complex free-electron quantum states. Lastly, measurements of the pulse characteristics and statistics of light collected through the fibre could reveal new insights into the correlations between optical excitations in the metasurface and their interaction with free electrons [240].

4.7 Appendix: Analytical derivation of the SPR signal

To derive the spectral power distribution of SPR that results from the coherent interaction between a point-like free electron and a grating, we resort to an approximate analytical expression as provided by Eq. (S2.5) in Chapter 3. Assuming the electron to propagate strictly parallel to the surface of the grating and orthogonal to the rulings at a constant grazing distance d, this expression is proportional to an integral of the form

$$S_m(\omega) \propto e^{-2\kappa d}\left|\int_{-L}^{L} \mathrm{d}z e^{-i\left(\frac{\omega}{c}\left(n\sin\theta+\beta^{-1}\right)-m\frac{2\pi}{p}\right)z}\right|^2, \tag{A1}$$

where θ is defined according to the light collection angle in the main text, and $2L$ is the interaction length for an integer number of $2N$ unit cells. The parameter $\kappa \approx \frac{\omega}{c}\sqrt{\beta^{-2}-n^2}$ describes the evanescent decay of the excitation strength normal to the grating surface, with $\beta = v/c$ the normalized electron velocity. Note, that we have generalized Eq. (S2.5) from Chapter 3 to an arbitrary diffraction order m as well as the emission of SPR in a homogenous, lossless medium with refractive index n.

Since the integrand in Eq. (A1) obeys the periodicity of the grating, we can reduce the problem to an integral over a single unit cell, while taking into account the relative phase contributions of all remaining cells in the lattice. Thus, we find

$$S_m(\omega) \propto e^{-2\kappa d}\left|\sum_{u=-N}^{(N-1)} e^{-i(\phi-2\pi m)u}\int_{-p/2}^{p/2} \mathrm{d}z e^{-i(\phi-2\pi m)\frac{z}{p}}\right|^2, \tag{A2}$$

where $\phi = \frac{\omega}{c}\left(n\sin\theta+\beta^{-1}\right)p$. Further, we can exploit the geometric sum identity $\sum_{u=0}^{2N-1}\rho^{(u-N)} = \rho^{-N}\left(1-\rho^{2N}\right)/\left(1-\rho\right)$ as well as the Fourier transformation of the box function $\int_{-\tau/2}^{\tau/2}\mathrm{d}t e^{-i2\pi f t} = \tau\,\mathrm{sinc}\left(f\tau\right)$, where τ is the box width and $\mathrm{sinc}(x) = \sin(\pi x)/(\pi x)$ is the normalized sinc function. For $\rho = \exp\left(-i\left(\phi+2\pi m\right)\right)$ we obtain $\left|\rho^{-N}\left(1-\rho^{2N}\right)/\left(1-\rho\right)\right| = \left|\sin\left(N\phi\right)/\sin\left(\phi/2\right)\right|$, which by substituting $N_m = 2N$ eventually yields the spectral lineshape of the SPR signal as

$$S_m(\omega) \propto e^{-2\kappa d}\left|\frac{\sin\left(N_m\frac{\phi}{2}\right)}{\sin\left(\frac{\phi}{2}\right)}\right|^2\left|\mathrm{sinc}\left(m-\frac{\phi}{2\pi}\right)\right|^2. \tag{A3}$$

5

Low-energy electron spectroscopy in the scanning electron microscope

Electron energy loss spectroscopy (EELS), cathodoluminescence (CL) spectroscopy, and photon-induced near-field electron microscopy (PINEM) form a powerful set of techniques to study the interaction of free electrons and light in nanophotonic systems. While the detection of CL is well-established in scanning electron microscopy (SEM), electron spectrometers that are suitable for EELS and PINEM are mainly implemented in transmission electron microscopes so far. Here, we demonstrate an electrostatic retarding field analyzer (RFA) that can be retro-fitted in an SEM to perform high-resolution spectroscopic measurements at non-relativistic electron energies. To enable measurements under pulsed electron beam conditions as in PINEM, we employ a silicon-based direct electron counter that provides single-electron sensitivity. The measured electron spectra vary in width from (0.69 ± 0.11) *eV to* (1.23 ± 0.03) *eV at electron energies between 4 keV and 11 keV. Limitations of the analyzer are identified regarding acquisition speed, alignment sensitivity, and rate capability. Our work opens up novel opportunities to study coherent interactions of free electrons and light in the SEM by combining CL analysis with electron spectroscopy.*

5.1 Introduction

Free electrons can couple to optical excitations in nanostructures on length scales far beyond the diffraction limit of light and on time scales shorter than an optical cycle [28, 31]. In recent years, this phenomenon has been extensively studied using spectroscopic techniques that are integrated with electron microscopy [32, 33, 101]. For one, this includes electron energy loss spectroscopy (EELS) which probes the characteristic energy loss that a free electron undergoes as it drives an optical material excitation [34–37]. Similarly, cathodoluminescence (CL) spectroscopy permits an indirect observation of this process by detecting the resulting emission of a far-field radiation [51–53]. For another, photon-induced near-field electron microscopy (PINEM) resolves the stimulated emission and absorption of photons by free electrons in the optical near field of a material that is excited by an external pump source [66]. As a result, the electrons undergo discrete electron energy-gain and -loss transitions that imprint a characteristic signature onto the electron wave function [68–70]. Aside from near-field imaging [72, 73, 76, 78], this mechanism enables a wealth of intriguing applications such as the generation of ultra-short free-electron wave packets [80, 90, 91], the transverse modulation of electron beams [92], and the synthesis of entangled free-electron-photon states [90, 91, 97–99].

So far, EELS and PINEM have been mainly performed in transmission electron microscopes (TEMs) that are equipped with a high-resolution magnetic spectrometer. These devices resolve subtle changes in the energy distribution of electrons with kinetic energies of tens to hundreds of kiloelectronvolts [39]. In addition, PINEM is typically performed in TEMs with a pulsed electron gun that is driven by a higher harmonic of the optical pump laser (ultra-fast TEM) [63–65, 241]. In CL spectroscopy, light is collected by a parabolic mirror and directed into an optical spectrometer, enabling not only the spectral but also the angle-, and polarization-resolved characterization of arbitrary sample geometries [54, 56, 242]. Such optics are mostly implemented in scanning electron microscopes (SEMs) which offer great flexibility through large specimen chambers. In view of their fundamental correlation [71, 76, 102], a combination of EELS, CL, and PINEM on a single platform is of keen interest, however, has not been realized to date.

Physically, SEMs offer the benefit of accessing non-relativistic electron energies (0.5 eV to 30 keV) that enable very high electron-light coupling efficiencies [76, 104, 174–176]. In addition, the spacious specimen chambers provide ample room for the integration of experimental infrastructure. However, the implementation of EELS and PINEM at low electron energies poses a major experimental challenge. For one, this is due the fact that the electrons cannot pass through thin specimens as in TEM, and for another there are no electron spectrometers commercially available to meet the demands on resolution and sensitivity. Recently, a home-built magnetic spectrometer has been integrated into an SEM to first demonstrate PINEM at a minimum electron energy of 10.4 keV [77].

Here, we demonstrate an alternative approach to resolve low-energy electron spectra using a compact retarding field analyzer (RFA) [243]. Rather than a magnetic field, this approach relies on an electrostatic potential barrier which serves as a tunable high-pass energy filter [243]. As a model setup, we use an SEM with an electrostatic beam deflector that enables both continuous and pulsed beam operation as in PINEM [61].

We first employ an RFA as described in ref. [244] to study the continuous beam emission of the SEM at an electron energy of 5 keV. In addition, we perform numerical simulations to model the energy filtering mechanism and determine the energy resolution of the analyzer. We then introduce a modified version of the RFA with an enhanced electrical breakdown threshold and a highly-sensitive direct electron counter. The measurements are performed in an electron energy range from 4 keV to 12 keV, and under variable pulsed beam conditions. We identify limitations regarding rate capability, beam alignment and acquisition speed that can be addressed by further technical optimization. Overall, we conclude that the modified RFA meets the resolution and sensitivity requirements for low-energy PINEM experiments in the SEM. In addition, we anticipate novel opportunities for correlated experiments by combining the electron spectroscopy with CL analysis.

5.2 Original and modified RFA configurations

A cross section through the original RFA developed in ref. [244] and re-used in this work is shown in Fig. 5.1a. The device comprises a stack of five cylindrical electrodes that is optimized to study the energy distribution of a beam of charged particles with a mean kinetic energy of 5 keV. In the middle, a pair of electrostatic lenses surrounds a centre electrode with a concentric 400-µm diameter aperture that acts as the energy filter. On the top and at the bottom, two further electrodes serve as the input and output anodes, respectively. An electron beam that is injected from the top is decelerated and focused by the upper lens onto the aperture in the centre electrode. Electrons that are transmitted through the aperture are collected by the lower lens, re-accelerated to their initial energy, and ejected through the output anode. Subsequently, the electrons are captured by a Faraday cup that is read out by a femto-amperemeter (6514 System Electrometer, Keithley Inc.).

The modified version of the RFA introduced in this work is intended to enable the acquisition of electron spectra over an extended range of kinetic energies and under pulsed electron beam conditions as in PINEM. To this end, a revised setup is implement in which the lower lens is removed and the upper lens is substituted by a thinner electrode that is stacked on top of the main electrode, as shown in Fig. 5.1b. In this configuration, the threshold potential for electrical breakdown is substantially enhanced. In addition, the Faraday cup is replaced by a direct electron counter (MiniPIX TPX3, Advacam s.r.o) with a segmented silicon sensor. The latter comprises a square array of 256 x 256 pixels (Timepix3 chip), each of which is capable of detecting single electrons up to a maximum count rate of several hundred kHz. The sensor information is read out by a computer via micro-USB port. To ensure stable operation at room temperature, the counter is thermally coupled to a nitrogen heat exchange system. Photographs of the modified RFA and the electron counting module are shown in Fig. 5.1c,d.

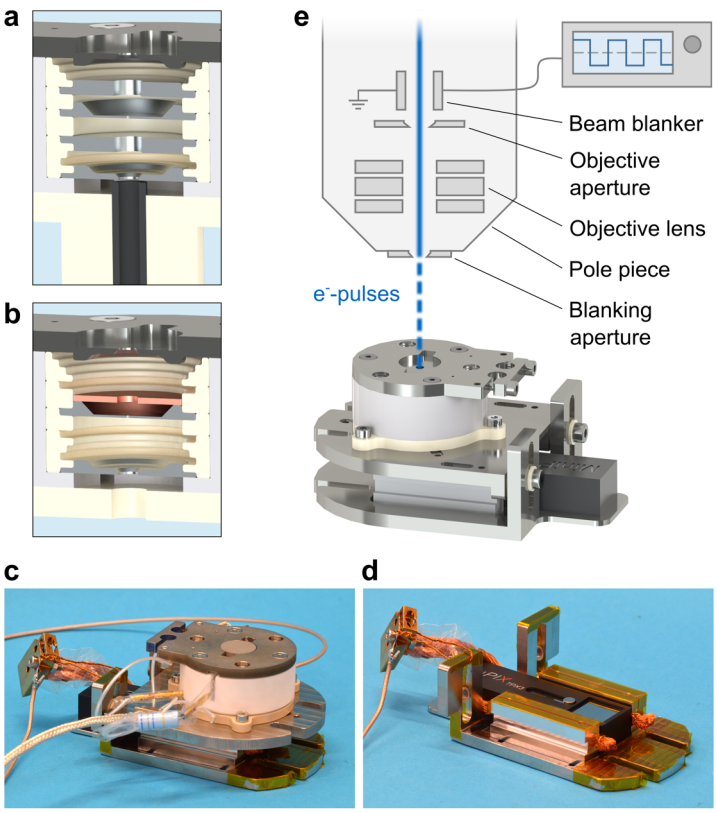

Figure 5.1: Rendered cross sections through **a** the original and **b** the modified configurations of the RFA. **c**, **d** Photographs of the modified RFA and the electron counter. The latter is thermally coupled to a nitrogen gas heat exchange system via the stranded copper wires that are clamped to the housing. **e** Experimental setup used for the acquisition of electron spectra under both pulsed and continuous electron beam conditions. The setup is based on an SEM with an integrated electrostatic beam blanker that is driven by a square-wave generator to sweep the electron beam over the blanking aperture.

5.3 Experimental setup

Fig. 5.1e depicts the experimental setup that is used for operation of the original RFA and its modified variant under continuous and pulsed beam conditions, respectively. We employ an SEM that is equipped with a Schottky field emission source (Quanta FEG 650, Thermo Fisher Scientific Inc.) and an electron beam column with an integrated beam blanker [44]. The latter comprises a pair of electrostatic deflection plates that is introduced above the objective lens and connected to a pulse generator (33622A, Keysight). By applying a square-wave signal, the electron beam is rapidly swept across a 400-µm diameter aperture at the end of the pole piece. As a result, electron pulses are generated with a tunable duration down to several hundred ps and a maximum

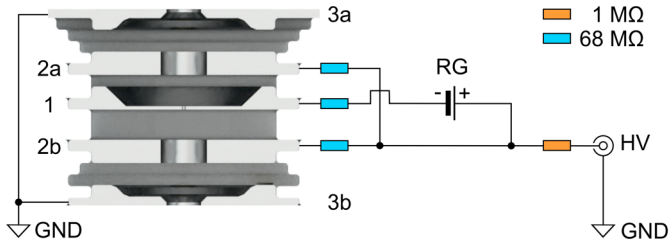

Figure 5.2: Electrical circuitry of the original RFA. A high voltage (HV) power supply provides a negative offset potential that is applied to the centre electrode (1) as well as to the upper (2a) and the lower lens electrodes (2b). In addition, the potential of the centre electrode is controlled by a battery-powered low voltage ramp generator (RG) that produces a negative stair step signal. The input (3a) and the output (3b) anodes are electrically grounded. In order to prevent damage in case of electrical breakdown, all HV electrodes are protected by high-ohmic resistors. The modified RFA is operated in a similar manner except for the lens and the centre electrodes being electrically coupled.

repetition rate of 100 MHz. The objective aperture below the deflection plates has no effect in pulsed beam configuration but only limits the current of the continuous beam. Instead, the charge density per pulse is actively controlled by a primary condenser lens (not shown) that manipulates the collection of electrons from the electron source and their subsequent transmission through the beam column.

To power the original RFA, a high voltage (HV) power supply (HCN-35-6500, FuG Elektronik GmbH) and a home-built low voltage ramp generator are operated in series. As illustrated in Fig. 2, the HV power supply is connected to both the lens and the centre electrodes, while the input and output anodes are electrically grounded. In addition, the centre electrode is coupled to the ramp generator which provides a negative stair case signal over a maximum range of 0 V to -30 V. The modified RFA is operated in a similar manner, with both the centre and the lens electrodes being electrically coupled (HV power supply HCL-35-12500, FuG Elektronik GmbH).

5.4 Numerical simulations

To provide a deeper understanding of the energy filtering mechanism of the RFA, we first perform a set of numerical simulations by which we model the transmission of an electron beam through the original two-lens electrode stack. We use a commercial simulation tool (SIMION) that employs a finite difference approach to calculate the field distribution within the system for a given configuration of static potentials [245]. The beam is represented by a total of 100 electrons with a kinetic energy of 5 keV that are emitted into cone with a half-opening angle of 0.143°. At the origin, we assume a point source that is located on the symmetry axis of the analyser and at distance of 14 mm above the input anode. Fig. 5.3a shows the transmitted number of electrons as a function of the applied centre electrode potential. The data follow a steep sigmoidal curve with an inflection point U_0 that lies slightly below the equivalent of the electron

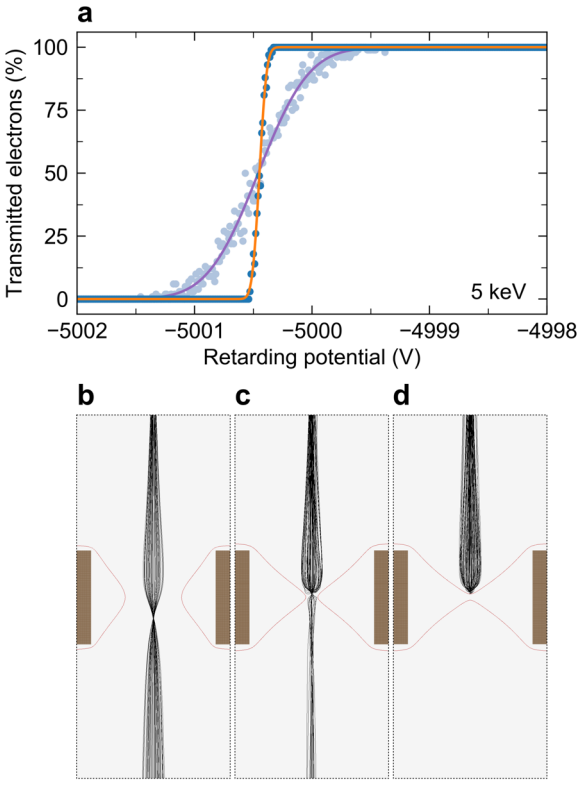

Figure 5.3: Numerical simulation of a divergent electron beam with a half-opening angle 0.143° and a kinetic energy of 5 keV that passes through the original RFA. **a** Transmitted fraction of electrons as a function of the applied centre electrode potential. The offset potential of the lens electrodes is -4998 V. The blue dots correspond to an infinitely narrow electron energy distribution, and the light-blue dots represent a Gaussian energy distribution with full-width-at-half-maximum of 0.8 eV. The solid curves show analytical model functions that are fitted to the data based on Eq. (5.1). **b**-**d** Electron trajectories near the aperture in the centre electrode at full transmission, partial transmission and full repulsion, respectively. The red curves indicate the equipotential line at -5 kV.

energy. For reference, Fig. 5.3b-d illustrates the trajectories of the electrons as they approach the aperture in the centre electrode at potentials above, near, and below the inflection point, respectively. The potential barrier within the aperture is represented by the red equipotential line at -5 kV. In Fig. 5.3b, this barrier is widely open so that all electrons can pass towards the output anode. In Fig. 5.3c, the barrier starts to close so that only a part of the electrons is transmitted, while in Fig. 5.3d all electrons are repelled. The observed electron trajectories are determined by their momentum component parallel to the local potential gradient [243]. Therefore, the energy resolution of the analyser depends on both the radial profile of the potential barrier and on the spatial

and the angular distribution of the incoming electrons.

To introduce the energy spread of a physical electron source, we assume a Gaussian energy distribution with a full-width-at-half-maximum (FWHM) of 0.8 eV. The corresponding set of simulations is represented by the light-blue dots in Fig. 5.3d. Again, the data follow a sigmoidal curve with a similar inflection as observed previously, however, with a shallower slope. For a quantitative analysis, we introduce an analytical model that is based on a combination of a Gaussian and a Cauchy distribution with a joint FWHM 2γ. The corresponding cumulative distribution can be written as

$$I(U) = \frac{I_0}{2}\left[k\left(1-\frac{2}{\pi}\arctan\left(\frac{(U_0-U)}{\gamma}\right)\right)+(1-k)\left(1-\mathrm{erf}\left(\sqrt{\ln 2}\frac{(U_0-U)}{\gamma}\right)\right)\right], \tag{5.1}$$

with $k \in [0,1]$ and I_0 the amplitude. Fitting Eq. (5.1) to the blue and the light-blue data points in Fig. 5.3d (see solid curves), we obtain an intrinsic energy resolution of (0.11 ± 0.00) eV and a measured energy width of (0.80 ± 0.02) eV, respectively. The latter is determined by the convolution of the response function of the RFA and the Gaussian energy distribution of the beam. Hence, we can write

$$\gamma = \sqrt{\gamma_{\mathrm{res}}^2 + \gamma_{\mathrm{e}}^2}, \tag{5.2}$$

where γ_{res} and γ_{e} denote the energy resolution and the electron energy width, respectively. In this example, the energy distribution of the electrons largely dominates the broadening that is introduced by the analyser itself due to its quadratic contributions in Eq. (5.1).

5.5 Continous beam measurements with the original RFA

A series of SEM images that show the original RFA during operation is to be seen in Fig. 5.4a. The images are acquired using a continuous electron beam with a kinetic energy of 5 keV that is focused onto the input anode. At an offset potential of -2 kV, the aperture in the centre electrode that sustains the potential barrier is recognized as a dark circle with an approximate diameter of 400 µm. The contrast of the electrode itself is largely enhanced by the retarding field which helps secondary electrons to escape from the input anode. At -4.99 kV, a de-magnified image of the aperture is obtained which is due to the effect of the upper lens electrode. At -5.01 kV, all electrons entering the analyser are repelled which is observed by the formation of a mirror image of the beam column. In Fig. 5.4b, we show an energy scan that is performed by directing the electron beam into the aperture of the centre electrode at an offset potential of approximately -4.99 kV. Each data point is acquired using an integration time of 200 ms. The measured beam current is plotted as a function of the ramp potential, with the inset showing the energy distribution of the electrons as obtained by numerical differentiation of the data. Overall, the measurement shows very good qualitative agreement with the simulations. Using the same fitting procedure as introduced above (see orange curve), we find an energy width of (0.88 ± 0.01) eV which lies well within the typical range for a Schottky field emission source [30, 241].

In Fig. 4c, we further study the effect of the configuration of the primary condenser lens on the measured energy width. The former is represented by a spot parameter that

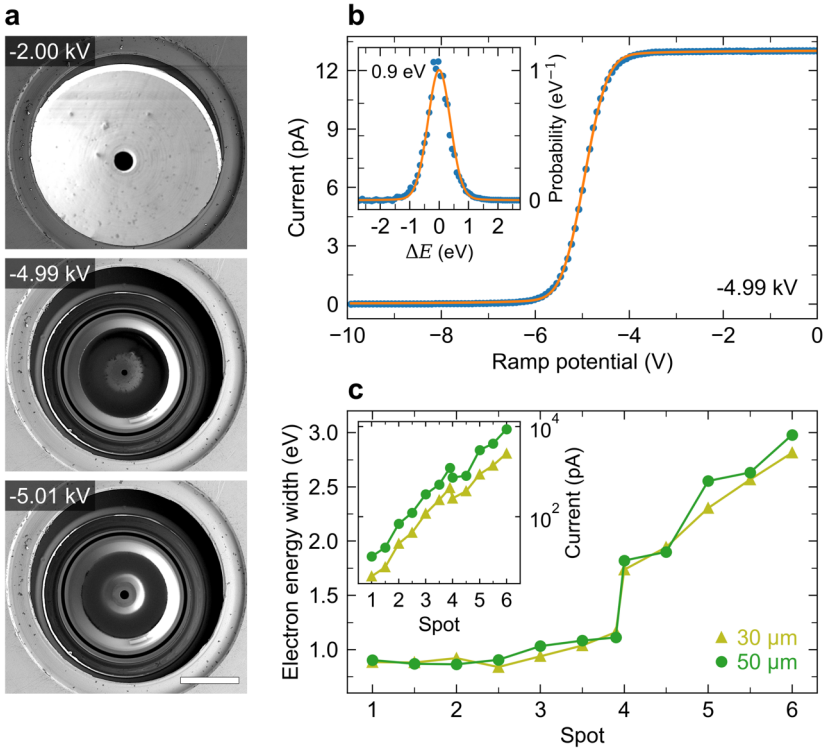

Figure 5.4: Energy scans with the original RFA using a continuous electron beam with a kinetic energy of 5 keV. **a** Series of SEM images that show a top-view of the RFA during operation at different HV offsets. **b** Measured electron beam current as a function of the applied ramp potential at an HV offset of -4.99 kV. The solid curve represents an analytical model fit to the data based on Eq. (5.1). The inset shows the corresponding energy distribution of the electrons, with the solid curve representing the derivative of the model fit. **c** Energy width as a function of the condenser lens configuration (spot parameter) for two different objective apertures with diameters of 30 µm and 50 µm. Minor statistical uncertainties on the fit are not shown (see text).

is set to a value between 1.0 and 6.0. In addition, the diameter of the objective aperture is varied from 30 µm to 50 µm. The inset displays the corresponding beam currents on a logarithmic scale. For the 30-µm objective aperture (olive triangles) we observe the energy width to marginally increase from (0.88 ± 0.01) eV to (1.16 ± 0.01) eV between spots 1.0 and 3.9, while at spot 4.0 it suddenly jumps to (1.74 ± 0.02) eV. Above this point, the energy width continues to rise until it reaches a maximum of (2.81 ± 0.03) eV at spot 6.0. The beam current grows from a minimum of 5 pA at spot 1.0 to a maximum of 2.5 nA at spot 6.0. However, between spots 3.9 and 4.0 the current declines by approximately 40 %. The data for the 50-µm objective aperture (green circles) follow a very similar trend, with only the beam currents scaling up by an approximate factor of 3 while the energy widths deviate by no more than 10 %. At Spot 6.0, we find a maximum energy width of (2.98 ± 0.02) eV and a beam current of 8.7 nA. To explain the above

observations, we note that the energy distribution of the electrons is highly correlated with their angular distribution as they are collected from the electron source [246]. As a result, the configuration of the primary condenser lens largely influences both the beam current and the energy width. Between spots 3.9 and 4.0, the projection of the electron source switches from virtual to real, causing the energy width to rise while the beam current simultaneously drops. The latter can be attributed to several apertures along the beam column that limit the angular width of the transmitted beam. After the source, the energy distribution of the collected electrons is no longer altered [247], in good agreement with the minor effect of the objective aperture on the measured energy distributions.

5.6 Pulsed beam measurements with the modified RFA

Using the above measurements as a reference, we now move on to characterize the performance of the modified RFA under pulsed beam conditions. To this end, we use a square-wave signal with a peak-to-peak amplitude of 5 V, a 10 ns edge time, and a frequency of 100 kHz. Due to both the rising and the falling edges of the signal, the latter translates into an effective electron pulse rate of $f_\mathrm{p} = 200$ kHz. Furthermore, the condenser lens is set to spot 1.0 in order to ensure a minimum energy width and the smallest possible electron density per pulse.

Fig. 5.5a shows a series of energy scans that are performed at electron energies between 4 keV and 12 keV. Each data point is acquired using an integration time of 250 ms, with the total acquisition time accumulating to approximately 45 s. The measured electron count rates are normalized to the total number of electrons that arrive at the input anode. To this end, the average beam current I_av is determined from a separate reference measurement with a Faraday cup. The corresponding values are shown in Fig. 5.5c, along with the number of electrons per pulse $N_\mathrm{e} = I_\mathrm{av} / \left(e f_\mathrm{p}\right)$, where e is the elementary charge. To account for the measurement uncertainty, we estimate a relative error of 10 %. As can be seen, at we operate the SEM in a regime of at most one electron per pulse. Overall, the acquired energy scans exhibit a very similar signature to those obtained with the original RFA. Model fits to the data (see orange curves) show an increase in energy width from (0.69 ± 0.11) eV at 4 keV to (1.23 ± 0.03) eV at 11 keV, as shown in Fig. 5.5b. At 12 keV, the applied HV offset becomes unstable, causing a non-representative narrowing of the measured distribution. Reassuringly, an energy width of (0.85 ± 0.07) eV at 5 keV closely resembles the value obtained for a continuous electron beam with the original RFA. This suggests a comparable energy resolution despite the modification of the electrode layout. Considering the normalized count rates, the detection efficiency of the electron counter is found to gradually increase with the electron energy until it reaches unity at approximately 10 keV. This is related to the absorption of electrons in a thin electrical contact layer on top of the silicon sensor. Normalized count rates greater than unity can be attributed to the uncertainty on the measured beam currents. Below 4 keV, the onset of a substantial noise floor defines the lower limit for operation of the analyser. In addition, the signal amplitude is observed to fluctuate with the ramp potential up to electron energies greater than 6 keV.

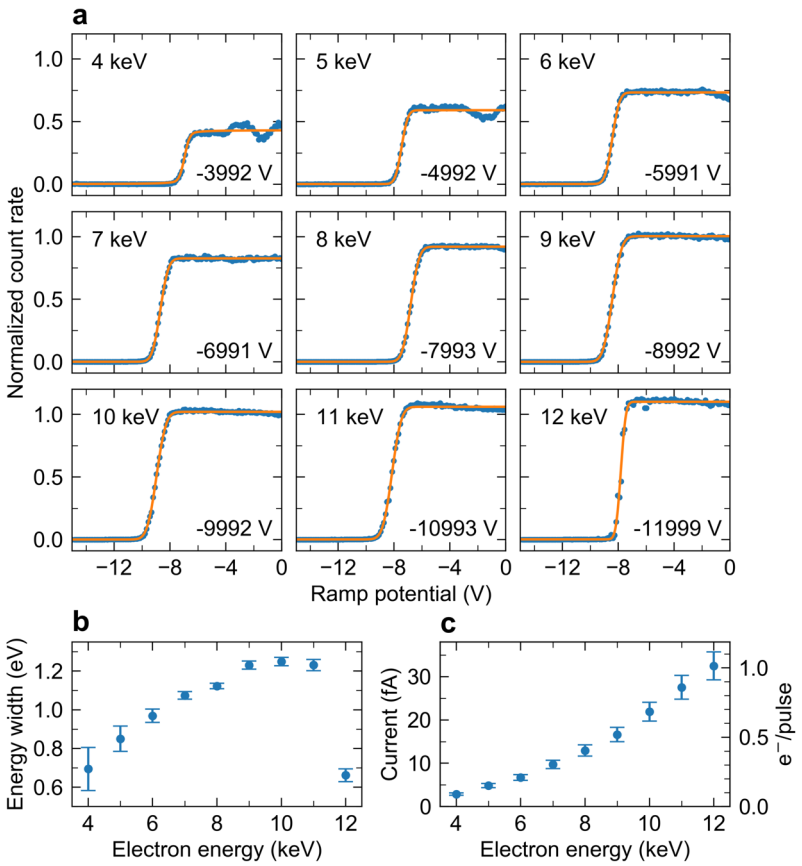

Figure 5.5: Energy scans with the modified RFA under pulsed electron beam conditions (electron pulse rate 200 kHz). **a** Normalized electron count rate as a function of the applied ramp potential for a range of electron energies between 4 keV and 12 keV. The corresponding HV offsets are indicated on the lower right of each panel. The solid curves represent analytical model fits to the data based on Eq. (5.2). **b** Measured energy width as a function of the electron energy as retrieved from the model fits in **a**. The error bars represent the statistical uncertainty on the fit. **c** Average beam current and corresponding number of electrons per pulse at the input anode as a function of the electron energy. The error bars represent an estimated measurement uncertainty of 10 %.

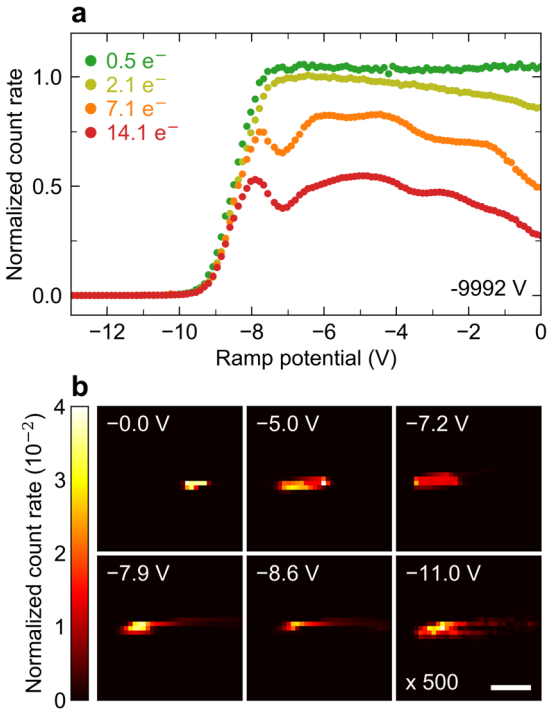

Figure 5.6: Energy scans with the modified RFA for a variable number of electrons per pulse at an electron energy of 10 keV. **a** Normalized electron count rate as a function of the applied ramp potential (HV offset of -9.992 kV, electron pulse rate 200 kHz). **b** Projection of the electron beam onto the sensor of the electron counter for different ramp potentials. The panels show the normalized count rate per pixel for an average number of 14.1 electrons per pulse (red data points in **a**). The scale bar is 0.5 mm.

Fig. 5.6a shows another series of energy scans at an electron energy of 10 keV for a variable number of electrons per pulse. To this end, the edge time of the square wave signal that is applied to the beam deflector is increased from 7.5 ns to 200 ns. As a result, the effective pulse duration is prolonged from approximately 1.3 ns to 38.7 ns, whereas the electron density remains constant. The data demonstrate a characteristic effect that is correlated with the finite rate capability of the electron sensor: As the number of electrons per pulse exceeds unity, the detection efficiency scales down and varies with the ramp potential. For one, this is due to the dead time of the sensor pixels being much greater than the electron pulse duration. Hence, a single pixel can only detect a single electron per pulse. For another, the RFA effectively resembles an Einzel lens that projects the transmitted electrons onto the sensor plane. Since this projection is highly dependent on the potential of the upper lens and the centre electrode [243, 248], the total number of pixels that are exposed to the electrons and hence the combined counting efficiency varies during the scan, as demonstrated in Fig. 5.6b. Notably, a

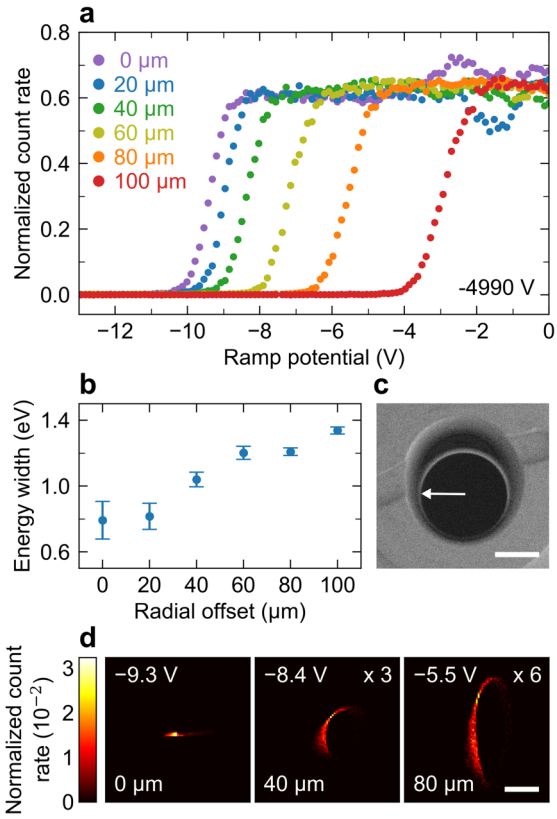

Figure 5.7: Transverse shift of the electron beam relative to the symmetry axis of the modified RFA. **a** Normalized electron count rate as a function of the applied ramp potential for different radial offsets (HV offset of -4.990 kV, electron energy 5 keV, electron pulse rate 200 kHz, < 0.2 electrons per pulse). **b** Measured energy width as a function of the radial offset as derived from model fits to the data based on Eq. (5.1). **c** SEM micrograph of the aperture in centre electrode near the threshold potential for electron repulsion. The white arrow indicates the direction of the beam shift and the scale bar is 100 µm. **d** Projection of the electron beam onto the sensor of the electron counter for different radial offsets. The panels show the normalized count rate per pixel for the ramp potential at which approximately one half of the incoming electron are transmitted. The scale bar is 1 mm.

similar effect is also responsible for the signal fluctuations that are observed at low electron energies in Fig. 5.5a. Although in this case the number of electrons per pulse is much smaller than unity, the count rate varies due to subtle differences in the sensitivity of the individual pixels. By introducing a suitable electron-optical element that disperses the transmitted electrons over the sensor plane, signal fluctuations could be largely eliminated and the rate capability of the analyser increased. Ultimately, the maximum count rate per pixel is limited to a few hundred kHz.

Finally, in Fig. 5.7a we demonstrate a series of energy scans at an electron energy of 5 keV in which the beam is radially shifted outwards from the symmetry axis of the analyser. The offset potential is set to -4990 V. For reference, an SEM micrograph of the aperture in the centre electrode is to be seen in Fig. 7c, with the arrow indicating the direction of the beam shift. As the radial offset is increased from 0 µm to 100 µm, the edge of the measured energy scans is found to drift towards larger ramp potentials, i.e., closer to the HV offset (note the negative scale). At the same time, the energy width gradually expands from (0.79 ± 0.11) eV to (1.34 ± 0.02) eV (see Fig. 5.7b), indicating a loss in energy resolution. These observations are consistent with the exponential-like growth of the potential barrier towards the periphery of the aperture as observed in the simulations in Fig. 5.3b. The energy broadening can be attributed to the corresponding radial asymmetry of the potential gradient. Notably, the latter also leads to an asymmetric projection of the transmitted electrons onto the sensor plane, as demonstrated in Fig. 5.7d. An upper limit to the energy resolution γ_{res} can be estimated using Eq. (5.2). Assuming $\gamma_{\mathrm{e}} \approx 0.8$ eV, we find values of $\gamma_{\mathrm{res}} \lesssim 0.7$ eV and $\gamma_{\mathrm{res}} \lesssim 1.1$ eV for radial offsets of 40 µm and 100 µm, respectively. In the centre of the analyser, the energy resolution is estimated to reach an optimum of $\gamma_{\mathrm{res}} \lesssim 0.3$ eV, as suggested by the simulations. For reference, in previous experiments using the original RFA the energy width of ultra-short electron pulses in an SEM with a laser-driven electron gun has been resolved down to a minimum of 0.3 eV [249].

5.7 Discussion & conclusion

In conclusion, we have demonstrated an electrostatic RFA as a compact, high-resolution spectroscopic tool to probe the energy distribution of low energy electrons in an SEM. To enable measurements under both continuous and pulsed electron beam conditions as in PINEM, we operate an SEM that is equipped with an ultra-fast electrostatic beam blanker. We first use an RFA as originally demonstrated in ref. [244] to characterize the continuous beam emission of the SEM at an electron energy of 5 keV. Our measurements reveal a minimum electron energy width of (0.88 ± 0.01) eV at a beam current of 5 pA and a maximum of (2.98 ± 0.02) eV at a beam current of 8.7 nA. Furthermore, we perform numerical simulations that suggest an optimum energy resolution of ~ 0.1 eV. We then introduce a modified version of the RFA to enable operation over an extended range of electron energies and under pulsed electron beam conditions as typically employed in PINEM experiments. To this end, we implement an electrode layout with an enhanced electrical breakdown threshold and a highly-sensitive direct electron counter. We acquire electron energy spectra in the range of 4 keV to 12 keV, while operating the SEM at an electron pulse rate of 200 kHz and in a regime of less than one

electron per pulse. Between 4 keV and 11 keV, the width of the measured electron spectra is found to scale from (0.69 ± 0.11) eV to (1.23 ± 0.03) eV. At an electron energy of 12 keV, we observe the onset of electrical breakdown, while the lower energy limit is given by the detection threshold of the electron counter. Overall, we find that the modified RFA meets the resolution and sensitivity requirements for future PINEM experiments in the SEM. However, we also identify three main limitations: Firstly, the stepwise acquisition of the electron spectra takes several tens of seconds of acquisition time. Second, the incident electron beam has to be aligned with respect to a narrow aperture on a scale of a few tens of microns. And finally, the limited rate capability of the electron counter leads to measurement artifacts as the number of electrons per pulse is greater than unity. From a technical viewpoint, we anticipate that these limitations can be largely improved. In particular, an optimization of the electrode configuration should allow for a reduced alignment sensitivity as well as a broader distribution of the transmitted electrons over the sensor of the electron counter. For the future, we envision that the compact design of the RFA in combination with additional timing capabilities of the electron counter open up novel possibilities for correlated EELS, CL and PINEM measurements at non-relativistic electron energies in the SEM.

Bibliography

[1] N. Zheludev, *The life and times of the LED — a 100-year history,* Nature Photonics **1**, 189 (2007).

[2] A. L. Schawlow and C. H. Townes, *Infrared and optical masers,* Physical Review **112**, 1940 (1958).

[3] T. H. Maiman, *Stimulated optical radiation in ruby,* Nature **187**, 493 (1960).

[4] R. N. Hall, G. E. Fenner, J. D. Kingsley, T. J. Soltys, and R. O. Carlson, *Coherent light emission from GaAs junctions,* Physical Review Letters **9**, 366 (1962).

[5] M. I. Nathan, W. P. Dumke, G. Burns, F. H. Dill, and G. Lasher, *Stimulated emission of radiation from GaAs p-n junctions,* Applied Physics Letters **1**, 62 (1962).

[6] T. M. Quist, R. H. Rediker, R. J. Keyes, W. E. Krag, B. Lax, A. L. McWhorter, and H. J. Zeigler, *Semiconductor MASER of GaAs,* Applied Physics Letters **1**, 91 (1962).

[7] A. E. Siegman, *Lasers* (University Science Books, 1986).

[8] M. Beckers, B. Weise, S. Kalapis, T. Gries, G. Seide, and C.-A. Bunge, *Basics of light guidance,* in *Polymer Optical Fibres*, edited by C.-A. Bunge, T. Gries, and M. Beckers (Woodhead Publishing, 2017) pp. 9–46.

[9] Y. Xu, *Nature and source of light for plant factory,* in *Plant Factory Using Artificial Light*, edited by M. Anpo, H. Fukuda, and T. Wada (Elsevier, 2019) pp. 47–69.

[10] J. C. Maxwell, *VIII. A dynamical theory of the electromagnetic field,* Philosophical Transactions of the Royal Society of London **155**, 459 (1865).

[11] A. Einstein, *Über einen die Erzeugung und Verwandlung des Lichtes betreffenden heuristischen Gesichtspunkt,* Annalen der Physik **322**, 132 (1905).

[12] L. Novotny and B. Hecht, *Principles of Nano-Optics* (Cambridge University Press, 2006).

[13] W. Demtröder, *Laser spectroscopy: Basic concepts and instrumentation*, 3rd ed. (Springer, 2002).

[14] M. Born, E. Wolf, A. B. Bhatia, P. C. Clemmow, D. Gabor, A. R. Stokes, A. M. Taylor, P. A. Wayman, and W. L. Wilcock, *Principles of Optics* (Cambridge University Press, 1999).

[15] A. F. Koenderink and A. Polman, *Nanophotonics: Shrinking light-based technology,* Science **348**, 516 (2015).

[16] S. A. Maier and H. A. Atwater, *Plasmonics: Localization and guiding of electromagnetic energy in metal/dielectric structures,* Journal of Applied Physics **98**, 011101 (2005).

[17] S. Linic, P. Christopher, H. Xin, and A. Marimuthu, *Catalytic and photocatalytic transformations on metal nanoparticles with targeted geometric and plasmonic properties,* Accounts of Chemical Research **46**, 1890 (2013).

[18] M. L. Brongersma, N. J. Halas, and P. Nordlander, *Plasmon-induced hot carrier science and technology,* Nature Nanotechnology **10**, 25 (2015).

[19] U. Aslam, V. G. Rao, S. Chavez, and S. Linic, *Catalytic conversion of solar to chemical energy on plasmonic metal nanostructures,* Nature Catalysis **1**, 656 (2018).

[20] S. Li, P. Miao, Y. Zhang, J. Wu, B. Zhang, Y. Du, X. Han, J. Sun, and P. Xu, *Recent advances in plasmonic nanostructures for enhanced photocatalysis and electrocatalysis,* Advanced Materials **33**, 2000086 (2021).

[21] H. A. Atwater and A. Polman, *Plasmonics for improved photovoltaic devices,* Nature Materials **9**, 205 (2010).

[22] M. L. Brongersma, Y. Cui, and S. Fan, *Light management for photovoltaics using high-index nanostructures,* Nature Materials **13**, 451 (2014).

[23] E. C. Garnett, B. Ehrler, A. Polman, and E. Alarcon-Llado, *Photonics for photovoltaics: Advances and opportunities,* ACS Photonics **8**, 61 (2021).

[24] N. Engheta, *Circuits with light at nanoscales: Optical nanocircuits inspired by metamaterials,* Science **317**, 1698 (2007).

[25] L. Thylén and L. Wosinski, *Integrated photonics in the 21st century,* Photonics Research **2**, 75 (2014).

[26] J. Wang, F. Sciarrino, A. Laing, and M. G. Thompson, *Integrated photonic quantum technologies,* Nature Photonics **14**, 273 (2020).

[27] Z. Zhou, X. Ou, Y. Fang, E. Alkhazraji, R. Xu, Y. Wan, and J. E. Bowers, *Prospects and applications of on-chip lasers,* eLight **3**, 1 (2023).

[28] B. J. Brenny, A. Polman, and F. J. García de Abajo, *Femtosecond plasmon and photon wave packets excited by a high-energy electron on a metal or dielectric surface,* Physical Review B **94**, 155412 (2016).

[29] M. M. Freundlich, *Origin of the electron microscope,* Science **142**, 185 (1963).

[30] R. Egerton, *Physical Principles of Electron Microscopy* (Springer International Publishing, 2016).

[31] F. J. García de Abajo, *Optical excitations in electron microscopy,* Reviews of Modern Physics **82**, 209 (2010).

[32] A. Losquin and T. T. Lummen, *Electron microscopy methods for space-, energy-, and time-resolved plasmonics,* Frontiers of Physics **12**, 127301 (2017).

[33] A. Polman, M. Kociak, and F. J. García de Abajo, *Electron-beam spectroscopy for nanophotonics,* Nature Materials **18**, 1158 (2019).

[34] J. Nelayah, M. Kociak, O. Stéphan, F. J. García de Abajo, M. Tencé, L. Henrard, D. Taverna, I. Pastoriza-Santos, L. M. Liz-Marzán, and C. Colliex, *Mapping surface plasmons on a single metallic nanoparticle,* Nature Physics **3**, 348 (2007).

[35] M. Bosman, V. J. Keast, M. Watanabe, A. I. Maaroof, and M. B. Cortie, *Mapping surface plasmons at the nanometre scale with an electron beam,* Nanotechnology **18**, 165505 (2007).

[36] M. Kociak and O. Stéphan, *Mapping plasmons at the nanometer scale in an electron microscope,* Chemical Society Reviews **43**, 3865 (2014).

[37] C. Colliex, M. Kociak, and O. Stéphan, *Electron energy loss spectroscopy imaging of surface plasmons at the nanometer scale,* Ultramicroscopy **162**, A1 (2016).

[38] R. F. Egerton, *Electron Energy-Loss Spectroscopy in the Electron Microscope* (Springer US, 1996).

[39] F. Hofer, F. P. Schmidt, W. Grogger, and G. Kothleitner, *Fundamentals of electron energy-loss spectroscopy,* IOP Conference Series: Materials Science and Engineering **109**, 012007 (2016).

[40] B. Schaffer, U. Hohenester, A. Trügler, and F. Hofer, *High-resolution surface plasmon imaging of gold nanoparticles by energy-filtered transmission electron microscopy,* Physical Review B - Condensed Matter and Materials Physics **79**, 041401(R) (2009).

[41] H. Brink, M. Barfels, R. Burgner, and B. Edwards, *A sub-50meV spectrometer and energy filter for use in combination with 200kV monochromated (S)TEMs,* Ultramicroscopy **96**, 367 (2003).

[42] O. Krivanek, G. Corbin, N. Dellby, B. Elston, R. Keyse, M. Murfitt, C. Own, Z. Szilagyi, and J. Woodruff, *An electron microscope for the aberration-corrected era,* Ultramicroscopy **108**, 179 (2008).

[43] O. L. Krivanek, T. C. Lovejoy, N. Dellby, T. Aoki, R. W. Carpenter, P. Rez, E. Soignard, J. Zhu, P. E. Batson, M. J. Lagos, R. F. Egerton, and P. A. Crozier, *Vibrational spectroscopy in the electron microscope,* Nature **514**, 209 (2014).

[44] R. Egoavil, N. Gauquelin, G. Martinez, S. V. Aert, G. V. Tendeloo, and J. Verbeeck, *Atomic resolution mapping of phonon excitations in STEM-EELS experiments,* Ultramicroscopy **147**, 1 (2014).

[45] M. J. Lagos, A. Trügler, U. Hohenester, and P. E. Batson, *Mapping vibrational surface and bulk modes in a single nanocube,* Nature **543**, 529 (2017).

[46] K. Venkatraman, B. D. A. Levin, K. March, P. Rez, and P. A. Crozier, *Vibrational spectroscopy at atomic resolution with electron impact scattering,* Nature Physics **15**, 1237 (2019).

[47] F. Hage, D. Kepaptsoglou, Q. Ramasse, and L. Allen, *Phonon spectroscopy at atomic resolution,* Physical Review Letters **122**, 016103 (2019).

[48] F. S. Hage, G. Radtke, D. M. Kepaptsoglou, M. Lazzeri, and Q. M. Ramasse, *Single-atom vibrational spectroscopy in the scanning transmission electron microscope,* Science **367**, 1124 (2020).

[49] C. A. Gadre, X. Yan, Q. Song, J. Li, L. Gu, H. Huyan, T. Aoki, S.-W. Lee, G. Chen, R. Wu, and X. Pan, *Nanoscale imaging of phonon dynamics by electron microscopy,* Nature **606**, 292 (2022).

[50] M. J. Lagos, I. C. Bicket, S. S. M. M., and G. A. Botton, *Advances in ultrahigh-energy resolution EELS: phonons, infrared plasmons and strongly coupled modes,* Microscopy **71**, i174 (2022).

[51] N. Yamamoto, K. Araya, and F. J. García de Abajo, *Photon emission from silver particles induced by a high-energy electron beam,* Physical Review B - Condensed Matter and Materials Physics **64**, 2054191 (2001).

[52] E. J. R. Vesseur, R. D. Waele, M. Kuttge, and A. Polman, *Direct observation of plasmonic modes in Au nanowires using high-resolution cathodoluminescence spectroscopy,* Nano Letters **7**, 2843 (2007).

[53] T. Coenen, B. J. Brenny, E. J. Vesseur, and A. Polman, *Cathodoluminescence microscopy: Optical imaging and spectroscopy with deep-subwavelength resolution,* MRS Bulletin **40**, 359 (2015).

[54] C. I. Osorio, T. Coenen, B. J. Brenny, A. Polman, and A. F. Koenderink, *Angle-resolved cathodoluminescence imaging polarimetry,* ACS Photonics **3**, 147 (2016).

[55] S. Mignuzzi, M. Mota, T. Coenen, Y. Li, A. P. Mihai, P. K. Petrov, R. F. Oulton, S. A. Maier, and R. Sapienza, *Energy-momentum cathodoluminescence spectroscopy of dielectric nanostructures,* ACS Photonics **5**, 1381 (2018).

[56] T. Coenen and A. Polman, *Energy-momentum cathodoluminescence imaging of anisotropic directionality in elliptical aluminum plasmonic bullseye antennas,* ACS Photonics **6**, 573 (2019).

[57] N. J. Schilder, H. Agrawal, E. C. Garnett, and A. Polman, *Phase-resolved surface plasmon scattering probed by cathodoluminescence holography,* ACS Photonics **7**, 1476 (2020).

[58] D.-S. Yang, O. F. Mohammed, and A. H. Zewail, *Scanning ultrafast electron microscopy,* Proceedings of the National Academy of Sciences **107**, 14993 (2010).

[59] M. Merano, S. Sonderegger, A. Crottini, S. Collin, P. Renucci, E. Pelucchi, A. Malko, M. H. Baier, E. Kapon, B. Deveaud, and J.-D. Ganière, *Probing carrier dynamics in nanostructures by picosecond cathodoluminescence,* Nature **438**, 479 (2005).

[60] M. Kociak and L. Zagonel, *Cathodoluminescence in the scanning transmission electron microscope,* Ultramicroscopy **176**, 112 (2017).

[61] S. Meuret, M. S. Garcia, T. Coenen, E. Kieft, H. Zeijlemaker, M. Lätzel, S. Christiansen, S. Y. Woo, Y. H. Ra, Z. Mi, and A. Polman, *Complementary cathodoluminescence lifetime imaging configurations in a scanning electron microscope,* Ultramicroscopy **197**, 28 (2019).

[62] S. Meuret, L. H. G. Tizei, F. Houdellier, S. Weber, Y. Auad, M. Tencé, H.-C. Chang, M. Kociak, and A. Arbouet, *Time-resolved cathodoluminescence in an ultrafast transmission electron microscope,* Applied Physics Letters **119**, 062106 (2021).

[63] L. Piazza, D. J. Masiel, T. LaGrange, B. W. Reed, B. Barwick, and F. Carbone, *Design and implementation of a fs-resolved transmission electron microscope based on thermionic gun technology,* Chemical Physics **423**, 79 (2013).

[64] K. Bücker, M. Picher, O. Crégut, T. LaGrange, B. W. Reed, S. T. Park, D. J. Masiel, and F. Banhart, *Electron beam dynamics in an ultrafast transmission electron microscope with Wehnelt electrode,* Ultramicroscopy **171**, 8 (2016).

[65] A. Feist, N. Bach, N. R. da Silva, T. Danz, M. Möller, K. E. Priebe, T. Domröse, J. G. Gatzmann, S. Rost, J. Schauss, S. Strauch, R. Bormann, M. Sivis, S. Schäfer, and C. Ropers, *Ultrafast transmission electron microscopy using a laser-driven field emitter: Femtosecond resolution with a high coherence electron beam,* Ultramicroscopy **176**, 63 (2017).

[66] B. Barwick, D. J. Flannigan, and A. H. Zewail, *Photon-induced near-field electron microscopy,* Nature **462**, 902 (2009).

[67] F. J. García de Abajo and M. Kociak, *Electron energy-gain spectroscopy,* New Journal of Physics **10**, 073035 (2008).

[68] F. J. García de Abajo, A. Asenjo-Garcia, and M. Kociak, *Multiphoton absorption and emission by interaction of swift electrons with evanescent light fields,* Nano Letters **10**, 1859 (2010).

[69] S. T. Park, M. Lin, and A. H. Zewail, *Photon-induced near-field electron microscopy (PINEM): Theoretical and experimental,* New Journal of Physics **12**, 123028 (2010).

[70] A. Feist, K. E. Echternkamp, J. Schauss, S. V. Yalunin, S. Schäfer, and C. Ropers, *Quantum coherent optical phase modulation in an ultrafast transmission electron microscope,* Nature **521**, 200 (2015).

[71] V. D. Giulio, M. Kociak, and F. J. García de Abajo, *Probing quantum optical excitations with fast electrons,* Optica **6**, 1524 (2019).

[72] A. Yurtsever and A. H. Zewail, *Direct visualization of near-fields in nanoplasmonics and nanophotonics,* Nano Letters **12**, 3334 (2012).

[73] L. Piazza, T. T. Lummen, E. Quiñonez, Y. Murooka, B. W. Reed, B. Barwick, and F. Carbone, *Simultaneous observation of the quantization and the interference pattern of a plasmonic near-field,* Nature Communications **6**, 6407 (2015).

[74] E. Pomarico, I. Madan, G. Berruto, G. M. Vanacore, K. Wang, I. Kaminer, F. J. García de Abajo, and F. Carbone, *meV resolution in laser-assisted energy-filtered transmission electron microscopy,* ACS Photonics **5**, 759 (2018).

[75] T. R. Harvey, J. W. Henke, O. Kfir, H. Lourenço-Martins, A. Feist, F. J. García de Abajo, and C. Ropers, *Probing chirality with inelastic electron-light scattering,* Nano Letters **20**, 4377 (2020).

[76] M. Liebtrau, M. Sivis, A. Feist, H. Lourenço-Martins, N. Pazos-Pérez, R. A. Alvarez-Puebla, F. J. García de Abajo, A. Polman, and C. Ropers, *Spontaneous and stimulated electron–photon interactions in nanoscale plasmonic near fields,* Light: Science and Applications **10**, 82 (2021).

[77] R. Shiloh, T. Chlouba, and P. Hommelhoff, *Quantum-coherent light-electron interaction in a scanning electron microscope,* Physical Review Letters **128**, 235301 (2022).

[78] J. H. Gaida, H. Lourenço-Martins, M. Sivis, T. Rittmann, A. Feist, F. J. García de Abajo, and C. Ropers, *Attosecond electron microscopy by free-electron homodyne detection,* (2023), arXiv:2305.03005 [physics.optics] .

[79] K. Wang, R. Dahan, M. Shentcis, Y. Kauffmann, A. B. Hayun, O. Reinhardt, S. Tsesses, and I. Kaminer, *Coherent interaction between free electrons and a photonic cavity,* Nature **582**, 50 (2020).

[80] Y. Morimoto and P. Baum, *Diffraction and microscopy with attosecond electron pulse trains,* Nature Physics **14**, 252 (2018).

[81] O. Kfir, H. Lourenço-Martins, G. Storeck, M. Sivis, T. R. Harvey, T. J. Kippenberg, A. Feist, and C. Ropers, *Controlling free electrons with optical whispering-gallery modes,* Nature **582**, 46 (2020).

[82] R. Dahan, S. Nehemia, M. Shentcis, O. Reinhardt, Y. Adiv, X. Shi, O. Be'er, M. H. Lynch, Y. Kurman, K. Wang, and I. Kaminer, *Resonant phase-matching between a light wave and a free-electron wavefunction,* Nature Physics **16**, 1123 (2020).

[83] J. W. Henke, A. S. Raja, A. Feist, G. Huang, G. Arend, Y. Yang, F. J. Kappert, R. N. Wang, M. Möller, J. Pan, J. Liu, O. Kfir, C. Ropers, and T. J. Kippenberg, *Integrated photonics enables continuous-beam electron phase modulation,* Nature **600**, 653 (2021).

[84] T. Fishman, U. Haeusler, R. Dahan, M. Yannai, Y. Adiv, T. L. Abudi, R. Shiloh, O. Eyal, P. Yousefi, G. Eisenstein, P. Hommelhoff, and I. Kaminer, *Imaging the field inside nanophotonic accelerators,* Nature Communications **14**, 3687 (2023).

[85] L. D. Broglie, *Waves and quanta,* Nature **112**, 540 (1923).

[86] C. Davisson and L. H. Germer, *Diffraction of electrons by a crystal of nickel,* Physical Review **30**, 705 (1927).

[87] G. P. Thomson and A. Reid, *Diffraction of cathode rays by a thin film,* Nature **119**, 890 (1927).

[88] D. J. Griffiths and D. F. Schroeter, *Introduction to Quantum Mechanics* (Cambridge University Press, 2018).

[89] K. E. Echternkamp, A. Feist, S. Schäfer, and C. Ropers, *Ramsey-type phase control of free-electron beams,* Nature Physics **12**, 1000 (2016).

[90] K. E. Priebe, C. Rathje, S. V. Yalunin, T. Hohage, A. Feist, S. Schäfer, and C. Ropers, *Attosecond electron pulse trains and quantum state reconstruction in ultrafast transmission electron microscopy,* Nature Photonics **11**, 793 (2017).

[91] G. M. Vanacore, I. Madan, G. Berruto, K. Wang, E. Pomarico, R. J. Lamb, D. McGrouther, I. Kaminer, B. Barwick, F. J. García de Abajo, and F. Carbone, *Attosecond coherent control of free-electron wave functions using semi-infinite light fields,* Nature Communications **9**, 2694 (2018).

[92] G. M. Vanacore, G. Berruto, I. Madan, E. Pomarico, P. Biagioni, R. J. Lamb, D. McGrouther, O. Reinhardt, I. Kaminer, B. Barwick, H. Larocque, V. Grillo, E. Karimi, F. J. García de Abajo, and F. Carbone, *Ultrafast generation and control of an electron vortex beam via chiral plasmonic near fields,* Nature Materials **18**, 573 (2019).

[93] I. Madan, V. Leccese, A. Mazur, F. Barantani, T. LaGrange, A. Sapozhnik, P. M. Tengdin, S. Gargiulo, E. Rotunno, J.-C. Olaya, I. Kaminer, V. Grillo, F. J. García de Abajo, F. Carbone, and G. M. Vanacore, *Ultrafast transverse modulation of free electrons by interaction with shaped optical fields,* ACS Photonics **9**, 3215 (2022).

[94] A. Feist, S. V. Yalunin, S. Schafer, and C. Ropers, *High-purity free-electron momentum states prepared by three-dimensional optical phase modulation,* Physical Review Research **2**, 043227 (2020).

[95] A. Konečná and F. J. García de Abajo, *Electron beam aberration correction using optical near fields,* Physical Review Letters **125**, 030801 (2020).

[96] O. Kfir, *Entanglements of electrons and cavity photons in the strong-coupling regime,* Physical Review Letters **123**, 103602 (2019).

[97] O. Reinhardt and I. Kaminer, *Theory of shaping electron wavepackets with light,* ACS Photonics **7**, 2859 (2020).

[98] V. D. Giulio and F. J. García de Abajo, *Free-electron shaping using quantum light,* Optica **7**, 1820 (2020).

[99] R. Dahan, A. Gorlach, U. Haeusler, A. Karnieli, O. Eyal, P. Yousefi, M. Segev, A. Arie, G. Eisenstein, P. Hommelhoff, and I. Kaminer, *Imprinting the quantum statistics of photons on free electrons,* Science **373**, eabj7128 (2021).

[100] A. Konečná, F. Iyikanat, and F. J. García de Abajo, *Entangling free electrons and optical excitations,* Science Advances **8**, eabo7853 (2022).

[101] F. J. García de Abajo and V. D. Giulio, *Optical excitations with electron beams: Challenges and opportunities,* ACS Photonics **8**, 945 (2021).

[102] A. Asenjo-Garcia and F. J. García de Abajo, *Plasmon electron energy-gain spectroscopy,* New Journal of Physics **15**, 103021 (2013).

[103] R. H. Pantell and M. A. Piestrup, *Free-electron momentum modulation by means of limited interaction length with light,* Applied Physics Letters **32**, 781 (1978).

[104] N. Talebi, *Strong interaction of slow electrons with near-field light visited from first principles,* Physical Review Letters **125**, 80401 (2020).

[105] J. Breuer and P. Hommelhoff, *Laser-based acceleration of nonrelativistic electrons at a dielectric structure,* Physical Review Letters **111**, 134803 (2013).

[106] Y. Adiv, K. Wang, R. Dahan, P. Broaddus, Y. Miao, D. Black, K. Leedle, R. Byer, O. Solgaard, R. J. England, and I. Kaminer, *Quantum nature of dielectric laser accelerators,* Physical Review X **11**, 041042 (2021).

[107] S. J. Smith and E. M. Purcell, *Visible light from localized surface charges moving across a grating,* Physical Review **92**, 1069 (1953).

[108] N. Yu and F. Capasso, *Flat optics with designer metasurfaces,* Nature Materials **13**, 139 (2014).

[109] D. Lin, P. Fan, E. Hasman, and M. L. Brongersma, *Dielectric gradient metasurface optical elements,* Science **345**, 298 (2014).

[110] S. Chen, Z. Li, Y. Zhang, H. Cheng, and J. Tian, *Phase manipulation of electromagnetic waves with metasurfaces and its applications in nanophotonics,* Advanced Optical Materials **6**, 1800104 (2018).

[111] S. M. Kamali, E. Arbabi, A. Arbabi, and A. Faraon, *A review of dielectric optical metasurfaces for wavefront control,* Nanophotonics **7**, 1041 (2018).

[112] D. Neshev and I. Aharonovich, *Optical metasurfaces: new generation building blocks for multi-functional optics,* Light: Science and Applications **7**, 58 (2018).

[113] J. Hu, S. Bandyopadhyay, Y. hui Liu, and L. yang Shao, *A review on metasurface: From principle to smart metadevices,* Frontiers in Physics **8**, 586087 (2021).

[114] E. Hasman, V. Kleiner, G. Biener, and A. Niv, *Polarization dependent focusing lens by use of quantized Pancharatnam–Berry phase diffractive optics,* Applied Physics Letters **82**, 328 (2003).

[115] F. Aieta, P. Genevet, M. A. Kats, N. Yu, R. Blanchard, Z. Gaburro, and F. Capasso, *Aberration-free ultrathin flat lenses and axicons at telecom wavelengths based on plasmonic metasurfaces,* Nano Letters **12**, 4932 (2012).

[116] M. Khorasaninejad, W. T. Chen, R. C. Devlin, J. Oh, A. Y. Zhu, and F. Capasso, *Metalenses at visible wavelengths: Diffraction-limited focusing and subwavelength resolution imaging,* Science **352**, 1190 (2016).

[117] W. T. Chen, A. Y. Zhu, V. Sanjeev, M. Khorasaninejad, Z. Shi, E. Lee, and F. Capasso, *A broadband achromatic metalens for focusing and imaging in the visible,* Nature Nanotechnology **13**, 220 (2018).

[118] S. Wang, P. C. Wu, V.-C. Su, Y.-C. Lai, M.-K. Chen, H. Y. Kuo, B. H. Chen, Y. H. Chen, T.-T. Huang, J.-H. Wang, R.-M. Lin, C.-H. Kuan, T. Li, Z. Wang, S. Zhu, and D. P. Tsai, *A broadband achromatic metalens in the visible,* Nature Nanotechnology **13**, 227 (2018).

[119] F. Yue, D. Wen, J. Xin, B. D. Gerardot, J. Li, and X. Chen, *Vector vortex beam generation with a single plasmonic metasurface,* ACS Photonics **3**, 1558 (2016).

[120] A. Faßbender, J. Babocký, P. Dvořák, V. Křápek, and S. Linden, *Direct phase mapping of broadband Laguerre-Gaussian metasurfaces,* APL Photonics **3**, 110803 (2018).

[121] H. Kwon, D. Sounas, A. Cordaro, A. Polman, and A. Alù, *Nonlocal metasurfaces for optical signal processing,* Physical Review Letters **121**, 173004 (2018).

[122] H. Kwon, A. Cordaro, D. Sounas, A. Polman, and A. Alù, *Dual-polarization analog 2D image processing with nonlocal metasurfaces,* ACS Photonics **7**, 1799 (2020).

[123] A. Silva, F. Monticone, G. Castaldi, V. Galdi, A. Alù, and N. Engheta, *Performing mathematical operations with metamaterials,* Science **343**, 160 (2014).

[124] A. Cordaro, H. Kwon, D. Sounas, A. F. Koenderink, A. Alù, and A. Polman, *High-index dielectric metasurfaces performing mathematical operations,* Nano Letters **19**, 8418 (2019).

[125] G. Li, S. Zhang, and T. Zentgraf, *Nonlinear photonic metasurfaces,* Nature Reviews Materials **2**, 17010 (2017).

[126] S. Keren-Zur, L. Michaeli, H. Suchowski, and T. Ellenbogen, *Shaping light with nonlinear metasurfaces,* Advances in Optics and Photonics **10**, 309 (2018).

[127] N. Nookala, J. Lee, M. Tymchenko, J. S. Gomez-Diaz, F. Demmerle, G. Boehm, K. Lai, G. Shvets, M.-C. Amann, A. Alu, and M. Belkin, *Ultrathin gradient nonlinear metasurface with a giant nonlinear response,* Optica **3**, 283 (2016).

[128] T. Santiago-Cruz, A. Fedotova, V. Sultanov, M. A. Weissflog, D. Arslan, M. Younesi, T. Pertsch, I. Staude, F. Setzpfandt, and M. Chekhova, *Photon pairs from resonant metasurfaces,* Nano Letters **21**, 4423 (2021).

[129] M. Semmlinger, M. L. Tseng, J. Yang, M. Zhang, C. Zhang, W.-Y. Tsai, D. P. Tsai, P. Nordlander, and N. J. Halas, *Vacuum ultraviolet light-generating metasurface,* Nano Letters **18**, 5738 (2018).

[130] L. Huang, S. Zhang, and T. Zentgraf, *Metasurface holography: from fundamentals to applications,* Nanophotonics **7**, 1169 (2018).

[131] H. Zhou, B. Sain, Y. Wang, C. Schlickriede, R. Zhao, X. Zhang, Q. Wei, X. Li, L. Huang, and T. Zentgraf, *Polarization-encrypted orbital angular momentum multiplexed metasurface holography,* ACS Nano **14**, 5553 (2020).

[132] O. A. M. Abdelraouf, Z. Wang, H. Liu, Z. Dong, Q. Wang, M. Ye, X. R. Wang, Q. J. Wang, and H. Liu, *Recent advances in tunable metasurfaces: Materials, design, and applications,* ACS Nano **16**, 13339 (2022).

[133] F. J. García de Abajo and M. Kociak, *Probing the photonic local density of states with electron energy loss spectroscopy,* Physical Review Letters **100**, 106804 (2008).

[134] A. Losquin and M. Kociak, *Link between cathodoluminescence and electron energy loss spectroscopy and the radiative and full electromagnetic local density of states,* ACS Photonics **2**, 1619 (2015).

[135] A. Losquin, L. F. Zagonel, V. Myroshnychenko, B. Rodríguez-González, M. Tencé, L. Scarabelli, J. Förstner, L. M. Liz-Marzán, F. J. García de Abajo, O. Stéphan, and M. Kociak, *Unveiling nanometer scale extinction and scattering phenomena through combined electron energy loss spectroscopy and cathodoluminescence measurements,* Nano Letters **15**, 1229 (2015).

[136] T. Coenen, J. V. D. Groep, and A. Polman, *Resonant modes of single silicon nanocavities excited by electron irradiation,* ACS Nano **7**, 1689 (2013).

[137] T. Coenen, F. B. Arango, A. F. Koenderink, and A. Polman, *Directional emission from a single plasmonic scatterer,* Nature Communications **5**, 3250 (2014).

[138] T. Coenen, D. T. Schoen, B. J. Brenny, A. Polman, and M. L. Brongersma, *Combined electron energy-loss and cathodoluminescence spectroscopy on individual and composite plasmonic nanostructures,* Physical Review B **93**, 195429 (2016).

[139] S. Raza, N. Stenger, A. Pors, T. Holmgaard, S. Kadkhodazadeh, J. B. Wagner, K. Pedersen, M. Wubs, S. I. Bozhevolnyi, and N. A. Mortensen, *Extremely confined gap surface-plasmon modes excited by electrons,* Nature Communications **5**, 4125 (2014).

[140] S. Raza, M. Esfandyarpour, A. L. Koh, N. A. Mortensen, M. L. Brongersma, and S. I. Bozhevolnyi, *Electron energy-loss spectroscopy of branched gap plasmon resonators,* Nature Communications **7**, 13790 (2016).

[141] E. J. R. Vesseur, T. Coenen, H. Caglayan, N. Engheta, and A. Polman, *Experimental verification of n=0 structures for visible light,* Physical Review Letters **110**, 013902 (2013).

[142] R. Sapienza, T. Coenen, J. Renger, M. Kuttge, N. F. V. Hulst, and A. Polman, *Deep-subwavelength imaging of the modal dispersion of light,* Nature Materials **11**, 781 (2012).

[143] S. Peng, N. J. Schilder, X. Ni, J. V. D. Groep, M. L. Brongersma, A. Alù, A. B. Khanikaev, H. A. Atwater, and A. Polman, *Probing the band structure of topological silicon photonic lattices in the visible spectrum,* Physical Review Letters **122**, 117401 (2019).

[144] C. Liu, Y. Wu, Z. Hu, J. A. Busche, E. K. Beutler, N. P. Montoni, T. M. Moore, G. A. Magel, J. P. Camden, D. J. Masiello, G. Duscher, and P. D. Rack, *Continuous wave resonant photon stimulated electron energy-gain and electron energy-loss spectroscopy of individual plasmonic nanoparticles,* ACS Photonics **6**, 2499 (2019).

[145] P. Das, J. D. Blazit, M. Tencé, L. F. Zagonel, Y. Auad, Y. H. Lee, X. Y. Ling, A. Losquin, C. Colliex, O. Stéphan, F. J. García de Abajo, and M. Kociak, *Stimulated electron energy loss and gain in an electron microscope without a pulsed electron gun,* Ultramicroscopy **203**, 44 (2019).

[146] N. Pazos-Perez, L. Guerrini, and R. A. Alvarez-Puebla, *Plasmon tunability of gold nanostars at the tip apexes,* ACS Omega **3**, 17173 (2018).

[147] E. Hao, R. C. Bailey, G. C. Schatz, J. T. Hupp, and S. Li, *Synthesis and optical properties of "branched" gold nanocrystals,* Nano Letters **4**, 327 (2004).

[148] C. L. Nehl, H. Liao, and J. H. Hafner, *Optical properties of star-shaped gold nanoparticles,* Nano Letters **6**, 683 (2006).

[149] F. Hao, C. L. Nehl, J. H. Hafner, and P. Nordlander, *Plasmon resonances of a gold nanostar,* Nano Letters **7**, 729 (2007).

[150] P. S. Kumar, I. Pastoriza-Santos, B. Rodríguez-González, F. J. García de Abajo, and L. M. Liz-Marzán, *High-yield synthesis and optical response of gold nanostars,* Nanotechnology **19**, 015606 (2008).

[151] C. Hrelescu, T. K. Sau, A. L. Rogach, F. Jäckel, G. Laurent, L. Douillard, and F. Charra, *Selective excitation of individual plasmonic hotspots at the tips of single gold nanostars,* Nano Letters **11**, 402 (2011).

[152] S. Mazzucco, O. Stéphan, C. Colliex, I. Pastoriza-Santos, L. M. Liz-Marzan, F. J. García de Abajo, and M. Kociak, *Spatially resolved measurements of plasmonic eigenstates in complex-shaped, asymmetric nanoparticles: Gold nanostars,* EPJ Applied Physics **54**, 33512 (2011).

[153] L. Shao, A. S. Susha, L. S. Cheung, T. K. Sau, A. L. Rogach, and J. Wang, *Plasmonic properties of single multispiked gold nanostars: Correlating modeling with experiments,* Langmuir **28**, 8979 (2012).

[154] P. Das, A. Kedia, P. S. Kumar, N. Large, and T. K. Chini, *Local electron beam excitation and substrate effect on the plasmonic response of single gold nanostars,* Nanotechnology **24**, 1 (2013).

[155] A. Maity, A. Maiti, P. Das, D. Senapati, and T. K. Chini, *Effect of intertip coupling on the plasmonic behavior of individual multitipped gold nanoflower,* ACS Photonics **1**, 1290 (2014).

[156] M. Sivis, N. Pazos-Perez, R. Yu, R. Alvarez-Puebla, F. J. García de Abajo, and C. Ropers, *Continuous-wave multiphoton photoemission from plasmonic nanostars,* Communications Physics **1**, 13 (2018).

[157] F. J. García de Abajo and A. Howie, *Retarded field calculation of electron energy loss in inhomogeneous dielectrics,* Physical Review B - Condensed Matter and Materials Physics **65**, 1154181 (2002).

[158] U. Hohenester and A. Trügler, *MNPBEM - A Matlab toolbox for the simulation of plasmonic nanoparticles,* Computer Physics Communications **183**, 370 (2012).

[159] U. Hohenester, *Simulating electron energy loss spectroscopy with the MNPBEM toolbox,* Computer Physics Communications **185**, 1177 (2014).

[160] L. Rodríguez-Lorenzo, R. A. Álvarez Puebla, I. Pastoriza-Santos, S. Mazzucco, O. Stéphan, M. Kociak, L. M. Liz-Marzán, and F. J. García de Abajo, *Zeptomol detection through controlled ultrasensitive surface-enhanced raman scattering,* Journal of the American Chemical Society **131**, 4616 (2009).

[161] A. Gloter, A. Douiri, M. Tencé, and C. Colliex, *Improving energy resolution of EELS spectra: An alternative to the monochromator solution,* Ultramicroscopy **96**, 385 (2003).

[162] M. Bosman, E. Ye, S. F. Tan, C. A. Nijhuis, J. K. Yang, R. Marty, A. Mlayah, A. Arbouet, C. Girard, and M. Y. Han, *Surface plasmon damping quantified with an electron nanoprobe,* Scientific Reports **3**, 1312 (2013).

[163] N. Kawasaki, S. Meuret, R. Weil, H. Lourenço-Martins, O. Stéphan, and M. Kociak, *Extinction and scattering properties of high-order surface plasmon modes in silver nanoparticles probed by combined spatially resolved electron energy loss spectroscopy and cathodoluminescence,* ACS Photonics **3**, 1654 (2016).

[164] N. Bach, T. Domröse, A. Feist, T. Rittmann, S. Strauch, C. Ropers, and S. Schäfer, *Coulomb interactions in high-coherence femtosecond electron pulses from tip emitters,* Structural Dynamics **6**, 014301 (2019).

[165] K. C. Vernon, A. M. Funston, C. Novo, D. E. Gómez, P. Mulvaney, and T. J. Davis, *Influence of particle-substrate interaction on localized plasmon resonances,* Nano Letters **10**, 2080 (2010).

[166] V. Myroshnychenko, J. Rodríguez-Fernández, I. Pastoriza-Santos, A. M. Funston, C. Novo, P. Mulvaney, L. M. Liz-Marzán, and F. J. García de Abajo, *Modelling the optical response of gold nanoparticles,* Chemical Society Reviews **37**, 1792 (2008).

[167] J. Schefold, S. Meuret, N. Schilder, T. Coenen, H. Agrawal, E. C. Garnett, and A. Polman, *Spatial resolution of coherent cathodoluminescence super-resolution microscopy,* ACS Photonics **6**, 1067 (2019).

[168] G. Boudarham and M. Kociak, *Modal decompositions of the local electromagnetic density of states and spatially resolved electron energy loss probability in terms of geometric modes,* Physical Review B - Condensed Matter and Materials Physics **85**, 245447 (2012).

[169] N. Talebi, W. Sigle, R. Vogelgesang, M. Esmann, S. F. Becker, C. Lienau, and P. A. V. Aken, *Excitation of mesoscopic plasmonic tapers by relativistic electrons: Phase matching versus eigenmode resonances,* ACS Nano **9**, 7641 (2015).

[170] B. J. Brenny, T. Coenen, and A. Polman, *Quantifying coherent and incoherent cathodoluminescence in semiconductors and metals,* Journal of Applied Physics **115**, 244307 (2014).

[171] Y. Pan and A. Gover, *Spontaneous and stimulated emissions of a preformed quantum free-electron wave function,* Physical Review A **99**, 052107 (2019).

[172] O. Kfir, V. D. Giulio, F. J. García de Abajo, and C. Ropers, *Optical coherence transfer mediated by free electrons,* Science Advances **7**, eabf6380 (2021).

[173] A. Karnieli, N. Rivera, A. Arie, and I. Kaminer, *The coherence of light is fundamentally tied to the quantum coherence of the emitting particle,* Science Advances **7**, eabf8096 (2021).

[174] N. Talebi, *Electron-light interactions beyond adiabatic approximation,* in *Near-Field-Mediated Photon-Electron Interactions* (Springer International Publishing, Cham, 2019) pp. 195–243.

[175] Y. Yang, A. Massuda, C. Roques-Carmes, S. E. Kooi, T. Christensen, S. G. Johnson, J. D. Joannopoulos, O. D. Miller, I. Kaminer, and M. Soljačić, *Maximal spontaneous photon emission and energy loss from free electrons,* Nature Physics **14**, 894 (2018).

[176] F. J. García de Abajo, *Multiple excitation of confined graphene plasmons by single free electrons,* ACS Nano **7**, 11409 (2013).

[177] J. Turkevich, *Colloidal gold. Part II,* Gold Bulletin **18**, 125 (1985).

[178] F. de la Peña, T. Ostasevicius, V. T. Fauske, P. Burdet, P. Jokubauskas, M. Nord, E. Prestat, M. Sarahan, K. E. MacArthur, D. N. Johnstone, J. Taillon, J. Caron, T. Furnival, A. Eljarrat, and S. Mazz, *Hyperspy 1.3,* (2017).

[179] T. Coenen, S. V. den Hoedt, and A. Polman, *A new cathodoluminescence system for nanoscale optics, materials science, and geology,* Microscopy Today **24**, 12 (2016).

[180] P. B. Johnson and R. W. Christy, *Optical constant of the nobel metals,* Physical Review B **6**, 4370 (1972).

[181] Z. Bomzon, G. Biener, V. Kleiner, and E. Hasman, *Space-variant Pancharatnam–Berry phase optical elements with computer-generated subwavelength gratings,* Optics Letters **27**, 1141 (2002).

[182] Z. Bomzon, G. Biener, V. Kleiner, and E. Hasman, *Radially and azimuthally polarized beams generated by space-variant dielectric subwavelength gratings,* Optics Letters **27**, 285 (2002).

[183] N. Yu, P. Genevet, M. A. Kats, F. Aieta, J.-P. Tetienne, F. Capasso, and Z. Gaburro, *Light propagation with phase discontinuities: Generalized laws of reflection and refraction,* Science **334**, 333 (2011).

[184] X. Ni, N. K. Emani, A. V. Kildishev, A. Boltasseva, and V. M. Shalaev, *Broadband light bending with plasmonic nanoantennas,* Science **335**, 427 (2012).

[185] E. Karimi, S. A. Schulz, I. D. Leon, H. Qassim, J. Upham, and R. W. Boyd, *Generating optical orbital angular momentum at visible wavelengths using a plasmonic metasurface,* Light: Science and Applications **3**, 167 (2014).

[186] G. Li, M. Kang, S. Chen, S. Zhang, E. Y.-B. Pun, K. W. Cheah, and J. Li, *Spin-enabled plasmonic metasurfaces for manipulating orbital angular momentum of light,* Nano Letters **13**, 4148 (2013).

[187] G. Zheng, H. Mühlenbernd, M. Kenney, G. Li, T. Zentgraf, and S. Zhang, *Metasurface holograms reaching 80% efficiency,* Nature Nanotechnology **10**, 308 (2015).

[188] E. Maguid, R. Chriki, M. Yannai, V. Kleiner, E. Hasman, A. A. Friesem, and N. Davidson, *Topologically controlled intracavity laser modes based on Pancharatnam-Berry phase,* ACS Photonics **5**, 1817 (2018).

[189] A. S. Solntsev, G. S. Agarwal, and Y. Y. Kivshar, *Metasurfaces for quantum photonics,* Nature Photonics **15**, 327 (2021).

[190] K. Rong, B. Wang, A. Reuven, E. Maguid, B. Cohn, V. Kleiner, S. Katznelson, E. Koren, and E. Hasman, *Photonic Rashba effect from quantum emitters mediated by a Berry-phase defective photonic crystal,* Nature Nanotechnology **15**, 927 (2020).

[191] M. Krüger, M. Schenk, and P. Hommelhoff, *Attosecond control of electrons emitted from a nanoscale metal tip,* Nature **475**, 78 (2011).

[192] A. Massuda, C. Roques-Carmes, Y. Yang, S. E. Kooi, Y. Yang, C. Murdia, K. K. Berggren, I. Kaminer, and M. Soljačić, *Smith-Purcell radiation from low-energy electrons,* ACS Photonics **5**, 3513 (2018).

[193] G. Adamo, K. F. MacDonald, Y. H. Fu, C.-M. Wang, D. P. Tsai, F. J. García de Abajo, and N. I. Zheludev, *Light well: A tunable free-electron light source on a chip,* Physical Review Letters **103**, 113901 (2009).

[194] P. G. O'Shea and H. P. Freund, *Free-electron lasers: Status and applications,* Science **292**, 1853 (2001).

[195] G. Adamo, J. Y. Ou, J. So, S. D. Jenkins, F. De Angelis, K. F. MacDonald, E. Di Fabrizio, J. Ruostekoski, and N. I. Zheludev, *Electron-beam-driven collective-mode metamaterial light source,* Physical Review Letters **109**, 217401 (2012).

[196] J. Christopher, M. Taleb, A. Maity, M. Hentschel, H. Giessen, and N. Talebi, *Electron-driven photon sources for correlative electron-photon spectroscopy with electron microscopes,* Nanophotonics **9**, 4381 (2020).

[197] S. E. Korbly, A. S. Kesar, J. R. Sirigiri, and R. J. Temkin, *Observation of frequency-locked coherent terahertz Smith-Purcell radiation,* Physical Review Letters **94**, 054803 (2005).

[198] T. Shintake, H. Tanaka, T. Hara, T. Tanaka, K. Togawa, M. Yabashi, Y. Otake, Y. Asano, T. Bizen, T. Fukui, S. Goto, A. Higashiya, T. Hirono, N. Hosoda, T. Inagaki, S. Inoue, M. Ishii, Y. Kim, H. Kimura, M. Kitamura, T. Kobayashi, H. Maesaka, T. Masuda, S. Matsui, T. Matsushita, X. Maréchal, M. Nagasono, H. Ohashi, T. Ohata, T. Ohshima, K. Onoe, K. Shirasawa, T. Takagi, S. Takahashi, M. Takeuchi, K. Tamasaku, R. Tanaka, Y. Tanaka, T. Tanikawa, T. Togashi, S. Wu, A. Yamashita, K. Yanagida, C. Zhang, H. Kitamura, and T. Ishikawa, *A compact free-electron laser for generating coherent radiation in the extreme ultraviolet region,* Nature Photonics **2**, 555 (2008).

[199] M. Shentcis, A. K. Budniak, X. Shi, R. Dahan, Y. Kurman, M. Kalina, H. H. Sheinfux, M. Blei, M. K. Svendsen, Y. Amouyal, S. Tongay, K. S. Thygesen, F. H. L. Koppens, E. Lifshitz, F. J. García de Abajo, L. J. Wong, and I. Kaminer, *Tunable free-electron X-ray radiation from van der Waals materials,* Nature Photonics **14**, 686 (2020).

[200] N. van Nielen, M. Hentschel, N. Schilder, H. Giessen, A. Polman, and N. Talebi, *Electrons generate self-complementary broadband vortex light beams using chiral photon sieves,* Nano Letters **20**, 5975 (2020).

[201] N. Talebi, S. Meuret, S. Guo, M. Hentschel, A. Polman, H. Giessen, and P. A. van Aken, *Merging transformation optics with electron-driven photon sources,* Nature Communications **10**, 599 (2019).

[202] G. Li, B. P. Clarke, J.-K. So, K. F. MacDonald, and N. I. Zheludev, *Holographic free-electron light source,* Nature Communications **7**, 13705 (2016).

[203] S. Tsesses, G. Bartal, and I. Kaminer, *Light generation via quantum interaction of electrons with periodic nanostructures,* Physical Review A **95**, 013832 (2017).

[204] Z. Su, B. Xiong, Y. Xu, Z. Cai, J. Yin, R. Peng, and Y. Liu, *Manipulating Cherenkov radiation and Smith–Purcell radiation by artificial structures,* Advanced Optical Materials **7**, 1801666 (2019).

[205] R. Remez, N. Shapira, C. Roques-Carmes, R. Tirole, Y. Yang, Y. Lereah, M. Soljačić, I. Kaminer, and A. Arie, *Spectral and spatial shaping of Smith-Purcell radiation,* Physical Review A **96**, 061801(R) (2017).

[206] Z. Wang, K. Yao, M. Chen, H. Chen, and Y. Liu, *Manipulating Smith-Purcell emission with Babinet metasurfaces,* Physical Review Letters **117**, 157401 (2016).

[207] L. Jing, X. Lin, Z. Wang, I. Kaminer, H. Hu, E. Li, Y. Liu, M. Chen, B. Zhang, and H. Chen, *Polarization shaping of free-electron radiation by gradient bianisotropic metasurfaces,* Laser and Photonics Reviews **15**, 2000426 (2021).

[208] Z. Su, F. Cheng, L. Li, and Y. Liu, *Complete control of Smith-Purcell radiation by graphene metasurfaces,* ACS Photonics **6**, 1947 (2019).

[209] Y. C. Lai, T. C. Kuang, B. H. Cheng, Y. C. Lan, and D. P. Tsai, *Generation of convergent light beams by using surface plasmon locked Smith-Purcell radiation,* Scientific Reports **7**, 11096 (2017).

[210] B. P. Clarke, J. So, K. F. MacDonald, and N. I. Zheludev, *Smith-Purcell radiation from compound blazed gratings,* (2017), arXiv:1711.09018 [physics.optics] .

[211] T. Fu, D. Wang, Z. Yang, Z. lan Deng, and W. Liu, *Steering Smith-Purcell radiation angle in a fixed frequency by the Fano-resonant metasurface,* Optics Express **29**, 26983 (2021).

[212] L. Li, K. Yao, Z. Wang, and Y. Liu, *Harnessing evanescent waves by bianisotropic metasurfaces,* Laser and Photonics Reviews **14**, 1900244 (2020).

[213] X. Shi, M. Shentcis, F. J. García de Abajo, and I. Kaminer, *Free-electron interactions with designed van der Waals materials: Novel source of lensed X-ray radiation,* (Optica Publishing Group, 2021) p. JTu3A.5.

[214] I. Kaminer, S. E. Kooi, R. Shiloh, B. Zhen, Y. Shen, J. J. López, R. Remez, S. A. Skirlo, Y. Yang, J. D. Joannopoulos, A. Arie, and M. Soljacic, *Spectrally and spatially resolved Smith-Purcell radiation in plasmonic crystals with short-range disorder,* Physical Review X **7**, 011003 (2017).

[215] Y. Yang, C. Roques-Carmes, I. Kaminer, A. Zaidi, A. Massuda, Y. Yang, S. E. Kooi, K. K. Berggren, and M. Soljačić, *Manipulating Smith-Purcell radiation polarization with metasurfaces,* (Optica Publishing Group, 2018) p. FW4H.1.

[216] A. Epstein and G. V. Eleftheriades, *Arbitrary power-conserving field transformations with passive lossless Omega-type bianisotropic metasurfaces,* IEEE Transactions on Antennas and Propagation **64**, 3880 (2016).

[217] H. Überall, *High-energy interference effect of Bremsstrahlung and pair production in crystals,* Physical Review **103**, 1055 (1956).

[218] V. G. Baryshevsky, I. D. Feranchuk, and A. P. Ulyanenkov, *Parametric X-Ray Radiation in Crystals*, Vol. 213 (Springer Berlin Heidelberg, 2005).

[219] V. Baryshevsky and I. Feranchuk, *Parametric X-rays from ultrarelativistic electrons in a crystal: Theory and possibilities of practical utilization,* Journal de Physique **44**, 913 (1983).

[220] K. Mizuno, J. Pae, T. Nozokido, and K. Furuya, *Experimental evidence of the inverse Smith–Purcell effect,* Nature **328**, 45 (1987).

[221] R. Remez, A. Karnieli, S. Trajtenberg-Mills, N. Shapira, I. Kaminer, Y. Lereah, and A. Arie, *Observing the quantum wave nature of free electrons through spontaneous emission,* Physical Review Letters **123**, 060401 (2019).

[222] L. Reimer, *Scanning Electron Microscopy*, Vol. 45 (Springer Berlin Heidelberg, 1998).

[223] S. Zhang, D. A. Genov, Y. Wang, M. Liu, and X. Zhang, *Plasmon-induced transparency in metamaterials,* Physical Review Letters **101**, 047401 (2008).

[224] M. Kuttge, E. J. Vesseur, A. F. Koenderink, H. J. Lezec, H. A. Atwater, F. J. García de Abajo, and A. Polman, *Local density of states, spectrum, and far-field interference of surface plasmon polaritons probed by cathodoluminescence,* Physical Review B - Condensed Matter and Materials Physics **79**, 113405 (2009).

[225] T. Bucher, R. Ruimy, S. Tsesses, R. Dahan, G. Bartal, G. M. Vanacore, and I. Kaminer, *Free-electron Ramsey-type interferometry for enhanced amplitude and phase imaging of nearfields,* (2023), arXiv:2305.02727 [physics.optics] .

[226] A. Karnieli, D. Roitman, M. Liebtrau, S. Tsesses, N. V. Nielen, I. Kaminer, A. Arie, and A. Polman, *Cylindrical metalens for generation and focusing of free-electron radiation,* Nano Letters **22**, 5641 (2022).

[227] Y. Yang, C. Roques-Carmes, S. E. Kooi, H. Tang, J. Beroz, E. Mazur, I. Kaminer, J. D. Joannopoulos, and M. Soljačić, *Photonic flatband resonances for free-electron radiation,* Nature **613**, 42 (2023).

[228] N. Talebi, *Schrödinger electrons interacting with optical gratings: Quantum mechanical study of the inverse Smith-Purcell effect,* New Journal of Physics **18**, 123006 (2016).

[229] J. K. So, K. F. MacDonald, and N. I. Zheludev, *Fiber optic probe of free electron evanescent fields in the optical frequency range,* Applied Physics Letters **104**, 201101 (2014).

[230] J. K. So, F. J. García de Abajo, K. F. MacDonald, and N. I. Zheludev, *Amplification of the evanescent field of free electrons,* ACS Photonics **2**, 1236 (2015).

[231] W. Liu, Y. Liu, Q. Jia, and Y. Lu, *Enhanced Smith–Purcell radiation by coupling surface plasmons on meta-films array with resonator modes on a grating,* Journal of Physics D: Applied Physics **52**, 075104 (2019).

[232] N. Yamamoto, F. J. García de Abajo, and V. Myroshnychenko, *Interference of surface plasmons and Smith-Purcell emission probed by angle-resolved cathodoluminescence spectroscopy,* Physical Review B - Condensed Matter and Materials Physics **91**, 125144 (2015).

[233] J. S. Huang, V. Callegari, P. Geisler, C. Brüning, J. Kern, J. C. Prangsma, X. Wu, T. Feichtner, J. Ziegler, P. Weinmann, M. Kamp, A. Forchel, P. Biagioni, U. Sennhauser, and B. Hecht, *Atomically flat single-crystalline gold nanostructures for plasmonic nanocircuitry,* Nature Communications **1**, 150 (2010).

[234] L. Skuja, *Optically active oxygen-deficiency-related centers in amorphous silicon dioxide,* Journal of Non-Crystalline Solids **239**, 16 (1998).

[235] J. Fournier, J. Néauport, P. Grua, V. Jubera, E. Fargin, D. Talaga, and S. Jouannigot, *Luminescence study of defects in silica glasses under near-UV excitation,* Physics Procedia **8**, 39 (2010).

[236] L. Rayleigh, *On the dynamical theory of gratings,* Proceedings of the Royal Society of London. Series A, Containing Papers of a Mathematical and Physical Character **79**, 399 (1907).

[237] B. Luk'Yanchuk, N. I. Zheludev, S. A. Maier, N. J. Halas, P. Nordlander, H. Giessen, and C. T. Chong, *The Fano resonance in plasmonic nanostructures and metamaterials,* Nature Materials **9**, 707 (2010).

[238] A. E. Miroshnichenko, S. Flach, and Y. S. Kivshar, *Fano resonances in nanoscale structures,* Reviews of Modern Physics **82**, 2257 (2010).

[239] B. Gallinet and O. J. F. Martin, *Ab initio theory of Fano resonances in plasmonic nanostructures and metamaterials,* Physical Review B **83**, 235427 (2011).

[240] A. Feist, G. Huang, G. Arend, Y. Yang, J.-W. Henke, A. S. Raja, F. J. Kappert, R. N. Wang, H. Lourenço-Martins, Z. Qiu, J. Liu, O. Kfir, T. J. Kippenberg, and C. Ropers, *Cavity-mediated electron-photon pairs,* Science **377**, 777 (2022).

[241] A. Arbouet, G. M. Caruso, and F. Houdellier, *Ultrafast transmission electron microscopy: Historical development, instrumentation, and applications,* in *Advances in Imaging and Electron Physics*, Vol. 207, edited by P. W. Hawkes (Elsevier, 2018) pp. 1–72.

[242] T. Coenen, E. J. R. Vesseur, A. Polman, and A. F. Koenderink, *Directional emission from plasmonic Yagi-Uda antennas probed by angle-resolved cathodoluminescence spectroscopy,* Nano Letters **11**, 3779 (2011).

[243] J. A. Simpson, *Design of retarding field energy analyzers,* Review of Scientific Instruments **32**, 1283 (1961).

[244] M. van der Heijden, *Energy spread measurement of the Nano Aperture Ion Source*, Master's thesis, Delft University of Technology (2011).

[245] D. A. Dahl, *SIMION for the personal computer in reflection,* International Journal of Mass Spectrometry **200**, 3 (2000).

[246] M. S. Bronsgeest, *Physics of Schottky electron sources*, Ph.D. thesis, Delft University of Technology (2009).

[247] R. Haindl, A. Feist, T. Domröse, M. Möller, J. H. Gaida, S. V. Yalunin, and C. Ropers, *Coulomb-correlated electron number states in a transmission electron microscope beam,* Nature Physics **19**, 1410 (2023).

[248] Y. Cui, Y. Zou, A. Valfells, M. Reiser, M. Walter, I. Haber, R. A. Kishek, S. Bernal, and P. G. O'Shea, *Design and operation of a retarding field energy analyzer with variable focusing for space-charge-dominated electron beams,* Review of Scientific Instruments **75**, 2736 (2004).

[249] M. M. Solà Garcia, *Electron-matter interaction probed with time-resolved cathodoluminescence*, Ph.D. thesis, University of Amsterdam (2021).

List of publications and author contributions

Chapter 2

Related publication: M. Liebtrau, M. Sivis, A. Feist, H. Lourenço-Martins, N. Pazos-Pérez, R.A. Alvarez-Puebla, F.J. García de Abajo, A. Polman, and C. Ropers, *Spontaneous and stimulated electron-photon interactions in nanoscale plasmonic near fields*, Light: Science & Applications **10**, 82 (2021).

Author contributions: M.L. performed the CL measurements. M.S., A.F., and H.L.M. performed the EELS and PINEM measurements. N.P.P. and R.A.A.P. synthesized and prepared the nanostar sample. M.L., M.S., A.F, and H.L.M. analysed the experimental data. M.L. performed the numerical BEM calculations with the help of F.J.G.d.A. M.L. and F.J.G.d.A. contributed to the analytical theory. A.P. and C.R. conceived and supervised the project. All authors contributed to writing and reviewing the manuscript.

Chapter 3

Related publication: A. Karnieli*, D. Roitman*, **M. Liebtrau***, S. Tsesses*, N. van Nielen, I. Kaminer, A. Arie, and A. Polman, *Cylindrical metalens for generation and focusing of free-electron radiation*, Nano Letters **22**, 5641-5650 (2022).

*Equal contributions.

Author contributions: M.L. performed the experiments with feedback from A.K., D.R, S.T., and N.v.N. A.K., D.R., and S.T. designed and fabricated the sample. M.L. took the SEM images. A.K. and D.R. performed the numerical simulations with feedback from M.L. and S.T. M.L., A.K., and D.R. analysed the data. A.K. designed and modelled the SRR metasurface with feedback from M.L., D.R, and S.T. A.K. and M.L. developed the analytical theory. I.K., A.A., and A.P. conceived and supervised the project. All authors contributed to writing and reviewing the manuscript.

Chapter 4

Related publication: M. Liebtrau and A. Polman, *Free-electron-light coupling in an optical fibre-integrated metagrating*, in preparation.

Author contributions: M.L. conceived the project, performed the experiments and analysed the data. A.P. supervised the project. M.L. and A.P. wrote the manuscript.

Chapter 5

Author contributions: M. Liebtrau, H. Zeijlemaker, D. Ursem, and B. Krijger build up the original RFA developed in the group of P. Kruit (Delft University of Technology).

B.K. designed the electronics to control the RFA. M.L. designed the modified version of the RFA with the help of M. Postma and H.Z. M.L. performed the experiments with assistance from H. Marks. M.L. analysed the experimental data. H. Niese performed the numerical simulations with advice from M.L. A. Polman supervised the project. M.L. and A.P. wrote the manuscript.

Other publications

1. K.W. Mauser, M. Solà-Garcia, **M. Liebtrau**, B. Damilano, P.-M. Coulon, S. Vézian, P.A. Shields, S. Meuret, and A. Polman, *Employing cathodoluminescence for nanothermometry and thermal transport measurements in semiconductor nanowires*, ACS Nano **15**, 11385-11395 (2021)

2. M. Solà-Garcia, K.W. Mauser, **M. Liebtrau**, T. Coenen, S. Christiansen, S. Meuret, and A.Polman, *Photon statistics of incoherent cathodoluminescence using continuous and pulsed electron beams*, ACS Photonics **8**, 916-925 (2021)

3. M. Prämassing, **M. Liebtrau**, H.J. Schill, S. Irsen, and S.Linden, *Interferometric near-field characterization of plasmonic slot waveguides in single- and polycrystalline gold films*, Optics Express **28**, 12998-13007 (2020)

4. M. Solà Garcia, **M. Liebtrau**, K. W. Mauser, S. Meuret, and A. Polman, *Electron energy spread measurements in an ultrafast scanning electron microscope*, in preparation.

Summary

Methods to generate and control light constitute a cornerstone for future technological advancement. Today, nanophotonic systems provide the means to confine, intensify, and manipulate light on very small length scales, enabling various applications such as driving catalytic reactions, harvesting sunlight in photovoltaics, or implementing novel telecommunication and computation schemes. The exploration of the optical phenomena that underly these applications, however, poses a fundamental challenge due to the diffraction limit of light. The latter constrains the spatial resolution of conventional optical microscopy and spectroscopy techniques to typically 200 nm - 300 nm in the visible spectral range. Therefore, the emergence of ever-complex and powerful nanophotonic devices relies on alternative experimental approaches to overcome this limit.

Since its advent almost 100 years ago, electron microscopy (EM) has evolved into a powerful platform to resolve structural material features at the nanometre or even atomic length scale using swift free electrons with kinetic energies of typically 5 keV - 300 keV. At the end of the last century, it has been realized that such electrons can also serve as a nanoscale source and probe of optical material excitations. This approach exploits the transient electromagnetic field of the electrons to locally polarize a specimen on time scales shorter than an optical cycle, thereby enabling the excitation of optical phenomena across the entire infra-red (IR), visible (VIS), and ultraviolet (UV) spectral range. As a result of this interaction, the electrons undergo a spontaneous energy loss that can be probed experimentally using electron energy-loss spectroscopy (EELS). Complementarily, cathodoluminescence (CL) spectroscopy can be applied to analyse the emission of radiation resulting from this process. Due to the highly localized nature of the electron-light-matter interaction, EELS and CL provide powerful spectroscopic tools to study the optical properties of nanophotonic systems fully independent of the optical diffraction limit. Vice versa, an external optical pump source that excites the optical near-field of a nanostructure can stimulate the emission and absorption of photons by the electron. The resulting modulation of the electron energy spectrum provides a direct measure of the electron-near-field interaction strength, facilitating a technique called photon-induced near-field electron microscopy (PINEM).

The study of electron-light-matter interactions using EELS, CL, and PINEM is a rapidly expanding research field. Scientists around the world are exploring the numerous opportunities that modern scanning electron microscopes (SEMs) and transmission electron microscopes (TEMs) offer to probe optical phenomena at ultra-small length and time scales, and, moreover, to manipulate, control, and harness the quantum properties of free electrons with light. These efforts are strongly correlated with recent advances in the field of nanophotonics. In particular, the emergence of nano-textured materials with artificial optical properties, called metasurfaces, offers unique potential to control the interaction of free electrons with structured optical fields. In this thesis, we make several steps to explore and demonstrate this potential. We study

the application of metasurfaces to control the generation of light by free electrons, and in turn, how this concept may be applied to manipulate the electrons themselves.

As a starting point, in Chapter 2, we investigate the fundamental correlation between the spontaneous and stimulated interaction of free electrons with light and matter. To this end, we perform spatially-resolved EELS, CL, and PINEM measurements that reveal the coupling of free electrons and photons in the optical near-field of a single chemically-synthesized gold nanostar. The latter features sharp conical protrusions with tip radii of curvature smaller than 3 nm that sustain highly-localized plasmonic resonances in the VIS to near-IR (NIR) spectral range. The CL experiments are performed in an SEM at AMOLF at an electron energy of 20 keV electron energy, while the EELS and PINEM experiments are performed in an ultra-fast TEM instrument that can be synchronized with an optical pump laser in the group of prof. Claus Ropers at the University of Göttingen at an electron energy of 200 keV. In EELS and CL, we observe the spontaneous coupling of free electrons to a number of plasmonic tip resonances in the VIS-NIR spectral range, while in PINEM we find a strong dependence of the electron-near-field interaction on the polarization of the optical pump field and its spectral overlap with these modes. By integrating the acquired EELS and CL spectra over a bandwidth of 50 meV around the tip resonance energies, we obtain spontaneous electron energy loss and photon emission probabilities in the order of 10^{-4} and 10^{-5}, respectively. In PINEM, we observe a modulation of the electron energy spectrum by up to three energy-gain and -loss sidebands at an optical pump field intensity of approximately 1 GW/cm^2 and a pump photon energy of 1.55 eV. Complemented by theory and numerical simulations, we show that all three types of measurements feature a common spatial dependence on the dipolar electric near-field distribution of a resonantly driven nanotip. Moreover, our simulations show that the interaction strength crucially depends on the electron velocity, as determined by the spatial Fourier transformation of the optical field along the electron trajectory. As a result, a maximum electron-light coupling efficiency is achieved for electrons passing by the tip apex with comparatively low kinetic energies in the range of few keV. This finding manifests a fundamental phase-matching condition for the coupling of free electrons and light that is independent of the stimulated or spontaneous nature of the interaction.

Next, in Chapter 3, we exploit the phase-matching condition for free-electron-light coupling to demonstrate spectral and angular control over the generation of Smith-Purcell radiation (SPR) by free electrons that excite a metasurface under grazing incidence. The project is performed in collaboration with the groups of prof. Ido Kaminer at Technion and prof. Ady Arie at Tel Aviv University. As a specific example, we implement metalenses based on chirped nano gratings that generate SPR with a converging (concave) or diverging (convex) wavefront in the VIS-NIR spectral range. Using focused ion beam milling, the structures are fabricated onto a silicon wafer with a thin gold layer, ranging in pitch from 163 nm to 228 nm over a total length of 20 μm. The orientation of the grating chirp determines the concave or convex curvature of the emission wavefronts. For reference, we also implement a periodic nano grating with a constant pitch of 189 nm, generating conventional SPR that is emitted in the form of plane waves. To characterize the different grating geometries, we apply hyperspectral angle-resolved CL detection in the SEM, revealing their far-field radiation patterns

across a broad spectral range. Remarkably, we achieve a coherent electron-sample interaction range over more than 100 metagrating periods. As a result, SPR that is excited at a nominal design wavelength of 580 nm is distributed over effective numerical apertures of 0.48 ± 0.05 and 0.45 ± 0.05, for the converging and the diverging metalenses, respectively. Our measurements are complemented by numerical simulations and analytical theory that display the correlation between the experimental data and the effects of focusing and defocusing, as well as the underlying electron-near-field coupling mechanism. Building up on the metalens concept, we further present numerical simulations of a split-ring resonator (SRR) metasurface that provides simultaneous focusing and polarization control over SPR by exploiting the optical bi-anisotropy of the SRR meta-atoms.

Considering the close correlation between the emission and absorption of photons by free electrons as demonstrated in Chapter 2, it becomes clear that the concept of shaping free-electron radiation by metasurfaces (Chapter 3) can be also inverted to structure optical fields that manipulate the electron wave function. In either configuration, interfacing the metasurface with suitable optics for the extraction or injection of radiation, respectively, is a critical challenge. In Chapter 4, we address this challenge by demonstrating the coupling of free electrons and light via the SP effect in a circular metagrating that is fabricated onto the input facet of a metal-coated multi-mode optical fibre. The structure extends over a total diameter of 100 µm with a constant radial pitch of 200 nm. Resorting to the same hyperspectral angle-resolved CL detection approach as in Chapter 3, we experimentally resolve the dispersion of SPR that is emitted into both free space and the fibre core, for variable electron energies in the range of 5 keV to 30 keV. In free space, we observe emission of first-, second-, and third-order SPR in the UV to NIR spectral range that follows the theoretically expected angular dispersion relation. At an electron energy of 30 keV, we measure photon emission probabilities of first- and second-order SPR of $4.7 \cdot 10^{-4}$ and $5.0 \cdot 10^{-5}$, respectively (spectral bandwidth ~0.2 eV). SPR that is generated inside the fibre and that escapes through the cladding layer shows a modified angular dispersion that is determined by the refractive index of the fibre core and its refraction at the fibre-vacuum interface. Furthermore, first-order SPR that is detected by a fibre-coupled spectrometer reveals the coherent excitation of guided optical modes, which are spectrally filtered according to the finite numerical aperture of the fibre. Along with the coherent excitation of SPR, we also detect a broadband distribution of incoherent CL that is generated by electrons penetrating the input facet of the fibre, and scattering inelastically. We distinguish the excitation of non-bridging oxygen hole centres (NBOHCs) and oxygen deficient centres (ODCs) with mean photon emission energies of 1.95 eV and 2.80 eV, respectively. In addition, we find that incoherent CL generated within the ODC spectral range couples to a Rayleigh anomaly of the metagrating, giving rise to a Fano resonance that overlaps with the dispersion of second-order SPR at 20-keV electron energy. This phenomenon demonstrates the great potential of metasurfaces to combine the SP effect with resonant electromagnetic excitations that are supported by the metasurface such as lattice resonances.

Finally, in Chapter 5, we explore the implementation of a suitable electron energy spectrometer to perform PINEM experiments in the SEM. In combination with the wide range of spectroscopic CL detection capabilities offered by our SEM-CL instrument,

such experiments could provide new fundamental insights into the quantum nature of the electron-light-matter interaction. Notably, SEMs offer the benefit of providing access to non-relativistic electron energies at which the electron-light coupling can be substantially enhanced as shown in Chapter 2. Furthermore, these instruments offer large specimen chambers which provide ample room for the integration of experimental infrastructure. So far, however, electron spectrometers that fulfil the demands on resolution and sensitivity to probe the interaction of free electrons and light have been mainly implemented in TEMs that operate at relativistic electron energies of several tens to hundreds of keV. Here, we demonstrate an electrostatic retarding field analyzer (RFA) that can be integrated into an SEM to perform high-resolution spectroscopic measurements at non-relativistic electron energies. We first use an RFA that was originally developed in the group of prof. Pieter Kruit at the Technical University of Delft to study the continuous-beam emission of our SEM-CL instrument at an electron energy of 5 keV. The measurements reveal electron energy spectra with a full-width-at-half-maximum (FWHM) of (0.88 ± 0.01) eV at a beam current of 5 pA and (2.98 ± 0.02) eV at a beam current of 8.7 nA. Furthermore, we perform numerical simulations that suggest an upper limit on the energy resolution of the RFA of 0.1 eV. We then introduce a modified version of the RFA that is prepared for operation over an extended range of electron energies and under pulsed electron beam conditions as typically employed in PINEM. These conditions are emulated using an electrostatic beam blanker that enables the generation of electron pulses with a variable number of electrons and a duration down to several hundred picoseconds. The RFA is equipped with a direct-electron counter based on a Timepix 3 CMOS chip that provides nearly single-electron sensitivity from an electron energy of 10 keV onwards. At an electron pulse rate of 200 kHz and in a regime of less than one electron per pulse, we resolve electron spectra at electron energies between 4 keV and 11 keV. The FWHM of these spectra ranges from (0.69 ± 0.11) eV to (1.23 ± 0.03) eV. Above 11 keV we observe the onset of electrical breakdown, while below 4 keV the sensitivity of the electron counter becomes insufficient. Present limitations of the RFA are identified regarding acquisition speed, alignment sensitivity, and rate capability, all of which can be improved by further technical modifications.

Altogether, this thesis demonstrates the great potential of optical metasurfaces to harness and control the interplay of free electrons, light, and matter at the nanometer length scale. We demonstrate the fundamental correlation of spontaneous and stimulated electron-photon interactions that permits the use of complementary nanophotonic systems to both generate light and manipulate the electron wave function. We show how near-field effects in a metasurface provide control over the spectral and angular distribution of free-electron radiation, and we demonstrate how guided optical modes in an optical fibre can be coupled to free electrons using a metagrating that is patterned onto the fibre end-facet. Finally, we show how an optical modulation of non-relativistic free electrons in the SEM could be probed experimentally using an electrostatic retarding field analyser. The insights from this thesis may enable the design of complex light sources that can operate over an ultra-broad spectral range, may inspire novel spectroscopic tools to resolve the dynamics of optical phenomena on ultra-small length and time scales, and, ultimately, may contribute to a deeper fundamental understanding of the electron-light-matter interaction.

Samenvatting

Ontwerp van de wisselwerking van vrije elektronen en licht met optische meta-oppervlakken

Methoden voor het genereren en manipuleren van licht zijn essentieel voor de toekomstige technologische vooruitgang in een groot aantal toepassingen. Tegenwoordig kan licht worden gericht en gecontroleerd op zeer kleine lengteschalen door middel van nanofotonische structuren. Dit maakt bijvoorbeeld het stimuleren van katalytische reacties mogelijk, het opvangen van zonlicht voor het opwekken van elektrische energie of het implementeren van nieuwe telecommunicatie- en gegevensverwerkingsmethoden. Experimenteel onderzoek naar de fysische verschijnselen die aan deze toepassingen ten grondslag liggen is echter een grote uitdaging. Dit laatste is te wijten aan de optische diffractielimiet, die de ruimtelijke resolutie van conventionele optische microscopie- en spectroscopietechnieken in het zichtbare spectrale bereik beperkt tot typisch 200 nm tot 300 nm. De ontwikkeling van steeds complexere en krachtigere nanofotonische componenten voor de verwerking van licht is daarom afhankelijk van alternatieve experimentele benaderingen die kunnen worden gebruikt om deze resolutielimiet te overwinnen.

Sinds de introductie bijna 100 jaar geleden is elektronenmicroscopie een sleuteltechnologie geworden voor het bestuderen van structurele eigenschappen van materialen in het lengtebereik van enkele nanometers of zelfs op atomaire lengteschalen. Dit wordt gedaan met behulp van vrije elektronen die worden versneld tot kinetische energieën van meestal 5 keV tot 300 keV. Aan het eind van de vorige eeuw werd erkend dat dergelijke elektronen ook uitstekend geschikt zijn om optische materiaaleigenschappen te onderzoeken. In deze benadering wordt het snel veranderende elektromagnetische veld van de elektronen gebruikt om een monster lokaal te polariseren. Door de typische tijdschaal waarop dit proces plaatsvindt, kunnen optische verschijnselen worden geëxciteerd in het hele infrarode, zichtbare en ultraviolette spectrum. Als gevolg hiervan ervaren de elektronen een spontaan energieverlies, dat experimenteel bestudeerd kan worden met behulp van elektronenenergieverliesspectroscopie (*electron energy-loss spectroscopy* – EELS). Bovendien kan de stralingsemissie als gevolg van dit proces, worden geanalyseerd met kathodeluminescentiespectroscopie (*cathodoluminescence (spectroscopy)* – CL). Door de ruimtelijk sterk gelokaliseerde interactie tussen elektronen, licht en materie bieden EELS en CL unieke spectroscopische technieken om de optische eigenschappen van nanofotonische systemen te bestuderen met een resolutie die volledig onafhankelijk is van de optische diffractielimiet. Omgekeerd kan een externe lichtbron, zoals een laser, worden gebruikt om het optische nabije veld van een nanostructuur te exciteren, waardoor de emissie en absorptie van fotonen door het elektron wordt gestimuleerd. De resulterende modulatie van het elektronenergiespectrum geeft een directe meting van de sterkte van de interactie tussen het elektron en het nabije veld,

een eigenschap die een techniek mogelijk maakt die foton-geïnduceerde nabije-veld elektronenmicroscopie (*photon-induced near-field electron microscopy* – PINEM) wordt genoemd.

De studie van de interactie tussen hoogenergetische vrije elektronen, licht en materie met behulp van EELS, CL en PINEM is de afgelopen jaren een snelgroeiend onderzoeksgebied geworden. Wetenschappers over de hele wereld verkennen de vele mogelijkheden die moderne rasterelektronenmicroscopen (*scanning electron microscopes* – SEM's) en transmissie elektronenmicroscopen (*transmission electron microscopes* – TEM's) bieden om optische verschijnselen op ultrakleine lengte- en tijdschalen te bestuderen en ook om de kwantumeigenschappen van vrije elektronen met licht te beheersen, manipuleren en benutten. Deze inspanningen zijn nauw verbonden met de recente vooruitgang op het gebied van nanofotonica. Met name de recente opkomst van nanogestructureerde materialen met kunstmatige optische eigenschappen, de zogenaamde meta-oppervlakken, biedt een uniek potentieel om controle te krijgen over de interactie van vrije elektronen met gestructureerde optische velden. Het doel van dit proefschrift is om de eerste stappen te zetten in het verkennen en experimenteel aantonen van dit potentieel. Hiertoe onderzoeken we het gebruik van meta-oppervlakken om de opwekking van licht door vrije elektronen te beïnvloeden en hoe dit concept op zijn beurt kan worden gebruikt om de elektronen zelf te manipuleren.

Om te beginnen onderzoeken we in Hoofdstuk 2 de fundamentele correlatie tussen de spontane en de gestimuleerde interactie van vrije elektronen met licht en materie. Hiervoor voeren we ruimtelijk-opgeloste EELS-, CL- en PINEM-metingen uit, waarmee we de koppeling van vrije elektronen en fotonen in het optische nabije veld van een chemisch gesynthetiseerde gouden nanoster detecteren. Deze wordt gekenmerkt door scherpe kegelvormige pieken met een kromtestraal van minder dan 3 nm, die zeer gelokaliseerde plasmonische resonanties vertonen in het zichtbare en nabij-infrarode spectrale bereik. De CL experimenten worden uitgevoerd in een SEM op AMOLF bij een elektronenenergie van 20 keV, terwijl de EELS- en PINEM-experimenten worden uitgevoerd bij een elektronenenergie van 200 keV in een ultrasnelle TEM in de groep van prof. Claus Ropers aan de Universiteit van Göttingen. Deze TEM kan worden gesynchroniseerd met een pomplaser voor optische excitatie van het monster ten behoeve van PINEM-metingen in de gepulseerde bundelmodus. Met behulp van de EELS- en CL-metingen observeren we de spontane koppeling van vrije elektronen aan een reeks plasmonische tipresonanties in het zichtbare en nabij-infrarode spectrale bereik, terwijl de PINEM-metingen een sterke afhankelijkheid van de elektron-veld interactie van de polarisatie van het optische pompveld en de spectrale overlap met de tipresonanties laten zien. Door de gemeten EELS- en CL-spectra te integreren over een bandbreedte van 50 meV rond de corresponderende resonantie-energieën, verkrijgen we spontane elektronenenergieverlies- en fotonemissiekansen van de orde van respectievelijk 10^{-4} and 10^{-5}. De PINEM-metingen tonen een modulatie van het elektronenspectrum met maximaal drie zijbanden voor energietoename en -verlies bij een optische pompveldintensiteit van ongeveer 1 GW/cm^2 en een fotonenergie van 1,55 eV. Aangevuld met theorie en numerieke simulaties laten we zien dat alle drie de typen metingen een vergelijkbare ruimtelijke afhankelijkheid hebben van de dipolaire elektrische nabije-veldverdeling van een resonant aangeslagen nanoster tip.

Verder tonen we op basis van simulaties aan dat de sterkte van de elektron-nabije-veld interactie sterk afhangt van de elektronensnelheid. Deze wordt bepaald door de ruimtelijke Fouriertransformatie van het optische veld langs het elektronentraject, wat resulteert in maximale elektron-lichtkoppeling wanneer de elektronen de tip passeren met relatief lage kinetische energieën in het bereik van enkele kiloelektronvolt. Dit toont een fundamentele voorwaarde voor de koppeling tussen vrije elektronen en licht door faseaanpassing, die onafhankelijk is van de gestimuleerde of spontane aard van de interactie.

In Hoofdstuk 3 maken we gebruik van de voorwaarde voor koppeling tussen vrije elektronen en licht door faseaanpassing om aan te tonen dat door middel van een meta-oppervlak dat geëxciteerd wordt door vrije elektronen onder een vlakke invalshoek, de opwekking van Smith-Purcell-straling (SPS) zowel spectraal als hoekafhankelijk kan worden gecontroleerd. Het project wordt uitgevoerd in samenwerking met de groepen van prof. Ido Kaminer van het Technion en prof. Ady Arie van de Universiteit van Tel Aviv. Als concreet voorbeeld implementeren we metalenzen op basis van aperiodieke nano-tralieroosters die SPS uitzenden met een convergerend (concaaf) of divergerend (convex) golffront in het zichtbare en nabij-infrarode spectrale bereik. Met behulp van gefocusseerd ionenstraal-frezen creëren we de structuren op een siliciumsubstraat dat is bekleed met een dunne goudlaag, waarbij we de roosterafstand variëren tussen 163 nm en 228 nm over een totale lengte van 20 µm. De oriëntatie van de roosters en dus de toename of afname van de roosterafstand ten opzichte van de elektronenbaan bepaalt de concave of convexe kromming van de emissiegolffronten. Als referentie maken we ook een periodiek nano-tralierooster met een constante roosterafstand van 189 nm dat conventionele SPS uitzendt in de vorm van vlakke golven. Om de verschillende roostergeometrieën te karakteriseren, voeren we hyper-spectrale hoek-opgeloste CL-metingen uit in de SEM, waarmee we de stralingskarakteristieken van de structuren in het verre veld kunnen bepalen over een breed spectraal bereik. Opmerkelijk genoeg bereiken we een coherente interactie van de elektronen met de monsters over meer dan 100 roosterperioden. Bij een nominale golflengte van 580 nm resulteert dit in de emissie van SPS door de convergerende en divergerende metalenzen binnen effectieve numerieke openingen van respectievelijk 0.48 ± 0.05 en 0.45 ± 0.05. Onze metingen worden aangevuld met numerieke simulaties en een analytisch model die de correlatie illustreren tussen de experimentele gegevens en het focusseren of defocusseren van SPS, evenals het onderliggende elektron-nabije-veld koppelingsmechanisme. Voortbouwend op het concept van metalens, presenteren we ook numerieke simulaties van een gespleten ringresonator (*split-ring-resonator* – SRR) meta-oppervlak dat gebruikt kan worden om tegelijkertijd SPS te focussen en de polarisatie ervan te controleren door gebruik te maken van de optische bi-anisotropie van de SRR-metatomen.

Gezien de nauwe correlatie tussen de emissie en absorptie van fotonen door vrije elektronen, zoals beschreven in Hoofdstuk 2, is het duidelijk dat meta-oppervlakken voor het manipuleren van vrije elektronenstraling (Hoofdstuk 3) conceptueel ook omgekeerd gebruikt kunnen worden om optische velden te structureren die op hun beurt de golffunctie van de elektronen zelf beïnvloeden. In elke configuratie vormt het koppelen van het meta-oppervlak aan geschikte optische componenten om straling te onttrekken of te injecteren een aanzienlijke uitdaging. In Hoofdstuk 4 pakken we deze uitdaging

aan door de koppeling van vrije elektronen en licht via het SP-effect aan te tonen in een cirkelvormig meta-tralierooster dat is afgezet op het ingangsfacet van een met metaal beklede meergolvige optische glasvezel. De structuur strekt zich uit over een totale diameter van 100 µm met een constante radiale roosterafstand van 200 nm. Met behulp van de hyper-spectrale hoek-opgeloste CL-detectie methode, die al is toegepast in Hoofdstuk 3, meten we experimenteel de hoekdispersie van SPS die wordt uitgezonden naar zowel de vrije ruimte als de glasvezelkern. De experimenten worden uitgevoerd bij variabele elektronenenergieën in het bereik van 5 keV tot 30 keV. In de vrije ruimte observeren we de emissie van eerste-, tweede- en derde-orde SPS in het ultraviolette tot nabij-infrarode spectrale bereik, waarvan de hoekspreiding overeenkomt met de theoretische verwachting. Bij een elektronenenergie van 30 keV zijn de emissiekansen van eerste- en tweede-orde SPS respectievelijk $4.7 \cdot 10^{-4}$ en $5.0 \cdot 10^{-5}$ (over een spectrale bandbreedte van ~0.2 eV). SPS die binnen de vezel wordt gegenereerd en vervolgens door de claddinglaag (huls) van de optische glasvezel ontsnapt, vertoont een gewijzigde hoekspreiding die wordt bepaald door de brekingsindex van de glasvezelkern en de breking van licht op het grensvlak tussen glasvezel en vacuüm. Verder toont de detectie van eerste-orde SPS met behulp van een glasvezelgekoppelde spectrometer de coherente excitatie van geleide optische modi waarvan de spectrale verdeling wordt bepaald door de eindige numerieke apertuur van de glasvezel. Verder meten we een breedbandige verdeling van incoherente CL gegenereerd door elektronen die het ingangsvlak van de glasvezel binnendringen en onelastisch verstrooien. We kunnen onderscheid maken tussen de excitatie van niet-overbruggende zuurstofvacatures (*non-bridging oxygen hole centres* – NBOHC's) en zuurstofdeficiëntiecentra (*oxygen deficient centres* – ODC's) met gemiddelde fotonemissie-energieën van respectievelijk 1,95 eV en 2,80 eV. Verder vinden we dat incoherente CL gegenereerd in het ODC-spectrumgebied koppelt aan een Rayleigh-anomalie van het meta-tralierooster, waardoor een Fano-resonantie ontstaat die overlapt met de hoekdispersie van SPS van de tweede orde bij een elektronenenergie van 20 keV. Dit fenomeen toont het grote potentieel aan van meta-oppervlakken om het SP-effect te combineren met resonante elektromagnetische excitaties, zoals tralieroosterresonanties ondersteund door het meta-oppervlak.

Ten slotte onderzoeken we in Hoofdstuk 5 de implementatie van een geschikte elektronenenergiespectrometer om PINEM-experimenten uit te voeren in een SEM. In combinatie met het brede scala aan spectroscopische mogelijkheden voor CL detectie die ons SEM-CL-instrument biedt, zouden dergelijke experimenten nieuwe fundamentele inzichten kunnen opleveren in de kwantumaard van de elektron-licht-materie-interactie. In het bijzonder bieden SEM's het voordeel dat ze toegang bieden tot niet-relativistische elektronenenergieën, waar de elektron-lichtkoppeling aanzienlijk kan worden versterkt, zoals aangetoond in Hoofdstuk 2. Bovendien hebben SEM's grote monsterkamers die voldoende ruimte bieden voor de installatie van experimentele infrastructuur. Tot nu toe zijn geschikte elektronenspectrometers die voldoende resolutie en gevoeligheid bieden om de interactie tussen vrije elektronen en licht te bestuderen echter voornamelijk beschikbaar in TEM's, die werken bij relativistische elektronenenergieën van tientallen tot honderden kiloelektronvolt. In dit hoofdstuk demonstreren we een elektrostatische veldvertragingsanalysator (*retarding field analyser* – RFA) die geïntegreerd kan worden in een SEM om hoge-resolutie spectroscopische

metingen uit te voeren bij niet-relativistische elektronenergieën. We gebruiken eerst een RFA, oorspronkelijk ontwikkeld in de groep van prof. Pieter Kruit aan de Technische Universiteit Delft, om de emissie van een continue elektronenbundel van ons SEM-CL instrument te bestuderen bij een elektronenenergie van 5 keV. De metingen leveren elektronenenergiespectra op met een halfwaardebreedte (HWB) van (0,88 ± 0,01) eV bij een bundelstroom van 5 pA en (2,98 ± 0,02) eV bij een bundelstroom van 8,7 nA. We voeren ook numerieke simulaties uit die een bovengrens voor de energieresolutie van de RFA van 0,1 eV suggereren. Vervolgens introduceren we een aangepaste versie van de RFA die werking mogelijk maakt over een groter bereik van elektronenenergieën en onder gepulseerde elektronenbundelcondities die typisch zijn voor PINEM-experimenten. Deze omstandigheden worden nagebootst met behulp van een elektrostatische bundelafbuiger, die het genereren van elektronenpulsen met een variabel aantal elektronen en een pulsduur van een paar honderd picoseconden mogelijk maakt. De RFA is uitgerust met een elektronenteller gebaseerd op een Timepix 3 CMOS chip, die een bijna enkelvoudige elektronengevoeligheid heeft vanaf een elektronenenergie van 10 keV. Bij een elektronenpulsfrequentie van 200 kHz en met een elektronaantal van minder dan één elektron per puls lossen we elektronenspectra op bij kinetische energieën tussen 4 keV en 11 keV. De HWB van deze spectra varieert van (0,69 ± 0,11) eV tot (1,23 ± 0,03) eV. Boven 11 keV vinden we de elektrische afbraakdrempel van de RFA, terwijl onder 4 keV de gevoeligheid van de elektronenteller onvoldoende wordt. Huidige beperkingen van de RFA worden ontdekt met betrekking tot de acquisitiesnelheid van energiespectra, een hoge gevoeligheid voor de oriëntatie van de elektronenbundel en de elektronentelsnelheid, die allemaal verbeterd kunnen worden door verdere technische aanpassingen.

Samenvattend toont dit werk het grote potentieel aan van optische meta-oppervlakken om de wisselwerking tussen vrije elektronen, licht en materie op nanometerschaal te controleren en volledig te benutten. We laten de fundamentele correlatie zien tussen de spontane en gestimuleerde interacties van vrije elektronen en fotonen, waardoor complementaire nanofotonische systemen kunnen worden gebruikt om zowel licht te genereren als de kwantummechanische golffunctie van elektronen te manipuleren. We laten zien hoe nabije-veldeffecten in een meta-oppervlak controle mogelijk maken over de spectrale en hoekverdeling van straling uitgezonden door vrije elektronen, en we laten zien hoe geleide optische modi in een optische glasvezel gekoppeld kunnen worden aan vrije elektronen door middel van een meta-tralierooster dat gemonteerd is op het ingangsfacet van de glasvezel. Tot slot laten we zien hoe de optische modulatie van niet-relativistische vrije elektronen in de SEM experimenteel kan worden onderzocht met behulp van een elektrostatische RFA. In de toekomst kan de kennis die is opgedaan in dit werk het ontwerp van complexe lichtbronnen mogelijk maken die een extreem breed spectraal bereik bestrijken, nieuwe spectroscopische technieken inspireren om de dynamica van optische verschijnselen op ultrakleine lengte- en tijdschalen te onderzoeken en uiteindelijk bijdragen aan een beter begrip van de interactie tussen elektronen, licht en materie.

Zusammenfassung

Gestaltung des Zusammenspiels von freien Elektronen und Licht mit optischen Meta-Oberflächen

Verfahren zur Erzeugung und Manipulation von Licht sind essentiell für den technologischen Fortschritt in den verschiedensten Anwendungsbereichen. Heutzutage kann Licht mittels nanophotonischer Strukturen auf sehr kleinen Längenskalen gebündelt und kontrolliert werden. Dies ermöglicht z.B. die Anregung katalytischer Reaktionen, das Einfangen von Sonnenlicht zur Gewinnung elektrischer Energie oder die Umsetzung neuartiger Telekommunikations- und Datenverarbeitungsverfahren. Experimentell stellt die Erforschung der physikalischen Phänomene, die diesen Anwendungen zugrunde liegen, allerdings eine große Herausforderung dar. Letzteres ist auf das optische Beugungslimit zurückzuführen, welches die räumliche Auflösung herkömmlicher optischer Mikroskopie- und Spektroskopietechniken im sichtbaren Spektralbereich auf typischerweise 200 nm bis 300 nm begrenzt. Die Entwicklung immer komplexerer und leistungsfähigerer nanophotonischer Komponenten zur Verarbeitung von Licht ist daher auf alternative experimentelle Ansätze angewiesen, mit Hilfe derer diese Auflösungsgrenze überwunden werden kann.

Seit Ihrer Einführung vor beinahe 100 Jahren hat sich die Elektronenmikroskopie zu einer Schlüsseltechnologie entwickelt, um strukturelle Eigenschaften von Materialien im Längenbereich von wenigen Nanometern oder gar auf atomaren Längenskalen zu untersuchen. Dies geschieht mit Hilfe freier Elektronen, die auf kinetische Energien von typischerweise 5 keV bis 300 keV beschleunigt werden. Ende des letzten Jahrhunderts hat man erkannt, dass sich solche Elektronen außerdem hervorragend eignen, um optische Materialeigenschaften zu untersuchen. Bei diesem Ansatz wird das zeitlich schnell veränderliche elektromagnetische Feld der Elektronen ausgenutzt, um eine Probe lokal zu polarisieren. Die typische Zeitskala, auf der dieser Prozess erfolgt, ermöglicht es, optische Phänomene im gesamten infraroten, sichtbaren und ultravioletten Spektralbereich anzuregen. Infolgedessen erfahren die Elektronen einen spontanen Energieverlust, der mit Hilfe der Elektronenenergieverlustspektroskopie (*electron energy-loss spectroscopy* – EELS) experimentell untersucht werden kann. Ferner kann mittels der Kathodolumineszenzspektroskopie (*cathodoluminescence (spectroscopy)* – CL) die aus diesem Prozess resultierende Emission von Strahlung analysiert werden. Aufgrund der räumlich stark lokalisierten Wechselwirkung zwischen Elektronen, Licht und Materie bieten EELS und CL einzigartige spektroskopische Verfahren zur Untersuchung der optischen Eigenschaften von nanophotonischen Systemen mit einer Auflösung gänzlich unabhängig vom optischen Beugungslimit. Umgekehrt kann eine externe Lichtquelle, wie etwa ein Laser, dazu genutzt werden, das optische Nahfeld einer Nanostruktur anzuregen und damit die Emission und Absorption von Photonen durch das Elektron

zu stimulieren. Die sich daraus ergebende Modulation des Elektronenenergiespektrums liefert ein direktes Maß für die Stärke der Elektronen-Nahfeld-Wechselwirkung, eine Eigenschaft, die ein Verfahren namens photoneninduzierte Nahfeldelektronenmikroskopie (*photon-induced near-field electron microscopy* – PINEM) ermöglicht.

Die Untersuchung der Wechselwirkung zwischen hochenergetischen freien Elektronen, Licht und Materie mit Hilfe von EELS, CL und PINEM hat sich in den letzten Jahren zu einem schnell wachsenden Forschungsgebiet entwickelt. Wissenschaftler auf der ganzen Welt erproben die zahlreichen Möglichkeiten, die moderne Rasterelektronenmikroskope (*scanning electron microscopes* – SEM) und Transmissionselektronenmikroskope (*transmission electron microscopes* – TEM) bieten, um optische Phänomene auf ultrakleinen Längen- und Zeitskalen zu untersuchen und darüber hinaus die Quanteneigenschaften freier Elektronen mit Licht zu steuern, zu manipulieren und nutzbar zu machen. Diese Bestrebungen stehen in engem Zusammenhang mit den jüngsten Fortschritten auf dem Gebiet der Nanophotonik. Insbesondere das rezente Aufkommen nanostrukturierter Materialien mit künstlichen optischen Eigenschaften, den sogenannten Meta-Oberflächen, bietet einzigartiges Potenzial, Kontrolle über die Wechselwirkung freier Elektronen mit strukturierten optischen Feldern zu erlangen. Das Ziel dieser Arbeit besteht darin, grundlegende Schritte zu unternehmen, dieses Potenzial zu erforschen und experimentell zu demonstrieren. Hierzu untersuchen wir die Anwendung von Meta-Oberflächen, um die Erzeugung von Licht mittels freier Elektronen zu beeinflussen und ergründen, wie dieses Konzept wiederum zur Manipulation der Elektronen selbst eingesetzt werden kann.

Zum Einstieg untersuchen wir in Kapitel 2 zunächst die grundlegende Korrelation zwischen der spontanen und der stimulierten Wechselwirkung freier Elektronen mit Licht und Materie. Zu diesem Zweck führen wir räumlich aufgelöste EELS-, CL- und PINEM-Messungen durch, anhand derer wir die Kopplung freier Elektronen und Photonen im optischen Nahfeld eines chemisch synthetisierten Goldnanosterns nachweisen. Letzterer zeichnet sich durch scharfe konische Spitzen mit Krümmungsradien von weniger als 3 nm aus, die hochlokalisierte plasmonische Resonanzen im sichtbaren und nahinfraroten Spektralbereich aufweisen. Die CL-Experimente werden in einem SEM am AMOLF bei einer Elektronenenergie von 20 keV durchgeführt, während die EELS- und PINEM-Experimente bei einer Elektronenenergie von 200 keV in einem ultraschnellen TEM in der Gruppe von Prof. Claus Ropers an der Universität Göttingen durchgeführt werden. Letzteres kann zum Zwecke der PINEM-Messungen im gepulsten Strahlbetrieb mit einem Pumplaser zur optischen Anregung der Probe synchronisiert werden. Anhand der EELS- und CL-Messungen beobachten wir die spontane Kopplung freier Elektronen an eine Reihe von plasmonischen Spitzenresonanzen im sichtbaren und nah-infraroten Spektralbereich, während die PINEM-Messungen eine starke Abhängigkeit der Elektronen-Nahfeld-Wechselwirkung von der Polarisation des optischen Pumpfeldes und dessen spektraler Überlappung mit den Spitzenresonanzen zeigen. Indem wir die gemessenen EELS- und CL-Spektren über eine Bandbreite von 50 meV um die entsprechenden Resonanzenergien integrieren, erhalten wir spontane Elektronenenergieverlust- und Photonenemissionswahrscheinlichkeiten in der Größenordnung von 10^{-4} bzw. 10^{-5}. Die PINEM-Messungen zeigen eine Modulation des Elektronenenergiespektrums durch bis zu drei Energiegewinn-

und -verlustseitenbänder bei einer optischen Pumpfeldintensität von etwa 1 GW/cm^2 und einer Photonenenergie von 1,55 eV. Ergänzt durch Theorie und numerische Simulationen zeigen wir, dass alle drei Arten von Messungen eine gemeinsame räumliche Abhängigkeit von der bipolaren elektrischen Nahfeldverteilung einer resonant angeregten Nanospitze aufweisen. Darüber hinaus demonstrieren wir anhand der Simulationen, dass die Stärke der Elektronen-Nahfeld-Wechselwirkung entscheidend von der Elektronengeschwindigkeit abhängt. Dies ist bestimmt durch die räumlichen Fourier-Transformation des optischen Feldes entlang der Elektronenbahn, woraus sich eine maximale Elektron-Licht-Kopplung ergibt, wenn die Elektronen die Spitze mit vergleichsweise niedrigen kinetischen Energien im Bereich von wenigen Kiloelektronenvolt passieren. Hierdurch manifestiert sich eine grundlegende Bedingung für die Kopplung zwischen freien Elektronen und Licht durch Phasenangleichung, die unabhängig von der stimulierten oder spontanen Natur der Wechselwirkung ist.

In Kapitel 3 nutzen wir die Bedingung zur Kopplung zwischen freien Elektronen und Licht durch Phasenangleichung aus, um zu demonstrieren, dass sich mittels einer Meta-Oberfläche, die von freien Elektronen unter streifendem Einfall angeregt wird, die Erzeugung von Smith-Purcell-Strahlung (SPS) sowohl spektral als auch winkelabhängig steuern lässt. Das Projekt erfolgt in Zusammenarbeit mit den Gruppen von Prof. Ido Kaminer am Technion und Prof. Ady Arie an der Universität von Tel Aviv. Als konkretes Beispiel implementieren wir Metalinsen auf der Basis von aperiodischen Nanogittern, die SPS mit einer konvergierenden (konkaven) oder divergierenden (konvexen) Wellenfront im sichtbaren und nah-infraroten Spektralbereich emittieren. Mit Hilfe eines fokussierten Ionenstrahls fräsen wir die Strukturen in ein mit einem dünnen Goldfilm beschichtetes Siliziumsubstrat, wobei der Gitterabstand über eine Gesamtlänge von 20 µm zwischen 163 nm und 228 nm variiert wird. Die Orientierung der Gitter und damit der Anstieg oder Abfall des Gitterabstands relativ zur Elektronenbahn bestimmt die konkave oder konvexe Krümmung der Emissionswellenfronten. Als Referenz stellen wir zudem ein periodisches Nanogitter mit einem konstanten Gitterabstand von 189 nm her, das konventionelle SPS in Form von ebenen Wellen emittiert. Um die verschiedenen Gittergeometrien zu charakterisieren, führen wir hyperspektrale winkelaufgelöste CL-Messungen im SEM durch, mittels derer wir die Abstrahlcharakteristik der Strukturen im Fernfeld über einen breiten Spektralbereich bestimmen können. Bemerkenswerterweise erreichen wir eine kohärente Wechselwirkung der Elektronen mit den Proben über mehr als 100 Gitterperioden. Bei einer nominellen Wellenlänge von 580 nm ergibt sich daraus die Emission von SPS durch die konvergierenden bzw. die divergierenden Metalinse innerhalb effektiver numerischer Aperturen von $0{,}48 \pm 0{,}05$ bzw. $0{,}45 \pm 0{,}05$. Unsere Messungen sind ergänzt durch numerische Simulationen und ein analytisches Model, welche die Korrelation zwischen den experimentellen Daten und der Fokussierung bzw. Defokussierung von SPS sowie dem zugrunde liegenden Elektronen-Nahfeld-Kopplungsmechanismus verdeutlichen. Aufbauend auf dem Metalinsenkonzept präsentieren wir außerdem numerische Simulationen einer Spaltringresonator- (*split-ring resonator* – SRR) Meta-Oberfläche, die es ermöglicht, SPS zugleich zu fokussieren und deren Polarisation zu kontrollieren, indem die optische Bi-Anisotropie der SRR-Meta-Atome ausgenutzt wird.

In Anbetracht der in Kapitel 2 dargestellten engen Korrelation zwischen der Emission und Absorption von Photonen durch freie Elektronen wird deutlich, dass Meta-Oberflächen zur Manipulation freier Elektronenstrahlung (Kapitel 3) konzeptionell auch umgekehrt eingesetzt werden können, um optische Felder zu strukturieren, die wiederum die Wellenfunktion der Elektronen selbst beeinflussen. In jedweder Hinsicht stellt die Kopplung der Meta-Oberfläche an geeignete optische Komponenten zur Extraktion bzw. Injektion von Strahlung eine substantielle Herausforderung dar. In Kapitel 4 gehen wir diese Herausforderung an, indem wir die Kopplung von freien Elektronen und Licht mittels des SP-Effekts in einem kreisförmigen Metagitter demonstrieren, das auf die Eingangsfacette einer metallbeschichteten optischen Multimoden-Glasfaser aufgebracht ist. Die Struktur erstreckt sich über einen Gesamtdurchmesser von 100 µm bei einem konstanten radialen Gitterabstand von 200 nm. Unter Verwendung des bereits in Kapitel 3 angewandten Verfahrens zur hyperspektralen winkelaufgelösten Detektion von CL messen wir experimentell die Winkeldispersion von SPS, die sowohl in den freien Raum als auch in den Faserkern emittiert wird. Diese Experimente erfolgen bei variablen Elektronenenergien im Bereich von 5 keV bis 30 keV. Im freien Raum beobachten wir die Emission von SPS erster, zweiter und dritter Ordnung im ultravioletten bis nah-infraroten Spektralbereich, deren Winkeldispersion der theoretischen Erwartung entspricht. Bei einer Elektronenenergie von 30 keV ergeben sich SPS-Emissionswahrscheinlichkeiten erster und zweiter Ordnung von $4,7 \cdot 10^{-4}$ bzw. $5,0 \cdot 10^{-5}$ (über eine spektrale Bandbreite ~0,2 eV). SPS, die innerhalb der Faser erzeugt wird und anschließend durch die Mantelschicht der optischen Faser entweicht, zeigt eine modifizierte Winkeldispersion, die durch den Brechungsindex des Faserkerns und der Brechung des Lichts an der Faser-Vakuum-Grenzfläche bestimmt wird. Darüber hinaus zeigt der Nachweis von SPS erster Ordnung mittels eines fasergekoppelten Spektrometers die kohärente Anregung geführter optischer Moden, deren spektrale Verteilung durch die endliche numerische Apertur der Faser bestimmt ist. Des Weiteren messen wir eine breitbandige Verteilung inkohärenter CL, die von Elektronen erzeugt wird, die in die Eingangsfacette der Faser eindringen und unelastisch streuen. Dabei können wir zwischen der Anregung nicht-brückenbildende Sauerstofffehlstellen (*non-bridging oxygen hole centres* – NBOHCs) und Sauerstoffmangelzentren (*oxygen deficient centres* – ODCs) mit mittleren Photonenemissionsenergien von 1,95 eV bzw. 2,80 eV unterscheiden. Außerdem stellen wir fest, dass inkohärente CL, die im ODC-Spektralbereich erzeugt wird, an eine Rayleigh-Anomalie des Metagitters ankoppelt, wodurch eine Fano-Resonanz hervorgerufen wird, die sich mit der Winkeldispersion von SPS zweiter Ordnung bei einer Elektronenenergie von 20 keV überschneidet. Dieses Phänomen zeigt das große Potenzial von Meta-Oberflächen, den SP-Effekt mit resonanten elektromagnetischen Anregungen zu kombinieren, wie z. B. Gitterresonanzen, die von der Meta-Oberfläche unterstützt werden.

Abschließend untersuchen wir in Kapitel 5 die Implementierung eines geeigneten Elektronenenergiespektrometers zur Durchführung von PINEM-Experimenten in einem SEM. In Kombination mit der breiten Palette an spektroskopischen Möglichkeiten zur Detektion von CL, die unser SEM-CL-Instrument bietet, könnten solche Experimente neue grundlegende Einblicke in die Quantennatur der Elektron-Licht-Materie-Wechselwirkung liefern. Insbesondere bieten SEMs den Vorteil, dass sie Zugang zu

nichtrelativistischen Elektronenenergien ermöglichen, bei denen die Elektronen-Licht-Kopplung, wie in Kapitel 2 gezeigt, erheblich verstärkt sein kann. Außerdem weisen SEMs große Probenkammern auf, die reichlich Platz für die Installation experimenteller Infrastruktur bieten. Bislang stehen geeignete Elektronenspektrometer, die eine ausreichenden Auflösung und Empfindlichkeit zur Untersuchung der Wechselwirkung zwischen freien Elektronen und Licht bieten, allerdings hauptsächlich in TEMs zur Verfügung, die mit relativistischen Elektronenenergien von einigen zehn bis hunderten keV arbeiten. In diesem Kapitel demonstrieren wir einen elektrostatischen Feldverzögerungsanalysator (*retarding field analyzer* – RFA), der in ein SEM integriert werden kann, um hochauflösende spektroskopische Messungen bei nichtrelativistischen Elektronenenergien durchzuführen. Wir verwenden zunächst einen RFA, der ursprünglich in der Gruppe von Prof. Pieter Kruit an der Technischen Universität Delft entwickelt wurde, um die Emission eines kontinuierlichen Elektronenstrahls von unserem SEM-CL-Instrument bei einer Elektronenenergie von 5 keV zu untersuchen. Die Messungen ergeben Elektronenenergiespektren mit einer Halbwertsbreite (HWB) von (0,88 ± 0,01) eV bei einem Strahlstrom von 5 pA und (2,98 ± 0,02) eV bei einem Strahlstrom von 8,7 nA. Außerdem führen wir numerische Simulationen durch, die eine Obergrenze für die Energieauflösung der RFAs von 0,1 eV suggerieren. Anschließend führen wir eine modifizierte Version des RFAs ein, die den Betrieb über einen erweiterten Bereich von Elektronenenergien und unter gepulsten Elektronenstrahlbedingungen ermöglicht, wie sie typischerweise bei PINEM-Experimenten eingesetzt werden. Diese Bedingungen werden mittels eines elektrostatischen Strahldeflektors emuliert, der die Erzeugung von Elektronenpulsen mit einer variablen Anzahl von Elektronen und einer Pulsdauer von wenigen hundert Pikosekunden ermöglicht. Der RFA ist mit einem Elektronenzähler auf der Basis eines Timepix 3 CMOS-Chips ausgestattet, der ab einer Elektronenenergie von 10 keV nahezu Einzelelektronenempfindlichkeit aufweist. Bei einer Elektronenpulsrate von 200 kHz und einer Elektronenanzahl von weniger als einem Elektron pro Puls lösen wir Elektronenspektren bei kinetischen Energien zwischen 4 keV und 11 keV auf. Die HWB dieser Spektren reicht von (0,69 ± 0,11) eV bis (1,23 ± 0,03) eV. Oberhalb von 11 keV stellen wir die elektrischen Durchschlagschwelle des RFAs fest, während unterhalb von 4 keV die Empfindlichkeit des Elektronenzählers unzureichend wird. Derzeitige Limitationen des RFAs bezüglich der Aufnahmegeschwindigkeit von Energiespektren, einer hohen Empfindlichkeit gegenüber der Ausrichtung des Elektronenstrahls und der Elektronenzählrate werden festgestellt, welche allesamt durch weitere technische Modifikationen verbessert werden können.

Zusammenfassend demonstriert diese Arbeit das große Potenzial optischer Meta-Oberflächen, das Zusammenspiel von freien Elektronen, Licht und Materie auf der Nanometer-Längenskala zu kontrollieren und umfassend nutzbar zu machen. Wir demonstrieren die fundamentale Korrelation zwischen der spontanen und stimulierten Wechselwirkung freier Elektronen und Photonen, die es erlaubt, komplementäre nanophotonische Systeme einzusetzen, um sowohl Licht zu erzeugen als auch die quantenmechanische Wellenfunktion der Elektronen zu manipulieren. Wir zeigen, wie Nahfeldeffekte in einer Meta-Oberfläche Kontrolle über die spektrale und winkelmäßige Verteilung der von freien Elektronen emittierten Strahlung

ermöglichen, und wir demonstrieren, wie mittels eines Metagitters, das auf die Eingangsfacette einer optischen Faser aufgebracht ist, geführte optische Moden in jener Faser mit freien Elektronen gekoppelt werden können. Schließlich zeigen wir, wie die optische Modulation nicht relativistischer freier Elektronen im SEM mit Hilfe eines elektrostatischen RFAs experimentell untersucht werden kann. In Zukunft könnten die in dieser Arbeit gewonnenen Erkenntnisse den Entwurf komplexer Lichtquellen ermöglichen, die einen extrem breiten Spektralbereich abdecken, neue spektroskopische Verfahren inspirieren, um die Dynamik optischer Phänomene auf ultrakleinen Längen- und Zeitskalen zu erforschen, und schließlich zu einem tiefgreifenderen Verständnis der Wechselwirkung zwischen Elektronen, Licht und Materie beitragen.

Acknowledgements

I can say that writing has not been the easiest part of my PhD, however, there is a big group of people that deserves me to finish this work with a few more words. You are the reason I have come to this point, and I am very grateful for that.

First of all, I want to thank you, **Albert**, for being the best supervisor I could have wished for. The environment you have created has made me grow in many respects. Thank you for the collaborations you have established for me to work with great scientists around the world and to define my PhD. You have given me both the guidance and freedom to discover my scientific interests, and to outlive my passion for building experimental equipment. I highly value the many opportunities you have opened up for me to become part of a vibrant research community at international conferences and workshops. Thank you for your support and patience to teach me handle my biggest challenges such as time management and writing. Moreover, I want to thank you for always being available to provide support and advice, despite your many duties as a group leader. Apart from being an excellent manager, your deep personal care for your team members distinguishes you as a supervisor. You have helped me to get through very tough and sorrowful challenges. The last five years have been a huge enrichment that I will cherish for the rest of my life. Thank you!

Femius, thank you for supporting me as my second supervisor, for helping me with mathematical mysteries, and for your valuable feedback at different stages of my PhD. Furthermore, I want to thank the members of my Doctorate Committee, **Paul**, **Florian**, **Jorik**, **Nahid**, and **Claus**, that have kindly agreed to evaluate my PhD thesis. I sincerely appreciate the time and effort you invest to enable my PhD defense.

Throughout the past five years, I was lucky to work with a lot of different collaborators who have made a deep impact on both my scientific and personal growth. The open culture that these people have created made me feel part of a very unique and pleasant research community. **Claus**, I want to express my deep gratitude for your support in my first project on the nanostars that substantially influenced the remaining course of my PhD, and that introduced me to the intriguing science of PINEM. I very much enjoyed the inspiring and fruitful discussions we had during both my visits in Göttingen and at various other occasions. **Javier**, I want to thank you for introducing me to the theory of free-electron-light-matter interactions and continuously helping me to develop a deeper fundamental understanding of the subject. I much enjoyed my short visit in Barcelona, and I greatly appreciate the opportunities I had to learn from you. **Ido** and **Ady**, thank you for your support and all the enlightening discussions on the Smith-Purcell project, which had a big impact on the direction of my PhD. **Pieter**, thank you for providing me with the RFA and your valuable advice on electron optics. Working with the RFA has been a great joy and deeply strengthened my passion for technical developments. **Shai**, **Dolev**, and **Aviv**, it was a great pleasure collaborating with you. Our wonderful project has been a big source of inspiration. Apart from the science, I often remember the great fun we had during your visit in Amsterdam. Getting to know such

kind and talented people has been a great enrichment. **Murat** and **Armin**, I feel blessed for our collaboration and for being in a continuous exchange with you throughout my PhD. I had a fantastic time together with you on our mutual visits in Göttingen and Amsterdam, and on several conferences, including the latest IMC20 in Seoul. Working on the UTEM and accompanying you in the lab was an invaluable experience that I will certainly remember as one of the most enjoyable parts of my academic journey. **Hugo**, you are gifted with the skill of reducing the theory to its essentials in such an elegant way. I greatly enjoyed the time we spent together at the NFO16 in Canada last year. Also, thanks a lot for giving me the opportunity to speak at the IMC20 in Seoul this year. This was an absolute highlight to conclude my PhD. **Ramon** and **Nicolas**, I want to thank you for being so openly willing to provide me with many different nanoparticles that have made the nanostars project possible.

Along with my collaborators, there is a large group of people that have accompanied me within AMOLF. These people have not only had a great impact on my work, but also made my time there so enjoyable. First of all, I want to thank the members of the **Photonic Materials** team, present and former. You are the best group I could have wished to be a part of with an outstanding sense of cohesion and mutual support. **Sophie**, in less than three months you thought me everything on using the SEM to perform the most complex CL experiments that laid the foundation for the success of this thesis. Your passion for working with electron microscopes and pushing their boundaries was very inspiring, a spirit that I tried to uphold after you left. Also, thanks for providing me with probably the best Oma-fiets I ever had, seemingly going by itself. **Nika**, I have very much enjoyed being your colleague from the moment you have joined the group. I admire your happy, open, and truly honest nature that has cheered me up many times. We have spent countless hours together in the lab and often enough we had to deal with unexpected issues. Nevertheless, we have never given up and I'm very grateful that you were my lab partner. Also, I'm glad about the many occasions to do fun things outside the lab such as having drinks at the *Brouwerij*, having dinner with the team, going out for hikes or celebrating *King's Day*. You are certainly a key driver of the great spirit in our group that I will greatly miss once it's time to leave. **Stefan**, starting my PhD with you and having you as my officemate was great fun, and I missed your company during your time in Australia. Luckily, you returned for us to have more beers and burritos, tuning up Cher's '*Believe*' in the office, going to the cinema, and having many great conversations. **Andrea**, thank you for organizing so many events with the group, various occasions to have Italian food, and getting drinks at the *Biertuin*. I will not forget the great time we had in Sicily, walking into your office to joke around, and always share a room with you at conferences. **Tom**, beyond being the most organized guy in the group you are a wonderful colleague to have. I admire your helpfulness, your great support with all kinds of technical stuff, and I very much enjoyed our shared passion for Apple screens and riding the electric car to Veldhoven. **Evelijn**, your concerts have been amazing and I hope to attend more of them in the future. Your dedication to organizing social events in the group and as a member of the PV is a blessing, and I admire your skill of combining work with all the other important aspects of life. **Magda**, I had a great time sharing the office with you and doing experiments together. Also, thank you for various habits you brought into my everyday routine, such as bringing kiwis

to AMOLF, rice crackers and a tooth brush :D. **Robin**, I much enjoyed your talent for classical music, practising my Dutch, and hearing you play the drum set on your phone to tune in with Mozart. **Hollie**, thank you for giving me a taste of the British culture, having English tea with you, and your great support in the lab. **Hannah**, advancing the RFA with you was great fun and I much appreciate your creativity. **Nick S.**, thank you for introducing me to coherent CL and helping me with its theoretical challenges. This strongly influenced the direction my PhD. Sitting on the roof-top terrace of your apartment and enjoying sum drinks in the sunset is a great memory to have, and I hope you get to enjoy more of that in Brazil! **Kelly**, your expertise on electronics was impressive and I had a lot of fun with you automizing measurements in the lab, while enjoying your American sense of humor. **Saskia**, thank you for the good time in the office, in the lab, and in Strasbourg! Further, I want to thank **Verena**, **Floris**, **Daphne**, **Kyra**, **Heleen**, and **Marnix** for the great time we shared together in the group. I'm also grateful for the close link between Delmic and the group. **Toon**, thank you for all your support with the CL setup and your advice on many of my experiments. Your role at Delmic has been a great inspiration to me from the beginning. Moreover, thank you **Éric** for your indispensable support in troubleshooting.

Aside from the Photonic materials group there is an entire team of LMPV and Nanophotonics that I want to thank for forming such a pleasant atmosphere within AMOLF. I very much enjoyed chatting with you during the coffee break, at the coffee corner, in the SEM lab, and occasionally in the cleanroom. To name just a few, I want to thank **Esther**, **Wiebke**, **Said**, **Bruno**, **Erik**, **Ewold**, **Falco**, **Deba**, **Nelson**, **Nick F.**, **Alex**, **Melanie**, **Yorick**, **Imme**, **Jeroen**, **Moritz**, **Elaina**, **Linde**, **Nikolai**, **Hongyu**, **Susan**, **Sarah**, **René**, **Jesse**, **Jente**, **Roel**, **Giel**, **Kevin**, **Mees**, **Patrick**, **Franscesca**, and **Eithan**.

Another aspect that made my time at AMOLF so joyful and productive is the outstanding technical support. Allereerst wil ik **Dion** bedanken voor het begeleiden en ondersteunen van mij bijna elke dag tijdens het werken met de RFA en bij verschillende andere gelegenheden. Je hebt een groot talent voor het bedenken van oplossingen voor de verschillende problemen die zich regelmatig voordoen in het lab. Je bent een onschatbare partner geweest in deze reis en ik heb echt genoten van de tijd die we samen hebben doorgebracht. Verder wil ik **Hinco** en **Niels** bedanken dat ze er altijd voor me waren als Dion er niet was en dat ik me altijd welkom voelde om af en toe een van jullie kantoorgenoten te zijn. Vervolgens wil ik mijn grote dank uitspreken aan **Max** die veel tijd heeft gestoken in het helpen ontwikkelen van een geheel nieuwe versie van de RFA. Jouw creativiteit in het ontwerpen van oplossingen was de sleutel in deze onderneming en ook jouw gevoel voor het vinden van een goede balans tussen de tijd en moeite die het kost om het te implementeren. In dat verband gaat er nog een grote dank uit naar het hele team van de Precision-Manufacturing-werkplaats die de verschillende onderdelen van de RFA met de grootste perfectie hebben gebouwd en die altijd klaarstonden om me te helpen dingen in een mum van tijd te repareren. Bedankt voor al jullie inspanningen **Jan**, **Mark**, **Niels**, **Wouter**, **Menno**, **Wessel**, **Ricardo** en **Olaf**. Next, I want to thank the entire Nanocenter team. **Hans**, it has been a great pleasure working with you. You taught me a lot about electron microscopy, and the many aspects of electronics and high-voltage engineering. Thank you for building up the RFA from the Tupperware box it came in, and the many times I could pop-up in your

office to ask for your advice. **Bob D.**, **Igor**, **Dylan**, and formerly **Dimitri**, you guys create a fantastic atmosphere both within the lab and at AMOLF. Your dedication to solving experimental challenges is exceptional, and it was always very enjoyable to work with you, even sweating for 90 minutes in an HF protection suit. Furthermore, I want to thank the Electronics Engineering department. In particular, I want to express my gratitude to **Bob K.** who helped me developing all the electronics to operate the RFA. I happily remember the high-voltage tests we did together, playing with the new oscilloscope, and looking for various electronic components in the hidden storages around AMOLF. Also, I want to thank **Mels** and **Duncan** for their valuable support. Not to forget, a big thanks to all the support people at ICT, finance, inkoop, facilities, reception, library, secretarial office, and human resources.

The endurance it took me to deal with the challenges of my PhD and those life had to offer otherwise is routed in the friends and family that have supported me at all times. After living on my own for more than a year, I was lucky to get to share an apartment with **Ruslan**, **Remmert**, and later with **Tim**. Samenwonen met jullie, 's avonds koken, eten, series kijken, en wandelen door het Vondelpark is een enorme verrijking die ik heel erg koester. Ik wil jullie bedanken dat jullie me Amsterdam echt hebt laten ervaren en waarderen als mijn nieuwe thuis. Back home in Germany, I'm glad to count on my dearest friends who made it really hard for me to leave in the first place. Danke **Christoph** und **Sophia**, dass Ihr mich so oft in Amsterdam besucht habt, für die gemeinsamen Urlaube, für die Zeit auf dem Hof, im Vitasol, und bei Euch in Köln. Danke **Peter** und **Timo** für die beste Studienzeit die ich mir hätte wünschen können und danke „**Adrian**" und **Bene**, dass wir trotz räumlicher Distanz schon so viele Jahre befreundet sind. **Jan** und **Verena**, ich bin Euch sehr dankbar, dass Ihr mich als Teil der Familie aufgenommen habt, dass Ihr Bonn für mich zu einem zu Hause macht, und dass ihr mir viele schwere Momente sehr erleichtert habt. Ihr seid mir eine unersetzliche Stütze. Das Gefühl von zu Hause kommt auch durch Euch, **Mientje**, **Yasper**, **Jelte**, **Johannes**, **Lena** und **Anna**. Ich freue mich jedes Mal auf Programm, Profi-Talk, Chili-Tastings, und Fahrradreperaturen im Wohnzimmer.

Als nächstes möchte ich Dir, **Anne**, für unseren Zusammenhalt danken, für die gemeinsamen Urlaube mit Mama und Rienne, Deine Besuche in Amsterdam, Deine mentale Unterstützung und Deinen kulturellen Einfluss ;). Ich bin sehr froh, Dich als meine Schwester zu haben. **Mama** und **Papa**, danke, dass ihr mir alle Möglichkeiten geschaffen habt mich dorthin zu entwickeln, wo ich jetzt stehe. **Mama**, danke, dass Du mich immer bestärkt hast meine Ziele zu verfolgen, einen so großen Wert auf unser gemeinsames zu Hause legst und mich häufig aufgebaut hast, wenn ich gezweifelt habe. Ich bin froh, dass wir viele Herausforderungen gemeinsam bewältigt haben. **Papa**, neben dieser Arbeit gibt es noch so viel mehr in meinem Leben, dass ich wünschte mit Dir teilen zu können. Du bist mir eine große Motivation und ich vermisse Dich sehr.

Abschließend danke ich meiner Freundin **Rienne**, die mich die ganze Zeit über begleitet hat und ohne deren Unterstützung, Verständnis und Geduld diese Arbeit nicht möglich gewesen wäre. Danke, dass Du die Herausforderung einer Fernbeziehung mit mir aufgenommen hast und dabei Ordnung in meine chaotische Planung gebracht hast. Danke, dass ich mich so bedingungslos auf Dich verlassen kann und dass Du mir so viele schöne Aspekte des Lebens eröffnet hast.

About the author

Matthias Liebtrau was born on October 11, 1993 in Cologne (Germany) where he grew up and obtained a high-school diploma from Gymnasium Rodenkirchen in 2012. Shortly after, he moved to Bonn to study physics at the University of Bonn. In 2016, he graduated with a Bachelor's thesis about the experimental characterisation of a charged particle detector, sparking his passion for electronic instrumentation. Afterwards, he continued his studies in Bonn with a Master's program in experimental physics, a part of which he spent abroad at Uppsala University in Sweden. The courses he attended in Uppsala raised his interest in the field of optics and nanophotonics. This inspired him to dedicate his Master's thesis to studying the propagation of light in nanoscale plasmonic slot waveguides using interferometric scanning near-field optical microscopy (SNOM). After graduating from the University of Bonn in 2018, he moved to Amsterdam to join the group of prof. dr. A. Polman at NWO-Institute AMOLF as a Ph.D. student. His research focused on the experimental study of the interaction between free electrons, light, and matter using cathodoluminescence (CL) spectroscopy and photon-induced near-field electron microscopy (PINEM). The results of his work are shown in this thesis. In his free time, he enjoys riding bikes and travelling on the tandem with his girlfriend, hiking, cooking, playing the guitar, and spending time with friends. Furthermore, he is very much interested in aviation and holds a private pilot licence for glider planes since 2010.

Errata: Shaping the interplay of free electrons and light with optical metasurfaces

Matthias Liebtrau

September 15, 2024

This document lists all changes with respect to the original printed booklet of the Ph.D. thesis '*Shaping the interplay of free electrons and light*' by M. Liebtrau that was defended at the University of Amsterdam on November 9, 2023. The original text is written in *black-italic font* with corrections marked in green font. Typos and errors are marked in red-font and as strike-through text. All edits are listed in order of appearance.

- **Preamble:**

1. Added European Research Council (ERC) as funding source under the European Union's research and innovation programme (Grant agreements No. 695343 (SCEON), No. 101017720 (eBEAM) and No. 101019932 (QEWS)).

- **Chapter 1 Introduction:**

2. Correction in Fig. 1.1 on p. 2: Slightly adjusted placement of logarithmic photon energy scale and replaced 10^{11} on the bottom wavelength scale was by 10^{10}.

3. Typo on p. 5: *"While a photon in free space cannot exchange energy with an electron due to a violation of momentum ~~conversation~~conservation, (…)"*

4. **Chapter 2.2 EELS, CL, and PINEM theory:**

5. Clarified notation of the integral term in Eqs. (2.1) and (2.2) on p. 12 and Eq. (2.4) on p. 13:

$$\left| \int_{-\infty}^{\infty} \mathrm{d}z \, u_z(\mathbf{R}, z, \omega) \, e^{-i\frac{\omega}{v}z} \right|^2$$

6. Typo on p. 12: "*The exponential term in the integral governing both Eqs. (2.1) and (2.2) describes the temporal phase oscillation of the field as the electron passes by the tip apex at a constant velocity v (time-position relation $t = ~~v/z~~z/v$).*"

7. Typo on p. 12: "*As a result, Γ_{EELS} and Γ_{CL} depend only on the Fourier transformation of u_z at an electron-velocity-dependent spatial frequency $q = \omega/v$.*"

8. Typo on p. 14: *"Figure 2.2~~c~~b shows the CL spectra acquired at approximately the same five positions."*

9. Typo on p. 20: *"The characteristic decay lengths are found to be* $\delta_{\text{CLEELS}} = (8.7 \pm 0.3)$ *nm,* $\delta_{\text{EELSCL}} = (10.5 \pm 0.2)$ *nm, and* $\delta_{\text{PINEM}} = (15.2 \pm 0.2)$ *nm."*

10. Typo on p. 23: *"As an example, the inset shows* $|\beta|^2$*, as a function of q for an impact parameter of d = 3 nm."*

- **Chapter 3.2 Metalens theory:**

11. Correction in Fig. 3.1 on p. 33: Cartoons in panels **a** and **b** have been swapped in accordance with the corresponding near-field simulations in panels **c** and **d** as well as the description in the main text and the figure caption.

- **Chapter 3.3 Sample fabrication and experimental setup**

12. Typo on p. 35: *"Subsequently, the raw experimental data were corrected for the collection solid angle and the spectral system response, as described in Section S10*~~10~~*8 of the Supplementary Information."*

13. Correction in the caption of Fig. 3.3 on p. 36: *"A 3.3 nA, 30-keV electron beam passes through a* ~~4~~*600 µm hole at the top of a parabolic mirror that is carved into a solid block of aluminium."*

14. Typo in the caption of Fig. 3.3 on p. 36: *"(…) (conversion between y and θ, as detailed in the Supplementary Information, Section* ~~10~~*S8)."*

- **Chapter 3.7 Supplementary Information:**

S1 Ray-optics model of the metalens:

15. Correction in Eq. (S1.2) on p. 42:

$$\theta(z) = \approx \mp \pm \frac{\lambda}{\lambda_0}\frac{z}{f} + - \left(1 - \frac{\lambda}{\lambda_0}\right)\beta^{-1} = \mp \pm \frac{z}{\tilde{f}(\lambda)} + - \Delta\theta(\lambda)$$

S2 Wave-optics model of the metalens:

16. Typo on p. 43: *"The probability for a point-like free electron of kinetic energy* E_0 *to excite this system at frequency* ω *and thus suffer a corresponding energy loss* $\hbar\omega_0 \ll E_0$ *can be written as [71] (…)"*

17. Typos in Eq. (S2.3) on p. 44:

$$\mathbf{u}_{\mathbf{k}}(\mathbf{r}) = \begin{cases} \sum_m \mathbf{A}_{\mathbf{k},m} e^{i\left(\sqrt{k^2-k_y^2-\left(k_z+\frac{2\pi}{\Lambda}m\right)^2}\,x+k_y y+\left(k_z+\frac{2\pi}{\Lambda}m\right)z\right)}, & \text{grating,} \\ \sum_m \mathbf{A}_{\mathbf{k},m} e^{i\left(\sqrt{k^2-k_y^2-\left(k_z+\frac{2\pi}{\Lambda(z)}m\right)^2}\,x+k_y y+k_z z+m\int_0^z \mathrm{d}z'\frac{2\pi}{\Lambda(z')}\right)}, & \text{metalenses} \end{cases}$$

18. Typo in Eq. (S2.5) on p. 45:

$$\frac{d^2 p_{\mathrm{rad}}}{d\Omega d\lambda} \propto \left|\mathbf{A}_{k_0\hat{\mathbf{n}},0}\right|^2 \left|\mathbf{A}_{k_0\hat{\mathbf{n}},1}\cdot\hat{\mathbf{z}}\right|^2 \cdot \begin{cases} \left|\int_{-\infty}^{\infty} \mathrm{d}z e^{-\kappa x_0(z)} e^{ik_0\left(\cos\Theta-\beta^{-1}+\frac{\lambda}{\Lambda}\right)z}\right|^2, & \text{grating,} \\ \left|\int_{-\infty}^{\infty} \mathrm{d}z e^{-\kappa x_0(z)} e^{ik_0\left(\cos\Theta z-\beta^{-1}z+\int_0^z \mathrm{d}z'\frac{2\pi}{\Lambda(z')}\right)}\right|^2, & \text{metalenses} \end{cases}$$

19. Typo in Eq. (S2.6) on p. 46:

$$\int_0^z \mathrm{d}z' \frac{2\pi}{\Lambda(z')} = \frac{2\pi}{\lambda_0}\int_0^z \mathrm{d}z' \left(\beta^{-1} \pm \frac{z'}{\sqrt{z'^2+f^2}}\right) = \frac{2\pi}{\lambda_0}\left(\beta^{-1}z \pm \sqrt{z^2+f^2}\right)$$

20. Correction in Fig. S3.3 on p. 49: Labels for differential photon emission probability on the top and the right-hand side of the figure were corrected by replacing $\mathrm{d}\omega$ in the denominator by $\mathrm{d}\lambda$, i.e., $\mathrm{d}p/(\mathrm{d}\Omega\mathrm{d}~~\lambda)$.

S4 Numerical FDTD Simulations:

21. Typo in Eq. (S4.2) on p. 48:

$$~~\mathbf{j}~~\mathbf{d}(\mathbf{r},\omega) = \mathbf{d}(\omega)\delta\left(\mathbf{r}_\perp - \mathbf{r}_{\perp,0}\right)\delta(z-z_0)e^{i\frac{\omega}{v}z_0}$$

22. Correction in Eq. (S4.3) on p. 50:

$$\mathbf{j}(\mathbf{r},\omega) = d(\omega)\hat{\mathbf{z}}~~e~~\delta\left(\mathbf{r}_\perp - \mathbf{r}_{\perp,0}\right)\sum_n e^{i\frac{\omega}{v}z_n}\delta(z-z_n)$$

S5 SPR excitation efficiency:

23. Typo on p. 50: *"By integrating over the corresponding spectra, we extract radiation efficiencies of $2.3\cdot10^{-3}$ and $2.4\cdot10^{-~~4~~3}$ for the periodic grating and the converging metalens, respectively, in good agreement with the values predicted in ref. [175]."*

S8 Spectral and angular system response calibration

24. Typo on p. 53: *"In addition, the hole for electron beam transmission provides a useful reference for upwards emission at an angle θ = 90°."*

25. Addition to Eq. (S8.2) on p. 53: *"Eventually, the calibrated data were normalized to the collection solid angle using an expression of the form*

$$\mathrm{d}\Omega_{\mathrm{n}} = A\frac{2az_n^2 - x_n}{(x_n^2 + z_n^2)^{\frac{3}{2}}},$$

with A a system-dependent constant and $x_n = az_n^2 - (4a)^{-1}$."

26. Typo in Eq. (S8.3) on p. 54:

$$\Delta\theta_n = \frac{a + \frac{1}{4az_n^2}}{1 + \left(az_{0n} - \frac{1}{4az_n}\right)^2}\Delta z = \frac{2az_n + \cot\theta_n}{1 + \cot^2\theta_n}\frac{\Delta z}{z_n}$$

- **Chapter 3.8 Appendix: Green's function formalism of the metalens:**

27. Typo in Eq. (A1) on p. 55:

$$\boldsymbol{\mathcal{E}}_\infty(r\hat{\mathbf{n}},\omega) = -\frac{ik_0}{2\pi}\hat{\mathbf{n}}\cdot\hat{\boldsymbol{\sigma}}\frac{e^{ik_0 r}}{r}\int \mathrm{d}^2\mathbf{s}\, e^{-ik_0\hat{\mathbf{n}}\cdot\hat{\boldsymbol{\sigma}}\mathbf{s}}\boldsymbol{\mathcal{E}}(\mathbf{s},\omega)$$

28. Typo in Eq. (A2) on p. 55:

$$\boldsymbol{\mathcal{E}}(\mathbf{sr},\omega) = i\omega\mu_0\int \mathrm{d}^3\mathbf{r}'\overleftrightarrow{\mathbf{G}}(\mathbf{r},\mathbf{r}',\omega)\cdot\mathbf{j}(\mathbf{r}',\omega)$$

29. Typos on p. 55: *"To derive an analytical form of $\overleftrightarrow{\mathbf{G}}(\mathbf{r},\mathbf{r}',\omega)$, we introduce a set of normal modes $\mathbf{u}_\mathbf{k}(\mathbf{r})$ with mode index $\mathbf{k}$ and eigenfrequencies $\omega_\mathbf{k}$ that satisfy the wave equation $\boldsymbol{\nabla}\times\boldsymbol{\nabla}\times\mathbf{u}_\mathbf{k}(\mathbf{r}) - \frac{\omega_\mathbf{k}^2}{c^2}\mathbf{u}_\mathbf{k}(\mathbf{r}) = 0$ as well as the orthogonality relation $\int \mathrm{d}^3\mathbf{r}\,\mathbf{u}_\mathbf{k}(\mathbf{r})\cdot\mathbf{u}^*_{\mathbf{k}'}(\mathbf{r}) = \delta_{\mathbf{k}\mathbf{k}'}$ [12]."*

30. Correction in Eq. (A4) on p. 55:

$$\begin{aligned}
\overleftrightarrow{\mathbf{G}}(\mathbf{r},\mathbf{r}',\omega) &= c^2\int\frac{\mathrm{d}^3\mathbf{k}}{(2\pi)^3}\frac{\mathbf{u}_{k\hat{\mathbf{k}}}(\mathbf{r})\otimes\mathbf{u}^*_{k\hat{\mathbf{k}}}(\mathbf{r}')}{\omega_{k\hat{\mathbf{k}}}^2 - \omega^2}\\
&= \frac{c^2}{8\pi^3}\int\mathrm{d}\Omega\int\mathrm{d}k\,\frac{k^2}{2\omega_{k\hat{\mathbf{k}}}}\left(\frac{1}{\omega_{k\hat{\mathbf{k}}} - (\omega + i\gamma)} + \frac{1}{\omega_{k\hat{\mathbf{k}}} + (\omega + i\gamma)}\right)\mathbf{u}_{k\hat{\mathbf{k}}}(\mathbf{r})\otimes\mathbf{u}^*_{k\hat{\mathbf{k}}}(\mathbf{r}')\\
&= \frac{1}{16\pi^3}\int\mathrm{d}\Omega\int\mathrm{d}k k\left(\frac{1}{k - \frac{1}{c}(\omega + i\gamma)} + \frac{1}{k + \frac{1}{c}(\omega + i\gamma)}\right)\mathbf{u}_{k\hat{\mathbf{k}}}(\mathbf{r})\otimes\mathbf{u}^*_{k\hat{\mathbf{k}}}(\mathbf{r}')
\end{aligned}$$

$$= \frac{i\omega}{8\pi^2 c} \int \mathrm{d}\Omega\, \mathbf{u}_{\frac{\omega}{c}\hat{\mathbf{k}}}(\mathbf{r}) \otimes \mathbf{u}^*_{\frac{\omega}{c}\hat{\mathbf{k}}}(\mathbf{r}')$$

31. Follow-up correction and typo in Eq. (A5) on p. 56:

$$\boldsymbol{\mathcal{E}}(\mathbf{sr}, \omega) = -\frac{\omega^2 \mu_0}{8\pi^2 c} \int \mathrm{d}\Omega\, \mathbf{u}_{\frac{\omega}{c}\hat{\mathbf{k}}}(\mathbf{r}) \left(\int \mathrm{d}^3\mathbf{r}' \mathbf{u}^*_{\frac{\omega}{c}\hat{\mathbf{k}}}(\mathbf{r}') \cdot \mathbf{j}(\mathbf{r}', \omega) \right)$$
$$= -\frac{\omega^2 \mu_0}{8\pi^2 c} e \int \mathrm{d}\Omega\, \mathbf{u}_{\frac{\omega}{c}\hat{\mathbf{k}}}(\mathbf{r}) \left(\int \mathrm{d}z' \int \mathrm{d}^2\mathbf{r}'_\perp \mathbf{u}^*_{\frac{\omega}{c}\hat{\mathbf{k}}}(\mathbf{r}'_\perp, z') \cdot \hat{\mathbf{z}}\, \delta(\mathbf{r}'_\perp - \mathbf{r}_{\perp,0})\, e^{i\frac{\omega}{v}z'} \right)$$

32. Follow-up correction in Eq. (A6) on p. 56:

$$\boldsymbol{\mathcal{E}}_\infty(r\hat{\mathbf{n}}, \omega) = \frac{ie\mu_0 \omega^{\cancel{2}3}}{16\pi^3 c^2} \frac{e^{i\frac{\omega}{c}r}}{r} \int \mathrm{d}\Omega \left(\int \mathrm{d}z\, \mathbf{u}_{\frac{\omega}{c}\hat{\mathbf{k}}}(\mathbf{r}_{\perp,0}, z) \cdot \hat{\mathbf{z}}\, e^{-i\frac{\omega}{v}z} \right)^* \int \mathrm{d}^2\mathbf{s}\, \mathbf{u}_{\frac{\omega}{c}\hat{\mathbf{k}}}(\mathbf{s})$$

33. Correction in Eq. (A7) on p. 56:

$$\int \mathrm{d}^2\mathbf{s}\, \mathbf{u}_{\frac{\omega}{c}\hat{\mathbf{k}}}(\mathbf{s}) = \int \mathrm{d}^2\mathbf{s}\, \mathbf{A}_{\frac{\omega}{c}\hat{\mathbf{k}},0} e^{i\frac{\omega}{c}\hat{\mathbf{k}}\cdot\mathbf{s}} = 4\pi^2 \frac{c^2}{\omega^2} \mathbf{A}_{\frac{\omega}{c}\hat{\mathbf{k}},0} \delta\big(\hat{\mathbf{k}} \cancel{-} \mathbf{s} - (\hat{\mathbf{k}} \cdot \hat{\boldsymbol{\sigma}})\hat{\boldsymbol{\sigma}}\big)$$

34. Typo on p. 56: *"Inserting the result back into Eq. (A4) and integrating over all possible orientations of* $\hat{\mathbf{k}}$*, it follows that* $\hat{\mathbf{k}} \cancel{\perp} \parallel \hat{\boldsymbol{\sigma}} = \hat{\mathbf{n}}$*."*

35. Follow-up correction and typo in Eq. (A8) on p. 56:

$$\boldsymbol{\mathcal{E}}_\infty(r\hat{\mathbf{n}}, \omega) = \frac{ie\mu_0 \omega^{\cancel{2}}}{4\pi \cancel{c}} \frac{e^{i\frac{\omega}{c}r}}{r} \mathbf{A}_{\frac{\omega}{c}\hat{\mathbf{n}},0} \left(\int \mathrm{d}z\, \mathbf{u}_{\frac{\omega}{c}\hat{\mathbf{k}}\hat{\mathbf{n}}}(\mathbf{r}_{\perp,0}, z) \cdot \hat{\mathbf{z}}\, e^{-i\frac{\omega}{v}z} \right)^*$$

36. Follow-up correction and typo in Eq. (A9) on p. 56:

$$\frac{\mathrm{d}^2 p}{\mathrm{d}\Omega \mathrm{d}\omega} = \alpha \frac{\omega^{\cancel{3}}}{4\pi^2 c^{\cancel{4}2}} \left| \mathbf{A}_{\frac{\omega}{c}\hat{\mathbf{n}},0} \right|^2 \left| \int \mathrm{d}z\, \mathbf{u}_{\frac{\omega}{c}\hat{\mathbf{k}}\hat{\mathbf{n}}}(\mathbf{r}_{\perp,0}, z) \cdot \hat{\mathbf{z}}\, e^{-i\frac{\omega}{v}z} \right|^2$$

37. Follow-up correction and typo in Eq. (A10) on p. 56:

$$\frac{\mathrm{d}^2 p}{\mathrm{d}\Omega \mathrm{d}\lambda} = \left| \frac{\mathrm{d}\omega}{\mathrm{d}\lambda} \right| \frac{\mathrm{d}^2 P}{\mathrm{d}\Omega \mathrm{d}\cancel{\lambda}\omega} = \frac{\alpha \cancel{4\pi^2}}{\lambda^{\cancel{5}3}} \left| \mathbf{A}_{k_0\hat{\mathbf{n}},0} \right|^2 \left| \int \mathrm{d}z\, \mathbf{u}_{k_0\hat{\mathbf{k}}\hat{\mathbf{n}}}(\mathbf{r}_{\perp,0}, z) \cdot \hat{\mathbf{z}}\, e^{-i\frac{\omega}{v}z} \right|^2$$

- **Chapter 4.1 Introduction:**

38. Addition on p. 58: *"On the one hand, the evanescent electromagnetic field of the electron itself can drive optical material excitations across a broad spectral range from the extreme ultraviolet (XUV) to the far infrared (IR) [28, 31]."*

39. Correction in Eq. (4.1) on p. 59 (in accordance with the expression used in the data analysis and plotted in Figs. 4.2, 4.3 and 4.4): *"(…) the angular dispersion of this radiation can be written as [107]*

$$\omega(\theta) = 2\pi c \frac{m}{p} (\beta^{-1} \cancel{=} + n \sin\theta)^{-1},$$

with ω the frequency, $\beta = ~~\omega~~v/c$ the electron velocity in units of the speed of light c in vacuum, θ the emission angle, and n the refractive index of the surrounding medium."

- **Chapter 4.2 Sample preparation and experimental setup**

40. Correction on p. 60: *"The coating consists of a ~~10~~5-nm thick Cr adhesion layer and a 4~~0~~5-nm thick Au film that are applied by sputter deposition (EM ACE600, Leica, Inc.)."*

- **Chapter 4.3 Coherent and incoherent signal contributions:**

41. Typo on p. 62: *"As shown by the red-dashed curves, the data are in good agreement with the theoretical dispersion relation predicted by Eq. (4.1) for n = 1.0, m = 1, 2 and p = 198.0 nm."*

42. Correction in Eq. (4.2) on p. 62 (in accordance with the expression used in the data analysis and plotted in Figs. 4.2, 4.3, 4.4 and 4.5):

$$\omega(\theta) = 2\pi c \frac{m}{p}\left(\beta^{-1} ~~-~~ + \sqrt{n^2 - ~~\sin~~\cos^2\theta}\right)^{-1}$$

43. Typo on p. 62: *"The resulting dispersion curve is in excellent agreement with the data for n = 1.46, m = 1, 2 and p = 198.0 nm (red-dashed line)."*

- **Chapter 4.4 Analytical signal modelling**

44. Typo on p. 64: *"The leading term in this expression describes an exponential decay of the signal strength with the grazing distance d, where $\kappa = \frac{\omega}{c}\sqrt{\beta^{-2} - n^{~~-~~2}}$ is the frequency-dependent decay constant."*

45. Typo on p. 65: *"The SP dispersion relation enters both terms through the parameter $\phi = \frac{\omega}{c}(n\sin\theta + \beta^{-1})p$ which we alternatively write as $\phi = \frac{\omega}{c}\left(\sqrt{n^2 - ~~\sin~~\cos^2\theta} + \beta^{-1}\right)p$ to take into account the refraction of SPR at the fiber/vacuum interface (cf. Eq. (4.2) for θ < 90°)."*

46. Correction on p. 65: *"Therefore, we estimate an effective N_m to describe the signal of each SP order separately, while assuming a fixed constant distance of d = ~~25~~10 nm."*

47. Correction of Eq. (4.6) on p. 65 (in accordance with the expression used in the data analysis and plotted in Fig. 4.2): *"The NBOHC and the ODC bands are modelled as a superposition of two exponentially-modified Gaussian distributions given by*

$$G_i(\omega) = \frac{A_i}{2}\exp\left(~~\alpha_i^2\Gamma_i^2~~ + \alpha_i\hbar(\omega - \omega_i)\right)~~\exp~~\mathrm{erfc}\left(\frac{1}{\sqrt{2}\sigma_i}\left(\alpha_i~~\Gamma~~\sigma_i^2 + ~~\Gamma_i~~\hbar(\omega - \omega_i)\right)\right),$$

where $\mathrm{erfc}(x)$ *denotes the complementary error function,* A_i *is the amplitude,* $\Gamma_i = 2\sqrt{2\ln 2}\sigma_i$ *is the linewidth,* α_i *is the asymmetry parameter, and* $\hbar\omega_i$ *is the mean photon emission energy of defect* i.

48. Addition on p. 65: *"The orange curve in Fig. 4.2b shows a least-squares fit of the full model to the spectrum at* $\theta \approx 66°$*, assuming* $n = 1.46$*,* $m = 1$*, 2 and* $p = 198.0$ *nm."*

49. Addition on p. 66: "The curves are based on the same assumptions for the parameters n, m, p, d, N_1, and N_2 as specified above, while all the remaining parameters are fitted separately."

- **Chapter 4.5 Free-electron light coupling via the metagrating:**

50. Correction on p. 66: *"In six consecutive measurements, the electron energy is lowered from 30 keV to 5 keV, corresponding to a reduction of the electron velocity from* $\beta \approx 0.3$~~2~~*3 to* $\beta \approx 0.1$~~3~~*4."*

51. Typo on p. 66: *"To this end, a constant grating pitch p is chosen between 198.*~~5~~*0 nm and 199.0 nm, assuming a small error margin of* $\Delta p = 1$ *nm."*

52. Typo in the caption of Fig. 4.3 on p. 67: *"The curves are derived assuming grating pitches p between 198.*~~5~~*0 nm and 199.0 nm."*

53. Correction on p. 68: *"However, up to a maximum velocity of* $\beta \approx 0.$ *0.3*~~2~~*3 as reached in our experiments, this probability and its variation with the electron energy is predicted to be comparatively small [175]."*

54. Correction in the caption of Fig. 4.5 on p. 71: *"**b** Analytical calculation of the spectral and angular distribution of first-order SPR that is generated on the fibre-core side of the metagrating at an electron energy of 20 keV (Eq. (4.4) with* N_1 *=* ~~8~~*60,* p *= 200 nm,* $n = 1.46$*, and* d *=* ~~25~~*10 nm)."*

55. Correction in the caption of Fig. 4.5 on p. 71: *"Light inside the fibre that is emitted under sufficiently large angles penetrates through the cladding layer and* ~~*diffracts*~~*refracts at the fibre/vacuum interface. The remaining waves undergo total internal* ~~*refraction*~~*reflection at the core/cladding interface, thereby coupling to guided optical modes."*

- **Chapter 4.7 Appendix: Analytical derivation of the SPR signal:**

56. Typo on p. 74: *"The parameter* $\kappa \approx \frac{\omega}{c}\sqrt{\beta^{-1^2} - n^2}$ *describes the evanescent decay of the excitation strength normal to the grating surface, (…)."*

57. Addition in Eq. (A2) on P. 74:

$$S_m(\omega) \propto e^{-2\kappa d}\left|\sum_{u=-N}^{(N-1)} e^{-i(\phi-2\pi m)u} \int_{-p/2}^{p/2} \mathrm{d}z e^{-i(\phi-2\pi m)\frac{z}{p}}\right|^2$$

58. Typo on p. 74: *"(…) where* ~~θ~~$\phi = \frac{\omega}{c}(n\sin\theta + \beta^{-1})p$*."*

- **Chapter 5.4 Numerical simulations:**

59. Typo on p. 81: *"(…), we introduce an analytical model that is based on a combination of a Gaussian and a Cauchy distribution with a joint FWHM* 2γ*."*

60. Correction of Eq. (5.1) on p. 81 (in accordance with the expression used in the data analysis and plotted in Figs. 5.3a, 5.4b and 5.5a):

$$I(U) = \frac{I_0}{2}\left[k\left(1 - \frac{2}{\pi}\arctan\left(\frac{(U_0 - U)}{\gamma}\right)\right) + (1-k)\left(1 - \mathrm{erf}\left(\sqrt{\ln 2}\,\frac{(U_0 - U)}{\gamma}\right)\right)\right]$$

- **Bibliography**

61. For a consistent citation style, replaced DOI identifier by the corresponding journal article number in references 16, 20, 27, 62, 69, 76, 94, 99, 100, 105, 112, 113, 120, 137, 138, 150, 164, 170, 173, 203, 205, 206, 207, 209, 214, 228, 232, 233, and 247.

62. Replaced article page number by the journal article number in references 28, 32, 40, 102, 133, 139, 140, 141, 152, 156, 162, 168, and 224.

63. Added electronic journal article number to reference 172.